Nanoconfinement modification of layered electrode materials: a pathway to enhanced ion transport and electrical conductivity for lithium- and sodium-ion batteries

Zur Erlangung des akademischen Grades eines

Doktors der Naturwissenschaften

(Dr. rer. nat.)

von der KIT-Fakultät für Chemie und Biowissenschaften
des Karlsruher Instituts für Technologie (KIT)

genehmigte

Dissertation

von

Mennatalla Elmanzalawy

KIT-Dekan: Prof. Dr. Martin Bastmeyer
1. Referent: Dr. Simon Fleischmann
2. Referent: Prof. Dr. Jens Tübke
Tag der mündlichen Prüfung: 12.12.2024

Table of Contents

Kurzfassung 4
Abstract 6
1. Motivation 8
2. Introduction 12
2.1 Basics of intercalation in lithium-ion batteries 12
2.2 Ion-solvent cointercalation 14
2.3 Electrode materials in sodium-ion batteries 16
2.4 Nanoconfinement in layered titanates 18
2.5 Organic interlayer functionalization of layered materials 20
2.5.1 Structure of interlayer-functionalized materials 21
2.5.2 Properties of interlayer-functionalized materials 41
2.5.3 Challenges and outlook of organic interlayer functionalization 51
2.6 Organically pillared materials as precursors of carbon nanocomposites 53
3. Objectives of the dissertation 55
4. Theory: Techniques and Instruments 57
4.1 Physicochemical Techniques 57
4.1.1 X-ray Diffraction (XRD) 57
4.1.2 Fourier Transform Infrared Spectroscopy (FTIR) 58
4.1.3 Raman Spectroscopy 60
4.1.4 Thermogravimetric Analysis 61
4.1.5 Scanning Electron Microscopy 62
4.1.6 Atomic Force Microscopy 64
4.1.7 Transmission Electron Microscopy 65
4.1.8 Electrochemical Quartz Crystal Microbalance 67
4.2. Electrochemical techniques 69
4.2.1 Electrochemical Cell Setups 69
4.2.2 Cyclic Voltammetry 70
4.2.3 Galvanostatic Charge and Discharge 71
4.2.4 Electrochemical Impedance Spectroscopy 73
5. Materials and Methods 75
5.1 Materials and methods for the study on: nanoconfinement-induced electrochemical ion-solvent cointercalation into layered titanate host materials 75
5.1.1 Materials synthesis 75
5.1.2 Structural and morphological characterization 75
5.1.3 Electrochemical characterization 77
5.2 Materials and methods for the study on: pillared layered titanates promote fast Na-ion intercalation 79

5.2.1 Materials synthesis 79
5.2.2 Structural and morphological characterization 79
5.2.3 Electrochemical characterization 80
5.3 Materials and methods for the study on: Mechanistic understanding of microstructure formation during synthesis of metal oxide/carbon nanocomposites 81
5.3.1 Materials synthesis 81
5.3.2 Structural and morphological characterization 82
5.3.3 Electrochemical characterization 83
6. Results and Discussion 85
6.1 Nanoconfinement-induced electrochemical ion-solvent cointercalation into layered titanate host materials 86
6.1.1 Physicochemical characterization 87
6.1.2 Electrochemical characterization 94
6.1.3 Conclusion 103
6.1.4 Supporting information 104
6.2 Pillared layered titanates promote fast Na-ion intercalation 110
6.2.1 Physicochemical characterization 111
6.2.2 Electrochemical characterization 113
6.2.3 Conclusion 116
6.2.4 Supporting information 118
6.3 Mechanistic understanding of microstructure formation during synthesis of metal oxide/carbon nanocomposites 122
6.3.1 Structural characterization 123
6.3.2 Electrochemical characterization 134
6.3.3 Conclusion 138
6.3.4 Supporting information 140
7. Summary and Conclusions 151
List of Abbreviations 153
List of Figures 156
References 168
List of Publications 198
Conferences and Symposia Contributions 200
Acknowledgements 202

Kurzfassung

Der Übergang zu erneuerbaren Energien erfordert die Entwicklung fortschrittlicher Batterien mit innovativen Elektrodenmaterialien, die in der Lage sind, wichtige Einschränkungen wie den trägen Ionentransport und die schlechte elektrische Leitfähigkeit zu überwinden. In dieser Dissertation wird eine neuartige Strategie zur Bewältigung dieser Herausforderungen vorgeschlagen, indem die Nanoconfinement-Bedingungen von schichtstrukturierten, Übergangsmetalloxid-basierten Elektrodenmaterialien verändert werden. Es werden organische Moleküle als „Pillars“ in die Zwischenschichtgalerien der Elektroden eingebaut, wodurch die Zwischenschichtabstände vergrößert und breitere Diffusionskanäle geschaffen werden. Mithilfe einer Reihe fortschrittlicher Charakterisierungsmethoden zeigt diese Arbeit, dass der Pillaring-Ansatz die Interkalation von solvatisierten Lithiumionen fördert, wobei der Mechanismus der Ionen-Lösungsmittel-Kointerkalation zu einer verbesserten Ratenleistung beiträgt und den Betrieb bei niedrigen Temperaturen ermöglicht. Der Pillaring-Ansatz ist auch im Natrium-Ionen-System wirksam, wo die aufgeweitete Struktur im Vergleich zur unmodifizierten Struktur eine verbesserte Natrium-Ionen-Transportkinetik aufweist.

Neben der Verbesserung des Ionentransports können die organischen Moleküle auch als Präkursoren für die Bildung von Kohlenstoff-Metalloxid-Nanokompositen mit verbesserter elektrischer Leitfähigkeit dienen. Durch einen Pyrolyseprozess werden die organischen Moleküle in eine Kohlenstoffphase umgewandelt, die in Metalloxid-Nanodomänen eingeschlossen ist. Diese Nanokompositstruktur weist nicht nur eine höhere elektrische Leitfähigkeit auf, sondern verbessert auch das Ratenverhalten und die Coulomb-Effizienz sowohl bei Interkalations- als auch bei Umwandlungsreaktionen. Es wird eine detaillierte mechanistische Studie vorgestellt, die die mikrostrukturelle Entwicklung während der Bildung des Nanokomposits sowie eine umfassende elektrochemische Analyse aufzeigt und wertvolle Erkenntnisse für die Entwicklung von Metalloxid-Kohlenstoff-Nanokompositen durch Pyrolyse mit maßgeschneiderten Mikrostruktureigenschaften liefert.

Zusammenfassend zeigt diese Dissertation, dass die Modifizierung der Nanoconfinement-Umgebung in schichtstrukturierten Metalloxiden mit Hilfe organischer Moleküle ein effektiver Ansatz zur Verbesserung des Ionentransports und zur Synthese von Metalloxid-

Kohlenstoff-Nanokompositen mit hoher elektrischer Leitfähigkeit ist. Dieser Ansatz bietet einen vielversprechenden Weg zur Überwindung der Limitationen des Ionentransports und der elektrischen Leitfähigkeit in schichtstrukturierten Elektrodenmaterialien und trägt damit zur Entwicklung von Batteriematerialien der nächsten Generation bei.

Abstract

The transition towards renewable energy requires the development of advanced rechargeable batteries. Innovative electrode materials play a key role in overcoming the limitations of current state-of-the-art batteries related to ionic and electronic transport. This dissertation proposes a novel strategy to address these challenges by modifying nanoconfinement conditions in layered electrode materials based on transition metal oxides. Specifically, organic pillar molecules are incorporated within the metal oxide interlayer galleries, expanding the interlayer spacing and creating wider diffusion channels. Using a range of advanced characterization methods, this work demonstrates that the pillaring approach promotes the intercalation of solvated lithium ions, where the ion-solvent cointercalation mechanism contributes to improved rate performance and enables low temperature operation. The interlayer pillaring strategy is also effective when lithium is replaced by sodium-ion charge carriers. Here, the pillared metal oxide structure enables enhanced sodium-ion diffusion kinetics and initial Coulombic efficiency compared to the unmodified structure.

In addition to improving ion transport, organic pillar molecules can serve as a precursor for the formation of carbon-metal oxide nanocomposites with enhanced electrical conductivity. Through a pyrolysis process, the organic pillars are converted into a carbon phase, confined within metal oxide nanodomains. This nanocomposite structure not only exhibits higher electrical conductivity, but also delivers improved rate capability and Coulombic efficiency of both intercalation and conversion reactions. A detailed mechanistic study is presented, elucidating the microstructural evolution during nanocomposite formation, alongside a comprehensive electrochemical analysis. This provides valuable insights for the design of metal oxide-carbon nanocomposites through pyrolysis with tailored microstructure properties.

In summary, this dissertation demonstrates that modifying the nanoconfinement environment in layered metal oxides using organic pillar molecules is an effective approach to enhance ionic transport and to synthesize metal oxide-carbon nanocomposites with high electrical conductivity. This approach offers a promising pathway to overcome ion transport and electrical conductivity limitations in layered metal oxide-based electrode materials, contributing to the development of next-generation battery materials.

1. Motivation

Climate change poses an urgent and complex challenge, threatening not only the environment but also the world's economic, political, and ecological systems. Human activities, particularly the reliance on fossil fuels for energy generation, have dramatically increased the concentration of greenhouse gases in the atmosphere, leading to widespread changes in climate patterns. Over the last decade alone, the average global surface temperature has risen by 2 °C above the pre-industrial average (**Fig. 1.1**).[1] This rapid temperature increase exacerbates extreme weather events, rising sea levels, and loss of biodiversity. The pressing need to mitigate the effects of climate change has brought about a global effort to transition towards alternative energy sources that can reduce our dependence on fossil fuels and cut greenhouse gas emissions.

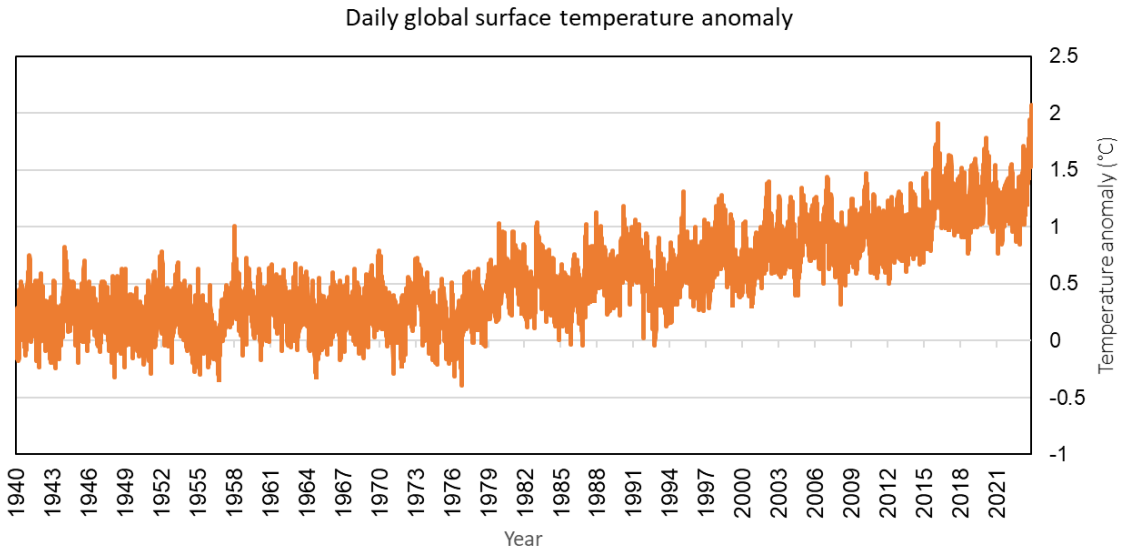

Figure 1.1: Global surface air temperature anomalies from January 1940 to November 2023, with reference to the 1850-1900 (pre-industrial period). Data from the European Centre for Medium-Range Weather Forecasts (ECMWF), Copernicus Climate Change Service (2023).

The Paris Agreement, signed in 2015, aims to limit global temperature increase below 2 °C with respect to pre-industrial levels, with efforts to further reduce it to 1.5 °C.[2] However, reaching this ambitious target requires drastic and sustained efforts to reduce emissions, mainly by transitioning away from fossil fuel-based energy sources to renewable ones.

Renewable energy sources such as wind, solar, and hydropower have emerged as alternatives to fossil fuels. However, a key challenge associated with renewable energy is its intermittent nature. As the reliance on renewable energy grows, so does the need for efficient storage technologies that can store surplus energy when generation exceeds demand and release it when needed. Energy storage options are numerous and include mechanical systems, such as pumped hydro, compressed air energy storage (CAES), and flywheels, as well as electrical solutions such as superconductive magnetic energy storage (SMES), and electrochemical devices such as batteries and supercapacitors.[3] Among the most important performance indicators of energy storage devices are their specific energy and power. These metrics are often displayed in a Ragone plot (**Fig. 1.2**).

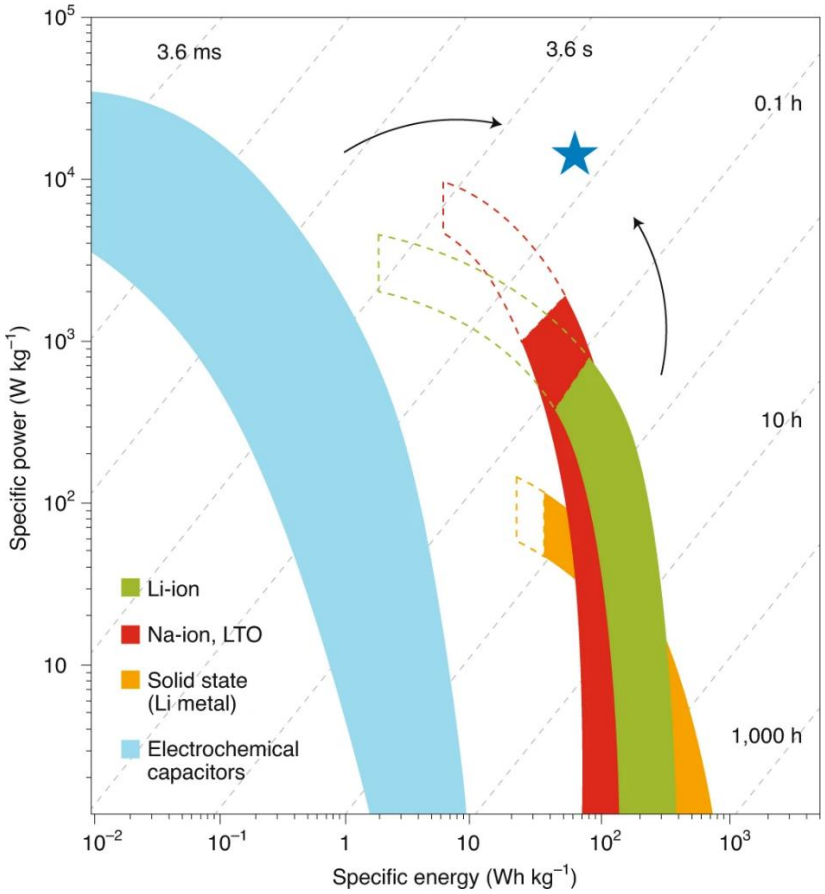

Figure 1.2: Ragone plot showing the status of power vs. energy densities of various electrochemical energy storage systems. The arrows depict the trend towards higher specific power for batteries and higher specific energy for electrochemical capacitors. Diagonal lines represent the time constant (operation time). Reproduced from Ref.[4] with permission, copyright © 2020, Springer Nature Limited.

When comparing different electrochemical energy storage devices, batteries fall within the high specific energy region. However, their specific power is limited, with typical durations for a full charge/discharge cycle of up to several hours.[4] Electrochemical capacitors are characterized by high specific power, but lower energy density compared to batteries, with operation times ranging from a few seconds to minutes. The increasing demand for reliable energy storage systems has led to significant advancements in electrochemical devices, particularly in batteries and supercapacitors, with research efforts aiming to increase either the specific power of batteries or the specific energy of electrochemical capacitors, approaching a balance between high specific power and specific energy as exemplified by the star on the Ragone plot.

Batteries are instrumental in the world's transition to clean energy. The lithium-ion battery (LIB) technology was commercialized in the 1990s and has since then played a crucial role in the global shift toward clean energy, especially in the transportation sector, where they power electric vehicles (EVs), reducing emissions and dependence on fossil fuels compared to vehicles using internal combustion engines.[5]

Because state-of-the-art LIBs rely heavily on critical resources, alternative battery chemistries, such as the sodium-ion battery (NIB), have been introduced as a more sustainable option, particularly for large-scale energy storage. In both LIBs and NIBs, layered materials represent an important class of electrode materials that are being widely explored. These materials are characterized by a structure that allows the reversible insertion of ions between the layers during charge and discharge cycles, enabling electrochemically driven oxidation and reduction reactions through which electrons are transferred. However, such reactions in layered materials are often kinetically limited by sluggish solid-state diffusion of ions within the interlayer space of these materials and/or the poor electrical conductivity of electrodes. Common strategies to solve ion diffusion limitations include nanosizing and morphology control, which shorten diffusion pathways and enhance solid-state ion transport.[6] To address the challenge of electrical conductivity, strategies such as applying conductive coatings, forming composites, and introducing dopants are commonly employed.[6]

Besides their chemical composition, the electrochemistry of such layered materials is also determined by the properties of the space confined between their individual layers, i.e.,

their interlayer space, where electrolyte ions are stored/released.[7] In this context, nanoconfinement refers to the spatial restriction of ions or molecules within nanosized pores or slits, which can significantly influence their behaviour during electrochemical redox reactions. Altering the nanoconfinement environment in layered materials therefore offers wide-ranging possibilities to influence various properties of the electrochemical intercalation process, including ion diffusion kinetics and charge storage mechanisms.[7]

Studying nanoconfinement in layered electrodes targets not only ion transport, but also electrical conductivity. This thesis shows that, by introducing carbon as a nanoconfined conductive species within the nanodomains of an electrode material, electrical conductivity can be greatly enhanced, addressing another common limitation of layered electrode materials.

In summary, the urgent need to address climate change and transition to a clean energy future has placed electrochemical energy storage at the forefront of scientific and technological innovation. Developing advanced electrode materials, particularly through the manipulation of nanoconfinement in layered structures, represents a promising strategy for addressing ionic and electronic transport limitations. The continued research and development of innovative electrode materials is pivotal in realizing a sustainable energy future and addressing the global threat of climate change.

2. Introduction

2.1 Basics of intercalation in lithium-ion batteries

Electrochemistry is the field describing chemical relationship involving electron transfers that are driven by an electrical potential difference. Electrochemical energy storage devices, such as batteries, rely on such oxidation and reduction reactions that reversibly convert chemical energy into electrical energy and vice versa. These devices are capable of storing (charging) and releasing (discharging) energy as needed, making them essential for various applications.

Among rechargeable batteries, the lithium-ion battery (LIB) stands out due to its high energy density and long cycle life.[8] LIBs are widely found in consumer electronics, electric vehicles, and renewable energy storage systems. The operation of a LIB relies on the shuttling, or "rocking," of lithium ions between two electrodes: the anode and the cathode. This rocking chair mechanism is enabled by intercalation – a process that is essential for modern-day batteries.

Intercalation is defined as the reversible insertion of guest species—such as ions, atoms, organic and inorganic molecules—into the vacant sites of a layered crystalline solid lattice. This process forms the foundation for contemporary electrochemical energy storage devices.[9] Layered materials are particularly important as intercalation hosts due to their ability to accommodate a variety of guest species.[10] The interaction between guest and host can vary broadly, encompassing weak van der Waals interactions as well as metallic, ionic, and covalent bonding.[11]

Intercalation reactions are ideally topotactic, meaning they involve reversible changes in the structural lattice parameters and bond lengths without causing diffusive rearrangement of host atoms.[12] However, this reversibility is often challenged by thermodynamic or kinetic constraints, limited by the structural stability of the host material in the forward and reverse reactions.[13] The intercalation of a guest species A into a host matrix B can be described by the reaction:

$$xA + \square_y[B] \leftrightarrow A_x\square_{y-x}[B] \qquad \textbf{(2.1)}$$

where □ is a vacant lattice site.[13]

In LIBs, intercalation reactions enable the reversible storage of Li ions into the anode and the cathode. The anode in most commercial lithium-ion batteries is made of graphite. During the discharging process, lithium ions move from the anode to the cathode. This process is reversible, meaning lithium ions re-insert into the graphite during charge.

The reaction at the anode during discharge can be expressed as:

$$LiC_6 \rightarrow C_6 + Li^+ + e^- \qquad \textbf{(2.2)}$$

Here, lithium ions (Li^+) leave the anode and transport through the electrolyte toward the cathode, while electrons move through the external circuit, providing electrical energy (**Fig. 2.1**).

On the other hand, the cathode is often composed of a layered transition metal oxide (TMO), such as lithium cobalt oxide ($LiCoO_2$). During discharge, lithium ions insert into the cathode material, coinciding with the reduction of the transition metal in the cathode. The reaction at the cathode during discharging can be written as:

$$Li_{x-n}MO_2 + nLi^+ + ne^- \rightarrow Li_xMO_2 \qquad \textbf{(2.3)}$$

Here, MO_2 represents the transition metal oxide, and n is the number of lithium ions released or inserted during the charge and discharge processes.

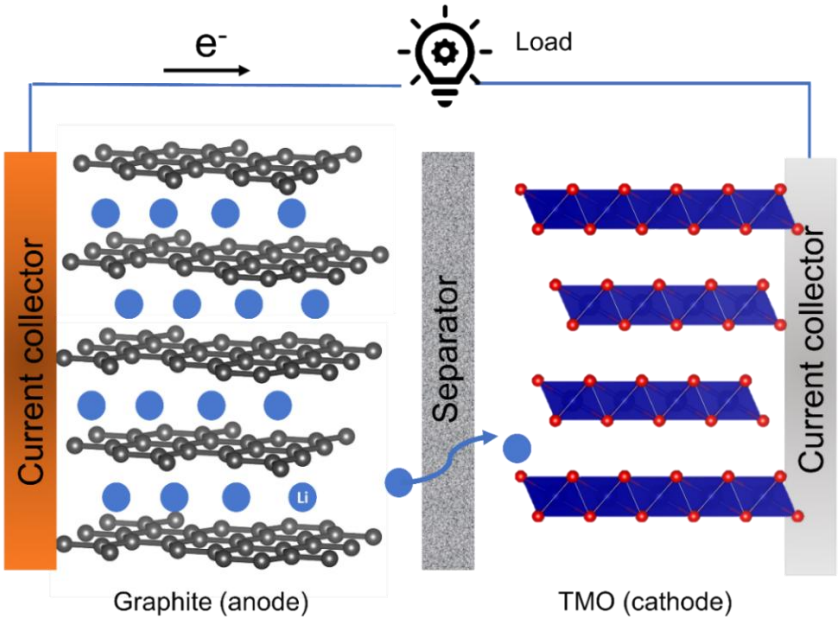

Figure 2.1: Schematic illustration of the cell setup of a lithium-ion battery.

2.2 Ion-solvent cointercalation

Electrochemical intercalation reactions consist of steps involving a) the transport of solvated ions from the electrolyte bulk to the interface, b) full or partial desolvation of ions at the interface, c) surface transport through the interphase layer to an insertion site, and d) solid-state diffusion of the intercalant through the host lattice to a vacant site (**Fig. 2.2**). The processes of desolvation and diffusion through the interphase are collectively termed the "charge transfer step". When intercalation reactions involve the insertion of multiple species (i.e., ions and solvents) into the host lattice, it is known as cointercalation, resulting in the formation of ion-solvent-host ternary intercalation compounds.[14]

The kinetics of the charge transfer step are influenced by the desolvation of the intercalating ion at the electrode-electrolyte interface. Full desolvation of the ion requires overcoming substantial energy barriers. Thus, the cointercalation phenomenon allows for the intercalation of (partially) solvated ions, with minimal reorganization of the solvation sheath.[14] This reduces the charge transfer resistance, enabling fast charging batteries.

The presence of a (partial) solvation sheath can shield Coulombic interactions between the intercalating ions and the host material, enabling multivalent ion intercalation. Moreover, reducing charge transfer resistance becomes particularly important during low temperature operation, where overcoming the high energy barriers required for desolvation becomes more difficult.

The ion-solvent cointercalation phenomenon can be triggered by two approaches: a) electrolyte formulation, by selecting strongly solvating solvents, or adjusting electrolyte composition (higher salt concentrations reduce solvation numbers due to increased ion pair interactions), and b) controlling the electrode host's nanoconfinement properties: tuning the interlayer distance or pore size allows for the accommodation of large ion-solvent complexes, and incorporating functionalities with adjustable polarity can enable matching the interlayer chemistry with the solvent.[14] Using either of these approaches, or a combination of them, can promote (or inhibit) ion-solvent cointercalation, creating opportunities for developing new cell chemistries, enabling fast charging kinetics, and allowing a broader temperature range operation.

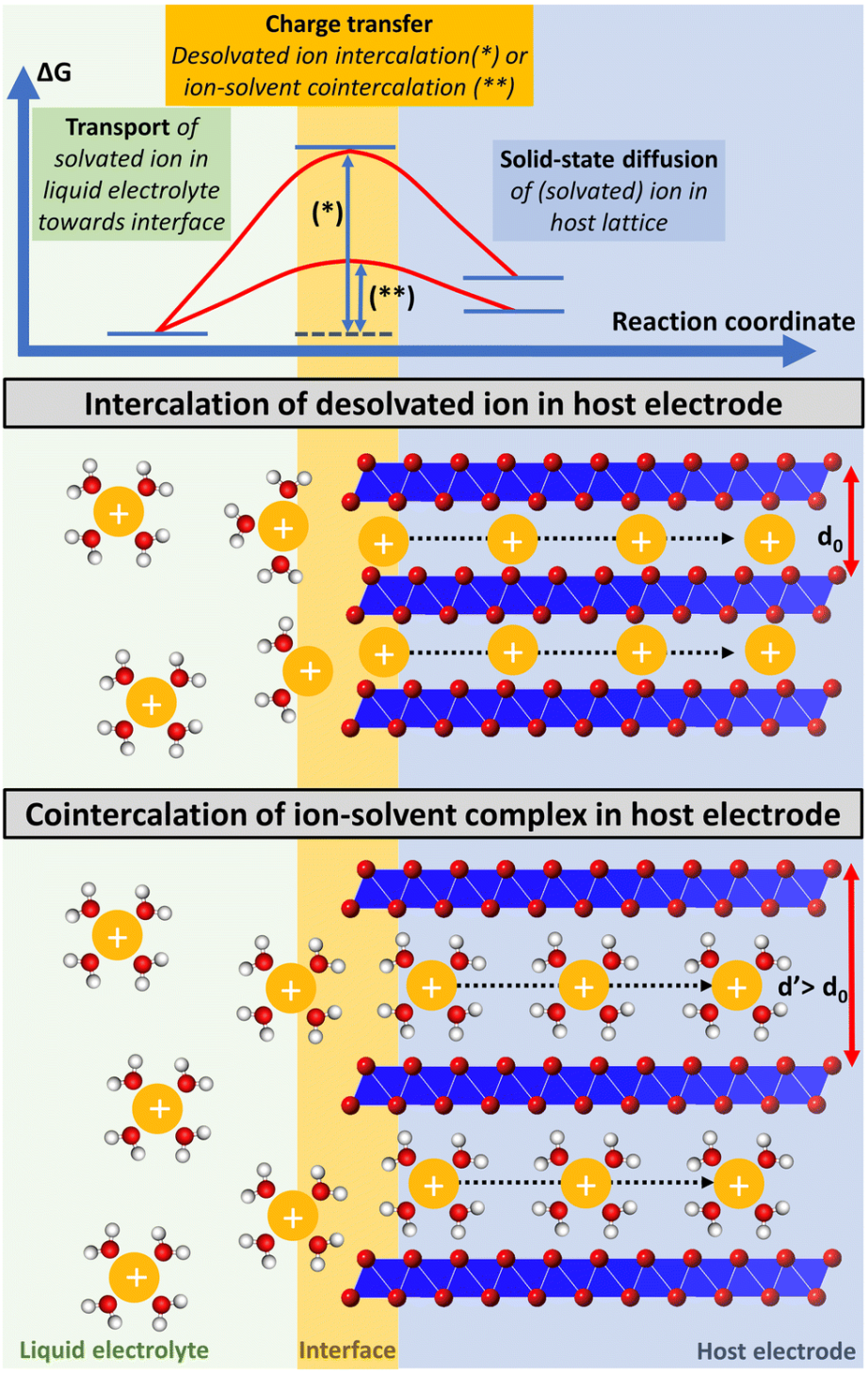

Figure 2.2: Exemplary energetic profile of a transition state for an intercalant during the charge transfer step, which is reduced for cointercalation. Schematic representation of a multi-step electrochemical (co-) intercalation process. In this process, solvated ions first transport through the liquid electrolyte towards the electrochemical interface, where ions either (partially) retain their solvation sheath (cointercalation) or shed it during the charge transfer step. The ions finally diffuse through the solid-state host to occupy a vacant lattice site. Reproduced with permission from Ref.[14,15] © The Royal Society of Chemistry 2024.

2.3 Electrode materials in sodium-ion batteries

Since their introduction to the market in the 1990s,[16] LIBs have enabled several modern-day technologies, relying on critical mineral such as lithium, cobalt, and nickel.[17] However, the increasing strain on lithium supplies, coupled with the demand for more sustainable energy solutions, drives the need for other material chemistries, particularly sodium ion batteries (NIBs). This need is especially critical for large-scale grid storage systems, where the energy density is not the most crucial parameter, and the abundance and lower cost of sodium and its compounds make it a promising candidate. For these reasons, there is a growing exploration of alternative intercalation chemistries to meet the evolving needs of energy storage devices.

NIBs have gained significant attention due to the wide availability and cost-effectiveness of sodium-containing compounds. Recently, large-scale production of Na-ion batteries was reported for the first time, motivating further research into advanced electrode materials.[18] Similar to LIBs, NIBs operate on the principle of intercalation electrodes, enabling a "rocking chair" mechanism where the ions shuttle back and forth between an anode and a cathode. A key challenge in advancing Na-ion batteries is identifying electrode materials with high Na-ion intercalation capacities at low potentials. This comes with challenges due to the larger ionic radius of Na^+ compared to Li^+, exemplified by the rather poor stability of Na_xCoO_2 cathodes due to multiple phase transitions compared to the stable performance of Li_xCoO_2.[19] Several suitable cathode materials have been identified, such as sodium layered oxides like $Na_xMn_yNi_zFe_{0.1}Mg_{0.1}O_2$,[20] polyanionic NASICON-like phases such as $Na_3V_2(PO_4)_3$,[21] and framework materials like Prussian blue analogues.[19]

Despite the success in identifying Na-ion intercalation cathodes, the options for anodes remain relatively limited. Current options are primarily categorized into alloying materials, carbon-based materials, titanium-based materials, and some metal oxides and sulfides (**Fig. 2.3**). Although alloying and conversion anodes can deliver high capacities, they are prone to large volumetric expansions and low cycle life due to particle pulverization during cycling.[22] This highlights the importance of intercalation anodes, which typically offer more stable performance. Sodium does not intercalate into graphite in its bare form, and research on sodium ion anodes has focused on hard carbons, which can uptake Na ions to varying degrees. However, the low sodiation potential of hard carbon anodes in non-

aqueous electrolytes (close to 0 V vs. Na^+/Na) raises important safety concerns because of the risk of sodium plating, particularly during fast charging. .[23] A possible alternative to carbon anodes is layered titanates, which have shown ability for sodium intercalation at moderately low potentials (0.3 V vs. Na^+/Na for $Na_2Ti_3O_7$),[24] and even near zero-strain intercalation properties such as in $K_2Ti_4O_9$.[25]

The versatility, low toxicity, and ease of synthesis of layered titanates have made them attractive candidates for use as sodium intercalation anodes. Extensive research has been conducted on sodium titanates, particularly the low voltage $Na_2Ti_3O_7$, and their application as sodium ion insertion anodes.[24,26–28] A large portion of such research has focused primarily on exploring new phases, capitalizing on the rich chemistries offered by ternary[24] and quaternary[27] layered titanates, to discover phases with lower intercalation potentials,[26] and minimal lattice strain.

Overall, the development of high-performance Na-ion anodes remains a challenge. Despite the widespread use of hard carbons, layered titanates have emerged as an alternative due to their safety, low toxicity, and ability to intercalate sodium at relatively low potentials. Future research on sodium-ion anodes should focus on further exploring titanate-based materials to fully realize their potential.

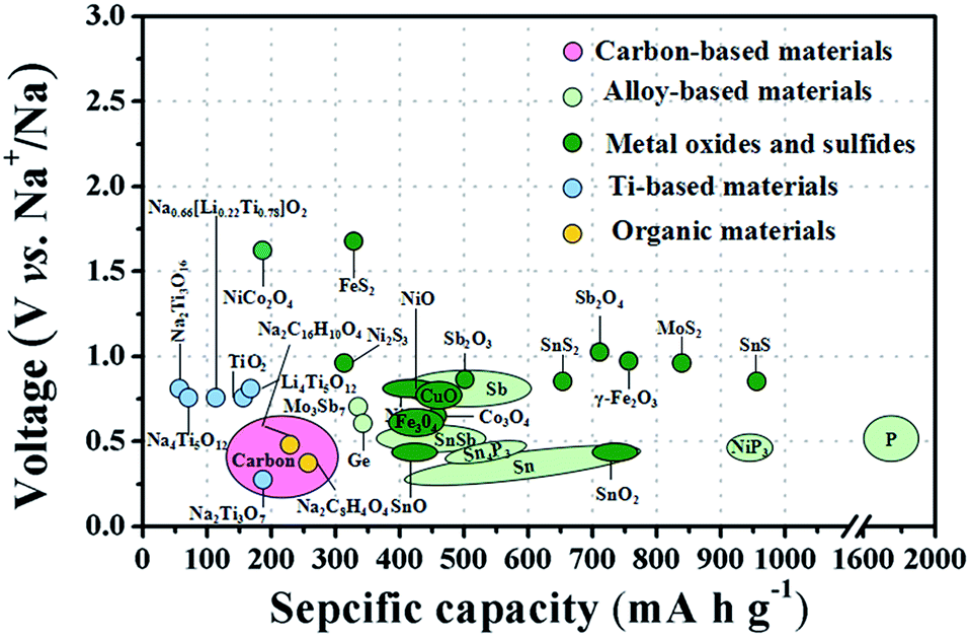

Figure 2.3: Average voltages and specific capacities of anode materials for NIBs. Reproduced from Ref.[29] with permission from the Royal Society of Chemistry.

2.4 Nanoconfinement in layered titanates

Layered transition metal oxides (TMOs) are common intercalation hosts utilized as cathode materials, and also serve as alternatives for carbon-based anode materials in both lithium- and sodium-ion batteries. Among them, titanate-based materials have attracted interest due to their relative abundance, low toxicity and structural/chemical tunability. They can often serve as host structures for both lithium- and sodium-ions making them highly versatile.[30–32]

Hydrogen titanates are a family of metastable materials derived from layered alkali titanates.[33,34] They are typically synthesized in acidic solution by etching and topotactic exchange of the alkali ion in the interlayer space by protons and/or water.[34–36] This provides them with a high degree of structural/chemical tunability of their nanoconfined interlayer composition, comparable to two-dimensional $Ti_3C_2T_x$ MXenes derived via a similar selective etching approach.[37,38] These materials' nanoconfinement environment, in turn, can have an effect on their electrochemical ion intercalation properties.[39–41]

In the layered hydrogen titanate $H_2Ti_3O_7$, it was found that confined interlayer protons are the determining structural feature to enable electrochemical H^+ intercalation.[42] This is because they separate the titanate layers, allowing to effectively compensate electrochemically induced strain by contraction/expansion without altering intralayer structure.[42] Interlayer-expansion of layered titanate hollow spheres by confined Mg^{2+} ions was demonstrated as a design strategy for electrochemical Na^+ intercalation hosts.[43] An investigation into different types of confined alkali ions (Li^+, Na^+, K^+, Cs^+) within lepidocrocite-type layered titanates revealed that the interlayer spacing is expanded with increasing ion size (0.68 to 0.85 nm).[44] However, sodium-modified titanate showed the highest capacity for electrochemical Na^+ intercalation hosts (153 mAh g^{-1}), even though this material has a smaller interlayer spacing than the cesium-modified titanate (95 mAh g^{-1}), demonstrating the importance of nanoconfinement chemistry in addition to just geometrical considerations.[44] In the layered hydrogen titanate $H_2Ti_2O_5$ system, it was found that K^+ intercalation can be accomplished most efficiently, especially at low temperatures (-40 °C), for the material with confined interlayer water ($H_2Ti_2O_5 \cdot H_2O$, "HTO"), compared to its dehydrated form with additional interlayer defects ("QTO") that also exhibits smaller interlayer spacing (0.78 nm for QTO vs. 0.84 nm for HTO).[45] The authors attribute this to ion-solvent cointercalation from the organic electrolyte into HTO, which is enabled by

strong K^+/1,2-dimethoxyethane binding energy (electrolyte effect) and a charge shielding effect of confined interlayer H_2O (electrode effect).[45]

Besides interlayer modification of layered titanates with simple cations or crystal water, the introduction of organic pillar molecules like alkylamines offers an even wider materials design space.[46–49] So far, to the best of our knowledge, only one study probed the electrochemical ion intercalation properties in *n*-alkylamine pillared hydrogen titanate.[50] The authors hypothesize that new ion storage sites can be created near alkyl chains in the expanded interlayer space, but the hydrophobicity of such chains may hinder ion diffusion.[50] However, the electrochemically induced volumetric expansion/contraction behavior or the possibility of solvent cointercalation in the widened interlayer galleries were not considered.

The studies demonstrate that there is a strong effect of the titanates' nanoconfined interlayer environment (geometry and chemical composition) on their electrochemical ion intercalation properties (**Fig. 2.4**). Interlayer modification by introduction of simple cations and/or larger molecules can influence diffusion barriers, storage sites, electrochemically-induced volume expansion, or induce ion-solvent cointercalation with a reduced charge transfer resistance.[51] However, no clear materials design rules for titanate intercalation hosts have emerged so far. Specifically, there is an urgent need to identify how electrochemically induced strain is compensated in strongly expanded / pillared titanates and whether layer-separating or cross-linking pillaring approaches favor electrochemical kinetics. Furthermore, the nature of intercalating species as a function of nanoconfinement properties must be analyzed with potential interactions between electrolyte solvent and strongly expanded interlayers.

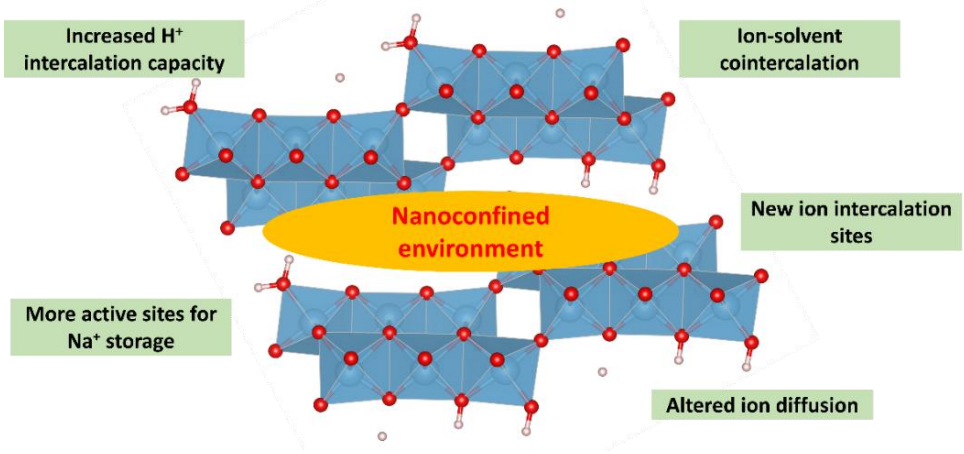

Figure 2.4: Nanoconfinement effects in layered titanates.

2.5 Organic interlayer functionalization of layered materials

This section is reproduced from the review article "Organic interlayer functionalization of layered materials", in preparation.

In energy storage applications, the interlayer galleries in layered materials function as diffusion channels for ionic species. While the electrochemical insertion of ions into layered materials is typically termed intercalation, tuning the interlayer environment by inserting ions or molecules is a deliberate chemical modification of the layered material, and is commonly referred to as *interlayer modulation*,[52] *interlayer engineering*,[53] *pillaring*,[54,55] or *interlayer doping*.[56] For consistency, this dissertation will use the term "*interlayer functionalization*" to refer to this process. When organic ions or molecules are used for this modification, the resulting compounds are sometimes referred to as "*organic-inorganic hybrids*",[57] "*hybrid superlattices*",[58] or "*interlayer expanded materials*".[59]

Interlayer functionalization and can significantly impact the physiochemical and electrochemical properties of the layered material. This includes improving ion diffusion kinetics,[60] stabilizing the layered host structure,[61,62] and improving the electronic conductivity.[63] The functionalization of the layered materials can be achieved by introducing ionic, organic, or inorganic species.

There are various examples in the literature where interlayer engineering of layered materials was explored, mainly using ions or water molecules as interlayer pillars, with organic molecules only briefly mentioned.[52,64–67] This chapter uniquely emphasizes the broad potential of organic molecules as pillars across various types of layered hosts. As outlined in **Fig. 2.5**, first, the structure of pillared electrodes is discussed, highlighting the intricate nature of host-pillar interactions. Then, the properties of pillared electrodes are summarized, particularly highlighting the influence of interlayer functionalization on ion intercalation, structure stability of the layered host, and stability of the pillar molecule. Finally, we explore the challenges and future directions in organic interlayer functionalization, underscoring its versatility and paving the way for innovations in the design of advanced layered electrodes for ion intercalation-based energy storage devices.

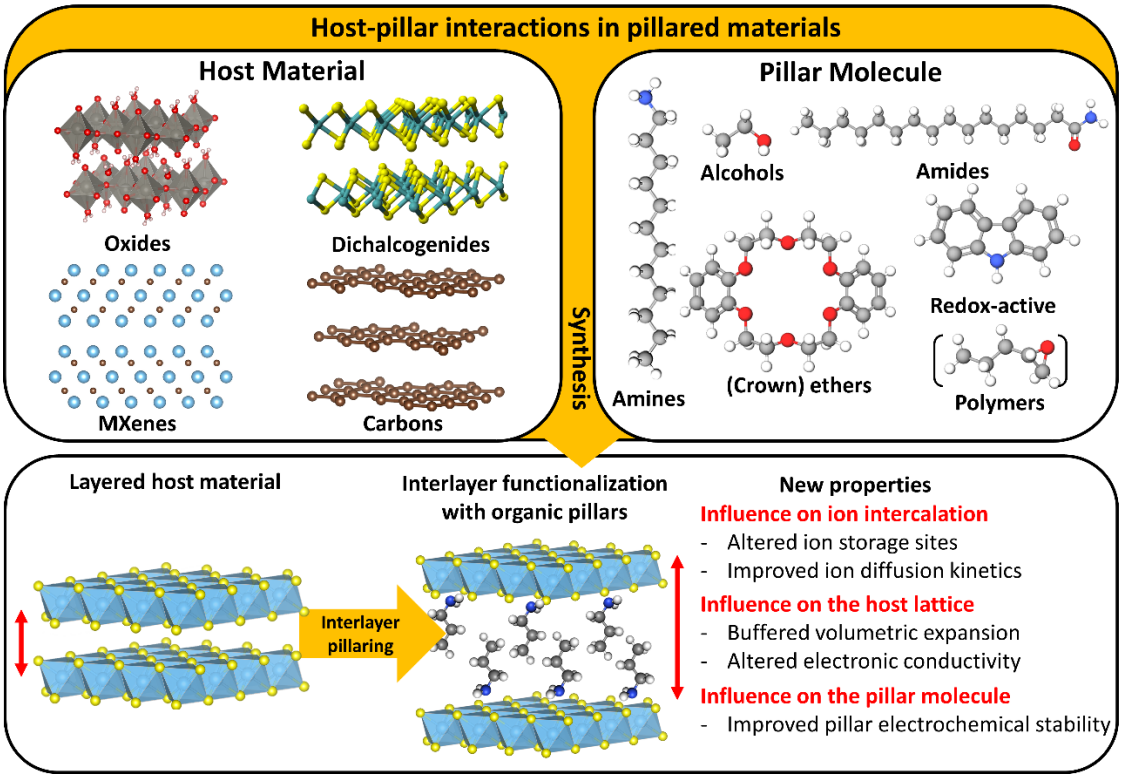

Figure 2.5: Schematic illustration of the main topics discussed in this section, covering pillared layered electrode structures and host-pillar interactions. New properties arising from the functionalization of the layered structures with organic molecules are highlighted, and characterization methods specific to them are discussed.

2.5.1 Structure of interlayer-functionalized materials

The abundance of layered materials capable of electrochemically intercalating ionic species has driven extensive exploration of their structural and electrochemical properties. Due to their inherent chemical and structural differences, different subclasses of layered materials require specialized synthesis methods for effective interlayer functionalization with organic molecules. For instance, layered oxides typically contain negative surface terminations, and often house exchangeable water molecules within the interlayer space.[68] In contrast, layered chalcogenides typically feature more inert, dangling bond-free surfaces.[69] These differences lead to diverse host-pillar interactions, ranging from ionic and covalent bonding to weaker hydrogen bonding and van der Waals interactions. This section provides an overview of the key attributes of various types of interactions between organic pillar molecules and layered hosts, highlighting the structural and electrochemical implications of these combinations.

2.5.1.1 Covalent host-pillar interactions

Covalent interlayer functionalization in transition metal dichalcogenides

Transition metal dichalcogenides (TMDs) are an important class of layered materials used in energy storage, exhibiting an MX_2 stoichiometry (where M is a transition metal and X is a chalcogen atom, such as S, Se, or Te). Notable examples of layered TMDs include MoS_2, TiS_2, and WS_2, which are commonly employed as electrodes for ion intercalation (**Fig. 2.6A**).

Interest in intercalation within layered TMDs sparked in the 1970s, when it was discovered that introducing organic molecules between the layers of metallic 2H TaS_2 could modify, and sometimes increase, its superconducting onset temperture.[70] A few years later, Li intercalation into TiS_2 was reported, leading to the first prototype Li-ion intercalation cathode.[71] Since then, numerous TMDs have been investigated as potential hosts for ion intercalation in electrochemical energy storage applications.

Interlayer functionalization of TMDs primarily aims to expand the *d*-spacing of the host structure, enhancing the kinetics of ion diffusion. In layered TMDs, the basal planes are typically inert,[69] and functionalization is believed to occur by the covalent attachment of organic molecules at chalcogen vacancies (**Fig. 2.6B**). Covalent bonding plays a critical role in ensuring higher stability of the pillared structures in different environments.[72] The degree of functionalization, defined by the number of functional groups per sulfur atom, can be tuned by inducing vacancy formation, allowing for greater control over the concentration of pillars in the functionalized material.[73]

The covalent functionalization of TMDs with amine-terminated molecules has been reported to occur through the interaction of nitrogen lone pairs with the transition metal atom.[74,75] However, group VI sulphides, such as MoS_2 are less likely to accept lone pair electrons due to their filled d_z band.[74] Therefore, the functionalization of group VI TMDs with amines requires additional steps, such as exfoliation or ion exchange of lithiated TMDs (**Fig. 2.6C**),[76] creating strong NH—S interactions that contribute to stabilizing the structure.[77] Other methods, such as *in situ* pillaring, involve introducing electrolyte additives that favourably bond to the TMD layers, contributing to stabilization and enhanced ion intercalation kinetics (**Fig. 2.6D**).[78]

The functionalization of TMDs with amides, while slower than with amines, also relies on covalent bonding (**Fig. 2.6B**).[74] For example, the functionalization of exfoliated MoS_2, WS_2, and $MoSe_2$ with amides is reported to proceed via reaction with amide-containing organohalides, such as iodoacetamide.[79] In this process, the halide atom acts as a leaving group and is absent from the final pillared structure. This covalent functionalization has been shown to improve ion rejection rates of membranes in water desalination systems.[80] These improvements in ion-sieving were attributed to nanoconfinement effects – a phenomenon that is also relevant when studying electrochemical ion intercalation in layered hosts.

Among the most commonly used pillar molecules in TMDs research are thiols (R—SH), which can covalently bond to chalcogen vacancies within the TMD layers.[81] These strong chemical bonds contribute to the stability and functionality of the TMD structure, allowing for the addition of other functional groups, such as $–NH_2$ and –F, which serve as dopants to fine-tune the electronic properties of TMDs (**Fig. 2.6E**).[82] This covalent bonding mechanism is crucial for optimizing TMDs, as it not only stabilizes the pillared structure but also enables the precise control over the host's electrical properties.

There is ongoing ambiguity regarding the interaction of organic pillars with TMD hosts, with some studies attributing it to strong covalent bonding and others to physisorption. Contradictory evidence for both mechanisms exists in the literature (**Fig. 2.6F**). For instance, two studies on the functionalization of MoS_2 with thiol-terminated cysteine have drawn different conclusions on the nature of bonding. Syari'ati et al. claimed covalent functionalization of 2H-MoS_2 by cysteine,[83] whereas a similar study by Chen *et al*. concluded that chemical modification of MoS_2 is unlikely and suggested that the cysteine itself might have undergone slight changes without forming chemical bonds with the host.[84] Both works based their conclusions on different interpretation of spectral data, leaving the type of bonding between thiol-terminated molecules and 2H-MoS_2 open to debate. Further research in area is necessary to resolve these discrepancies.

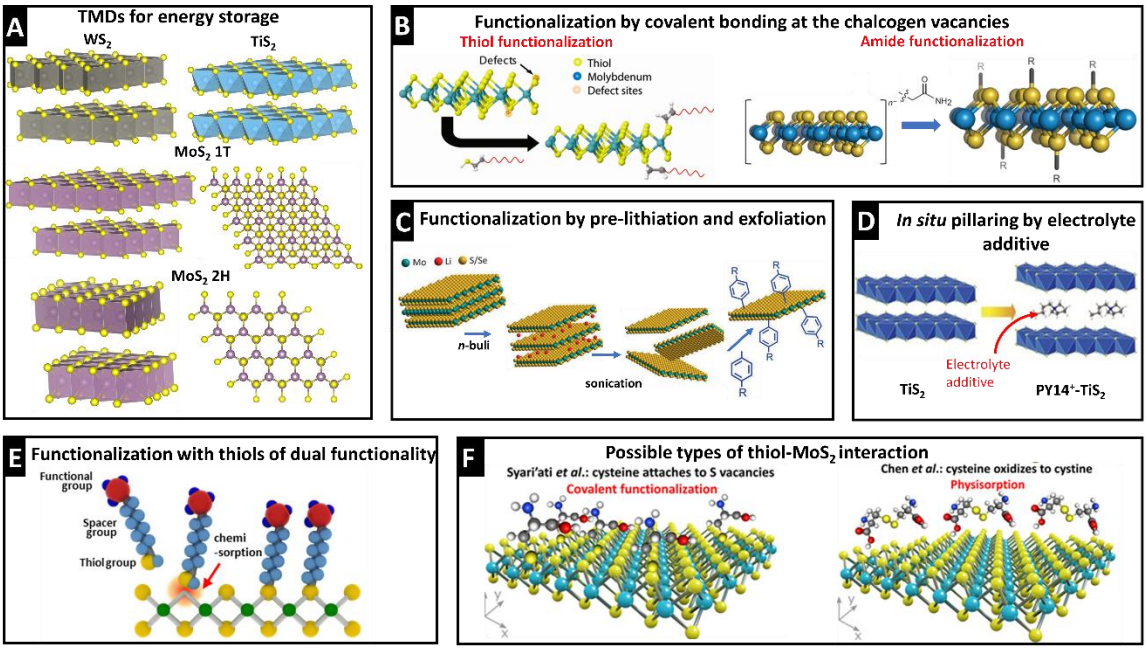

Figure 2.6: A) Structures of common layered TMD electrode materials. Illustrated using VESTA software with CIF data from the Materials Project.[85] B) Schematic illustrations of functionalization at the chalcogen vacancies and amide functionalization, reproduced from Ref.[79,86] with permission from Springer Nature Limited and Creative Commons public use license. C) Functionalization by a pre-lithiation step, adapted from Ref.[87] with permission from Wiley-VCH Verlag GmbH & Co. KGaA, Weinheim. D) *in situ* pillaring of TiS_2 by electrolyte additive, adapted with permission from Ref.[78] E) TMD functionalization with a dual functionality thiol, reproduced with permission from Ref.[82] Copyright © 2015 American Chemical Society. F) Schematic of possible thiol-MoS_2 interactions.

Covalent interlayer functionalization in layered carbon materials

Graphene, a two-dimensional material composed of sp^2-hybridized carbon atoms arranged in a honeycomb pattern, serves as the fundamental building block of various carbon-based materials of diverse dimensionalities (**Fig. 2.7A**).[88] The unique electronic conductivity and cost-effectiveness of graphene, along with its derivatives such as graphene oxide and graphite, make it highly valuable in energy storage applications.[89] However, pristine graphene is chemically inert, necessitating functionalization to adapt it for various applications.[88,90] Covalent functionalization is an important approach for modifying graphene and its related structures, enabling the integration of organic molecules through robust chemical bonds. This functionalization can occur at the reactive edges of graphene, where dangling bonds are present,[89] or on the basal plane through covalent attachment to sp^2 carbon atoms.[91]

Covalent interactions in graphene typically involve reactions between free radicals and C=C bonds, or between organic molecules and oxygen in graphene oxide. These reactions can occur through wet-synthesis techniques, such as in diazonium chemistry,[92] or hydrothermal methods.[93] Such covalent modifications are crucial for tuning graphene's properties, making it more versatile for various applications, particularly energy storage.

The applications of interlayer functionalization of carbon materials are particularly impactful in the field of ion intercalation research. While graphite is a well-known host for lithium intercalation, the reversible Na-ion intercalation in it is thermodynamically unfavourable. To address this limitation, a promising strategy involves expanding the interlayer spacing through covalent functionalization. Sun *et al*. demonstrated this by synthesizing a Janus graphene phase, where graphene sheets were asymmetrically functionalized with aminobenzene (AB) as a molecular pillar (**Fig. 2.7B**).[92] The resulting expanded structure enabled the study of bare Na^+ intercalation in stacked pillared graphene, a process not feasible in pristine graphite (see **section 2.5.2.1**).

Beyond intercalation batteries, covalent functionalization of graphene also finds notable applications in supercapacitors. For example, graphene oxide (GO) can be functionalized with a variety of water-soluble non-aromatic amines, such as ethylene diamine (EDA), butane-1,4-diamine (BDA), hexane-1,6-diamine (HDA), 1,4-cyclohexane diamine (CHDA), ether diamine (EA148), and tris(2-aminoethyl) amine (Tris) (**Fig. 2.7C**).[93] Following a hydrothermal reduction step, functionalized reduced graphene oxide (rGO) forms, with a slightly smaller *d*-spacing compared to functionalized GO (**Fig. 2.7D**). In this example, covalent functionalization with amine pillar molecules effectively prevents the agglomeration of rGO sheets, thereby stabilizing the pillared structure.

Despite the advantages of covalent functionalization of layered carbons, excessive expansion of interlayer gaps in these electrode materials can be detrimental. As the *d*-spacing expands, the interlayer space could turn into an electrolyte-accessible surface, leading to excessive solid electrolyte interface (SEI) formation.[94] Therefore, managing these undesired side effects of interlayer functionalization of graphite and other layered carbon materials is crucial.

In summary, the extensive study of covalent interlayer functionalization in graphene-based materials is motivated by their broad applications. Beyond energy storage, functionalized

graphene and its related pillared structures are employed in various fields, such as flexible electronics,[95] biosensors,[96] and organic pollutant management,[97] unlocking their potential in a wide range of advanced applications.

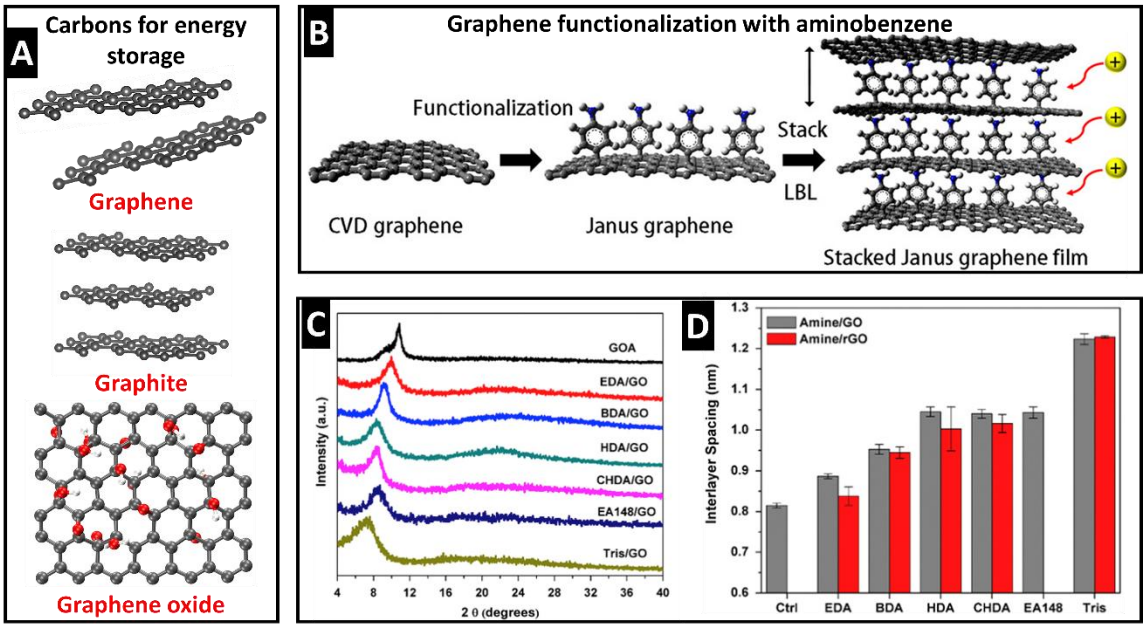

Figure 2.7: Covalent pillaring of layered carbon materials. A) Illustrations of carbon materials used in energy storage, drawn using VESTA. GO illustration was reproduced with permission from Ref.[98] Copyright © 2022, American Chemical Society. B) Schematic illustration of graphene functionalization yielding stacked Janus graphene films. Reproduced from Ref.[92] with permission from AAAS. C) XRD patterns of GO-amine compounds and D) *d*-spacing values of amine-GO and amine-rGO pillared compounds (i.e., before and after the reduction of GO). Reproduced from Ref.[93] with permission from Elsevier Ltd.

2.5.1.2 Ionic host-pillar interactions

Ionic functionalization in transition metal dichalcogenides

Beyond the covalent functionalization of TMDs at chalcogen vacancies, ionic interactions offer a versatile approach to modifying TMD layers through the attachment of charged pillars, such as alkylammonium ions. For example, hexylammonium-functionalized TiS_2 (HA-TiS_2), synthesized by electrochemical intercalation in dimethyl sulfoxide (DMSO) followed by solvent exchange with water (**Fig. 2.8A**), exhibits improved thermoelectric performance and mechanical flexibility compared to pristine TiS_2.[99] The impact of the ionic pillars is evident in the significant increase in in-plane electrical conductivity observed in

HA-TiS_2, demonstrating that interlayer functionalization with ionic organic species can effectively tune electronic transport properties in layered TMDs (see **Section 2.5.2.2**).

Redox-active organic molecules, a class of pillar species commonly used in layered host matrices, also rely on ionic interactions to bond to the host lattice. These molecules, typically aromatic or heterocyclic with delocalised π systems, are capable of producing stable radicals through oxidation/reduction processes.[100] These characteristics are commonly found in molecules containing quinone,[101] imide,[102] carbazole,[103] metallocene,[104] and triphenyl-amine groups,[105] among others (**Fig. 2.8B**). Kuo *et al*. explored the confinement of ferrocene, a molecule consisting of two cyclopentadienyl anions bound to an Fe^{2+} centre, within the interlayer of MoS_2 and WS_2 (**Fig. 2.8C, D**).[104] It was observed that the ferrocene pillar and the TMD lattice engage in an electron transfer, suggesting that strong ionic interactions stabilize the pillared structure. The confinement of redox-active ferrocene pillars has significant implications on ion storage mechanisms (see **Section 2.5.1.1**).

In summary, ionic interactions play a pivotal role in the interlayer functionalization of TMDs with organic pillars, significantly influencing their structural, electronic, and electrochemical properties. Charged organic species, such as alkylammonium ions, not only expand the interlayer spacing but also may alter the host structure's properties, such as electronic conductivity. Moreover, the integration of redox-active organic pillars introduces additional functionality, enabling complex charge storage mechanisms. As the field progresses, understanding and harnessing ionic host-pillar interactions, and ion-pillar interactions, will be critical for optimizing the performance and stability of pillared TMDs in next-generation devices.

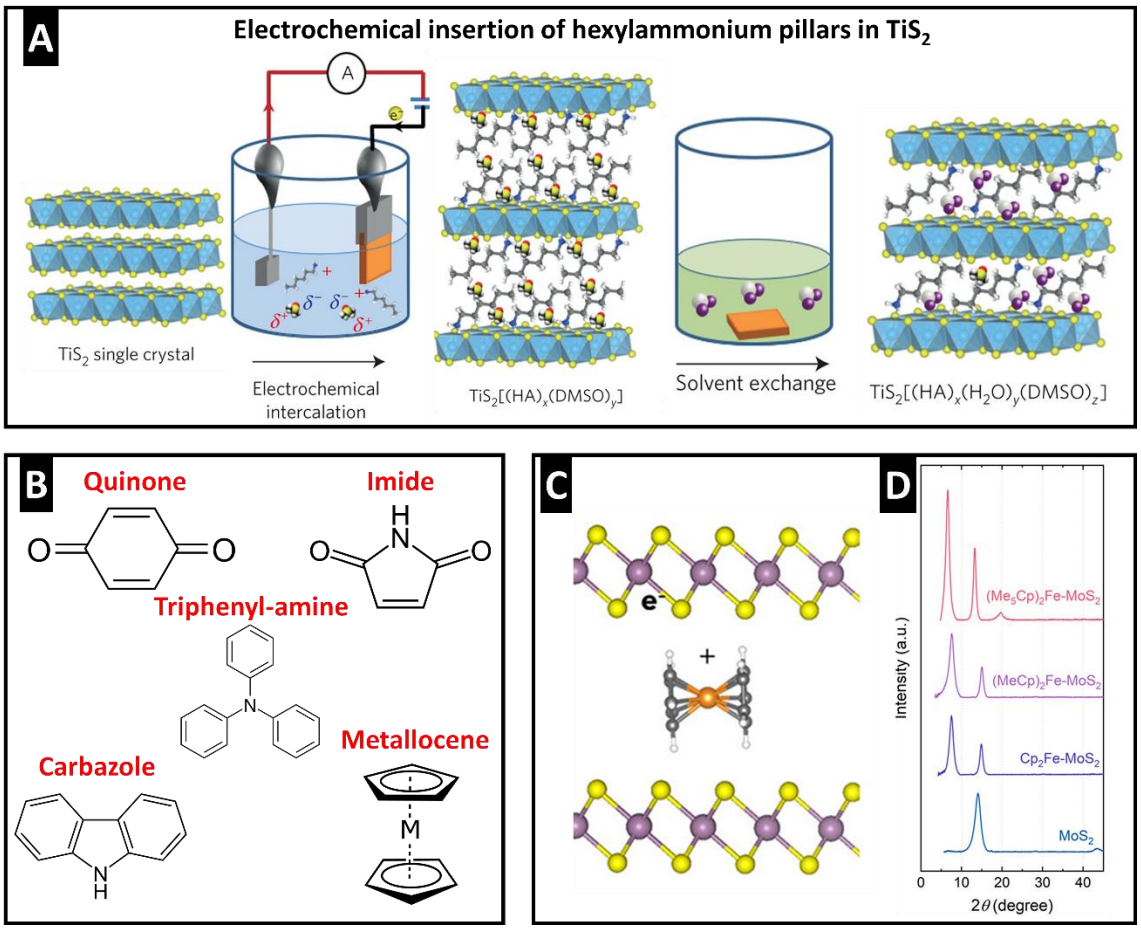

Figure 2.8: Ionic interactions in pillared TMDs. A) Schematic of electrochemical functionalization of TiS_2 by hexylammonium ions. Reproduced from ref.[99] with permission from Springer Nature Limited. B) Chemical structures of key functional groups in redox-active organic molecules. C) Schematic of ferrocene-functionalized MoS_2 and D) XRD patterns of MoS_2 functionalized with ferrocene (Cp_2Fe), 1,1′-dimethylferrocene ($(MeCp)_2Fe$), and decamethylferrocene ($(Me_5Cp)_2Fe$). The interlayer spacing expands to various extents depending on the identity of the metallocene. Reproduced with permission from Ref.[104] Copyright © 2022, American Chemical Society.

Ionic functionalization in transition metal oxides

Layered transition metal oxides (TMOs), represented by the general formula M_xO_y (where M is a transition metal and O is oxygen), are known for their versatility and high specific capacities, making them attractive candidates for ion intercalation electrodes (**Fig. 2.9A**).[106] Despite their advantages, layered TMO electrodes suffer from poor electrical conductivity and limited cycling stability due to significant volumetric changes during cycling, particularly in multivalent ion systems.[107] Interlayer functionalization with organic molecules aims to address these limitations by expanding the interlayer gap, which

improves ionic transport and buffers volumetric changes, as well as introducing conductive pillars that enhance electronic conductivity.[63]

In TMOs, surface –OH groups facilitate interlayer functionalization by ionic interactions with positively-terminated organic species.[108] Amines (R–NH_2), particularly alkylamines (**Fig. 2.9B**), are a commonly used class of pillar molecules for interlayer functionalization, as their Brønsted basic –NH_2 groups act as electron donors and readily participate in ionic interactions with the acidic –OH groups on the TMOs surface.[109] This proton transfer reaction results in the formation of alkylammonium ions according to:

$$RNH_2 + (H_3O)^+ \leftrightarrows (RNH_3)^+ + H_2O \qquad \textbf{(2.4)}$$

which are incorporated into the interlayer space, expanding the *d*-spacing of TMOs and forming a pillared compound of the formula $(RNH_3)_x^+(RNH_2)_y(MX_2)^{x-}$.[109,110]

Additionally, it has been proposed that alkylamines can also interact with transition metal ions through coordination, provided that the metal centres have available coordination sites.[13] These two mechanisms (proton transfer and coordination) highlight the versatility of alkylamines in interlayer functionalization of layered materials.

In TMOs like MoO_3, alkylamine functionalization can be achieved *via* simple wet chemistry reactions.[111,112] Different alkylamine lengths produce structures with varying *d*-spacings and morphologies (**Fig. 2.9C, D**). However, due to steric effects, the insertion of linear amines becomes increasingly challenging as the number of carbon atoms in the chain increases. To address this limitation, a common solution involves pre-functionalization with a shorter amine molecule before introducing a longer one.[113] This sequential approach facilitates the insertion of larger molecules, expanding the range of possible pillared TMO structures.

The amount of pillar molecules occupying the interlayer space plays a critical role in the performance of TMOs. Studies have shown that the pillar molecule packing density influences the thermal stability and overall properties of the pillared material. In general, the alignment of linear amines in layered structures depends on the surface layer charge density and the chain length of the alkylammonium ion.[109] Shorter chains typically form monolayer arrangement, while longer chains give rise to bilayer arrangements (**Fig. 2.9E**).[114] As packing density increases, pseudo-trimolecular and paraffin-type

arrangements prevail. Airoldi *et al*., studied the functionalization of *n*-alkyldiamines into layered titanates and attributed the increased thermal stability of the pillared structure to the paraffin-like arrangement of the organic pillars,[115] highlighting the importance of considering pillar arrangement in the interlayer space.

In multivalent-ion batteries, such as the Al-ion system, interlayer functionalization has been explored to improve performance. For example, MnO_2 pillared with benzoquinone-coordinated Al ions (BQ-Al_x) was obtained via a hydrothermal bottom-up method, where the pillared compound was formed *in situ* from precursors of the host and pillar species (**Fig. 2.9F**).[116] Although the type of pillar-host interaction was not explicitly determined, the reduced average oxidation state of Mn in the pillared compound suggest the possibility of ionic interaction. This pillaring approach enables stable long-term cycling and enhanced intercalation kinetics by shielding the strong electrostatic interactions between the MnO_2 lattice and the intercalating Al^{3+} ions (see **Section 2.5.1.2**).

In hydrous oxides, layered titanates have emerged as promising TMOs for ion intercalation anodes.[117] Hydrous layered titanates, such as $H_2Ti_3O_7$ and $H_2Ti_4O_9{\cdot}nH_2O$ can uptake polar organic molecules, such as *n*-alkylamines, via wet chemistry process.[118,115] Interestingly, some similar structures, such as potassium titanate ($K_2Ti_4O_9$) do not uptake *n*-alkylamine molecules, suggesting that the functionalization reaction strongly depends on the nature of the cation occupying the interlayer space. Similarly, in some non-hydrous layered TMOs, such as K_xMnO_2, functionalization is often preceded by the intercalation of protons, which subsequently react with the organic pillar molecules (**Fig. 2.9G**).[119] Therefore, it is likely that protonation is essential to establish ionic functionalization with alkylammonium ions, as suggested earlier in **Eq. 2.4**. In some applications, such as aqueous batteries, the presence of interlayer water molecules is often beneficial, because they shield the electrostatic ion-host interactions, improving intercalation kinetics.[120] However, in non-aqueous electrolytes, where the presence of interlayer water is undesirable, it is crucial to control the functionalization process to ensure the complete removal of interlayer water.

Despite extensive research into TMO interlayer functionalization, several areas remain unexplored. For example, alkali-rich ternary layered oxides, such as lithium-rich layered oxides (LLOs), offer high capacities and energy densities, but suffer from structural instability due to lattice dislocations and transition metal migration.[121] Doping the interlayer (where Li^+ ions occupy the spaces between the TM-O slabs) has been suggested

to enhance the structural stability,[122] but organic pillaring remains largely unexplored. However, the sodium ternary oxide $Na_{0.71}CoO_2$ (NCO) has demonstrated the ability to incorporate organic pillars *via* a two-step process involving first, partial Na^+ exchange with protons, then reaction with *n*-alkylamines, similar to the mechanism illustrated in **Fig. 2.9G**.[123] This strategy may also enable alkylamine functionalization in other alkali-rich layered oxides, potentially improving their structural stability and performance.

Polyfunctional amines, which feature other functional groups in addition to $–NH_2$, can also serve as pillars in interlayer functionalization and engage in an ionic interaction with the host matrix. For example, alkanolamines combine the nucleophilic amino group, which drives the functionalization reaction, with the hydrophilic hydroxyl group. This combination offers advantages in aqueous electrochemical systems by leveraging both interlayer expansion and wettability, optimizing interaction with the electrolyte and contributing to enhanced electrochemical behaviour in aqueous systems.[124]

In conclusion, amines present an attractive choice of pillar molecule due to their versatility and reactivity toward many layered materials through ionic pillar-host interactions, addressing limitations in ion transport and structural stability in TMOs, and providing avenues for fundamental studies on nanoconfinement in pillared layered electrodes.

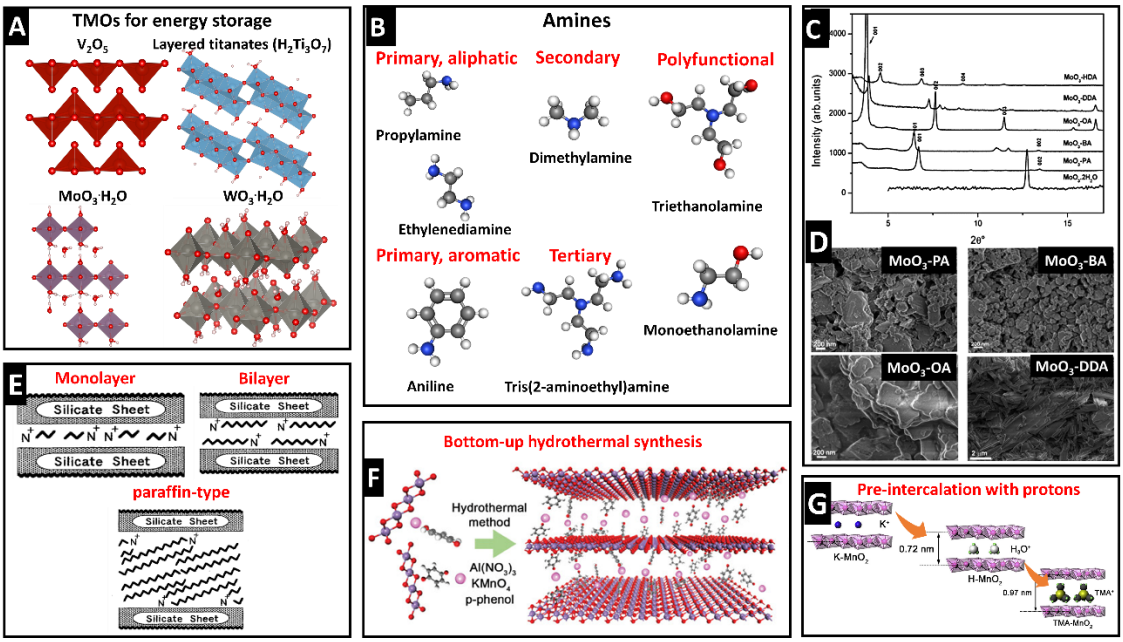

Figure 2.9: A) Structures of common layered TMOs, drawn with VESTA© software, CIF data from the Materials Project.[85] B) Structures of several subclasses of amines. C) Powder XRD

patterns, and D) SEM images of alkylamine-pillared MoO_3. PA: propylamine, BA: butylamine, OA: octylamine, DDA: dodecylamine, and HDA: hexadecylamine. Reproduced with permission from Ref.[113] Copyright © 2006, American Chemical Society. E) Schematics of alkylammonium ion arrangements in the interlayer of silicates, reproduced with permission from Ref.[114] Copyright © 2006, © 1997 The Chemical Society of Japan. F) Schematic of bottom-up hydrothermal synthesis of BQ-Al_x-pillared MnO_2, reproduced with permission from ref.[116] © 2024 Wiley-VCH GmbH.G) Tetramethyl ammonium (TMA^+) interlayer functionalization of $KMnO_2$ by protonation and subsequent ion-exchange. Adapted with permission from ref.[119] © 2019 Elsevier B.V.

2.5.1.3 Hydrogen bonding in host-pillar interactions

Hydrogen bonding in pillared MXene structures

First reported in 2011, MXenes are a novel class of 2D materials with the general formula $M_{n+1}X_nT_x$, where M is a transition metal, X is carbon or nitrogen, and T denotes surface terminations such as –OH, –F, or –Cl (**Fig. 2.10A**).[125] The rich surface chemistry of MXenes is largely dictated by these surface terminations, which can render them either hydrophilic or hydrophobic and play a significant role in their electrochemical activity.[126] The nature of these surface terminations is primarily controlled by the synthesis method used to obtain the MXene phase.[127]

Due to their diverse surface chemistries, MXenes can be functionalized with a variety of species. The inherent hydrophilicity of most MXenes, stemming from –O and –OH surface terminations, enables functionalization with organic molecules of high dielectric constants. For example, molecules such as dimethyl sulfoxide (DMSO) and hydrazine monohydrate (HM) have been shown to spontaneously insert into MXenes.[128] An array of functionalization methods are employed for interlayer and surface functionalization of MXenes, ranging from soft-chemistry synthesis and hydrothermal methods to *in situ* polymerization and vacuum-assisted filtration,[129] each offering different levels of complexity and control over the process.

Owning to their exceptional electronic conductivity and versatile electrochemical applications, MXenes and their pillared structures are extensively explored as energy storage materials.[65,66] An example of the application of functionalized MXenes in capacitor electrodes is shown by Xia *et al*., who successfully incorporated a large surfactant molecule, hexaethylene glycol monododecyl ether ($C_{12}E_6$) into Ti_3C_2 using a facile wet chemistry synthesis (**Fig. 2.10B**). This process resulted in a liquid crystal MXene phase

(MXLLC) with a large *d*-spacing of ca. 5.8 nm (**Fig. 2.10C**). The authors propose that strong hydrogen bonds form between the –OH groups of $C_{12}E_6$ and the MXene's –F and –O surface terminations. This unique structure enables the vertical alignment of MXene sheets with respect to the current collector, providing unique thickness-independent electrochemical behaviour (See **section 2.5.2.1**).[130]

Hydrogen bonding between MXene sheets and pillar molecules is essential in interlayer functionalization. A recent molecular dynamics (MD) study examined the pillaring behaviour of six different organic pillars in bilayer $Ti_3C_2O_2$ (**Fig. 2.10D**).[131] In this context, effective pillaring is defined as the complete separation of MXene sheets in a manner that prevents restacking. The simulations revealed the number of molecules required to achieve pillaring and the resulting interlayer spacing for each pillared compound (**Fig. 2.10E**). Notably, the study found that branched pillars occupy less surface area on MXenes compared to ring structures, which tend to adopt flat conformations with high surface area. Such insights are crucial for tailoring the interlayer environment to meet specific application needs.

An example of pillars which engage in hydrogen bonding with layered hosts is presented by amides, which are organic molecules where a nitrogen atom is connected to a carbon atom of a carbonyl group (C=O) (**Fig. 2.10F**). Primary amides are expressed as R—ONH_2, and are weaker bases than amines, therefore, in many cases they do not feasibly functionalize layered materials such as TMOs. However, their hydrogen bonding capabilities make them suitable for other hosts such as layered double hydroxides (LDHs) and MXenes.[132,133] In MXenes, common amides such as urea and *N,N*-dimethylformamide (DMF) have been used for interlayer expansion.[134] However, the thermal stability of these systems presents a limitation, as the pillars tend to desorb when heated above their boiling point. The mechanism behind amide functionalization is believed to involve weak hydrogen bonding between the amide and the –OH surface groups on the MXene, similar to what is observed in clay chemistry,[135] and in LDHs (**Fig. 2.10G**).[133] While hydrogen bonding facilitates interlayer functionalization, the weak nature of these bonds limit applicability of the resulting functionalized structures, particularly in environments requiring thermal stability.

In summary, understanding hydrogen bonding in pillar-host interactions is important in interlayer functionalization of MXenes and other layered materials. Pillared MXenes

exhibit a range of desirable qualities that make them suitable for applications beyond energy storage, such as electromagnetic interference shielding,[136] humidity sensing,[137] and flame retardancy.[138] Much like how MXenes have benefited from insights gleaned from clay chemistry,[139] many lessons learned from MXene chemistry can be extended to other 2D and layered materials. Future research on interlayer functionalization of energy materials should leverage these similarities and build upon the foundational knowledge established with MXenes to advance the development of novel materials and applications.

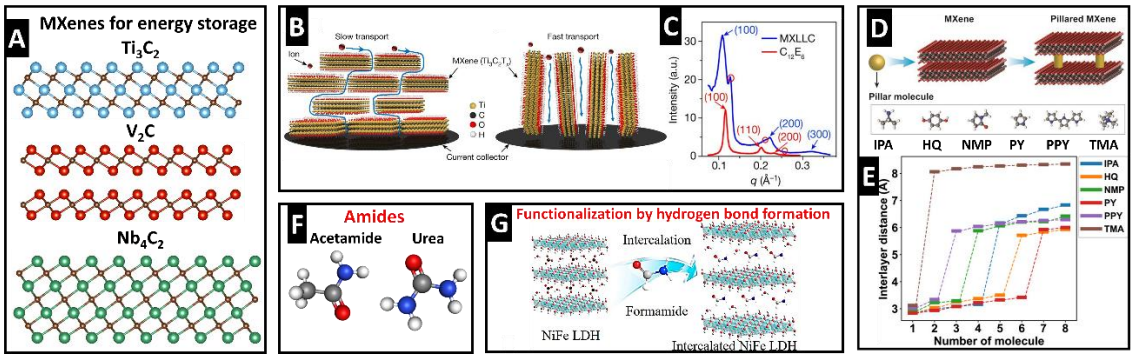

Figure 2.10: A) Structures of some MXenes, drawn with VESTA software, CIF files provided by the Materials Project. Surface terminations not shown. B) Schematic illustration of ion transport in horizontally (left) and vertically (right) aligned $Ti_3C_2T_x$ MXenes. Vertical alignment allows for shorter diffusion paths and therefore fast kinetics. C) Small-angle X-ray scattering (SAXS) measurements of the functionalized (liquid crystal) MXenes (MXLLC) and the hydrogen-bonded pillar molecule $C_{12}E_6$. The scattering vector q of the (100) peak is 0.108 Å, from which the d-spacing is calculated to be ca. 5.8 nm. Reproduced with permission from Ref.[130] Copyright © 2018, Macmillan Publishers Ltd. D) Schematic of 6 molecules insertion into MXene (IPA: isoproplyamine; HQ: hydroquinone; NMP: N-methyl-2-pyrrolidone; PY: pyrrole; PPY: polypyrrole; and TMA: tetramethylammonium) and E) Dependence of average interlayer distance on the number and type of pillar molecules. Adapted with permission from Ref.[131] Copyright © 2023, American Chemical Society F) Structures of some amides. G) Amide functionalization by hydrogen bond formation in LDH. Reproduced with permission from Ref.[133] © 2017 Elsevier B.V.

2.5.1.4 Adsorption in pillared layered materials

Weakly-bonded molecules in layered TMOs

Other types of interactions between pillars and layered materials exist, such as physical adsorption, where molecules are bound to the surface of the material *via* weak, intermolecular van der Waals forces. These interactions, though weaker than covalent or ionic bonds, are crucial in many functionalization strategies for layered materials, as they

offer a means of modifying material properties while preserving the intrinsic electronic structure of the host.

Alcohols, organic molecules featuring at least one hydroxyl group (–OH) bound to an aliphatic carbon atom (**Fig. 2.11A**), provide an example of weak host-pillar interaction. Only a few systems have been reported to spontaneously incorporate alcohols into their interlayers *via* weak intermolecular interactions. One notable example is $V_2O_5 \cdot nH_2O$, which has strong affinity to the adsorption of alcohols with carbon chains up to seven atoms long.[140] Despite this potential, no reports currently exist demonstrating the use of alcohol-functionalized layered materials in electrochemical energy storage applications.

Unlike amines, which engage readily in one-step acid-base reactions, alcohols, with their weaker proton-accepting ability, generally require a more complex insertion process.[141] Typically, a two-step approach is employed: first, pre-functionalization with an amine, followed by the introduction of the alcohol. This method has been successfully applied to materials such as $HTiNbO_5$[141] and various layered perovskite phases (**Fig. 2.11B**),[142] highlighting the versatility of multi-step functionalization reactions, particularly when relying on weak intermolecular forces, to insert pillar molecules like alcohols into layered materials.

In redox-active organic pillars, which we discussed previously in **Section 2.5.1.1**, several kinds of host-pillar interactions can be achieved, whether weak interactions leveraged through simple mixing methods, or covalent bonding through diazonium chemistry methods (**Fig. 2.11C**). Each method results in different electrochemical properties of the resulting pillared material,[143] with non-covalent functionalization often favoured when maintaining the host's structural and electronic integrity is critical. For example, the functionalization of MXenes with redox-active quinones is particularly notable, as it combines the intrinsic mechanical robustness and electronic conductivity of the MXene host, with the pseudocapacitive properties of the quinone pillar.[143]

Another example of weak host-pillar interactions is seen in oxyethylene (CH_2CH_2O) pillars, which are well-known for their ability to complex metal ions.[144] These materials, with their stability in organic solvents and electrolyte solutions, offer significant potential for electrochemical applications when confined within layered hosts. Extensive work by Lara and Ruiz-Hitzky led to the development of several oxyethylene-MoS_2 pillared

compounds (**Fig. 2.11D**),[145] which showed increased Li^+ diffusion, demonstrating the effectiveness of the pillaring approach. The interaction of the oxyethylene pillar with the host lattice is likely weak, given that the organic pillars can be removed by simply washing with water. Other similar pillars like azacrowns likely interact with host lattice *via* weak interactions.

In layered carbons, while most functionalization reactions are reported to occur by covalent functionalization (see **Section 2.5.1.1**), there has been a growing interest in non-covalent functionalization methods. In non-covalent functionalization, $\pi - \pi$ interactions, van der Waals forces, and weak hydrogen bonds are employed (**Fig. 2.11E**), allowing for modification of carbon materials like graphene without significantly disrupting their electronic properties.[146]

In summary, weak interactions, such as van der Waals forces, play a crucial role in the functionalization of layered materials. These methods offer a less invasive alternative to covalent functionalization, enabling the enhancement of material properties while preserving key characteristics of the host matrix. The continued exploration of van der Waals interactions in pillared materials holds promise for the development of advanced ion intercalation electrode materials. However, due to the inherent weak nature of these interactions, some important questions remain regarding the long-term stability of the pillars during electrode cycling.

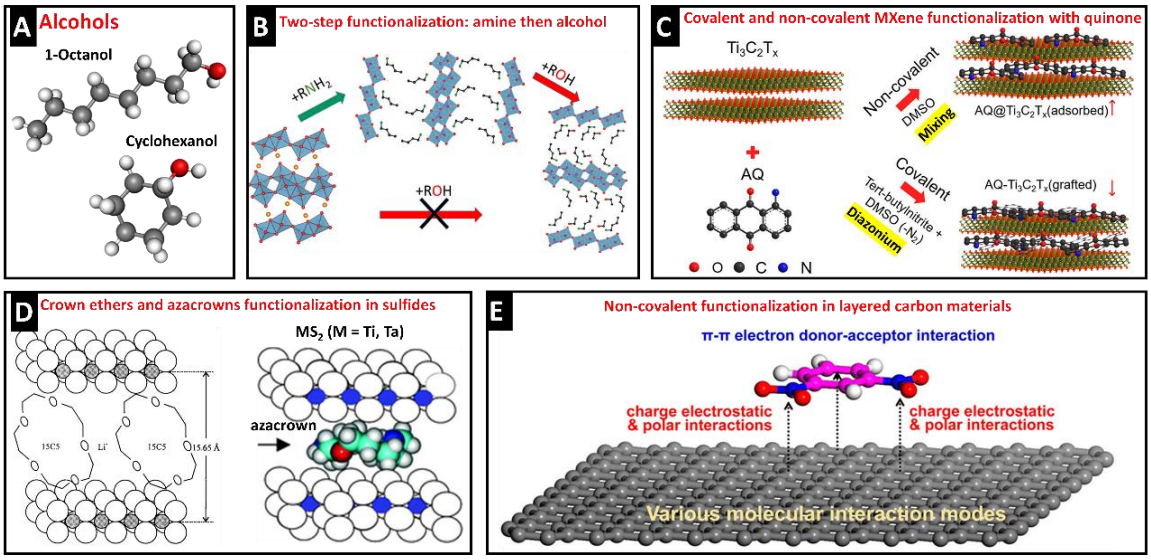

Figure 2.11: A) Examples of alcohols, B) Illustration of a two-step insertion of alcohols in layered titanoniobates. Reproduced with permission from Ref.[141] Copyright © 2017, American Chemical

Society. C) Schematic of covalent and non-covalent functionalization routes of MXenes with aminoquinone (AQ). Adapted with permission from Ref.[143] Copyright © 2020, American Chemical Society. D) Left: Illustration of Li_xMoS_2 functionalized with a crown ether, 15C5. Reproduced with permission from Ref.[145] Copyright © 1996 Sociedade Brasileira de Química. Right: Illustration of azacrown insertion in metal sulfide MS_2. Adapted with permission from ref.[147] Royal Society of Chemistry. E) Modes of non-covalent interactions in pillared layered carbons. Reproduced with permission from Ref.[148] Copyright © 2015 American Chemical Society.

Weakly-bonded or adsorbed polymers in layered hosts

Extensive research into the functionalization of layered materials with organic molecules has led to the use of macromolecules and polymers as interlayer pillars. Polymers offer a dual functionality: they serve as structural pillars, expanding the interlayer spacing, and act as conductive additives due to their ionic or electrical conductivity. Among polymers, two key classes are particularly relevant for energy storage applications: ionically conducting polymers, which enable ion transport; and electrically conducting polymers, which enhance the electrical conductivity in layered materials (**Fig. 2.12A**).

The incorporation of polymers into layered materials can be achieved through two primary methods: direct insertion, which involves inserting pre-formed polymers into the interlayer space; and *in situ* polymerization, where monomers are introduced into the layered structure and then polymerized within the interlayer region.[149] The choice between these methods and the type of polymer used depends on the desired properties and application of the pillared material. Typically, the interaction between polymer pillars and the host lattice involves weak van der Waals forces or electrostatic interactions.[150,151] These weak forces are critical for achieving uniform dispersion of the polymer within the solid matrix while preserving the chemical structure of the host. This allows for the enhancement of ionic or electrical conductivity without compromising the host's intrinsic properties.

Poly(ethylene oxide) (PEO), a polymer with the formula $(CH_2CH_2O\text{-})_n$, is a popular choice of pillar in layered materials due to its electrochemical inertness, ability to complex alkali metal ions, and ionic conductivity, qualities that also make it the most extensively studied solid polymer electrolyte (SPE) system.[152,153] PEO has been successfully incorporated into TMOs such as V_2O_5 xerogel matrices through wet chemistry methods by mixing aqueous solutions of the polymer and TMO.[154] On the other hand, in TMDs, PEO functionalization

requires a preliminary lithiation and exfoliation step to facilitate organic molecule insertion.[155]

The flexibility of PEO chains introduces some uncertainty regarding their arrangement within the interlayer space of the host material. Predictions based on geometric calculations and *d*-spacing values calculated from XRD suggest that PEO chains might adopt various conformations, such as straight-chain, helical, or zig-zag structures (**Fig. 2.12B**). However, experimental evidence to confirm these theoretical arrangements is still limited.[154–156] As discussed in **Section 2.5.1.2**, it is possible that conformations of the organic pillar in the interlayer space have implications on the pillared host properties.

While ionically conductive polymers are well-suited as pillar species in conductive or semi-conductive hosts such as TMDs, electronically conducting polymers are valuable for enhancing the conductivity of poor electrical conductors, like TMOs. These polymers, characterized by conjugated bonds within their macromolecule, offer substantial benefits for energy storage applications.[149]

Polypyrrole (PPy, **Fig. 2.12A**) is an electrically conducting polymer that is characterized by facile synthesis, good thermal stability, eco-friendliness, and low cost.[157] It is formed through the oxidative polymerization of pyrrole, making it particularly suitable as a pillar in oxidizing layered hosts, such as hydrated V_2O_5 and $VOPO_4$.[158] In non-oxidizing hosts like MoS_2, oxidative polymerization is achieved using external oxidants such as $FeCl_3$,[159] or through electrochemical oxidation.[160] Interactions between PPy and MoS_2 are mainly attributed to non-covalent van der Waals forces.[151]

In hydrated layered host materials, the introduction of PPy often results in the expulsion of interlayer water. This expulsion can sometimes be undesired; for example, in hydrated $VOPO_4$, pillaring with PPy decreases the *d*-spacing as higher PPy loading expels more water molecules.[158] One effective strategy to counteract this shrinkage is a pre-functionalization step using another organic pillar, such as pyridine sulfonic acid (PSA). PSA not only helps to open up the structure but also promotes the polymerization of PPy within the interlayer space, mitigating the *d*-spacing reduction caused by the loss of interlayer water.[161]

Polyaniline (PANI) is an electrically conductive polymer whose structure consists of repeating units of vinyl rings featuring –NH groups (**Fig. 2.12A**). PANI has received attention as a pillar species due to its ability to: a) expand the interlayer spacing, creating larger diffusion channels for intercalating ions, b) maintain structural stability by acting as a structural pillar, and c) form an intermediate energy band across the Fermi level, facilitating electron transport during electrochemical processes.[63] Additionally, PANI is redox-active through protonation and deprotonation within the polymer backbone in acidic electrolytes,[162] or by amine (–NH—) to imine (–N=) transformation in alkaline electrolytes.[163] Through surface redox reactions, PANI is reported to exhibit pseudocapacitive behaviour, albeit with limited cycle life due to instability of the backbone during cycling.[164]

PANI is typically incorporated into layered materials through the insertion of aniline, followed by *in situ* polymerization within the interlayer region.[165] In layered carbons, weak pillar-host interactions, mainly $\pi - \pi$ interactions, allow for effective insertion into the structure, which not only expands the *d*-spacing of the structure, but also serves as a carbon and nitrogen source in subsequent carbonization processes.[54]

Although van der Waals forces are often cited as the main host-pillar interaction in TMDs and carbon layered materials, there is some debate regarding the nature of interactions in polymer-pillared TMOs. In V_2O_5, the insertion of PANI occurs through *in situ* polymerization, and has been shown to effectively expand the interlayer spacing (**Fig. 2.12C**), not only enhancing electrical conductivity, but also the capacity and rate capability for Zn^{2+} intercalation.[166] Contrary to studies suggesting weak pillar-host interactions, this study reports the presence of C=O bonds, suggesting the formation of strong chemical bonding with the host material.[166] Other similar studies on PANI-pillared V_2O_5 suggest the presence of hydrogen interactions between the $–NH_2$ group and the V-O layers.[167] As a result, it remains unclear whether *in situ* polymerization of PANI in layered hosts proceeds via weak interactions or through the formation of stronger chemical bonds.

Poly(3,4-ethylenedioxythiophene) (PEDOT) is a conjugated conductive polymer known for its high stability, conductivity, and mechanical flexibility.[168] In TMDs, PEDOT can attach to the layered material by weak electrostatic interactions.[169] PEDOT can be obtained by chemical oxidation or electrochemical polymerization, therefore its incorporation into oxidative hosts, such as V_2O_5, facilitates the polymerization reaction.[170] Interlayer

functionalization of V_2O_5 with PEDOT occurs through a facile soft chemistry synthesis at ambient temperature. Here, hydrogen bonding between the oxygen atoms in V_2O_5 and the EDOT's hydrogen is believed to facilitate the polymerization reaction.[139]

Despite PEDOT's promising features, the main drawback of PEDOT is its poor water solubility, which makes aqueous processing challenging.[171] Moreover, interlayer functionalization with PEDOT has been reported to result in ultrathin nanostructures of lower crystallinity. Additionally, PEDOT is prone to decomposition upon thermal treatment.[170] These limitations should be carefully considered when designing PEDOT-functionalized layered electrodes to ensure optimal performance and stability.

In summary, many ionically and electrically conductive polymers can function as effective interlayer pillars in layered electrode materials, facilitating interlayer expansion, enhanced conductivity, and, in some cases, pseudocapacitive behaviour. Van der Waals interactions, which often govern these systems, provide a flexible and minimally invasive means of functionalization, enabling the tuning of host material properties without significant chemical modification. However, not all polymer-host interactions are governed by van der Waals forces. The literature also presents cases where stronger interactions, particularly in pillared transition metal oxides (TMOs), play a significant role. Clarifying the nature of these interactions is crucial to understanding the stability of these structures and their viability for electrochemical energy storage across varying conditions.

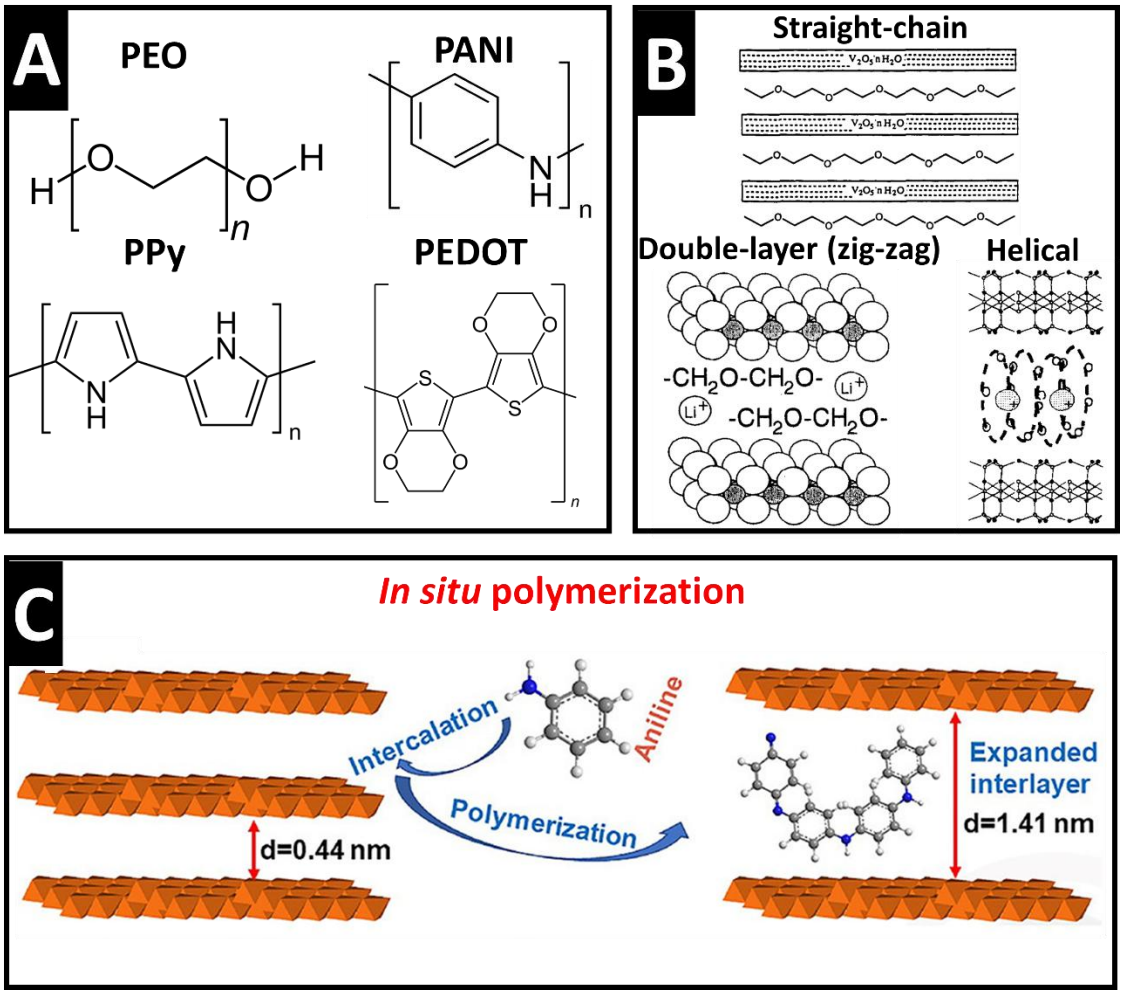

Figure 2.12: A) Structures of common polymers used as pillars in layered materials. B) Proposed conformations of PEO in layered hosts, reproduced with permission from Ref.[154,155,172] Copyright © 1991, American Chemical Society, Copyright © 1993 Verlag GmbH & Co. KGaA, Weinheim, Copyright © 1993 Verlag GmbH & Co. KGaA, Weinheim. C) Schematic illustration of *in situ* PANI polymerization in V_2O_5 leading to the expanded hybrid PVO, reproduced with permission from Ref.[166] Copyright © 2021, American Chemical Society.

2.5.2 Properties of interlayer-functionalized materials

The insertion of organic pillar molecules into the interlayer space of layered host materials induces significant modifications to the ion intercalation process, as well as properties of the host and the pillar itself. In this section, we review the diverse properties that emerge from interlayer functionalization and analyse their impact on ion intercalation, the structural characteristics of the host lattice, and the stability of the pillar molecules.

2.5.2.1 Influence on electrochemically intercalating ions

Modification of ion storage sites and mechanisms

The insertion of organic molecules into inorganic layered hosts can significantly alter the ion storage sites within the lattice, leading to the formation of energetically favourable environments for ion intercalation. Graphene, which typically does not allow bare Na^+ ion intercalation, benefits from interlayer functionalization. The covalent attachment of AB pillars to graphene layers (see **Section 2.5.1.1**) effectively creates favourable sites for reversible Na^+ intercalation, as indicated by DFT calculations (**Fig. 2.13A**). *Operando* Raman spectroscopy measurements reveal a clear G-band shift (**Fig. 2.13B**), indicative of C—C bond contraction due to Na^+ intercalation. This demonstrates the potential of covalent interlayer functionalization in graphene to unlock new intercalation chemistries that would otherwise be energetically unfavourable.

Modifications to ion storage mechanisms can also arise from complexation. In ethylenediamine-functionalized vanadium oxide (EDA-VO), the amine pillars not only expand the *d*-spacing, resulting in good cycling stability (**Fig. 2.13C**), but also contribute to charge storage by forming complexes with Zn ions, as confirmed with spectral studies.[57] Moreover, the pillared EDA-VO structure exhibits a high average voltage plateau (*vs*. Zn^{2+}/Zn) when compared to other vanadium-based Zn hosts.

Another modification to ion storage mechanisms can arise from the introduction of redox-active molecules. For example, when ferrocene is confined as a pillar in MoS_2, it not only retains its redox activity (**Fig. 2.13D**), but also is influenced by the electrolyte cations, which play a key role in regulating the charge within the partially reduced MoS_2 interlayer. The redox potentials of ferrocene were observed to vary with cation strength (**Fig. 2.13E**), and when crown ether was used to impede cation movement, the Faradaic processes were suppressed as charge regulation was disturbed (**Fig. 2.13F**), confirming the role of cations in enabling the redox of confined ferrocene. This emphasizes the importance of considering the interplay between intercalating ions and the redox-active pillar species, as this interaction can alter the charge storage mechanism of the overall pillared compound.

In summary, the interlayer functionalization of layered materials with organic pillars introduces a range of beneficial effects on ion storage mechanisms. By modifying the interlayer environment in the host lattice, new ion storage sites can be created, redox-active

pillars can be leveraged for charge storage, and complexation reactions between the intercalating ion and the pillar species can occur, expanding the range of possible charge storage mechanisms. These multifaceted enhancements offer significant opportunities for optimizing ion intercalation and tuning electrochemical performance, highlighting the potential of organic interlayer functionalization for next-generation energy storage systems.

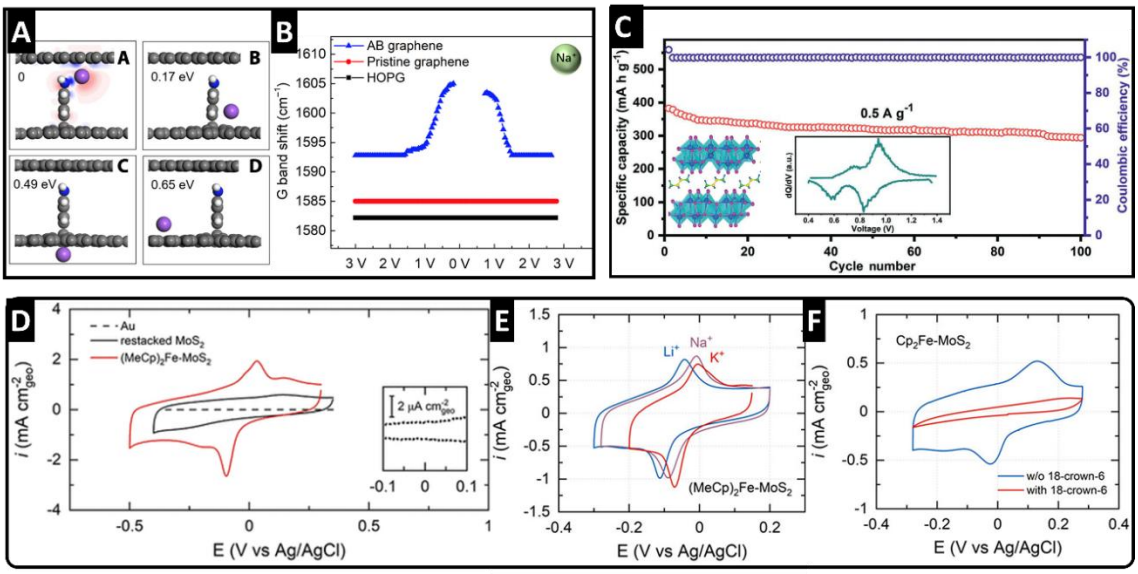

Figure 2.13: A) DFT modelling of Na^+ intercalation in AB-functionalized graphene at different configurations. The relative energy is indicated with respect to the most stable position. B) Raman shift of G band position during Na^+ intercalation for highly oriented pyrolytic graphite (HOPG), graphene, and AB graphene. The G band shift in AB graphene is indicative of Na^+ intercalation. Reproduced from Ref.[92] with permission from AAAS. C) Galvanostatic cycling of EDA-VO electrode against Zn^{2+}/Zn. Insets: structure of EDA-VO and the corresponding dQ/dV curve. Adapted with permission from Ref.[57] © 2021 Wiley-VCH GmbH. D) Cyclic voltammograms (CVs) of restacked MoS_2 (black) and ferrocene-functionalized MoS_2 (red). Dashed lines represent the Au substrate to account for background current. E) CVs of ferrocene-functionalized MoS_2 in 0.5 M Li_2SO_4 (blue), Na_2SO_4 (purple), and K_2SO_4 (red). F) CVs of ferrocene-intercalated MoS_2 in 0.5 M K_2SO_4 (blue) and in 0.5 M K_2SO_4 with 2 equivalents of 18-crown-6 (red). Reproduced with permission from Ref.[104] Copyright © 2022, American Chemical Society.

Modification of ion transport kinetics in interlayer-functionalized materials

The manipulation of electrode's *d*-spacing is a well-established strategy for enhancing ion intercalation kinetics by expanding the diffusion channels, improving ion diffusion within the crystalline lattice. The diffusion coefficient of the intercalating ion, D, depends on several factors that are influenced by the interlayer environment, according to:

$$D = p\lambda^2 v^* \exp\left(-\frac{E_B}{kT}\right) \qquad \textbf{(2.5)}$$

where p is a geometrical factor, λ is the hopping distance, v^* is the vibrational frequency, and E_B is the activation energy barrier for hopping. This energy barrier in particular is sensitive to changes due to the interlayer environment, such as the introduction of pillar molecules, and has an exponential effect on the diffusion coefficinet.[68,173] This suggests that even minor modifications to the interlayer environment can lead to significant changes in the diffusion coefficient. For example, in PANI-V_2O_5, the expansion of the *d*-spacing enables fast Zn^{2+} ion diffusion in V_2O_5, as evidenced by *D* calculations (**Fig. 2.14A**) and by the lower charge transfer resistance (**Fig. 2.14B**) compared to hydrated vanadium oxide (HVO).[63]

However, in a similar work involving PANI-V_2O_5, the improvements in Zn-ion diffusion were attributed to not only the physical expansion of the diffusion channels, but also the interactions between Zn ions and PANI pillars. In the pillared PANI-V_2O_5, the binding energy for Zn ions is remarkably lower than that for pristine V_2O_5 due to the repulsion between the positively charged Zn^{2+} and the H atoms of PANI, improving intercalation kinetics (**Fig. 2.14C**).[63] This demonstrates that both interlayer expansion and the chemical interaction between pillar species and intercalating ions contribute to enhanced ion diffusion kinetics in functionalized layered materials.

Similarly, interlayer pillar molecules can enhance ion diffusion by improving ion adsorption. For example, thiol groups have been shown to exhibit large affinities towards certain ions, such as Zn^{2+}.[174] In rGO, the incorporation of covalently-bonded thiol pillars lowers the energy barrier for Zn adsorption, facilitating the adsorption and desorption of Zn ions during charge and discharge and enabling pseudocapacitive surface redox of the Zn-ion on the rGO (**Fig. 2.14D**).[51,52] This strategy builds upon previous quantitative estimations of thiophilicity and oxophilicity of various ions, guiding the selection of appropriate pillar molecules based on the specific ion engaging in charge storage.[175]

Organic pillars can also enhance ion diffusion kinetics by charge shielding. In multivalent ion batteries, such as Al-ion batteries, strong electrostatic interactions between the ion and the host can hinder intercalation. MnO_2, a promising host for Al-ion intercalation, benefits from interlayer functionalization using a pillar species like BQ-complexed Al (BQ-Al_x, see **Section 2.5.1.2**), which not only expands the interlayer of MnO_2, but also mitigates

electrostatic field of Al^{3+} ions by charge shielding, enabling fast intercalation kinetics. This strategy results in improved electrochemical performance and cycling stability, outperforming both Al-preintercalated MnO_2 (Al_xMnO_2) and BQ alone (**Fig. 2.14E**). This work presents an effective strategy to enhancing Al diffusion through charge shielding, thus using the pillar beyond acting as a spacer.

Another innovative approach to improving ion diffusion involves using organic pillars to align sheets of 2D materials vertically, shortening diffusion pathways. In MXenes, the insertion of hexaethylene glycol monododecyl ether ($C_{12}E_6$), as discussed in **section 2.5.1.3**, enables the vertical alignment of MXenes with respect to the current collector. Vertically aligned MXene sheets exhibit enhanced capacitive performance compared to their horizontally aligned counterparts prepared by vacuum filtration, demonstrating film thickness-independent behaviour (**Fig. 2.14F**). This is an innovative approach, leveraging the ability of large pillar molecules to direct 2D materials in a desired orientation favourable to fast ion diffusion.

While ion diffusion kinetics typically benefit from interlayer pillaring, the effectiveness of this strategy is highly dependent on the nature of the pillar molecule. In oxyethylene-MoS_2 compounds, ether pillars improve Li^+ diffusion in a Li-ion system, as indicated by the quasi-open circuit potential values at various stages of lithiation (**Fig. 2.14G).**[145] However, slight modifications to ether pillar can significantly impact electrochemical performance. Nitrogen-containing crown ether pillars (azacrowns) in TiS_2 were found to decrease the Li^+ ion diffusion coefficient drastically (**Fig. 2.14H**).[147] One of the possible explanations is that the N atoms in the crown may engage in charge transfer with the host matrix, limiting its ability for electrochemical reduction. This example highlights that both the physical expansion of the interlayer and the nature of the pillar molecule play important roles in governing diffusion kinetics.

In conclusion, the insertion of organic pillar molecules into layered materials represents a powerful strategy for enhancing ion intercalation kinetics, particularly through expanding diffusion channels and modulating the properties interlayer environment. While the primary effect of interlayer pillaring is the physical expansion of the electrode's *d*-spacing, the chemical nature of the pillars introduces additional mechanisms that influence electrochemical performance. These include ion adsorption, charge shielding, and interactions between the pillars and intercalating ions. Therefore, a deeper understanding

of both the structural and chemical roles of pillar molecules is crucial for the rational design of pillared layered materials with optimized ion transport properties.

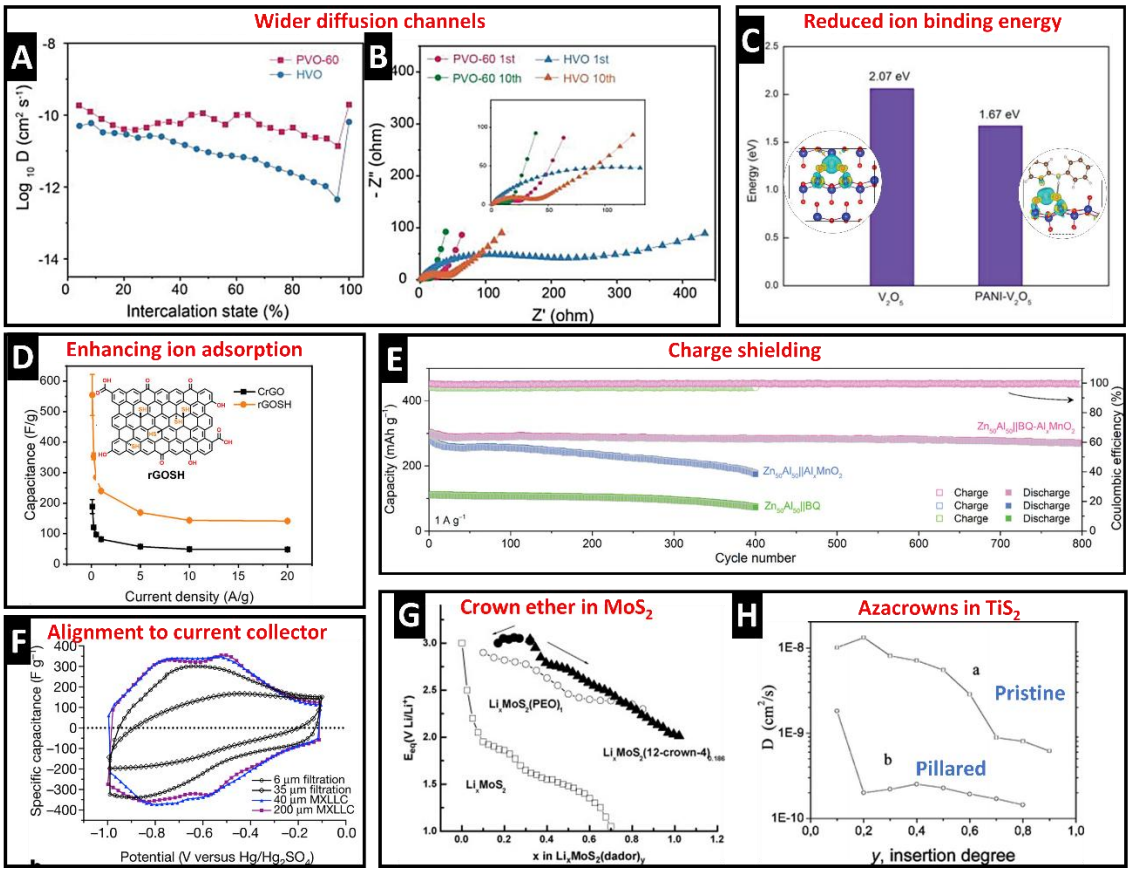

Figure 2.14: Modifications of ion transport kinetics in layered materials. A) Zn-ion diffusion coefficient in PVO and HVO, B) Nyquist plots of PVO and HVO and 1st and 10th cycles. Reproduced with permission from Ref.[63] © 2020 WILEY-VCH Verlag GmbH & Co. KGaA, Weinheim. C) Calculated binding energy for Zn ion intercalated in V_2O_5 and PANI-V_2O_5 and the corresponding differential charge density illustrations. Yellow and cyan regions represent charge accumulation and depletion. Adapted with permission from Ref.[63] © 2020 WILEY-VCH Verlag GmbH & Co. KGaA, Weinheim. D) Capacitance of chemically reduced GO (CrGO) and thiol-functionalized GO (rGOSH) at different current densities in Zn-ion system. Reproduced with permission from Ref.[174] E) cycling of BQ-Al_x-MnO_2 (pink), compared to Al-MnO_2 (blue) and BQ (green), in Al-ion cell vs. $Zn_{0.5}Al_{0.5}$ anode. Reproduced with permission from Ref.[116] © 2024 Wiley-VCH GmbH. F) CVs of horizontally aligned (6 um and 35 um filtration) $Ti_3C_2T_x$, showing thickness-dependent capacitance, and MXLLC of two different thicknesses showing superior and thickness-independent capacitance. Reproduced with permission from Ref.[130] Copyright © 2018, Macmillan Publishers Ltd. G) Evolution of quasi-equilibrium potential at various states of lithiation in Li_xMoS_2-12C4, as compared to PEO- and Li- MoS_2. Reproduced with permission from Ref.[176] Copyright © 2007 Elsevier Ltd. H) Diffusion coefficient of TiS_2-diaza-15C5 compared to pristine

TiS_2 at different stages of lithiation. Reproduced from Ref.[147] with permission from the Royal Society of Chemistry.

2.5.2.2 Influence on host lattice

Buffering volumetric changes and stabilizing the structure

The mechanical behaviour of electrode materials during cycling is a critical factor for battery cycle life. During charge-discharge cycles, electrodes undergo internal stresses and strains due to volumetric expansion and contraction, a phenomenon commonly referred to as lattice breathing.[177] The accumulation of these mechanical stresses can cause structural disintegration of electrode particles, decreasing their lifespan and performance. Interlayer functionalization with organic molecules has proven effective in buffering these volumetric changes, contributing to higher cycling stability by relieving lattice strains.[166] For example, in PANI-V_2O_5, PANI pillars stabilize the material by buffering volumetric changes and maintaining the integrity of the electrode during Zn-ion (de-)intercalation, as demonstrated by the evolution of *d*-spacing of the (001) plane (**Fig. 2.15A).**[63]

Organic interlayer functionalization is particularly valuable in 2D materials like graphene, MXenes, and 2D-TMDs, whose unique properties such as high electrical conductivity and surface area are realized in their 2D form. In their pristine state, strong van der Waals interactions between the layers promote restacking (aggregation) during electrode processing, causing a drop in the active surface area and losing desirable 2D properties.[178] Introducing organic pillars into the interlayer space not only prevents restacking (**Fig. 2.15B**), contributing to higher cycle stability, but can also potentially adds other desirable properties such as ionic conductivity or redox activity. This approach expands the applications of 2D materials in energy storage applications.

In summary, organic pillar molecules play a vital role in stabilizing the structure of layered and two-dimensional (2D) host materials. By buffering volumetric changes during cycling, they enhance the cycle life and durability of electrode materials. Additionally, they prevent the agglomeration and restacking of 2D sheets, thereby preserving their unique properties and improving overall performance in energy storage applications.

Altering the electronic structure

Interlayer functionalization with molecules that serve as conductive additives can alter the properties of the pillared compound, extending beyond expanding the interlayer spacing. The insertion of electronically conducting polymers as pillars in poorly conducting inorganic matrices can enhance the conductivity of the resulting pillared structure. In this context, the pillared compound can be viewed as a (nano-)composite, where the rule of mixtures applies, and bulk properties can be predicted based on the properties of the individual constituents.

However, interlayer functionalization often induces chemical modifications in the host material, which further influence its properties. In layered transition metal compounds, the insertion of organic molecules can change the average oxidation state of the transition metal, leading to what is known as mixed transition metal valence, a phenomenon that is believed to enhance electronic conductivity (**Fig. 2.15C**).[158,179] In carbon materials, a similar effect is observed, for example the functionalization of GO with organic molecules leads to the reduction of GO, which also improves its electronic conductivity (**Fig. 2.15D**).[94] These chemical changes in the oxidation states of the host atoms are often advantageous for the overall electronic conductivity of the pillared electrodes.

In other cases, the introduction of pillar molecules leads to changes in the bandgap energy of the material. For example, in functionalized rGO structures, as discussed in **Section 2.5.1.1**, BDA-functionalized rGO demonstrates nearly twice the capacitance of unmodified rGO across different scan rates. Despite not resulting in the largest *d*-spacing increase among the studied pillars, DFT calculations reveal that BDA-rGO and EDA-rGO possess the smallest band gaps, enhancing charge carrier mobility and resulting in superior rate performance. Conversely, the poor rate performance of CHDA-rGO can be attributed to its higher band gap, likely caused by the cyclohexane ring impeding charge propagation through the graphene layers.[93] These observations highlight the importance of selecting appropriate pillar molecules to meet specific performance requirements.

In TMOs, a similar effect is observed. The incorporation of the electronically conducting polymer PEDOT was found to significantly reduce the bandgap from 2.63 to only 0.37 eV, as indicated by density of states calculations (**Fig. 2.15E**).[170] This illustrates a case where a pillar is used to simultaneously improve the diffusion kinetics for ion (Mg^{2+}) intercalation, as well as improve the overall electronic conductivity of the pillared structure.

In summary, organic pillar molecules can effectively enhance electronic conductivity, not only through their inherent conducting nature, such as in the case of conductive polymers, but also through altering the valence states or the bandgap properties of the host material.

Altering surface properties

In addition to modifying the electronic structure, the insertion of organic molecules can change the surface properties of the host material by adding hydrophobic or hydrophilic functionalities. For example, in graphene, interlayer functionalization with hydrophilic group-containing molecules, such as aminobenzene (AB) and nitrobenzene (NB) induces hydrophilic surface properties, as indicated by contact angle measurements (**Fig 2.15F**).[92] Hydrophilic interlayer properties are particularly relevant in aqueous battery systems, where enhanced surface interaction with the electrolyte promotes fast charge and discharge kinetics.[180]

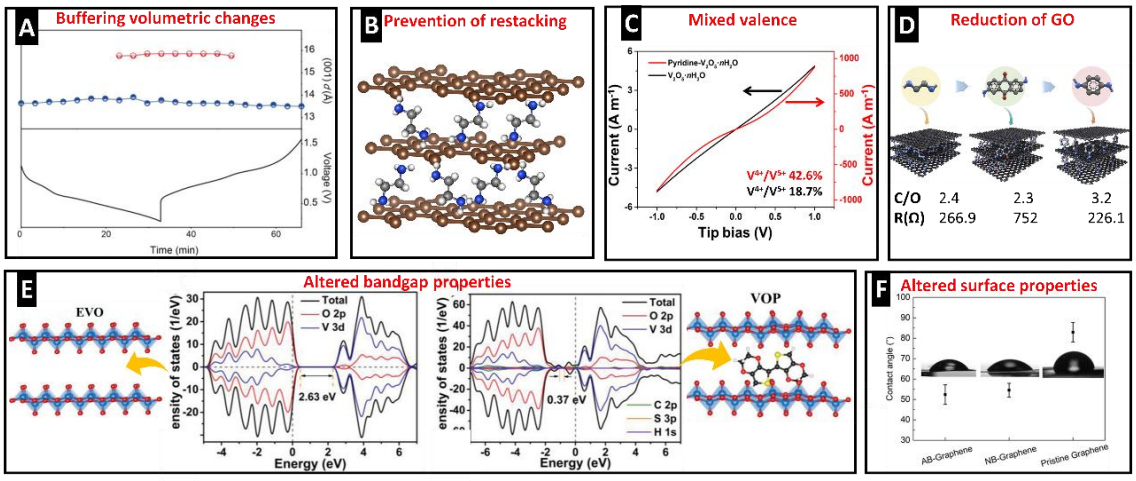

Figure 2.15: A) Structural evolution during cycling of PANI-V_2O_5: Interlayer distance *d* estimated from the (001) diffraction peak (blue) and an additional peak (001)* appearing at lower voltages (red). Reproduced with permission from Ref.[63] © 2020 WILEY-VCH Verlag GmbH & Co. KGaA, Weinheim. B) Pillaring prevents restacking of graphene layers. C) I-V curves of functionalized and pristine V_2O_5 showing higher electronic conductivity due to enhanced mixed valence in Pyridene-V_2O_5. Adapted with permission from Ref.[179] © 2019 WILEY-VCH Verlag GmbH & Co. KGaA, Weinheim. D) Carbon-to-oxygen ratio and resistivity vales for (left to right): ethylenediamine, 2,6-diaminoanthraquinone, and 1,4-phenylenediamine- functionalized GO. Adapted with permission from Ref.[94] © 2022 Elsevier Inc. E) Structures of expanded vanadium oxide (EVO) and PEDOT-functionalized vanadium oxide (VOP) and the corresponding calculated density of state. Adapted with permission from Ref.[170] © 2021 Wiley-VCH GmbH. F) Contact angle measurements for AB, NB- functionalized, and pristine graphene. Reproduced from Ref.[92] with permission from AAAS.

2.5.2.3 Influence on the pillar molecule

The incorporation of organic pillar molecules into inorganic host matrices can induce significant changes in the properties of the pillar molecule itself, which can influence overall pillared material performance in electrochemical applications. For instance, although polyaniline (PANI) is known for its pseudocapacitive properties, it faces challenges with cycling stability when used in isolation. However, by confining PANI into layered matrices such as MoS_2, its stability and performance can be substantially improved.[164] In MoS_2-PANI nanocomposites, the specific capacitance shows up to 86% retention after 1000 cycles, in stark contrast to the 42% retention after 600 cycles for pure PANI (**Fig. 2.16A**). This example demonstrates that interlayer pillaring not only modifies the properties of the host lattice but also stabilizes the pillar molecules themselves, enhancing the durability and functionality of the composite material.

However, while PANI can benefit from increased stability through its incorporation into layered hosts, it can also experience a reduction in electronic conductivity compared to its free-standing form. Layered compounds containing PANI generally exhibit lower electronic conductivity than pure PANI (**Fig. 2.16B**),[149] with the notable exception of PANI-$Ti_3C_2T_x$, which benefits from the highly conductive nature of its MXene host matrix.[181] This suggests that while interlayer functionalization can improve stability, it may also impose limitations on the electronic properties of the pillar molecule. Therefore, optimizing the balance between stability and conductivity is essential for maximizing the utility of PANI in energy storage systems.

In summary, interlayer functionalization not only brings changes to the host lattice and the intercalation of ions, but can also significantly impact the behaviour of the pillar molecules themselves. Careful attention to the interplay between the host and the pillar molecules, and the intercalating ions, is essential for maximizing the electrochemical performance and long-term stability of functionalized layered materials.

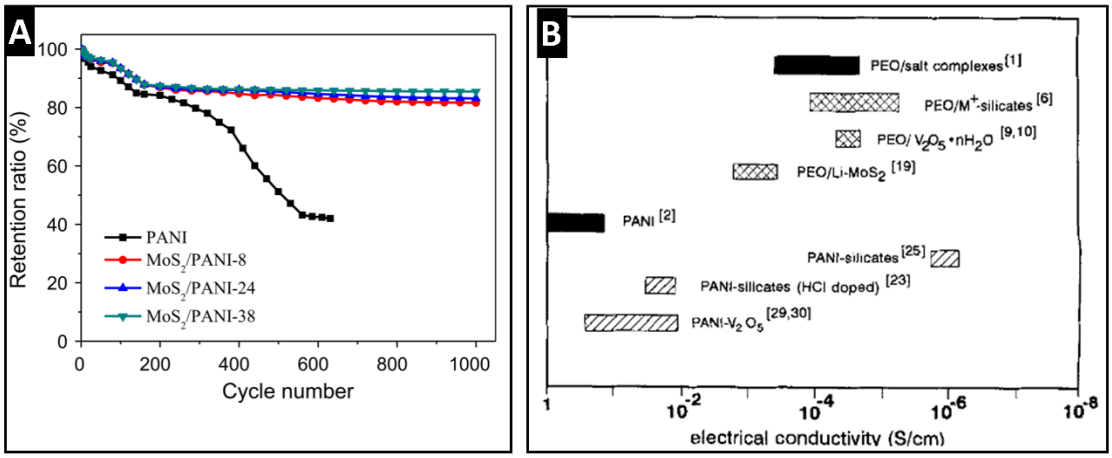

Figure 2.16: A) Capacity retention of PANI and MoS_2-PANI. Reproduced with permission from Ref. [164] Copyright © 2014 Elsevier B.V. B) Electrical conductivity of PANI and PANI-based composite electrodes. Reproduced with permission from ref.[149] Copyright © 1993 Verlag GmbH & Co. KGaA, Weinheim.

2.5.3 Challenges and outlook of organic interlayer functionalization

The increasing demand for novel electrochemical energy storage materials has catalysed innovations in electrode engineering approaches, with interlayer functionalization emerging as a promising strategy. This approach has been widely explored to enhance electrochemical properties such as ion intercalation kinetics, rate performance, and capacity, as well as to induce desired physiochemical properties, such as electronic conductivity (see **Section 2.5.2.2**). It has been suggested as a method of enabling ion-solvent cointercalation – a phenomenon that unlocks multivalent ion chemistries, low temperature cycling, and fast intercalation kinetics.[14] However, interlayer functionalization is not without its drawbacks (**Fig. 2.17**).

Modifying certain materials with organic pillars can lower redox potentials, induce structural disorders, and result in poorly defined redox plateaus, which are undesirable in many battery applications.[152] Additionally, designing new electrodes for energy storage requires meeting stringent performance criteria. The resulting structures must exhibit thermal, electrochemical, and structural stability, which can be challenging to achieve with organically functionalized electrodes.

Another limitation stems from the volatile nature of many pillar molecules and their solubility in many organic solvents used in electrolytes. Researchers in the field must consider that organic pillar molecules can leach out of the interlayer, evaporate, or sublime

during electrode processing and slurry drying, or later during cell cycling. Therefore, it is crucial to study the nature of interactions between host lattice and pillar molecules, as well as their evolution during electrode storage and cycling.

Moreover, an excessive amount of organic pillar can decrease the overall gravimetric and volumetric capacity by adding electrochemically inactive mass and volume to the active material's structure. This excess may also induce unfavourable phase transformations due to weakened van der Waals interaction.[182] Therefore, rational interlayer engineering requires careful regulation of both interlayer spacing and the amount of pillar species, to ultimately achieve a balance between enhanced diffusion paths and maintaining high energy density.

Additionally, it is worth noting that pillaring with organic molecules can lead to the exfoliation of the inorganic host into single- or few-layered 2D structures. While exfoliation can provide unique electrochemical properties, it also introduces new challenges that must be managed, such as increased activity toward electrolytes and poor volumetric energy density.

In conclusion, while interlayer functionalization with organic pillar molecules presents promising avenues for developing advanced ion intercalation electrodes, the field is still in its infancy, and much remains to be explored. Fully exploiting the potential of organically functionalized layered materials requires meticulous optimization of material design. Tailoring the combination of pillar molecule and layered host, while carefully considering their interactions is essential for advancing this innovative approach.

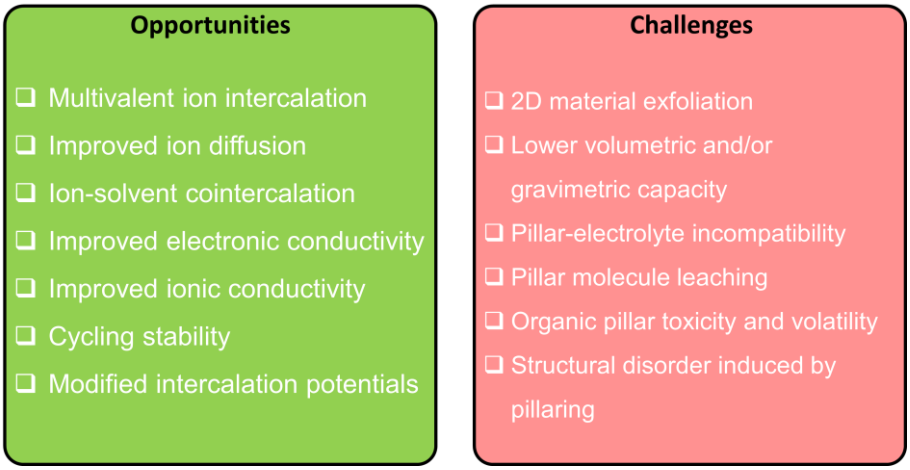

Figure 2.17: Opportunities and challenges of interlayer functionalization of layered materials.

2.6 Organically pillared materials as precursors of carbon nanocomposites

*This section is partially reproduced from the published article: "Mechanistic understanding of microstructure formation during synthesis of metal oxide/carbon nanocomposites", **J. Mater. Chem. A**, 2023, 11, 17125-17137, DOI: 10.1039/D3TA01230A. See also section 6.3.*

Transition metal oxides (TMOs) can electrochemically react with Li^+ via intercalation[183] and conversion reactions.[184] The exact mechanism depends on the extent of electron transfer which determines the degree of structural distortion, with intercalation reactions favored for up to ~ 1 Li^+/e^- per transition metal and conversion reactions for > 1 Li^+/e^- per transition metal. Many TMOs are semiconductors or insulators and require the addition of conductive carbon to the electrode for high-rate operation. Electrochemical conversion-type reactions in TMOs are further associated with large volumetric changes, leading to reduced efficiency and cycle life. One strategy to alleviate this issue is to confine TMO particles in a carbonaceous matrix to buffer volumetric expansion.[185,186] Both functionalities - improved electronic percolation and volumetric buffering - can be achieved with TMO/carbon (nano)composite electrodes.[187,188]

Among many synthesis approaches for TMO/carbon nanocomposites, one of the most widely adopted is the addition of an organic species to the TMO particles and its subsequent carbonization (**Fig. 2.18**).[186,189] Recent works have shown that the carbonization of amine molecules added into the interlayer of layered TMOs can produce TMO/C nanocomposites with a well-dispersed carbon phase.[186,190–194] In some cases, it was described that this synthesis route yielded heterostructured TMO/C[190,194] (and transition metal dichalcogenide / carbon[195]) nanocomposites, where layers of dissimilar phases alternate. This particular microstructure results in abundant heterointerfaces which may synergistically combine beneficial electrochemical properties of the individual building blocks (redox-activity, electrical conductivity).[196,197]

Comparison of these studies[186,190–194] reveals variations in structural properties of the resulting TMO/C materials, especially in terms of nanocomposite microstructure (i.e., phase distribution), degree of TMO reduction, and carbon hybridization. A more generalized understanding of the synthesis process is required to be able to precisely tune the resulting nanocomposite properties. Therefore, it is important to develop mechanistic insights into the microstructure evolution during carbonization. Understanding the process

via *in situ* characterization methods, as well as microscopic analysis representative of the bulk volume of the nanocomposites can give valuable insights into the microstructure evolution. This is essential to further optimize nanocomposite electrode materials for electrochemical energy storage applications and beyond.

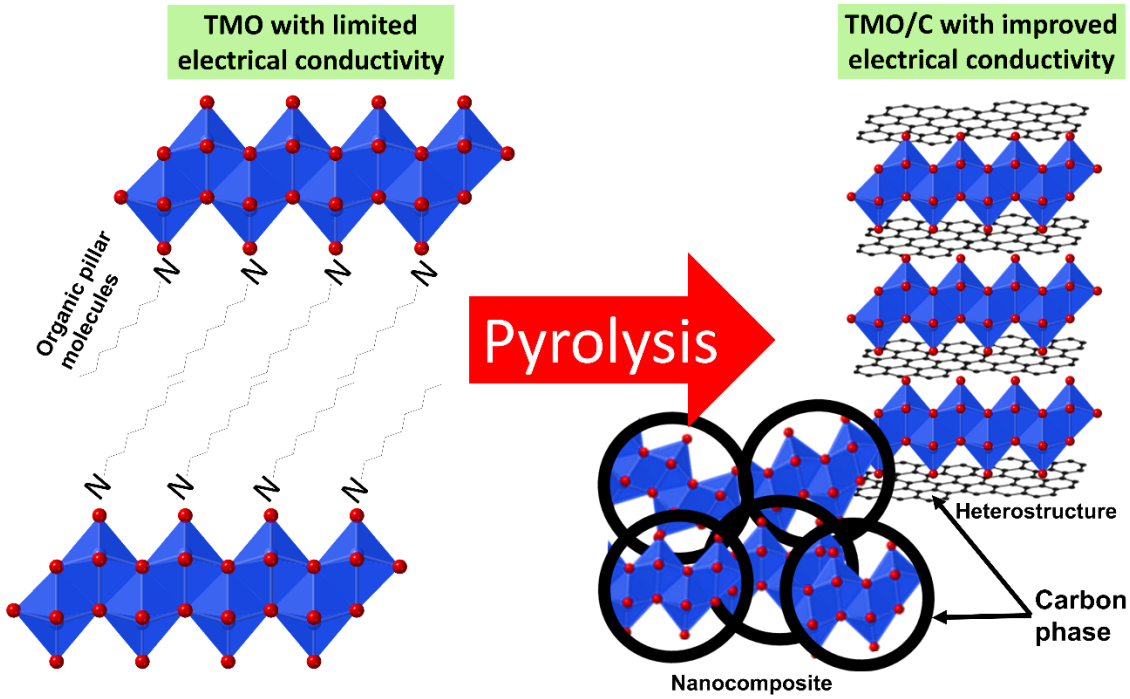

Figure 2.18: Schematic of nanocomposite formation from the pyrolysis of as pillared TMO precursor.

3. Objectives of the dissertation

The demand for innovative energy storage solutions is critical in today's world, and battery electrode materials play a central role in addressing this challenge. Among these materials, layered structures are of particular importance due to their capacity for reversible ion intercalation. To enable new battery chemistries, novel energy storage mechanisms, and fast intercalation kinetics, controlling nanoconfinement within the interlayer space of layered materials is a novel and innovative approach. It offers the unique possibilities not only to improve ion transport properties but also to enhance electrical conductivity, and it can be applied to a variety of intercalation chemistries, including lithium- and sodium-ion.

To address the challenge of limited ion diffusion kinetics, the dissertation firstly focuses on the interlayer functionalization of layered titanate electrodes using organic pillar molecules, altering the nanoconfinement environment in the interlayer. In the context of lithium-ion batteries, the pillared electrodes are explored in detail, with particular emphasis on the role of nanoconfinement design in enabling **ion-solvent cointercalation**, enhancing diffusion kinetics, and altering intercalation potentials. Hence:

Objective 1: Enhancing Li-ion diffusion kinetics in layered electrode materials by promoting ion-solvent cointercalation.

The second part of the dissertation expands the scope to sodium-ion batteries. It examines how the nanoconfinement environment in layered titanates influences the energy storage mechanism in a Na-ion system, where titanate electrodes are employed as anodes. The study highlights the versatility of the interlayer functionalization approach and its ability to unlock **new charge storage behaviours** in sodium-ion intercalation electrodes. The part contributes to:

Objective 2: Enhancing Na-ion intercalation kinetics in layered electrode materials by altering the host material's interlayer environment.

Finally, the dissertation addresses the challenge of electrical conductivity in TMO-based electrode materials. Interlayer-confined organic molecules within a layered oxide can also

serve as sources for a highly electrically conducting carbon phase. Through a pyrolysis treatment, these organic pillars are converted into carbon, forming a transition metal oxide/carbon (TMO/C) nanocomposite, where a **carbon phase is confined within the nanodomains of TMO phases**. A detailed mechanistic analysis is provided, examining the steps involved in the formation of the carbon phase from the pillar molecules. A comprehensive analysis of the nanocomposite's electrochemical intercalation and conversion reactions is provided.

Objective 3: Improving electrical conductivity in layered electrode materials through the formation of carbon nanocomposites.

As summarized in **Figure 3.1**, this dissertation establishes interlayer functionalization with organic pillar molecules as a versatile strategy for designing advanced layered electrodes with deliberately designed nanoconfinement conditions, with improved ionic transport and enhanced electrical conductivity, thereby contributing to the development of next-generation battery materials.

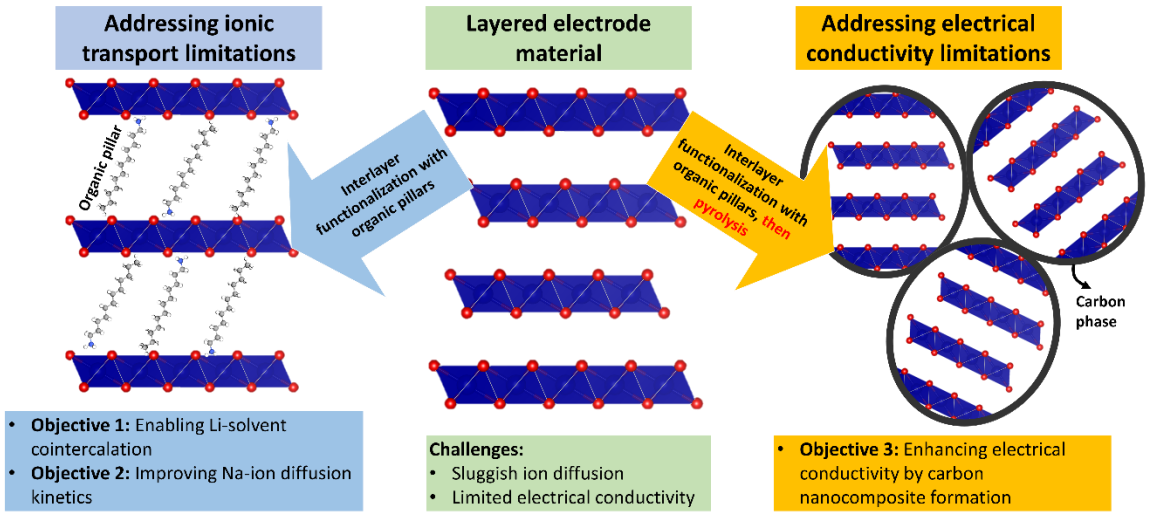

Figure 3.1: Overview of the objectives of this dissertation, aimed at addressing challenges related to layered electrode materials.

4. Theory: Techniques and Instruments

4.1 Physicochemical Techniques

4.1.1 X-ray Diffraction (XRD)

X-ray diffraction (XRD) is a powerful analytical technique used to study the structure of crystalline materials. It is based on the principle that X-rays, when directed at a crystal, are scattered in specific directions due to their interaction with the crystal's periodically arranged atomic planes. The technique relies on Bragg's Law, which relates the wavelength of the incident X-rays to the angle of diffraction and the spacing between the crystal planes.[198] Bragg's law is expressed as

$$n\lambda = 2d \sin\theta \qquad (4.1)$$

where n is the order of diffraction, λ is the wavelength of the X-rays, d is the distance between the crystal planes, and θ is the angle of incidence.

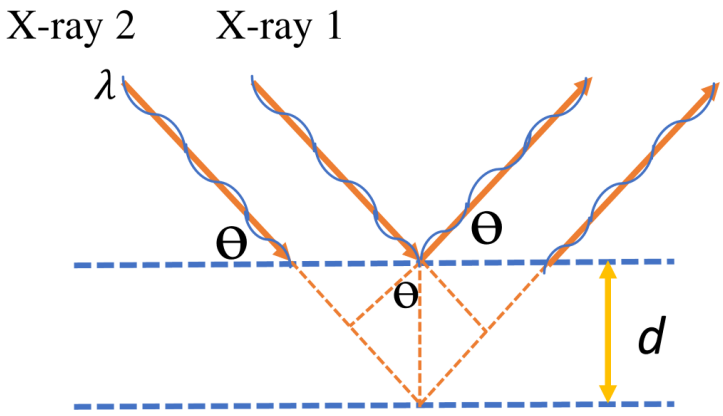

Figure 4.1: Schematic representation of Bragg diffraction.

An XRD apparatus typically consists of an X-ray tube, a sample holder, a detector, and a goniometer that precisely controls the angle of incidence and detection. The X-ray tube generates a beam of X-rays, usually produced by bombarding a metal target (in this work, Cu and Mo metal targets were used) with high-energy electrons. The sample is then placed in the path of the X-ray beam, and as the goniometer rotates, the detector records the intensity of the diffracted X-rays at various angles.

In the context of layered electrode materials, *operando* XRD is used to detect changes in the crystal structure during battery cycling. For *in situ* studies, an electrochemical cell can be integrated within the XRD setup, allowing real-time monitoring of structural changes as the battery is charged and discharged. This capability is crucial for understanding phase transitions, structural evolution, and stability of electrode materials under operating conditions.

XRD can be performed in either reflection or transmission geometry. In reflection mode, the X-ray beam strikes the sample at an angle θ relative to the sample surface, and the scattered X-rays are detected at the same angle, following Bragg's law. In transmission geometry, the X-ray beam passes through the sample perpendicularly. In this work, *in situ* XRD was performed in transmission geometry. An *in situ* electrochemical cell for transmission XRD requires two openings to allow the X-rays to pass through the cell, where Kapton tape was used. The cell used in *in situ* XRD measurements discussed in this dissertation is presented in **Fig. 4.2**.

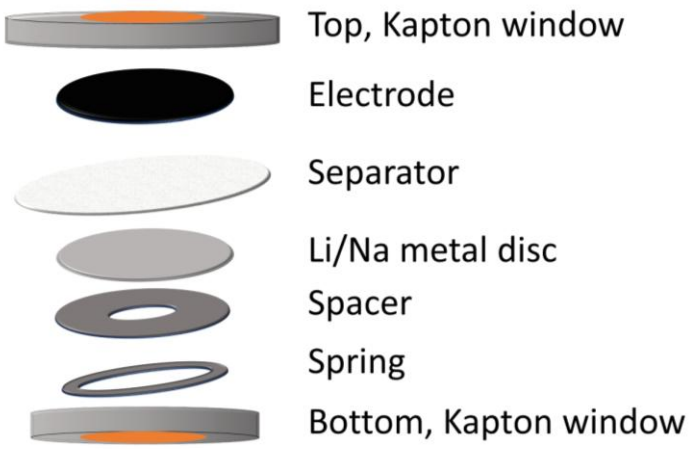

Figure 4.2: Components of a coin cell designed for *in situ* XRD experiments.

4.1.2 Fourier Transform Infrared Spectroscopy (FTIR)

Infrared (IR) spectroscopy is a vital analytical technique used to study the chemical structure of materials by examining how molecules or lattices absorb infrared light. This absorption occurs at specific frequencies that correspond to the energy of molecular or lattice vibrations, making IR spectroscopy particularly useful for identifying functional groups within a molecule or bonds in a crystalline lattice. The Fourier transform (FT) refers to a mathematical method used to convert the raw data (an interferogram) into a readable

spectrum that represents the sample's molecular vibrations and chemical bonds. The absorption frequencies are typically measured in wavenumbers (cm^{-1}).

When molecules absorb infrared light, the photon energy is sufficient to induce vibrational excitations rather than electronic transitions. Covalent bonds within molecules behave like stiff springs that can stretch and bend, and the absorption of IR radiation causes these vibrations. Each type of bond or functional group (e.g., O-H, C=O) absorbs infrared light at characteristic frequencies. Consequently, IR spectroscopy provides a unique spectrum for each organic compound, reflecting its specific molecular structure.

In this work, IR spectroscopy is performed using Attenuated Total Reflection mode (ATR), which involves directing the IR beam through a crystal, causing multiple reflections at the interface between the crystal and the sample (**Fig. 4.3**). ATR can be used to analyse materials either deposited on the crystal or pressed against it. This approach enhances sensitivity and provides detailed information on molecular functionality within a layered electrode sample.[199]

While FTIR spectroscopy is a fast and relatively straightforward characterization technique, it faces some limitations such as the detection of species at only one spot rather than providing comprehensive mapping of the sample. Additionally, FTIR spectroscopy can be susceptible to contaminants and artefacts, depending on the environmental conditions.[200] Repeating measurements at several spots and combining FTIR with other characterization tools is advantageous to minimize measurement errors and enhance accuracy.

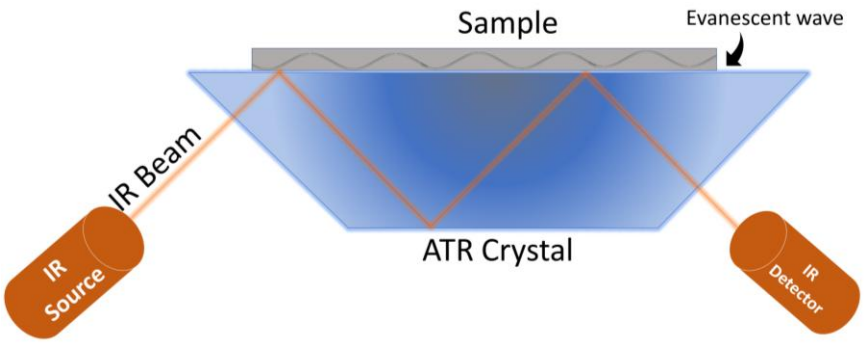

Figure 4.3: Schematic showing the basic principle of ATR-FTIR.

4.1.3 Raman Spectroscopy

Raman spectroscopy is a powerful analytical technique widely used in the study of solid materials and liquids, and is important in the field of battery research. It is a non-destructive method that provides detailed information about the vibrational modes of molecules and inorganic crystalline lattices, which can be directly related to the chemical composition, structure, and interactions within a material. This makes Raman spectroscopy an invaluable tool for investigating the complex processes occurring when the structure of battery materials is modified, e.g. with organic pillar molecules.

Raman spectroscopy is based on the inelastic scattering of a monochromatic laser light. When light interacts with a material, most photons are scattered elastically (Rayleigh scattering), retaining their original energy. However, a small fraction of the light is scattered inelastically, resulting in an energy shift corresponding to the vibrational modes of the molecules or crystal lattices in the material (**Fig. 4.4**). This shift provides a unique spectral fingerprint that can be used to identify the material's structure and bonds. Furthermore, Raman spectroscopy can be performed under various environmental conditions, including *operando*, allowing the study of battery materials in real-time during operation.[201] This capability is crucial for understanding the dynamic processes that occur during battery cycling, such as phase transitions and bond length changes.

Raman spectroscopy offers the advantages of accessibility and straightforward sample preparation. However, interpreting the spectra can be rather complex, and laser irradiation may induce structural transformations in sensitive host materials,[202] or decomposition of organic pillar molecules. Along with Raman spectroscopy, other methods, such as X-ray photoelectron spectroscopy (XPS), are frequently used in conjunction to probe the chemical environment of functionalized electrode structures.[203]

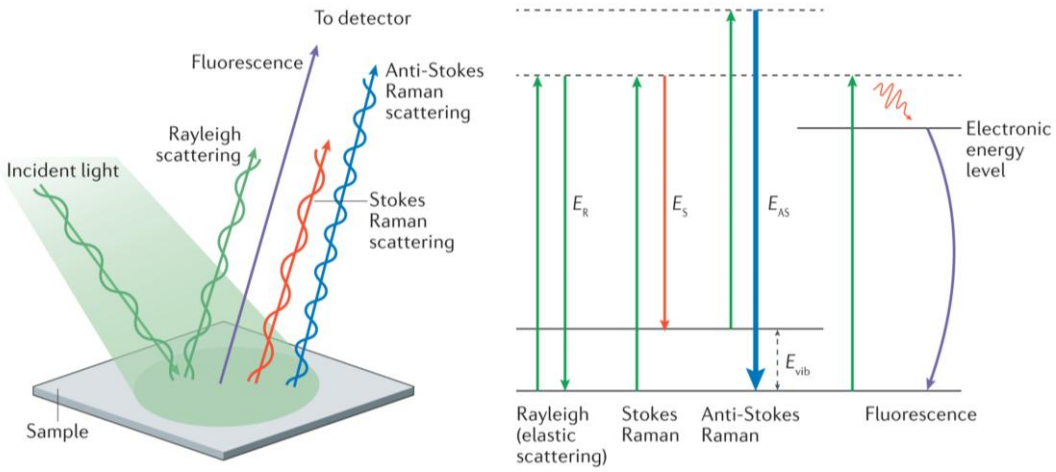

Figure 4.4: Types of interactions of incident light with sample. Adapted from Ref.[204]

4.1.4 Thermogravimetric Analysis

Thermogravimetric analysis (TGA) is a technique used to measure mass changes in a sample as it undergoes temperature variations.[205] It operates by continuously recording the mass of a sample as it is heated or cooled in a controlled environment, typically in the presence of an inert gas like nitrogen or helium, or a reactive gas such as oxygen or synthetic air. The sample is put in a crucible made of aluminium, alumina, or other materials, then placed on a high-precision balance within a furnace (**Fig. 4.5**). As the temperature increases, the sample may undergo various changes at certain temperatures or within temperature intervals, such as decomposition, oxidation, reduction, or evaporation, each of which results in a measurable change in mass.

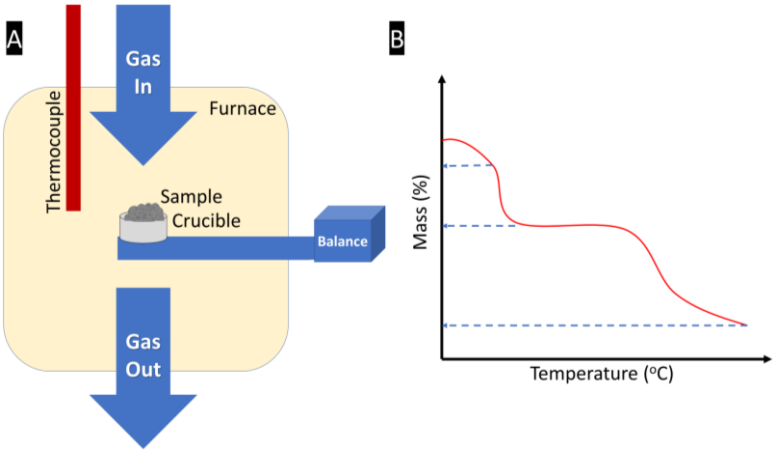

Figure 4.5: A) Schematic showing the main parts of a TGA instrument and B) an illustration of the resulting mass loss *vs*. temperature plot.

TGA is particularly valuable in the study of functionalized layered materials, as it enables quantifying the amount of organic species incorporated within the layers. This quantification facilitates the determination of the optimal amount of guest molecules necessary to achieve pillaring while avoiding the addition of excessive pillar molecules that act as dead weight. Additionally, TGA offers insights into the thermal stability of the hybrid material, indicating how well the pillars withstand various thermal conditions.

When coupled with online FTIR and/or mass spectrometry (MS), the types of gaseous species evolving during mass change can be identified, providing detailed understanding of the thermal behaviour of the material.[206] In pillared layered electrodes, this allows for a better understanding of the mechanism of guest molecule decomposition.

Despite its advantages, TGA faces certain limitations in the characterization of pillared layered materials. The simultaneous evolution of multiple species can complicate their quantification, particularly if they evolve or decompose within overlapping temperature ranges. Additionally, TGA measurements are susceptible to errors that can arise from balance inaccuracies and sample inhomogeneity.[205]

4.1.5 Scanning Electron Microscopy

Scanning Electron Microscopy (SEM) is a powerful and versatile technique used to study the surface morphology and composition of materials at high resolution. SEM uses a focused beam of electrons (typical incident energies of primary electron: 2 – 20 keV) to scan the sample surface, enabling imaging with nanometre-scale detail. This makes SEM an essential tool in analysing battery electrode materials. SEM operates by scanning across the sample surface with a finely focused electron beam in a high vacuum environment. The primary electron beam interacts with a certain sample volume (pear shaped, depth depending on material and primary electron energy), and it generates several types of signals, including secondary electrons, backscattered electrons, and characteristic X-rays (**Fig. 4.6**). These signals originate from different sample depths; they are detected and used to create detailed images and gather compositional information.[207]

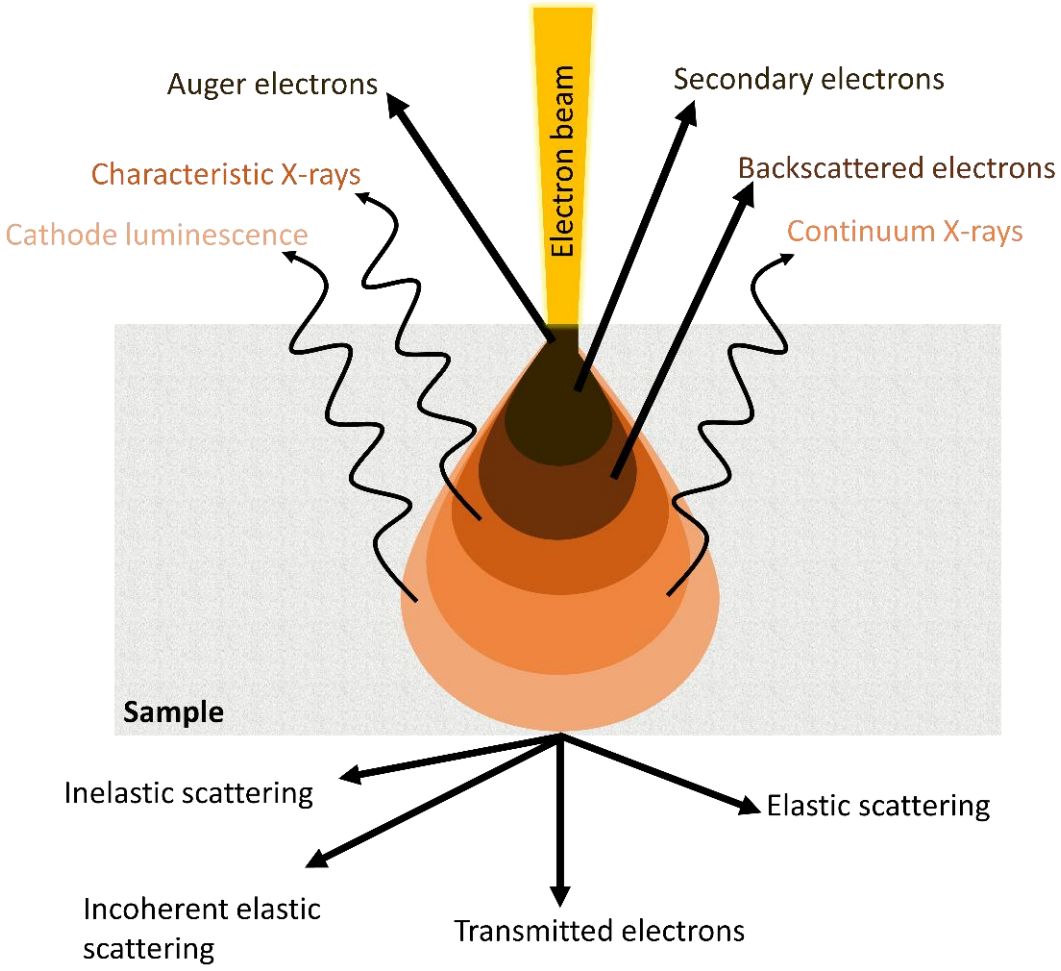

Figure 4.6: Schematic of electron beam interaction with a sample in electron microscopy.

Secondary electron imaging mode is among the most common modes of SEM imaging, which is highly sensitive to surface features. Secondary electrons are low-energy electrons (<50 eV) that are ejected from the atoms in the sample due to inelastic scattering with the incident primary electrons. [208] Because of their low energy, these electrons originate from a shallow depth within the sample, typically a few nanometres, allowing SEM to produce images with fine surface detail and high resolution.

Backscattered electrons, on the other hand, have much higher energy and are scattered back from deeper within the sample. This mode provides contrast based on the atomic number of the elements in the sample—heavier atoms scatter electrons more effectively, resulting in brighter regions in the image. This atomic number contrast makes SEM particularly useful for differentiating between different materials, for example in a composite electrode.

In addition to imaging, SEM also allows for elemental analysis through the detection of characteristic X-rays emitted from the sample. When the primary electron beam interacts with the atoms in the sample, it can eject inner-shell electrons. This leaves behind an electron hole, which is subsequently filled by an outer shell electron of a higher energy state, leading to the emission of an X-ray with a characteristic wavelength corresponding to the energy difference between the inner and outer electron shells. These X-rays have energies that are characteristic of the elements present in the sample, allowing for qualitative and quantitative analysis of the material's composition through the Energy Dispersive X-ray (EDX) technique. For this purpose, SEMs are often equipped with an EDX detector.

4.1.6 Atomic Force Microscopy

Atomic Force Microscopy (AFM) is a widely used technique that enables detailed investigation of surfaces and structures at the nanometre to micrometre scale. It operates in various environments, including ambient air, liquids, and vacuum, making it a versatile tool for analysing different types of materials in different environments. AFM works by scanning a probe tip across the sample surface to collect localized information about topography and other surface properties, with scan sizes ranging from over 100 micrometres to the angstrom scale.

In AFM, a sharp tip mounted on a flexible cantilever is brought into proximity with the sample surface. The interaction between the tip and the surface—whether repulsive or attractive—generates forces that cause the cantilever to deflect. These deflections are monitored using a laser beam reflected from the cantilever onto a position-sensitive photodetector (**Fig. 4.7**).[209] The data collected allows the AFM to map the surface topography with high precision, producing images that reveal surface structures down to molecular resolution.

The two most common AFM imaging modes are contact mode and intermittent (tapping) mode. In contact mode, the tip remains in constant contact with the sample surface, and the cantilever’s deflection is kept constant by a feedback loop. This mode allows for detailed mapping of surface topography and can measure both repulsive and attractive forces through force–displacement curves, which are used to analyse mechanical properties and adhesive interactions.

However, contact mode AFM can exert shear forces on the sample, potentially deforming or damaging soft materials. Furthermore, some materials might exhibit strong electrostatic interaction with the tip. To mitigate this, intermittent contact modes, such as tapping mode AFM, are used. In tapping mode, the cantilever is oscillated at or near its resonance frequency, and the tip only intermittently contacts the surface. This reduces shear forces, making it more suitable for analysing samples with surface charges, such as layered transition metal oxides. The feedback loop in tapping mode adjusts the cantilever's position to maintain a consistent oscillation amplitude, providing topographical data with minimal sample disturbance.

AFM's ability to operate in diverse environments without requiring extensive sample preparation is a significant advantage. This capability makes it a powerful tool for studying a wide range of materials, including layered battery electrodes, both in their native states and in *operando*.[210]

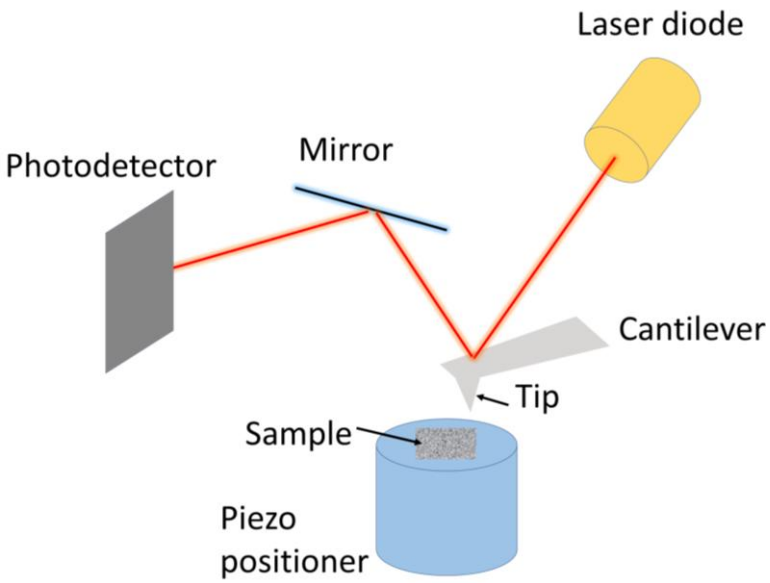

Figure 4.7: Schematic of AFM working principle

4.1.7 Transmission Electron Microscopy

Transmission Electron Microscopy (TEM) is a crucial analytical tool in battery research, enabling the exploration of microstructural and atomic-level details of electrode materials. TEM provides exceptional resolution and the ability to analyse the composition and

structure of battery materials, making it indispensable for understanding and optimizing their performance, durability, and safety.

TEM works by transmitting a focused beam of electrons through an ultra-thin specimen (typically <100 nm). The interaction between the electrons and the sample generates detailed images that reveal the internal structure of the material at the nanoscale. The high-energy primary electron beam used in TEM (typically 80 – 300 keV) has a short wavelength, allowing for atomic-level resolution. As the primary electrons pass through the specimen, they are scattered by the atoms, and these interactions are recorded to create high-resolution images.

In battery research, TEM is particularly valuable because it can visualize features as small as individual atomic columns, allowing for the examination of key materials like electrode components, (solid or vitrified liquid) electrolytes, and interfaces. This capability is essential for analysing the micro- and nanostructure of battery materials, which directly influence the electrochemical performance.

When the electron beam is aligned parallel to the basal plane, high resolution transition electron microscopy (HRTEM) can directly measure lattice spacings,[59] providing detailed structural information of layered electrode materials.

Beyond imaging, TEM facilitates other analytical techniques, such as selected area electron diffraction (SAED), which offers crystallographic insights into the material, and energy-dispersive X-ray spectroscopy (EDX), which provides data on elemental composition and spatial distribution of elements.[211]

Despite being powerful analytical techniques for layered electrodes, electron microscopy techniques come with limitations. The electron beam may damage sensitive host-guest materials, and the high-vacuum environment might not be suitable for imaging layered materials containing weakly-bound interlayer species. Cryogenic electron microscopy (Cryo-TEM) has been proposed as a solution to this issue,[212] potentially preserving guest molecules in the interlayer space. Additionally, TEM requires extremely thin samples, typically less than 100 nanometres thick, which can be challenging to prepare without altering the material's structure. These challenges require careful sample preparation to ensure accurate and meaningful results.

4.1.8 Electrochemical Quartz Crystal Microbalance

Electrochemical Quartz Crystal Microbalance (EQCM) is a powerful analytical tool that combines electrochemistry with an indirect mass measurement at the nanogram level, making it particularly valuable in the study of battery materials. By utilizing a quartz crystal resonator, EQCM can monitor changes of the resonance frequency in real-time as an electrochemical reaction occurs, which can be converted to mass changes on an electrode's surface and/or bulk. This capability is crucial for understanding the dynamic processes in battery systems, such as ion intercalation, electrodeposition, and the formation of solid-electrolyte interphases (SEI).

EQCM operates on the principle of the Sauerbrey equation, which is relates the change in resonance frequency of a quartz crystal resonator to the mass change on its surface.[213] The equation is given by:

$$\Delta m = -C n \cdot \Delta f \quad \textbf{(4.2)}$$

where Δm is the mass change on the crystal surface, C is the mass sensitivity constant (which depends on the properties of the quartz crystal, such as its density and shear modulus), n is the overtone number (where the fundamental frequency corresponds to $n = 1$), and Δf is the change in resonance frequency.

For the Sauerbrey equation to be valid, it is crucial that no significant change in the dissipation factor (D) occurs. D is defined by the ratio of the full resonance width peak W to the related resonance frequency f. In other words, D represents the hydrodynamic contribution to EQCM responses,[214] as expressed by

$$D = (W/n)/(f/n). \quad \textbf{(4.3)}$$

This requirement relies on two main conditions (**Fig. 4.8**):

a) The electrode coating must be rigidly attached to the quartz crystal surface and maintain its rigidity both in air and in contact with the electrolyte during cycling, regardless of the applied potential. This ensures that there is minimal internal dissipation within the solid matrix of the electrode.

b) The electrode must not undergo significant volume or porosity changes during cycling, as such changes can alter hydrodynamic interactions at the electrode-electrolyte interface, leading to dissipation changes.[215]

When these conditions are satisfied, the electrode's frequency response can be considered purely inertial, meaning the mass changes can be directly related to the frequency shift as indicated by the Sauerbrey equation.

In battery research, EQCM is often used to track the mass of ions as they intercalate into electrode materials during charge and discharge cycles. For instance, EQCM can provide insights into the (de-)solvation behaviour of lithium ions in electrolytes, revealing whether these ions intercalate in their bare or solvated forms. This real-time data is essential for understanding fundamental phenomena, such as ion-solvent cointercalation in battery materials.

The sensitivity of EQCM allows the detection of even minor changes in mass, enabling the study of subtle processes that would be difficult to observe using other techniques. This includes monitoring the growth of SEI layers, which play a critical role in the performance and safety of batteries. By understanding these processes at a fundamental level, researchers can design better materials and improve the overall performance of energy storage devices.

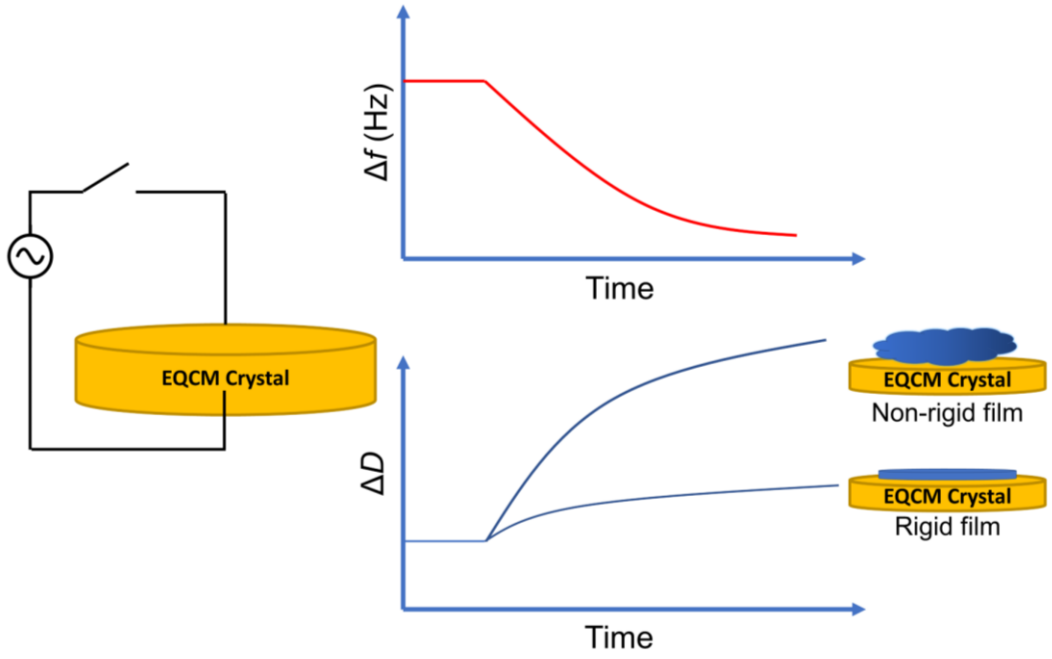

Figure 4.8: Schematic of EQCM crystal response when measuring a rigid and a non-rigid film.

4.2. Electrochemical techniques

4.2.1 Electrochemical Cell Setups

Electrochemical cells are fundamental tools in the study of electrochemical processes. An electrochemical cell typically consists of a working electrode (WE), which is the active material where the electrochemical reactions of interest take place, a counter electrode (CE) which completes the circuit by allowing the flow of charge, and a reference electrode (RE), which ideally has a fixed potential, allowing to control and monitor the potential of the WE. The design of electrochemical cells varies depending on the specific application, with most falling into two main categories: 2-electrode and 3-electrode setups (**Fig. 4.9**). The choice between them depends on the experiment's objectives and the nature of the system under study.

In a 2-electrode electrochemical cell, the system consists of a WE and another electrode that acts as both RE and CE. At the working electrode side, electrochemical reactions of interest occur, while at the counter electrode completes the circuit by allowing charge to flow. The potential of the WE is monitored with respect to the RE. In this dissertation, metallic Li and Na discs were used in 2-electrode setups as RE/CE. It should be noted that metallic Li and Na are called *pseudo*-reference electrodes, since they are subject to reactions with carbonate-based electrolytes, which may influence the value of the measured potentials. The key advantage of the 2-electrode setup is its simplicity, as these cells are typically easy to assemble and sufficiently stable during cycling.[216]

In the 3-electrode cell setup, the system consists of a WE, RE, and CE. The RE can monitor the potential of the WE independently from the CE. The major advantage of a 3-electrode setup is the ability to isolate the behaviour of the WE, therefore eliminating any errors arising from the CE, therefore, this configuration is often used in studying full cells. When working with full cells, The N/P ratio, or the negative-to-positive electrode capacity ratio, is a crucial parameter, representing the balance between the capacity of the anode and the cathode. An optimal N/P ratio allows efficient utilization of both electrodes and helps prevent issues such as lithium plating on the anode or degradation of the cathode.[217] The N/P ratio is often set slightly higher than 1 to compensate for irreversible capacity losses during the first few cycles, especially at the anode, which undergoes SEI (solid electrolyte

interphase) formation. A well-balanced N/P ratio is critical for improving the cycle stability, initial coulombic efficiency, energy density, and safety of the cell.

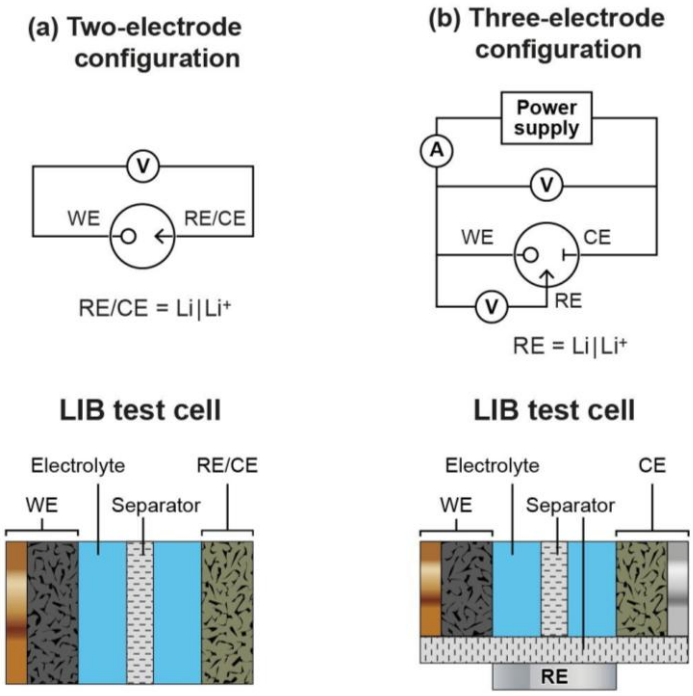

Figure 4.9: Illustration of 2- and 3-electrode configurations of lithium-ion battery cells. Reproduced with permission from Ref.[218] © 2019 Elsevier Ltd.

4.2.2 Cyclic Voltammetry

Cyclic voltammetry (CV) is a widely used electrochemical technique that provides detailed information about the redox behaviour of a chemical species. It is particularly useful in studying the electron transfer processes of various systems, especially between electrode materials and ionic charge carriers in the electrolyte.

In a cyclic voltammetry experiment, the potential of a working electrode is swept linearly over time, first in one direction and then reversed, forming a cyclic voltammogram. This potential sweep induces a current that is recorded as a function of the applied potential. In battery materials, the resulting plot, a cyclic voltammogram, typically features peaks corresponding to the oxidation and reduction processes occurring during the potential sweep. However, in materials where charge storage is dominated by surface processes, e.g., capacitor-like materials, the resulting CV is typically rectangular. In pseudocapacitive

materials, where redox processes happen near the surface or by fast intercalation processes, the CV typically looks rectangular with small redox features (**Fig. 4.10**).

Cyclic voltammetry is highly versatile and can be applied under various conditions, such as in different electrolytes, at various temperatures, and at different scan rates. This versatility makes it an essential tool in the study of complex redox processes, especially in the development of new materials for electrochemical applications.

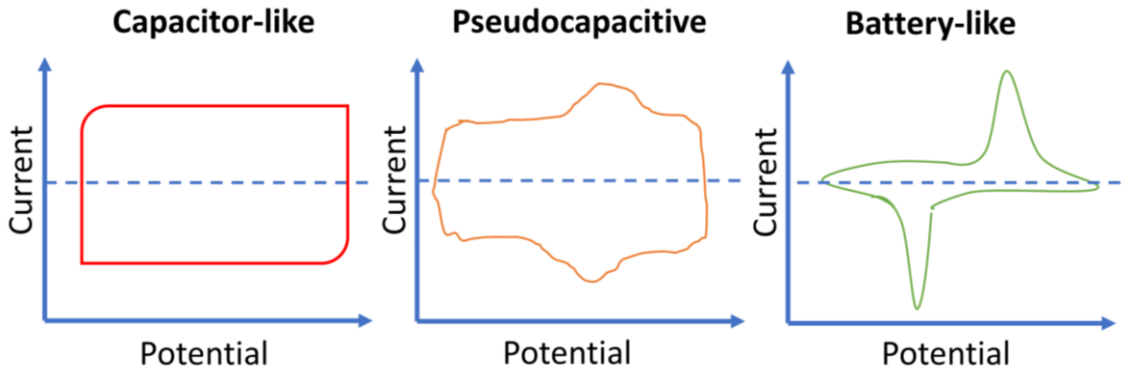

Figure 4.10: Schematic of cyclic voltammograms of capacitive, pseudocapacitive, and batter-like behaviour, inspired by Ref.[219] with permission from the American Chemical Society, Copyright © 2018.

4.2.3 Galvanostatic Charge and Discharge

Galvanostatic charge and discharge (GCD) is a fundamental technique used to evaluate the performance and stability of electrochemical energy storage devices, such as batteries and supercapacitors. The technique involves applying a constant current to an electrochemical cell while monitoring the voltage response over time. This method is particularly valuable in determining key parameters such as capacity, energy density, power density, rate handling, and cycle life of electrodes.

During a galvanostatic charge, a constant current is applied to the electrochemical cell, causing the cell voltage to rise as the battery charges. This process continues until a predetermined voltage limit is reached (called the upper cut-off voltage), at which the current is turned off or switched to a discharge mode. In the discharge phase, the current is reversed, and the voltage is monitored as it decreases until a lower voltage limit is reached (called the lower cut-off voltage). The voltage response during both charging and discharging provides insight into the internal processes occurring within the cell. When

choosing a three-electrode electrochemical cell setup employing working, counter and reference electrodes, it is possible to monitor the electrode potential of the working electrode (versus the reference electrode) instead of monitoring the cell voltage. This will yield useful information on a materials level instead of cell level.

One of the primary functions of GCD is its ability to simulate real-world operating conditions, as many applications of batteries and supercapacitors involve charging and discharging at constant currents. This method allows the measurement of the gravimetric specific capacity C, given by

$$C = \frac{I\,t}{m_{AM}} \qquad \textbf{(4.4)}$$

Where C is gravimetric specific capacity, I is applied current, t is time, and m_{AM} is the mass of electrode active material.

GDC also helps determine the Coulombic efficiency, which is the ratio of the charge output during discharge (negative current) to the charge input during charging (positive current). A high Coulombic efficiency indicates minimal losses due to irreversible reactions, i.e., a high chemical reversibility of the electrochemical reactions.

Similar to CV, the shape of the voltage profiles obtained by GCD also indicates the charge storage mechanism, from capacitor-like, to pseudocapacitive, to battery-like (**Fig. 4.11**).[219] Additionally, by repeating the charge-discharge cycles, one can assess the cycle life of the device, which indicates how many cycles the device can undergo before its capacity significantly fades, making it a vital metric for the longevity of batteries and capacitors.

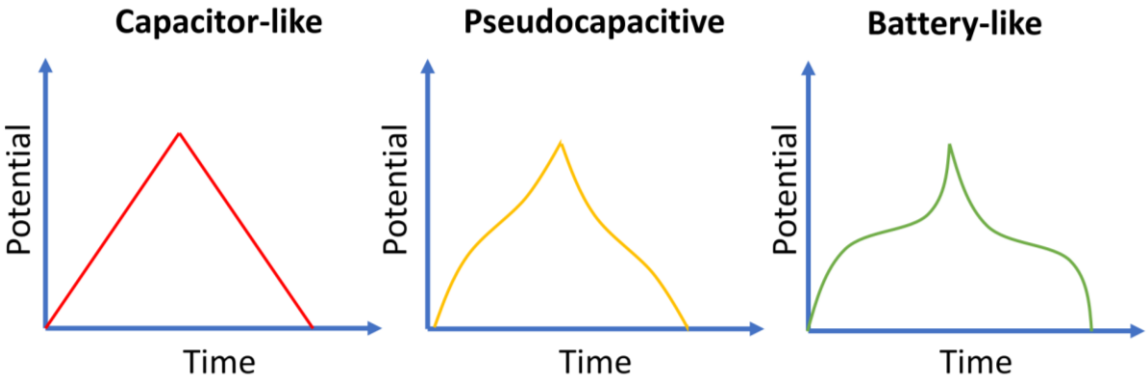

Figure 4.11: Schematic of GCD profiles of capacitive, pseudocapacitive, and battery-like electrodes showing linear and non-linear evolution of potential with time.

4.2.4 Electrochemical Impedance Spectroscopy

Electrochemical impedance spectroscopy (EIS) is a powerful, versatile, and non-destructive analytical technique used to characterize the electrical properties of electrochemical systems. EIS provides insights into electronic and ionic conductivity, charge transfer, and other dynamic processes occurring within electrochemical energy storage systems.[220]

In EIS, the impedance that a system presents to an alternating current (AC) over a range of frequencies is measured. Impedance is a complex quantity with both amplitude and phase components, which vary depending on the frequency of the applied signal (as opposed to the resistance, which is frequency-independent). The impedance is expressed by:

$$Z(\omega) = |Z|(cos\varphi + jsin\varphi) = Z' + jZ'' \qquad \textbf{(4.5)}$$

where Z' is the real component of impedance, representing resistance, and Z'' is the imaginary component representing reactance, $|Z|$, the module of impedance, and $\varphi = \omega t$, is the phase.[221]

By sweeping through a range of frequencies, EIS generates a spectrum that can be used to infer various properties of the system under study, typically represented as a Nyquist plot (**Fig. 4.12**). In a Nyquist plot, the real part of the impedance, Z', is plotted against the imaginary part, Z''. These plots provide a representation of the system's response to the applied AC signal and can be used to distinguish between different processes, such as resistive, capacitive, and inductive responses.

The interpretation of EIS data often depends on equivalent circuit models, which simulate the battery's behaviour through a network of simple electrical circuit elements. Such circuit elements include resistors (R), capacitors (C), and Warburg impedance (W), which is a complex quantity representing the mass transfer of redox species to the electrode surface, typically appearing as a 45° line at the low frequency range. These models allow us to calculate physical quantities, such as individual contributions of difference sources of impedance in the battery. However, it's crucial to recognize that they provide only a partial understanding of the battery's physical processes. This limitation stems from the fact that the correlation between the electrical elements in the circuit and the electrochemical

processes within the battery is largely phenomenological, rather than being a direct measure of the underlying physical phenomena.[222] Therefore, effective interpretation of EIS data requires careful selection of equivalent circuit model.

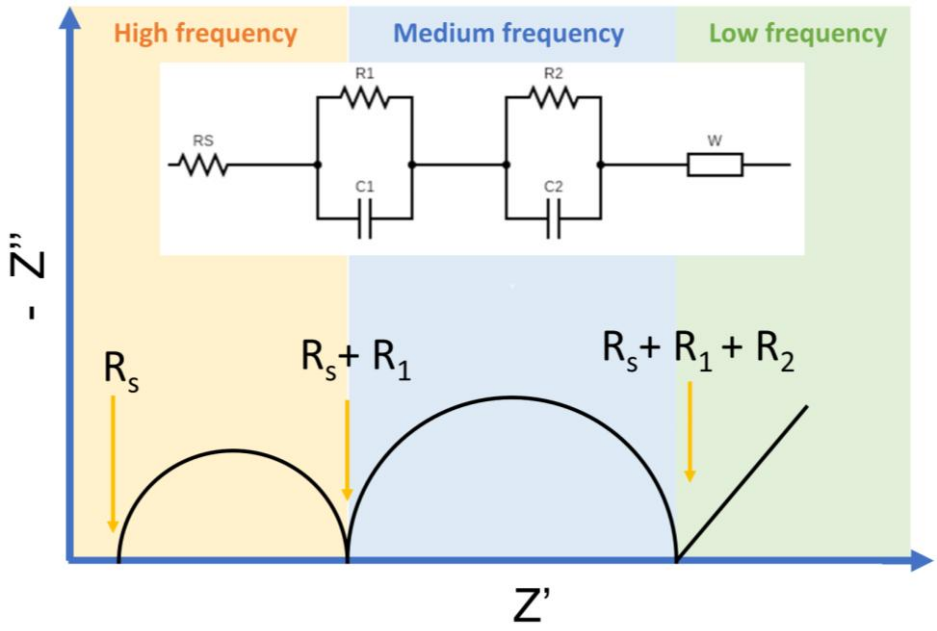

Figure 4.12: Illustration of a Nyquist plot and the corresponding equivalent circuit representation.

5. Materials and Methods

5.1 Materials and methods for the study on: nanoconfinement-induced electrochemical ion-solvent cointercalation into layered titanate host materials

The experimental details discussed in this chapter were reported in submitted or published manuscripts, see ***Chapter 6.1.***

5.1.1 Materials synthesis

Hydrogen tetratitanates ($H_2Ti_4O_9 \cdot H_2O$, hereon referred to as HTO) was synthesized as per the process reported by Izawa et al where first a potassium tetratitanate ($K_2Ti_4O_9$) precursor was obtained by heating a mixture of potassium carbonates (K_2CO_3, VWR Chemicals) and titanium (IV) oxide (TiO_2, Thermo Scientific) in a 1:3.5 molar ratio at 800°C for 20h in a muffle furnace (Nabertherm P330) and then another 20h after grinding with a mortar and pestle.[35] Then, to obtain HTO, 1 g of the obtained $K_2Ti_4O_9$ was stirred in 200 mL of 1 M hydrochloric acid (HCl, VWR Chemicals) for 3 days at 60°C. The acid solution was changed daily to remove the exchanged K^+. The obtained product was filtered and dried at room temperature under air flow before subsequent characterization.

To obtain alkylamine-pillared HTO, the HTO powder was stirred in aqueous solutions of the alkylamine at room temperature for 3 days as per a modified protocol similar to Izawa's. [35] For HTO-PA, 200 mg of HTO powder was added to 6.66 ml of a 50 vol% aqueous solution of propylamine (C_3H_9N, Thermo Scientific). For HTO-HDA, 200 mg of HTO were added to 6.66 ml of 60 vol% aqueous solution of *1,6*-Hexanediamine ($C_6H_{16}N_2$, VWR Chemicals). The obtained powder was filtered and washed with deionized water several times until the pH of the solution was neutral, then left to dry in air at room temperature.

5.1.2 Structural and morphological characterization

Powder X-ray diffraction (XRD) patterns of the samples were obtained using a Bruker D8 Advance equipped with a Cu K_α radiation source (λ = 0.15406 nm). The patterns were recorded in Bragg-Brentano mode in the 2θ range between 2° and 40° 2θ with 0.02° step size.

Scanning electron microscopy (SEM) imaging was performed using a ZEISS Crossbeam 340 electron microscope operated at 5 kV and working distance of 7.4 mm. Raman spectra were obtained using a Renishaw Invia Raman spectrometer equipped with an Nd:YAG laser with a wavelength of 633 nm using 1.7 mW laser power. Thermogravimetric analysis of the powder samples was performed using a NETZSCH TG 209 F1 Libra thermal analyzer under O_2/N_2 flow at a heating rate of 5 K min^{-1} in Al crucibles loaded with ca. 5 mg of material.

Fourier-transform infrared spectroscopy (FTIR) spectra of the LP30 electrolyte and the cycled electrodes were obtained using a PerkinElmer Spectrum Two™ spectrometer in the wavenumber range 4000 to 400 cm^{-1}. Prior to obtaining the spectra, the electrodes were cycled in coin cells at constant current of 50 mA g^{-1}, held at the desired potential for 12 hours, then recovered from coin cells and washed in an Ar-filled glovebox with DMC solvent, and finally dried in vacuum for 5 minutes at room temperature. For *postmortem* TEM imaging, the electrodes underwent a similar washing and drying step after 50 cycles.

Inductively Coupled Plasma (ICP) analysis was performed using a Spectro ARCOS FHS12 inductively coupled plasma optical emission spectrometer (ICP-OES). The sample was dissolved in aqua regia (mixture of HCl:HNO_3 with molar ratio 3:1), and treated in a microwave twice to dissolve the solid powder particles.

X-ray photoelectron spectroscopy (XPS) of the synthesized powder samples was performed in a fixed analyzer transmission mode, using a monochromatic Al Kα ($h\nu$ = 1.487 eV) X-ray and a Phoibos 150 XPS spectrometer (Surface Concept) with a micro-channel plate and Delay Line Detector (DLD). High resolution Ti 2p, C 1s, N 1s, and O 1s regions were acquired with an X-ray power source of 200 W (12 kV) , pass energy of 30 eV , and 0.1 eV energy steps. The spectra analysis was carried out by CasaXPS software, using a nonlinear Shirley-type background.

Transmission Electron Microscopy (TEM) of the HTO, HTO-PA, and HTO-HDA samples was performed using a ThermoFisher Talos F200i TEM at a low acceleration voltage of 80 kV. Samples were prepared for TEM analysis by collecting a small amount of powder on a holey carbon TEM grid.

Density functional theory (DFT) calculations were performed using the Vienna ab initio Simulation Package (VASP)[223,224] with the Perdew–Burke–Ernzerhof (PBE)[225] form of the generalized-gradient-approximation exchange correlation functional. The projector augmented wave (PAW) potential was used to describe the electron–nuclei interaction.[226] An energy cutoff of 450 eV was used for the plane wave basis sets. Based on the ratios of HTO to HDA (1:1), HTO to PA (1:1.5), and the different symmetries in the distribution of PA, we constructed the following structures: the structures of HTO-HDA were simulated by a supercell containing 4 $H_2Ti_4O_9$ and 4 $NH_2C_6H_{12}NH_2$ formula units, HTO-PA were simulated by a supercell containing 4 $H_2Ti_4O_9$ and 6 $C_3H_7NH_2$ formula units or 8 $H_2Ti_4O_9$ and 12 $C_3H_7NH_2$ formula units. All degrees of freedom were relaxed with a force convergence criterion of 0.05 eV $Å^{-1}$ and energy convergence criterion of 10^{-5} eV. A 1 × 2 × 2 Monkhorst–Pack k-point grid was adopted for Brillouin zone integration.[227] DFT-D3 was used to account for the van der Waals interaction.[228]

5.1.3 Electrochemical characterization

The synthesized powder samples were used to make electrode slurries where the active material, conductive carbon (C65, C.Energy), and polyvinylidene fluoride (PVdF, Solvay) binder (2 wt.% PVDF dispersed in N-Methyl-2-pyrrolidone, NMP, Thermo Scientific) were mixed in an 8:1:1 mass ratio. The slurries were then cast on carbon-coated aluminium current collector using a Doctor Blade, and the wet thickness was set to 60 µm. The cast electrodes were then left to dry overnight in circulating air (fume-hood) at room temperature, and then further in vacuum at room temperature overnight.

Electrochemical measurements in the Li-ion system were performed in 2032-type coin cells versus 12 mm diameter metallic Li (Honjo) disc electrode, LP30 (1M $LiPF_6$ in 1:1 vol% EC:DMC, Solvionic) was used as electrolyte, and a 19 mm diameter Whatman glass microfiber (grade GF/A) was used as a separator. For electrochemical impedance measurements, three-electrode cells (stainless-steel Swagelok-type “T-cells”) were used with a 12 mm diameter Li metal disk and a small, 5 mm diameter Li metal piece were used as counter and quasi-reference electrodes, respectively. A 13 mm diameter Whatman glass microfiber disk was used as separator. For full-cell characterization, electrodes compromising 92 wt.% $LiNi_{0.6}Mn_{0.2}Co_{0.2}O_2$ (NMC622, BASF), 4 wt.% C65 conductive

carbon, and 4 wt.% PVDF were used as positive electrodes in T-cell configuration with a 5 mm diameter Li-metal disk as an auxiliary quasi-reference electrode.

To make electrode slurries for *in situ* X-ray diffraction measurements, the active material powder, conductive C65 carbon, and PVDF were mixed in 7:2:1 ratio. The slurry was drop-cast onto a 12 mm diameter Ti mesh, achieving a mass loading of ca. 5 mg cm^{-2}, and left to dry under air circulation, then later under vacuum at room temperature. *In situ* X-ray diffraction patterns were recorded during galvanostatic cycling of the cast electrodes against Li metal in LP30 electrolyte with a current rate of 50 mA g^{-1} using a Bio-Logic SP-300 potentiostat, in a coin cell setup with x-ray-transparent thin Kapton® windows on both sides of the coin cell. The diffractograms were recorded using a STOE STADI-p diffractometer in transmission geometry with Mo $K_{\alpha 1}$ radiation (0.70932 Å), equipped with a DECTRIS MYTHEN 1 K strip detector.

Staircase potential electrochemical impedance spectroscopy (SPEIS) measurements in the Li-ion system were recorded using 3-electrode T-cells in the frequency range 200 kHz to 100 mHz, with a voltage amplitude of 10 mV. The potential was changed from OCV to 1 V vs. Li^+/Li in 100 mV increments, with a 2-hour holding step at each potential prior to recording an impedance spectrum.

Galvanostatic intermittent titration technique (GITT) measurements were conducted in coin cells after one galvanostatic cycle at 50 mA g^{-1} current rate. The measurements were performed by applying a 30-minute, 20 mA g^{-1} current pulse followed by a 2-hour rest. Internal resistance was calculated by dividing the overpotential (difference between the voltage at the end of the current pulse step and the voltage at the end of the relaxation step) by the applied current.

For EQCM measurements, electrodes were prepared by drop casting 35 µL of a dispersion of HTO or HTO-PA onto a gold-coated (Au with Ti adhesion layer) 5 MHz quartz crystal (AWSensors). The dispersions consisted of 95 wt.% active material powder to 5 wt.% PVDF binder dispersed in NMP at 2 mg ml^{-1} concentration. This resulted in active material loadings of ca. 60 µg cm^{-2}. Dispersions were sonicated for 2 hours in an ice-cooled sonication bath prior to drop casting. Hermetically sealed EQCM cells were assembled in a glovebox, with Li metal strip as CE/RE and 1M $LiClO_4$ in EC:DMC as electrolyte. The hexafluorophosphate salt from typical LP30 electrolyte must be avoided in EQCM

experiments due to side reactions with the gold coating of the sensor. The measurements were conducted using an AWSensors X1 Platform was used in combination with Bio-Logic SP-300 potentiostat with the temperature control unit set to 23°C.

Electrochemical dilatometry (ECD) measurements were conducted using an ECD-4-nano dilatometer (EL-CELL Co.). Free-standing electrodes were prepared by mixing the active material, conductive carbon (C-NERGY Super C65, Imerys), and polytetrafluoroethylene (PTFE, 60 wt. % aqueous solution, Sigma-Aldrich) in a ratio of 80 wt. %, 10 wt. %, and 10 wt. %, respectively. Once the mixture achieved a dough-like consistency, it was calendared to form a sheet with a uniform thickness of ca. 50 µm. The sheet was then dried under vacuum at 60 °C, and 8 mm diameter electrodes were subsequently cut. After assembly, the ECD cell was allowed to rest at open circuit potential (OCP) for 6 hours before the electrochemical measurements. All ECD measurements were carried out in a climate-controlled chamber at 22 °C.

5.2 Materials and methods for the study on: pillared layered titanates promote fast Na-ion intercalation

The experimental details discussed in this chapter were reported in submitted or published manuscripts, see ***Chapter 6.2.***

5.2.1 Materials synthesis

Hydrogen tetratitanates (HTO), propylamine-pillared tetratitanate (HTO-PA) were synthesised using the same procedure described in **Section 5.1.1.**

5.2.2 Structural and morphological characterization

Powder X-ray diffraction (XRD) patterns of the samples were obtained using a Bruker D8 Advance equipped with a Cu Kα radiation source (λ = 0.15406 nm). The patterns were recorded in Bragg-Brentano mode in the 2θ range between 2° and 40° with 0.02° step size.

Atomic force microscopy (AFM) measurements were recorded using a Bruker Dimension Icon® device and a Bruker SCM-PIT-V2 tip in tapping mode. Prior to imaging, the powder samples were dispersed in *N*-Methyl-2-pyrrolidone (NMP) solution, sonicated, then drop cast on glassy carbon substrates and left to dry in circulating air overnight.

Scanning electron microscopy (SEM) imaging was performed using a ZEISS Crossbeam 340 electron microscope operated at 5 kV and working distance of 7.4 mm.

5.2.3 Electrochemical characterization

The synthesized powders were used to make electrode slurries where the active material, conductive carbon (C65, C.Energy), and polyvinylidene fluoride (PVdF, Solvay) binder (2 wt% PVDF dispersed in *N*-Methyl-2-pyrrolidone, NMP, Thermo Scientific) were mixed in a 8:1:1 mass ratio. The slurry was then cast onto carbon-coated Al current collectors using a DoctorBlade with a wet film thickness set to 60 µm. The cast slurries were set to dry overnight in circulating air, then subsequently cut into 12-mm discs and dried overnight in vacuum at room temperature.

Except for electrochemical dilatometry, all electrochemical measurements in the Na-ion system were performed in 2032-type coin cells versus a 12 mm diameter metallic Na disc electrode (Acros Organics, 99.8%), 1M $NaPF_6$ in EC:PC (UBE) was used as electrolyte, and Whatman glass microfiber (grade GF/A) as separator. All electrochemical measurements of Na-ion cells were conducted at 20 °C.

Electrochemical dilatometry (ECD) measurements were conducted using an ECD-4-nano dilatometer (EL-CELL Co.). Free-standing electrodes were prepared by mixing the active material, conductive carbon (C-NERGY Super C65, Imerys), and polytetrafluoroethylene (PTFE, 60 wt.% aqueous solution, Sigma-Aldrich) in a ratio of 80 wt.%, 10 wt.%, and 10 wt.%, respectively. Once the mixture achieved a dough-like consistency, it was calendared to form a sheet with a uniform thickness of ca. 50 µm. The sheet was then dried under vacuum at 60°C, and 8 mm electrodes were subsequently cut. After assembly, the ECD cell was allowed to rest at open circuit potential (OCP) for 6 hours before the electrochemical measurements. All ECD measurements were carried out in a climate-controlled chamber at 22°C.

5.3 Materials and methods for the study on: Mechanistic understanding of microstructure formation during synthesis of metal oxide/carbon nanocomposites

The experimental details discussed in this chapter were reported in submitted or published manuscripts, see ***Chapter 6.3.***

5.3.1 Materials synthesis

Molybdenum oxide dihydrate ($MoO_3 \cdot 2H_2O$) was synthesized via a modified Freedman method.[229] 50 grams of sodium molybdate dihydrate $Na_2MoO_4 \cdot 2H_2O$ (VWR International) were dissolved in 100 mL of deionized H_2O and slowly added to 300 mL of 5 mol L^{-1} HNO_3 (VWR International) through a burette under continuous stirring. The solution was stirred at room temperature for about 2 weeks, then the stirring was stopped for another week, until a significant amount of yellow precipitate was visible. The precipitated $MoO_3 \cdot 2H_2O$ was recovered via filtration of the solution through a Büchner funnel (reaction yield around 20 g), subsequent washing with about 3 L of deionized H_2O and drying at room temperature for 1 week.

Octylamine-functionalized molybdenum oxide (MoO_x-OA) was synthesized by dispersing 2 grams of $MoO_3 \cdot 2H_2O$ in 57 mL of ethanol under stirring, before adding 1.43 grams (1.825 mL) of octylamine (Sigma Aldrich) to obtain a molar ratio of Mo:OA of 1:1. The solution was stirred for 3 days at room temperature until a white precipitate formed. The precipitate was recovered by washing and centrifugation with ethanol at 2000 rpm for 5 minutes for 3 times and drying at 80 °C overnight. While in this study, a molar ratio of Mo:OA of 1:1 was chosen, variation of the ratio yields structures with similar crystallography (**Fig. S3.1**).

Octylamine-derived molybdenum oxide-carbon composite (MoO_x-C) was synthesized by pyrolysis of MoO_x-OA in a tube furnace under flowing argon atmosphere at 700 °C for 2 hours, with a heating rate of 5 K min^{-1}, then allowed to cool to room temperature.

In order to compare the electrochemical properties to conventional molybdenum oxide, $MoO_3 \cdot 2H_2O$ underwent the same thermal treatment described above, but without assembly of OA in the interlayer (i.e., in absence of the carbon source). This led to a partially reduced form of molybdenum oxide (MoO_{3-x}).

5.3.2 Structural and morphological characterization

Powder X-ray diffraction (XRD) patterns of all the samples were obtained using a Bruker D8 Advance equipped with a Cu $K\alpha_1$ radiation source ($\lambda = 0.15406$ nm). The patterns were recorded in Bragg-Brentano mode in the 2θ range between 2° and 60° 2θ with 0.02° step size.

X-ray photoelectron spectroscopy (XPS) of MoO_x-C powder was performed in a Fixed Analyzer Transmission mode, using a monochromatic Al Kα ($h\nu = 1.487$ eV) X-ray and a Phoibos 150 XPS spectrometer (Surface concept) equipped with a micro-channel plate and Delay Line Detector (DLD). High resolution Mo 2p, C 1s, and O 1s regions were acquired with a X–ray power source of 200 W (12 kV), pass energy of 30 eV, and 0.1 eV energy steps. The spectra analysis was carried out by CasaXPS software, using a nonlinear Shirley-type background and 70% Gaussian and 30% Lorentzian profile functions.[230]

Scanning electron microscopy (SEM) imaging was performed using a ZEISS Crossbeam 340 electron microscope operated at 5 kV and working distance of 7.7 mm. Raman spectra were obtained using a Renishaw Invia Raman spectrometer equipped with an Nd:YAG laser with a wavelength of 532 nm using 0.25 to 5 mW laser power. Thermogravimetric analysis coupled with simultaneous mass spectroscopy (TGA-MS) and Fourier transform infra-red spectrometry (TGA-FTIR) of the pyrolysis gas was performed using a NETZSCH TG 209 F1 Libra thermal analyzer under Ar flow at a heating rate of 10 K min^{-1} from 40 to 700 °C in Al_2O_3 crucibles of 80 µL loaded with ca. 20 mg of material. MS data were acquired with a QMS 403 Aëolos Quadro mass spectrometer in the 10-300 m/z range, while FTIR spectra were recorded using a Bruker Invenio spectrophotometer in absorption mode, in the range of 4500-650 cm^{-1} and at a resolution of 2 cm^{-1}.

Scanning transmission electron microscopy (STEM) was carried out at 200 kV and with a semi-convergence angle of 24.7 mrad in an aberration-corrected Titan G2 60-200 CREWLEY microscope (ThermoFisher Scientific, formerly FEI, Netherlands) equipped with a high-brightness field emission electron gun and a Super-X energy-dispersive X-ray spectroscopy (EDS) system. High-angle annular dark-field (HAADF) images were acquired to make use of the associated Z-number contrast with a semi-collection angle of 69-200 mrad.

Samples for STEM were prepared using a dual-beam Helios NanoLab400S (ThermoFischer Scientific, formerly FEI, Netherlands) focused ion beam (FIB). Powder particles were fixated on a conventional scanning electron microscope stub using glue. Afterwards, regions of high particle density were identified, and Pt was deposited on top to make a good connection between the particles. A conventional lift-out technique was applied to transfer the thick TEM lamella onto a TEM grid. Before thinning the lamella, the side of it was again glued with Pt to maintain a good particle connection during thinning. Finally, the sample was thinned down to electron transparency with a final thinning step consisting of 5 kV ion polishing to reduce beam damage and Ga contamination as much as possible.

5.3.3 Electrochemical characterization

The electrode slurries were prepared by mixing 80 wt.% active material and 10 wt.% conductive carbon black (Super C65, C-NERGY) in an agate mortar, followed by the addition of 10 wt.% polyvinylidene fluoride (PVDF, Solef 6020, Arkema Group) in N-Methyl-2-pyrrolidone solvent (NMP, anhydrous, Sigma-Aldrich, 2 wt.% of PVDF in NMP). The slurries were homogenized using a planetary mixer (Thinky, ARE-250) and then cast onto aluminium and copper foil current collectors (Wellcos Corporation) using a laboratory scale doctor blade (wet film thickness set to 60 µm). The cast electrodes were further dried in an oven set at 80 °C overnight. Electrode discs 12 mm in diameter were then punched with active material loading ranging between 0.7 to 0.9 mg cm^{-2}, and dry coating thickness ranging between 12.0 to 13.8 µm.

All cyclic voltammetry and galvanostatic cycling measurements were done in 2-electrode configuration coin cells, where 12 mm diameter metallic Li discs were used as a counter and reference electrode and glass microfiber (Whatman grade GF/A) as separator. Standard LP30 (1 M $LiPF_6$ in 1:1 volume mixture of ethylene carbonate and dimethyl carbonate, Solvionic) was used as the electrolyte. Electrochemical measurements were performed in temperature-controlled chambers (Binder) at 20 °C using a potentiostat/galvanostat (Bio-Logic VMP3). The potential window was between 1.1 and 3.1 V vs. Li^+/Li (for MoO_x-C) or 1.5 and 3.5 V vs. Li^+/Li (for MoO_{3-x}) to study the Li^+ intercalation reaction. To study the conversion reactions at more negative potentials, the electrodes were cycled between 0.01 and 3 V vs. Li^+/Li.

Electrochemical impedance spectroscopy (EIS) measurements were performed in custom-made 3-electrode cells, where the components are sandwiched between two spring-loaded titanium pistons, and Li foils were used as separate counter and reference electrodes. Detailed description of the cell is found in ref.[231]. Impedance spectra were recorded under open circuit potential conditions with sinusoidal potential amplitude of 10 mV, in the frequency range between 200 kHz and 100 mHz.

6. Results and Discussion

The results discussed in this chapter have been reported in the following either already published articles or ones under preparation:

- Section 6.1: **Mennatalla Elmanzalawy**, Haohong Song, Maciej Tobis, Robert Leiter, Jaehoon Choi, Hyein Moon, Wan-Yu Tsai, De-en Jiang, and Simon Fleischmann (2025), *Nanoconfinement-Induced Electrochemical Ion-Solvent Cointercalation in Pillared Titanate Host Materials*, Angewandte Chemie International Edition, 64, e202423593. DOI: 10.1002/anie.202423593

- Section 6.2: **Mennatalla Elmanzalawy**, Maciej Tobis, Wan-Yu Tsai, and Simon Fleischmann. *Interlayer expansion of hydrogen titanate anodes improves electrochemical Na^+ intercalation kinetics and reversibility*, pre-print. DOI: 10.26434/chemrxiv-2024-d9x01

- Section 6.3: **Mennatalla Elmanzalawy**, Alessandro Innocenti, Maider Zarrabeitia, Nicolas J. Peter, Stefano Passerini, Veronica Augustyn and Simon Fleischmann (2023), *Mechanistic understanding of microstructure formation during synthesis of metal oxide/carbon nanocomposites*. Journal of Materials Chemistry A, 11(32), 17125–17137. DOI: 10.1039/D3TA01230A

6.1 Nanoconfinement-induced electrochemical ion-solvent cointercalation into layered titanate host materials

This section is reproduced from the published article: Nanoconfinement-Induced Electrochemical Ion-Solvent Cointercalation in Pillared Titanate Host Materials, Angewandte Chemie International Edition, 64, e202423593. DOI: 10.1002/anie.202423593

Abstract

Electrode materials for Li-ion batteries require both high capacity and power capability. However, the kinetics of Li^+ intercalation in layered materials are often limited by the charge transfer step, which involves (partial) desolvation and ion transport to intercalation sites within the host material. Expanding the interlayer spacing of layered materials through the insertion of molecular pillars offers a promising strategy to improve Li^+ intercalation kinetics by enabling the cointercalation of solvent molecules, thus reducing the energy barrier for charge transfer. In this study, we investigate the effects of interlayer pillaring on the Li^+ intercalation kinetics in a layered hydrogen titanate, ($H_2Ti_4O_9 \cdot H_2O$, HTO), functionalized with two types of organic pillars: a non-cross-linking monoamine, propylamine (PA), and a cross-linking diamine, hexanediamine (HDA). Electrochemical characterization reveals that HTO functionalized with propylamine (HTO-PA) outperforms both unmodified HTO and HTO functionalized with hexanediamine (HTO-HDA) in terms of capacity, rate capability, cycling stability, and reduced charge transfer resistance across various potentials. A range of advanced characterization techniques suggested that the ion-solvent cointercalation mechanism plays a key role in HTO-PA, leading to improved intercalation kinetics. *Operando* XRD showed a large expansion of the *d*-spacing during lithiation of HTO-PA, in contrast to a contraction observed during lithiation in HTO, and these results were supported by electrochemical dilatometry, indication the insertion of a larger species, such as solvated Li^+ ions. *Ex situ* FTIR measurements suggest the presence of solvent molecules in the lithiated state of the HTO-PA electrodes, and EQCM measurements confirmed the insertion of a species with a large molar mass during lithiation. Overall, our findings demonstrate the potential of molecular pillars to modify the interlayer nanoconfinement environment, promoting ion-solvent cointercalation and facilitating fast intercalation kinetics and low temperature operation.

In this work, we investigate the layered titanate $H_2Ti_4O_9 \cdot H_2O$ and increase its interlayer spacing from 0.88 to 1.58 nm by chemical insertion of organic molecular pillars. This allows in a first step to study the influence of nanoconfinement geometry on the electrochemical ion intercalation properties. Furthermore, using either *n*-propylamine (PA) or *1,6*-hexanediamine (HDA) pillars, an identical expanded interlayer spacing is obtained. But while HDA pillars with two ammonium groups cross-link the titanate layers, PA pillars are non-crosslinking, likely impacting how electrochemically induced strain is compensated within the host lattice. We utilize a combination of experimental and theoretical methods to derive precise structural models of the pillared titanates. Electrochemical Li^+ intercalation capacity from organic electrolyte can be increased from ca. 2.1 to 2.95 Li^+ per tetratitanate when pillaring with non-cross-linking PA molecules. Using a combination of *operando* X-ray diffraction (XRD), electrochemical dilatometry (ECD) and electrochemical quartz crystal microbalance (EQCM), we unambiguously identify a pillaring-induced change in intercalation mechanism from solid-solution intercalation to ion-solvent cointercalation.

6.1.1 Physicochemical characterization

Layered potassium tetratitanate is synthesized via a solid-state approach, yielding monoclinic $K_2Ti_4O_9$ (KTO) with a rod-like morphology (**Fig. S1.1-2**). The confined interlayer potassium is subsequently exchanged by protons and water via treatment in HCl according to earlier work of Izawa et al.[35]. The resulting hydrogen tetratitanate $H_2Ti_4O_9 \cdot H_2O$ (HTO) retains the rod-like morphology of KTO as indicated by scanning electron microscopy (SEM, **Fig. 6.1A**). The rods measure up to several microns in lengths and several hundreds of nanometers in diameter, in agreement with previous reports.[232] The chemical composition of the nanoconfined interlayer environment of HTO can be further modified with organic amine-based molecular pillars replacing interlayer water[46] without leading to any visible modification of the macroscopic rod-like morphology as shown by SEM micrographs (**Fig. 6.1A-C**). Propylamine (PA) and 1,6-hexanediamine (HDA) are selected as molecular pillars with one or two anchoring amine groups, respectively. The reason is the assumption that monofunctional PA bonds to one layer of the titanate host resulting in a separated HTO structure, while bifunctional HDA interacts with two adjacent titanate layers leading to a cross-linked HTO structure. Hence the pillar choice allows to

compare the influence of interconnectivity of the pillared structure on the volumetric expansion behavior when used as electrochemical ion intercalation hosts.

To examine the pillar-induced changes in crystal structure, powder X-ray diffraction (XRD) patterns of the pristine HTO and the molecularly pillared HTO-PA and HTO-HDA are shown in **Fig. 6.1D**. The XRD pattern of as-synthesized HTO is in close agreement with that reported in literature (PDF 00-036-0655), which indicates the successful synthesis of the protonated/hydrated phase from the precursor $K_2Ti_4O_9$. ICP results (**Table S1.1**) show that only negligible amounts of potassium remain in the structure (ca. 0.2 wt.%), indicating successful ion exchange by acid treatment. Upon the introduction of the molecular pillars, both HTO-PA and HTO-HDA exhibit a strong shift of the peak of the (200) set of planes to lower angles, indicative of an increase in the interlayer spacing from 0.88 nm in the pristine HTO to 1.58 nm in both HTO-PA and HTO-HDA. The similar interlayer spacing and morphology of the two molecularly pillared titanates, HTO-PA and HTO-HDA, permits to exclusively assess the impact of cross-linking versus layer-separating/non-cross-linking molecular pillars on the electrochemical properties.

Quantification of nanoconfined interlayer molecules (water, or organic pillars) is conducted using thermogravimetric analysis (TGA, **Fig. 6.1E**). Heating to 600 °C in synthetic air atmosphere converts $H_2Ti_4O_9$ into 4 TiO_2 by dehydration/dehydroxylation[233,234] (corresponding to 94.7 % of the initial mass). At the same time, there is a complete removal of nanoconfined molecular species by combustion and/or evaporation, hence any additional mass loss can be attributed to interlayer molecules.[235] Powder XRD patterns recorded after each mass loss step show the structural changes occurring during heating (**Fig. S1.3**). For pristine HTO, an overall mass loss of 10.1 % is measured, indicating an initial composition with a structural formula $H_2Ti_4O_9 \cdot 0.99H_2O$. The measured overall mass loss for HTO-PA is 24.7 %, indicating the initial composition $H_2Ti_4O_9 \cdot 1.47PA$, and for HTO-HDA it is 28.8 % suggesting the structural formula $H_2Ti_4O_9 \cdot 0.96HDA$. Hence it is reasonable to approximate the nanoconfined interlayer chemistry of HTO, HTO-PA and HTO-HDA as 1 H_2O, 1.5 PA and 1 HDA molecules, respectively. These values are further utilized for theoretical calculation of the structure.

Considering the measured interlayer spacing of HTO-PA and HTO-HDA, as well as the quantification of nanoconfined pillaring molecules from TGA, the energetically favourable pillar conformation within the interlayer space is calculated using density functional theory

(DFT, **Fig. 6.1F-G**). For the HTO-PA system, since PA is a smaller molecule, we considered three main configurations: fully perpendicular, fully parallel, and mixed models with respect to the HTO basal plane. The calculations show that, in the fully perpendicular configuration, the *d*-spacing is only 1.38 nm. As more PA molecules align parallel to the basal plane, the d-spacing gradually increases. The PA bilayer structure allows the monofunctional PA molecules to interact effectively with the –OH groups on both the upper and lower HTO layers, forming hydrogen bonds, thereby achieving a *d*-spacing of 1.58 nm and a relatively low energy state.

For the HTO-HDA system, we mainly considered two scenarios: HDA aligned parallel or perpendicular to the HTO basal plane. DFT structural optimization revealed that in the perpendicular configuration, both $–NH_2$ functional groups of HDA can symmetrically interact with the –OH groups of the top and bottom HTO layers, forming hydrogen bonds and achieving the lowest relative energy. In contrast, when HDA is aligned parallel to the basal plane, the *d*-spacing is 1.51 nm. Due to the mismatch between the length of HDA single molecule and the spacing between –OH groups in HTO, insufficient hydrogen bonding occurs, resulting in slightly higher energy compared to the perpendicular configuration.

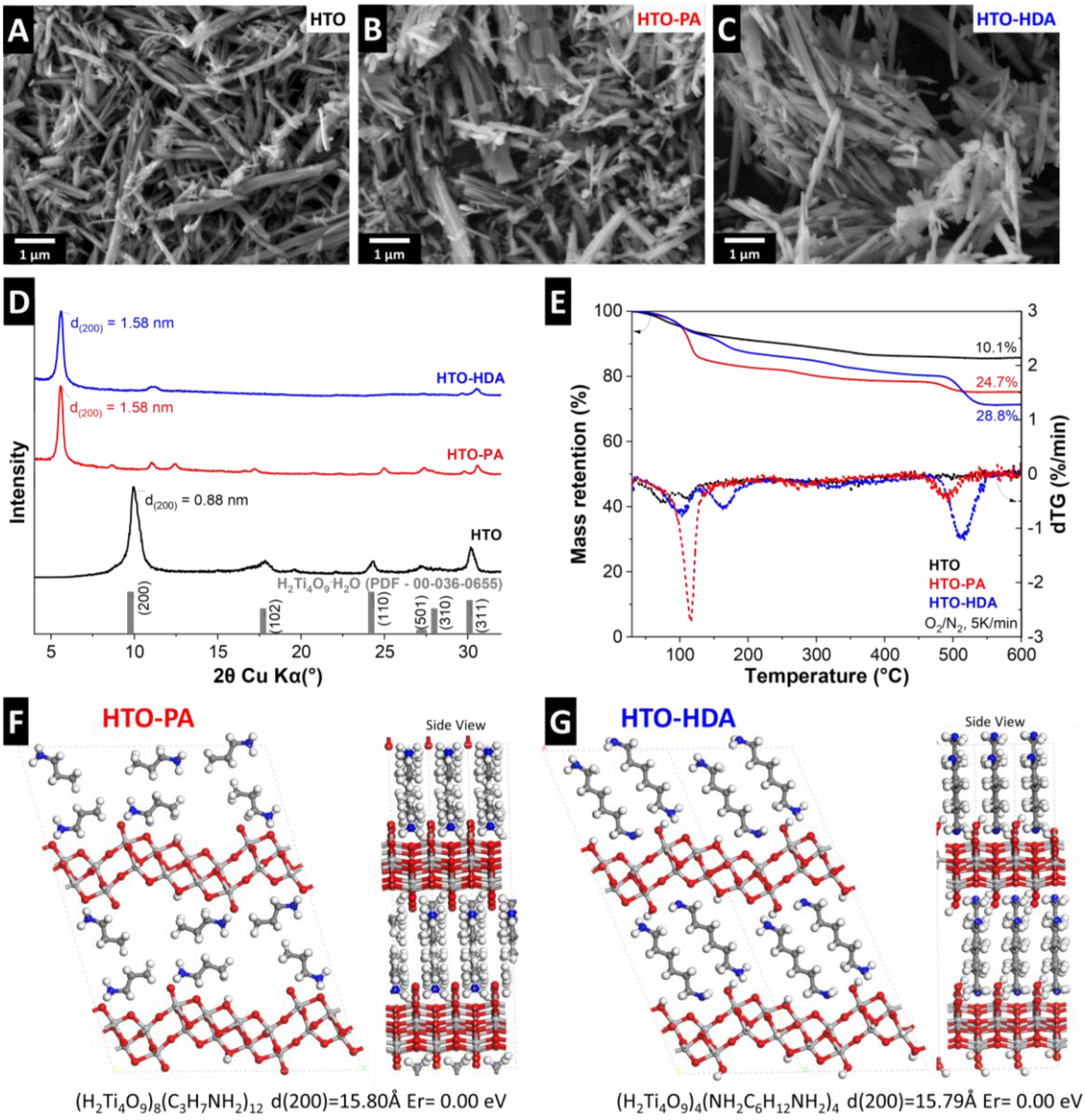

Figure 6.1: Structure and composition of HTOs: Scanning electron microscopy images of (A) $H_2Ti_4O_9{\cdot}H_2O$ (HTO), (B) HTO-HDA and (C) HTO-PA. (D) Powder XRD patterns of HTO, HTO-PA, HTO-HDA, and the PDF of $H_2Ti_4O_9{\cdot}H_2O$ as reported in the literature. (E) TGA and dTG (derivative thermogravimetry) plots for HTO, HTO-PA and HTO-HDA, showing mass loss steps and quantities. Optimized crystal structures of (F) HTO-PA and (G) HTO-HDA, obtained from DFT calculations and considering structural formulae derived from TGA.

The structural properties of hydrogen titanate oxides (HTOs) with different nanoconfinement chemistries were analysed at the nanoscale using transmission electron microscopy (TEM, **Fig. 6**.2). All samples—HTO, HTO-PA, and HTO-HDA—exhibit a consistent rod-like morphology (**Fig. 6.2A-B, 6.2D-E, 6.2G-H**), in agreement with the images obtained from SEM. This morphology allows for the further analysis of individual

free-standing rods via selected area electron diffraction (SAED). The recorded SAED patterns for single crystals were subsequently compared with density functional theory (DFT)-calculated crystal structures to validate the proposed models.

For the pristine HTO sample, the SAED pattern (**Fig. 6.2C**) aligns well with the simulated powder XRD pattern (see **Fig. S1.4** for the simulated powder XRD patterns and supporting information for the crystallographic information file, CIF). Specifically, the (002) reflection gives a *d*-spacing of 5.6 Å, which closely matches the 5.7 Å obtained from the calculated powder XRD pattern. Similarly, the (110) and (220) reflections, with *d*-spacings of 3.7 Å and 1.9 Å, respectively, correspond precisely to the values derived from the XRD diffractogram (3.7 Å and 1.9 Å).

For the HTO-PA sample, the SAED-measured (008) reflection with *d*-spacing measuring 2.9 Å was comparable to the simulated XRD value of 2.87 Å, and the (220) reflection at 1.9 Å also agreed with the simulated XRD diffractogram. Similarly, for the HTO-HDA sample, the SAED-derived (40-4) reflection with *d*-spacing of 3.0 Å and (1-10) with *d*-spacing of 3.8 Å were consistent with the corresponding simulated XRD values of 3.0 Å and 3.8 Å, respectively.

Overall, the TEM and SAED analysis confirm the validity of the proposed structural models for the pillared tetratitanates. It should be noted that the experimental structural analysis is limited to the titanate host, while the conformation of organic pillars is indirectly concluded based on minimized free energy and previous literature reports of confined alkyl(di)amine pillars.[236–238]

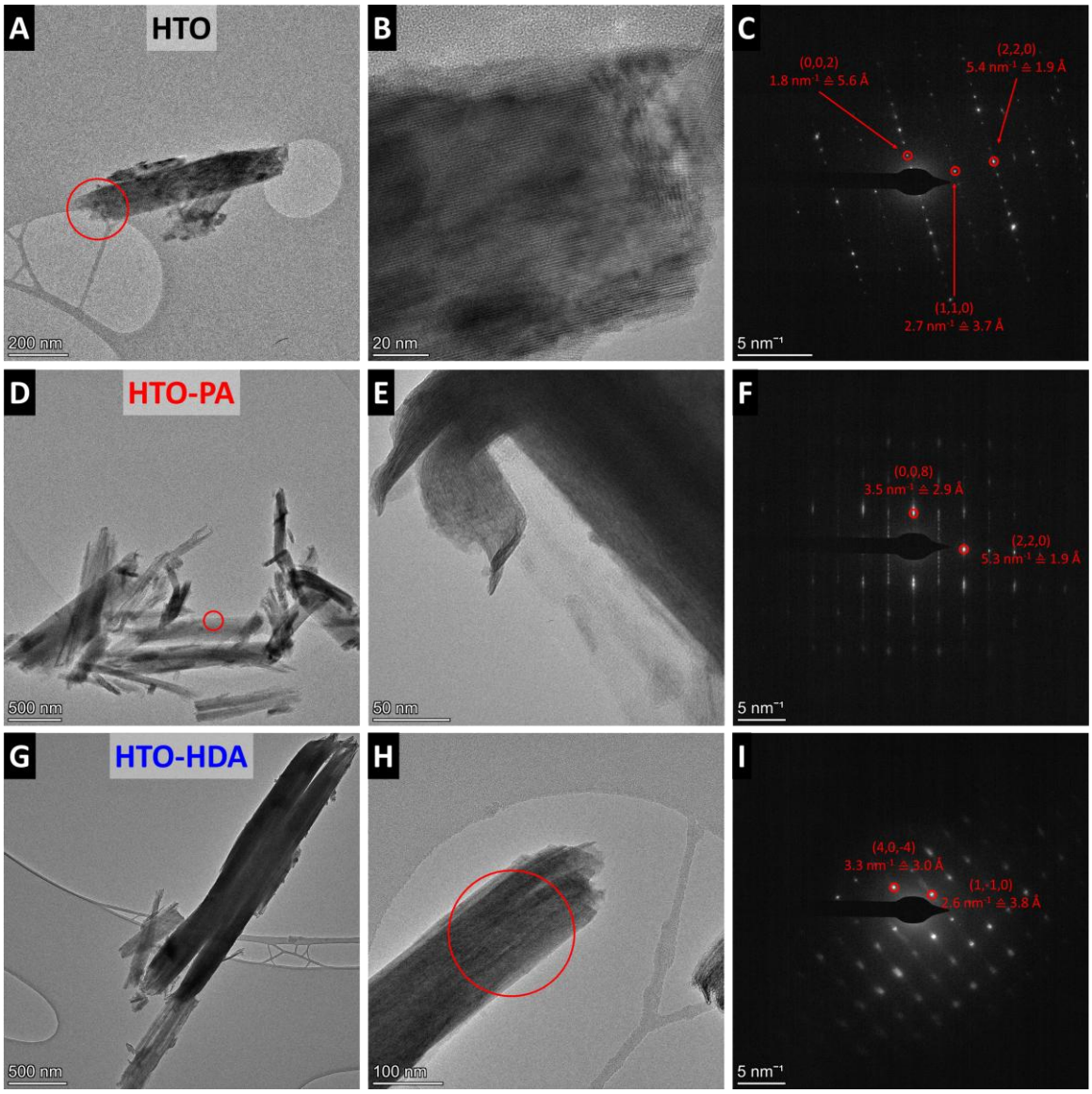

Figure 6.2: Transmission electron microscopy images and selected area electron diffraction pattern (area indicated by red circle) of (A-C) HTO, (D-F) HTO-PA, and (G-I) HTO-HDA.

The interaction between nanoconfined pillars within the interlayer and the HTO-based host lattice is analysed by Raman spectroscopy (**Fig. 6.3A**). This allows to assess any organic pillaring-induced changes in bonding environment. The presence of organic pillars in HTO-PA and HTO-HDA is confirmed by signals in the C-H stretching region (2800 to 3000 cm^{-1}).[239] Moreover, the spectra of HTO, HTO-PA and HTO-HDA are highly comparable in the wavenumber region below ca. 900 cm^{-1} typically assigned to the Ti-O lattice vibrations,[240] with no new major signals appearing. Shifts or broadening of certain signals can provide information about host-pillar interactions. In HTO, the band at 267 cm^{-1} attributed to the Ti-OH bonds[241,242] blue shifts to 275 cm^{-1} after pillaring with either PA

or HDA. The Raman signals of HTO at 394, 452, 681 and 866 cm^{-1} have previously been assigned to protonated tetratitanate.[243,244] They are still present (394 and 452 cm^{-1}), red shift (681 to ca. 661 cm^{-1}) or broaden (866 cm^{-1}) after organic pillaring with PA and HDA. Other peaks arising from the organic pillars are present in HTO-PA and HTO-HDA and can be attributed to different components of the organic molecules (**Fig. S1.5**). The overall strong similarity of the spectra is indicative of the tetratitanate intralayer structure remaining intact after pillaring. Slight shifts/broadening of protonated titanate related signals suggests an interaction between the organic pillars and the terminal protons of the titanate layers.

The nature of this interaction is further elucidated using X-ray photoelectron spectroscopy (XPS, **Fig. 6.3B-C**). The Ti 2p region in pristine HTO and pillared HTO-PA and HTO-HDA all contain a mixture of Ti oxidation states Ti^{4+} and Ti^{3+} (**Fig. 6.3B**). The Ti^{3+}/Ti^{4+} signal intensity ratio increases from 0.196 in pristine HTO to 0.212 in HTO-PA and further to 0.355 in HTO-HDA. Pillaring of HTO with PA or HDA therefore results in the reduction of the average Ti oxidation state, with more reduction in the case of HTO-HDA. This could be explained by the overall higher number of amine groups in HTO-HDA compared to HTO-PA (ca. 2 versus 1.5 amine groups per $H_2Ti_4O_9$, respectively). The N 1s core-level spectra **(Fig. 6.3C**) reveal the coexistence of NH_3^+ and NH_2 species in the pillared materials, suggesting that the organic pillar exists in the structure in both its free and ionic (alkylammonium ion) forms.[245] The ratio of NH_3^+ to NH_2 was estimated to be ca. 4 to 1 in HTO-PA, and 2.5 to 1 in HTO-HDA, respectively. The higher NH_3^+/NH_2 peak intensity ratio in HTO-PA suggests a higher tendency for the organic pillars to exist in their ionic form compared to HTO-HDA, where the alkyldiamine molecule might contain an ionized NH^{3+} on one end and a neutral NH_2 on the other. Moreover, it is unlikely that covalent Ti-N bonds are forming due to the absence of a Ti-N peak at 397.2 eV.[246] These findings agree with previous works that detected mixed NH_2 and NH_3^+ species in alkylamine-pillared titanates[50] and alkyldiamine-pillared vanadia.[238]

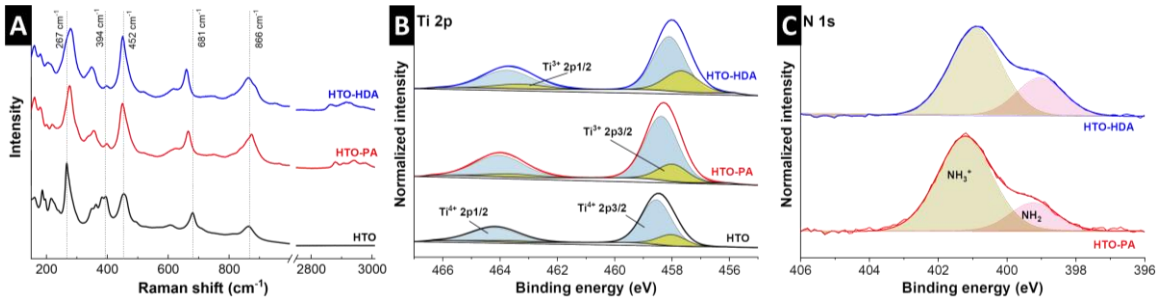

Figure 6.3: (A) Raman spectra, and XPS of (B) Ti 2p and (c) N 1s regions of HTO, HTO-PA, and HTO-HDA samples.

6.1.2 Electrochemical characterization

With HTO, HTO-PA and HTO-HDA samples exhibiting highly comparable morphology and intralayer crystal structure, the influence of their interlayer properties on the lithium intercalation reaction can be analysed. Specifically, the comparison of pristine versus pillared HTO allows to study the influence of interlayer spacing on the ion intercalation mechanism. For pillared HTOs, nanoconfined propylamine (PA) or hexanediamine (HDA) pillars lead to separated or cross-linked titanate layers, respectively. With both HTO-PA and HTO-HDA exhibiting the same interlayer spacing, insights into the impact of electrochemo-mechanics on the ion intercalation reaction can be gained.

Galvanostatic charge/discharge (GCD) profiles of the first five cycles of HTO, HTO-PA and HTO-HDA at 50 mA g^{-1} in standard organic electrolyte (LP30) are shown in **Fig. 6.4A-C**. All three samples exhibit a pronounced plateau for the lithium intercalation reaction. The reduction plateau is located at ca. 1.7 – 1.5 V for HTO and at ca. 1.5 – 1.3 V for HTO-PA and HTO-HDA, indicating a slight shift to a lower lithiation potential. All three samples exhibit comparable initial coulombic efficiencies (72 - 77 %) with slight performance degradation over the first five cycles (least pronounced for HTO-PA). This indicates that organic pillars do not contribute to a decrease in initial efficiency or stability compared to pristine HTO.

Cyclic voltammograms at a sweep rate of 0.1 mV s^{-1} (**Fig. 6.4D**) give additional insights into the (de)lithiation process. The shift to a lower lithiation potential for PA- and HDA-pillared materials is clearly visible. The position of the delithiation (oxidation) peak for the

three materials is different, showing a variation of the overpotential of the (de)lithiation reaction. HTO-PA shows the lowest overpotential (ca. 150 mV) compared to HTO-HDA (ca. 280 mV) and HTO (ca. 220 mV), indicating the highest electrochemical reversibility of the three different host materials for nanoconfined PA pillars. Additionally, there is an identical lower intensity set of redox peaks visible around 1.75 – 1.8 V for all samples. These can be attributed to (de)lithiation of anatase TiO_2 impurity,[247] indicative of minor secondary phases across all three titanate samples resulting from unreacted TiO_2 precursor of the solid-state synthesis of $K_2Ti_4O_9$. Since it is present equally in each sample, its influence on the overall comparability between the samples is negligible.

Quantitative analysis of the lithium intercalation capacity and kinetics is carried out by GCD at varying rates between 50 – 5,000 mA g^{-1} (**Fig. 6.4E**). The specific delithiation capacities at low rates (fifth cycle) of HTO, HTO-PA and HTO-HDA are 157, 186 and 150 mAh g^{-1}, respectively. There is a varying mass contribution of the different nanoconfined interlayer molecules in the three samples, which are not participating in the reversible charge storage process, namely 1.0 H2O, 1.5 PA, or 1.0 had. The normalized maximum reversible lithium storage capacities of the materials per tetratitanate is calculated as ca. 2.10 Li^+ for HTO, 2.95 Li^+ for HTO-PA, and 2.52 Li^+ for HTO-HDA. This demonstrates that the maximum reversible ion storage capacity per transition metal is increased in interlayer-expanded, organically pillared HTO materials. At increasing GCD rates, the performance of HTO-PA remains superior compared to HTO and HTO-HDA. This indicates superior charge storage kinetics when using separating/non-cross-linking PA pillars compared to cross-linking HDA pillars, in line with the reduced overpotential observed in HTO-PA and the lower internal resistance at low potentials obtained from galvanostatic intermittent titration technique (GITT) measurements (**Fig. S1.6**). However, the capacity retention of cross-linked HTO-HDA at high rates is still superior compared to pristine HTO, indicating the general favourability of increased interlayer spacing for charge storage kinetics. This is also in line with previous reports of our group on alkyldiamine-pillared vanadium oxide host materials.[28]

The cycling stability of HTO-based materials is tested by GCD at an intermediate rate of 500 mA g^{-1} (**Fig. 6.4F**). The performance degradation is most severe for pristine HTO, with a retention of 36 % of its initial capacity, while HTO-PA and HTO-HDA both retain about 55 % of their initial capacity after 1,000 cycles. The strong performance degradation for

HTOs in organic lithium ion-based systems has been observed before and attributed to hydrogen gas evolution at strongly reductive potentials.[248] This adverse effect on the cycling stability appears to be weakened in HTO-PA and HTO-HDA. We hypothesize that this is due to a stabilization of confined structural protons due to NH^{3+} formation after introduction of amine groups. Postmortem TEM images were recorded after cycling the show no visible signs of exfoliation or structural degradation (**Fig. S1.7**). However, follow-up work on the precise degradation mechanism of pillared HTO is required.

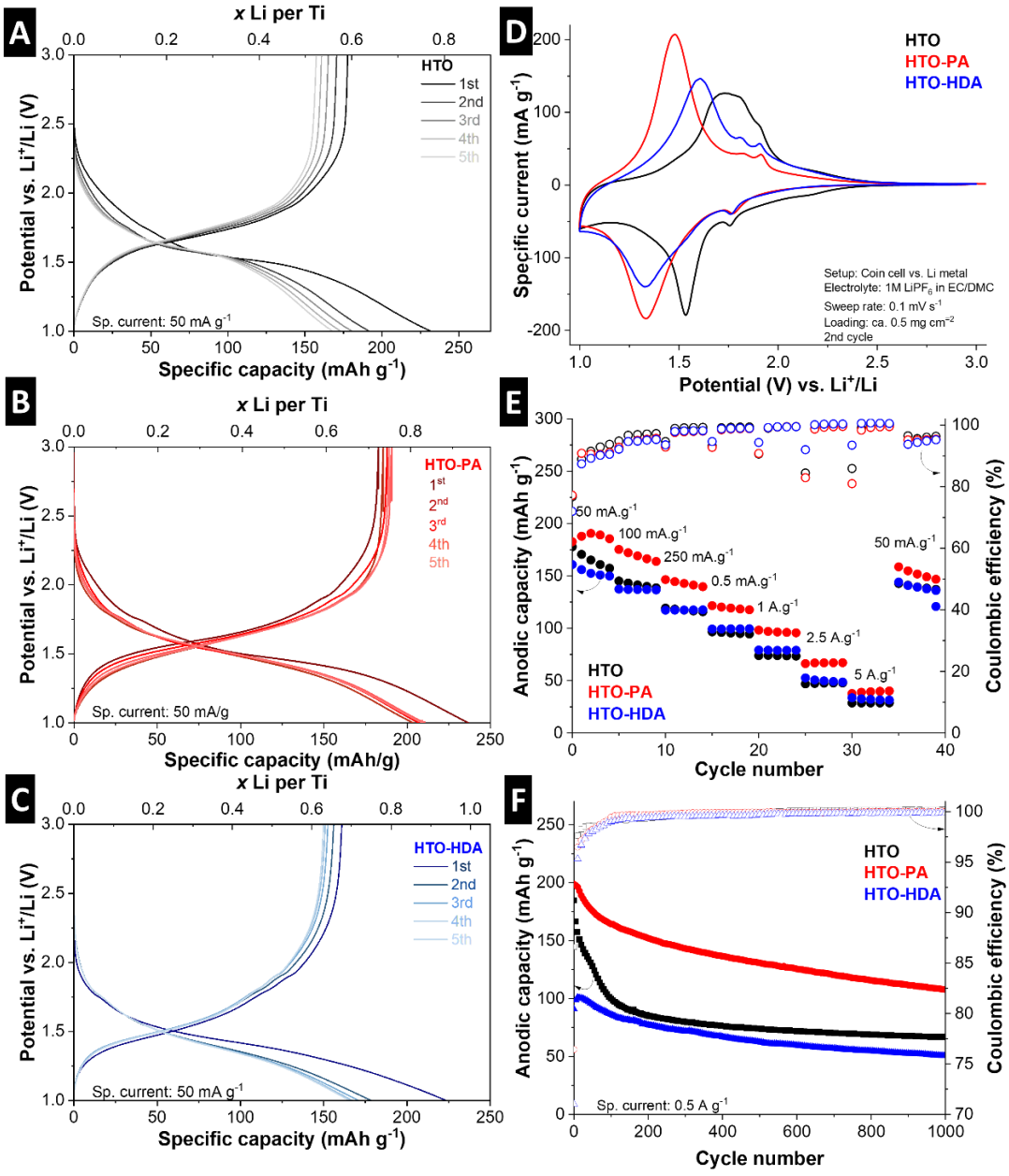

Figure 6.4: Electrochemical performance of HTO and pillared HTO in the Li-ion system. A-C) Galvanostatic charge and discharge plots of HTO, HTO-PA, and HTO-HDA showing the first 5

cycles at specific current rate 50 mA g^{-1} and the number of Li ions per Ti. D) CVs of HTO, HTO-PA, and HTO-HDA showing the 2nd cycle, cycled at scan rate 0.1 mV s^{-1} E) Rate handling of HTO, HTO-PA, and HTO-HDA, showing anodic capacity at various values of specific current and the corresponding coulombic efficiency of each cycle. F) Cycling performance of HTO, HTO-PA, and HTO-HDA at specific current rate 0.5 A g^{-1} and the corresponding coulombic efficiency.

The higher charge storage capacity, the shifted lithiation potential and the superior kinetics of pillared HTOs (HTO-PA and HTO-HDA) compared to pristine HTO suggest that the materials exhibit a different lithium intercalation mechanism. Therefore, the lithiation-induced structural changes occurring in the different host materials are analysed during electrochemical cycling using *operando* XRD. The electrode materials are cycled by GCD at 50 mA g^{-1} in a modified coin cell setup with Kapton-sealed windows, while X-ray diffractograms are continuously recorded in Debye-Scherrer geometry (transmission) with a focus on the signal representative of the interlayer spacing, i.e., the (200) set of planes. For pristine HTO, a continuous shift towards smaller interlayer spacing is observed during electrochemical lithiation (**Fig. 6.5A**), indicating a contraction of titanate layers upon insertion of a positive charge in the interlayer space. In the fully lithiated state, the HTO interlayer spacing contracted from ca. 0.8 to 0.74 nm. The interlayer spacing reversibly expands to its initial value after full electrochemical delithiation, suggesting a solid-solution intercalation mechanism of Li^+. The behaviour is fully reversible and is in line with previous observations of interlayer contraction of titanates upon proton or lithium insertion.[13]

For HTO-PA and HTO-HDA, the *operando* XRD profiles show a different behaviour (**Fig. 6.5B-C**). For interlayer-expanded HTO-PA, upon lithiation, the interlayer spacing further increases from 1.54 nm to ca. 1.68 nm. Upon delithiation, a further expansion to ca. 1.73 nm is observed. Similarly, the interlayer spacing of HTO-HDA further expands upon initial lithiation to ca. 1.66 nm. Furthermore, in the second lithiation cycle, the signal corresponding to the (200) plane loses intensity for both HTO-PA and HTO-HDA, which indicates a loss of long-range crystalline order in these structures. This behaviour is indicative of a different lithium intercalation mechanism in the two pillared HTO materials, where the intercalating species apparently leads to stronger structural changes compared to pristine HTO. We hypothesize that this is due to the intercalation of (partially) solvated Li^+ from the electrolyte (ion-solvent cointercalation mechanism) induced by the different nanoconfinement properties of the HTO hosts. The intercalation of large ion-solvent

complexes could qualitatively explain the observed further expansion of the interlayer spacing. Furthermore, this electrochemically induced expansion is likely facilitated by the non-cross-linked structure of HTO-PA, explaining its superior kinetics compared to HTO-HDA.

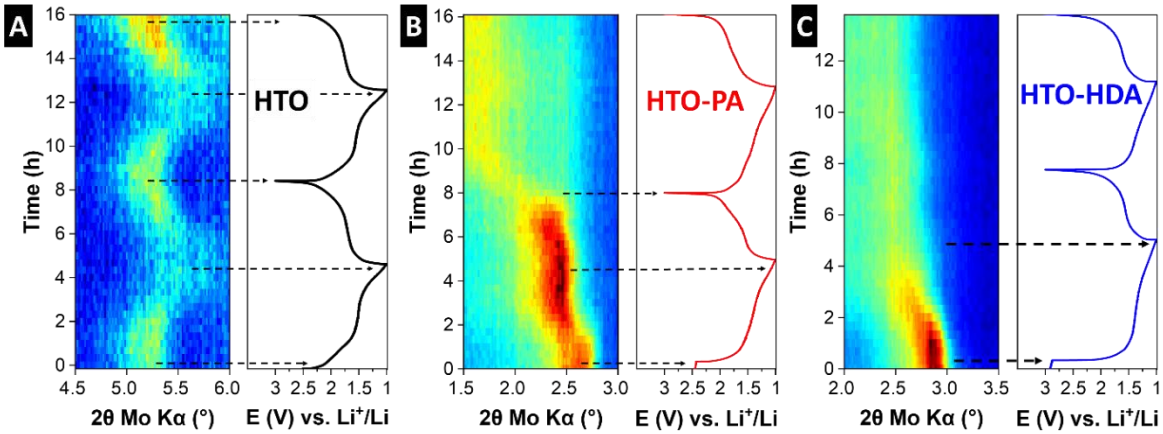

Figure 6.5: *Operando* X-ray diffraction for A) HTO, B) HTO-PA, and C) HTO-HDA, highlighting changes to the (200) plane peak during 2 cycles of galvanostatic charge and discharge at a current rate of 50 mA g^{-1}.

Given the difficulty of analysing the structural changes of electrode materials with reduced crystalline long-range order during electrochemical cycling with XRD, we employ complementary electrochemical dilatometry (ECD) analysis on HTO and HTO-PA electrodes. The technique assesses the macroscopic height change of electrodes upon electrochemical (de)lithiation.[249] This allows us to verify the hypothesis of a nanoconfinement-induced change in intercalation mechanism in HTO-PA. Electrochemical (de)lithiation of HTO and HTO-PA electrodes over five consecutive cycles at a rate of 50 mA g^{-1} and the associated dilatometric responses are shown in **Fig. 6.6A, B**. The significant dilatometric height change in HTO-PA is in line with previously identified cointercalation phenomena by ECD, such as the sodium-diglyme system in graphite, though smaller in absolute magnitude.[250] This can be explained by the already pre-expanded structure of pillared HTO-PA that can more readily accommodate (partially) solvated ions. It underlines that nanoconfinement-design of host materials can address the issue of excessive volumetric change of cointercalation reactions that was identified, for example, in the graphite case.[251]

With strong indications of cointercalation phenomena in HTO-PA given from the perspective of the host material response, we now employ electrochemical quartz crystal microbalance (EQCM) measurements to directly probe the nature of the intercalating species. The method makes use of the linear relation between the change of resonance frequency of a gold-coated quartz sensor and its mass according to the Sauerbrey equation.[213] The dissipation of the crystal at different overtones was monitored in air, prior to cycling, to ensure the rigidity of the film. To verify the rigidity of the coating, values of changes in dissipation ΔD should be minimal and the frequency shift ($\Delta f/n$) should be independent of overtone (**Figure S1.8**).[252] The linearity between frequency and mass change is only valid for ideally rigid coatings on the sensor, which is why we employ a thin film coating of active material and binder by drop-casting. This now allows us to investigate the mass change of the HTO-based electrodes during electrochemical intercalation (**Fig. 6.6C-D**). Plotting of the electrode mass change against the stored charge then allows for (semi-)quantitative analysis of the intercalant, where the slope can be combined with Faraday's law of electrolysis to obtain the molar mass of the intercalant (**Fig. 6.6E,F**). For pristine HTO, lithiation is accompanied by a mass increase that becomes especially pronounced at the region below 1.5 V. Analysis of the molar mass of the intercalant in HTO yields two slopes, with an intercalant of relatively low molar mass of 18 g mol^{-1} and 34 g mol^{-1} (**Fig. 6.6E**). While the molar mass of lithium is only 6.9 g mol^{-1}, the excess mass likely corresponds to solvent molecules adsorbed at the electrode interface. [253]

In HTO-PA, three distinct lithiation regimes (1-3) are identified (**Fig. 6.6F**). Initial lithiation likely occurs in the desolvated state ($M_{w,1}$ = 51 g mol^{-1}), coinciding with the initial shrinking detected by ECD. Subsequently, a drastic increase in the intercalant mass is detected ($M_{w,2}$ = 110 g mol^{-1}), indicating Li^+ intercalation together with solvent molecules. Finally, the mass is decreased when the electrode is almost fully reduced, i.e., the interlayer space is almost completely filled ($M_{w,3}$ = 69 g mol^{-1}). The larger average intercalant molar mass observed in HTO-PA further supports the hypothesis of solvent co-intercalation during the lithiation process.

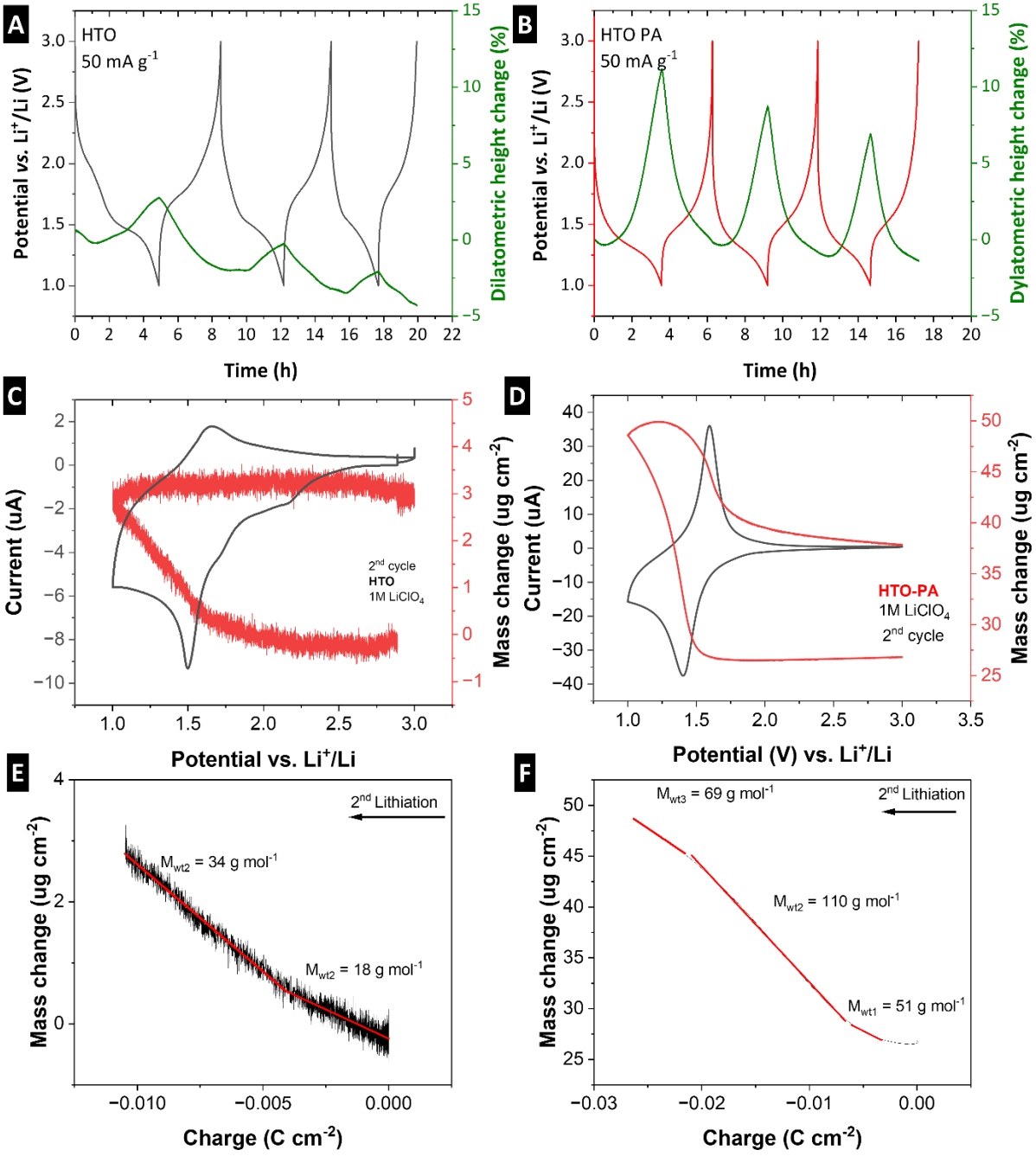

Figure 6.6: Electrochemical dilatometry measurement of A) HTO, B) HTO-PA. EQCM measurements of C) HTO, and B) HTO-PA, showing mass change with cycling. Data is displayed for the third cycle. Mass change vs. charge of E) HTO and F) HTO-PA. Molar mass of the intercalating species is indicated by the slope.

The charge transfer resistance of electrochemical intercalation reactions is strongly affected by the ion desolvation step at the electrochemical interface.[254–256] Hence cointercalation reactions are hypothesized to exhibit a reduced charge transfer resistance compared to the corresponding desolvated ion intercalation process. We probe this behavior using

electrochemical impedance spectroscopy (EIS) at various states of charge ("staircase potentio electrochemical impedance spectroscopy"). The Nyquist plots of HTO and HTO-PA at open circuit voltage (OCV, ca. 3.1V vs. Li^+/Li) are shown in **Fig. 6.7A**. An equivalent circuit consisting of the elements described in **Fig. S1.9** is used to model the impedance response of the intercalation process.[257] Plotting the extracted charge transfer resistance clearly shows strongly reduced values for the charge storage process in HTO-PA compared to HTO across the entire potential range (**Fig. 6.7B**). The results clearly support the assignment of the cointercalation mechanism in HTO-PA and demonstrate the potential of nanoconfinement-driven cointercalation reactions to contribute to superior kinetics of intercalation reactions.

The electrolyte solvent molecules EC and DMC can be detected using Fourier-transform infrared spectroscopy (FTIR). Different fingerprint signals of free solvent (1392 cm^{-1} for -COO stretching in free EC and C-O-C stretching at 1293 cm^{-1} for free DMC) and Li^+-coordinating solvent (1422 cm^{-1} for Li^+-EC and 1321 cm^{-1} for Li^+-DMC) can be detected in the FTIR spectrum of LP30 electrolyte (**Fig. 6.7C**). To examine the presence of solvent molecules in the electrodes at different stages of cycling, *ex situ* FTIR spectra were obtained after the electrodes were cycled to 1.0 V and to 3.0 V, recovered from coin cells then rinsed with DMC and dried briefly in vacuum. For comparison, uncycled electrodes were soaked in LP30 solvent then washed and dried similarly to the cycled electrodes. The signals corresponding to Li^+-EC and Li^+-DMC can be identified in *ex situ* FTIR spectra of the lithiated HTO-PA electrode at 1.0 V vs. Li^+/Li. However, these signals cannot be detected neither for HTO-PA cycled back to 3.0 V vs. Li^+/Li nor for the HTO-PA electrode simply submerged in the electrolyte, suggesting that solvent cointercalation is an electrochemically induced process. On the other hand, HTO and HTO-HDA did not show similar peaks relating to solvated Li in either potential (**Fig. S1.10**).

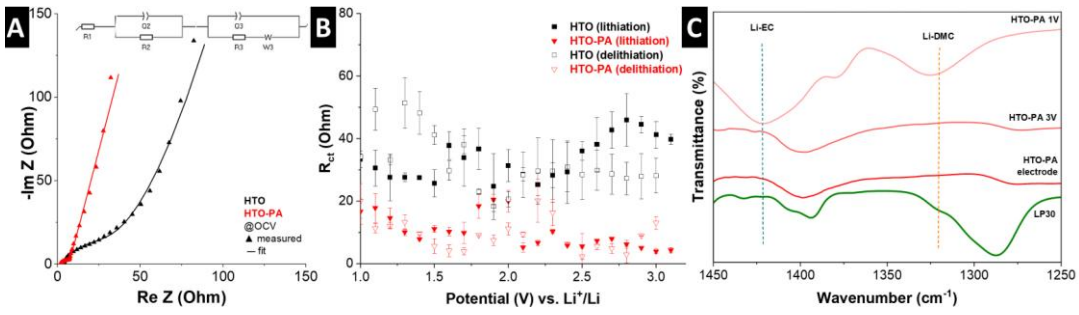

Figure 6.7: A) Electrochemical impedance spectroscopy (EIS) Nyquist plots for HTO and HTO-PA at OCV, fitted using the equivalent circuit shown in the inset. B) R_{ct} values at different stages

of lithiation and delithiation for HTO and HTO-PA. Error bars are based on multiple measurements. C) FTIR spectra for LP30 and HTO-PA electrodes at various states of charge. Peak positions for the vibration of EC- and DMC-solvated Li are highlighted by dashed lines.

Due to ion-solvent co-intercalation being associated with a reduced diffusion energy barrier, as evidenced by the decreased charge transfer resistance, it is expected to facilitate intercalation at low temperatures. Galvanostatic cycling of HTO, HTO-PA, and HTO-HDA electrodes at -20°C revealed the lowest polarization for the HTO-PA electrode, consistent with its reduced charge transfer resistance (**Fig. 6.8A**). Additionally, low-temperature rate handling tests showed that HTO-PA delivered a higher capacity at increased current densities (**Fig. 6.8B**). The enhanced rate capability and lower polarization of HTO-PA at low temperatures support the hypothesis that solvent co-intercalation takes place in the pillared structure.

To further assess the performance of the HTO-PA electrode, both HTO and HTO-PA were tested in full cells, using NMC622 as the positive electrode, with an N/P ratio of 1.4, meaning the capacity of the negative electrode is higher than the capacity of the positive electrode by a factor of 1.4 (**Fig. 6.8C**). Additionally, a spectator reference electrode is used to monitor the potential development of both anode and cathode. When cycled between 1.8 and 3.0 V, the HTO-PA cell delivered a charge capacity of 56 mAh g^{-1}, while the HTO cell achieved a charge capacity of 46 mAh g^{-1}. Importantly, the average discharge voltage of the HTO-PA based cell is higher by ca. 240 mV, leading to a higher cell energy compared to HTO-based cells. Further optimization of parameters, such as the N/P ratio and voltage window, may unlock additional performance benefits from the HTO-PA negative electrode.

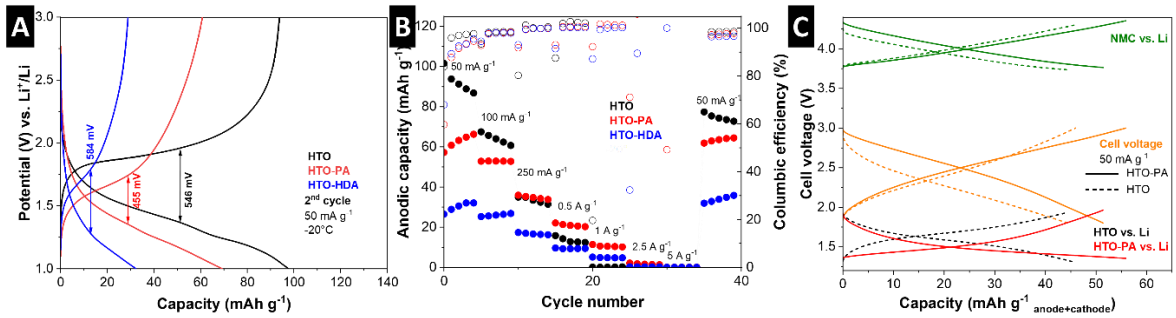

Figure 6.8: A) Voltage profiles for HTO, HTO-PA, and HTO-HDA cycled at -20 °C at current rate 50 mA g^{-1}, showing the second cycles. Overpotential is calculated by the difference in voltage at

the midpoint of capacity. B) Rate handling of the three materials at different current rates, C) Full cell voltage profiles for HTO against NMC (dashed lines) and HTO-PA against NMC (solid lines) at N/P ratio of 1.4. Dashed lines refer to HTO-based cells, solid lines refer to HTO-PA-based cells.

6.1.3 Conclusion

In summary, interlayer functionalization of layered titanates was achieved using two types of pillar species: a short-chain monoamine and a longer diamine. Notably, the monoamine-pillared titanate (HTO-PA) exhibited superior electrochemical properties, including high-rate capability, reduced charge transfer resistance, and lower polarization at low temperatures. Comprehensive experimental investigations using FTIR, *operando* XRD, ECD, and EQCM supports the presence of solvent molecules in lithiated HTO-PA electrodes, indicating that ion-solvent co-intercalation is the charge storage mechanism in play. This phenomenon is closely linked to the improved rate performance observed in HTO-PA. While most research on ion-solvent co-intercalation focuses on electrolyte formulation, this work demonstrates that the co-intercalation mechanism can be activated in layered electrodes through the deliberate design of the interlayer nanoconfinement environment with the use of organic pillar molecules. The ion-solvent cointercalation mechanism leads to favourable electrochemical kinetics, resulting in improved low temperature and full cell performance. This work paves the way for further exploration of tailored interlayer nanoconfinement environments in layered materials, offering new directions for advancing the design of layered electrodes in next-generation batteries.

6.1.4 Supporting information

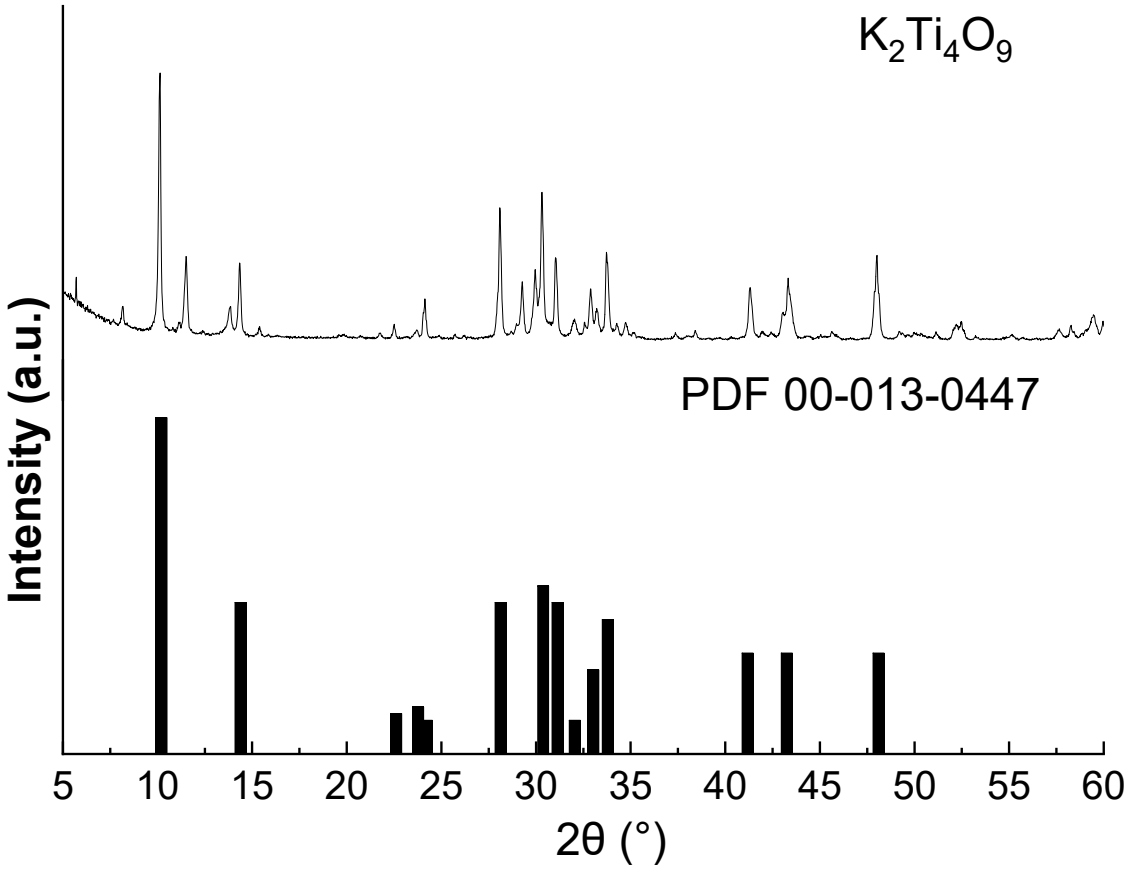

Figure S1.1: powder XRD pattern of as-synthesized $K_2Ti_4O_9$ and the corresponding PDF data.

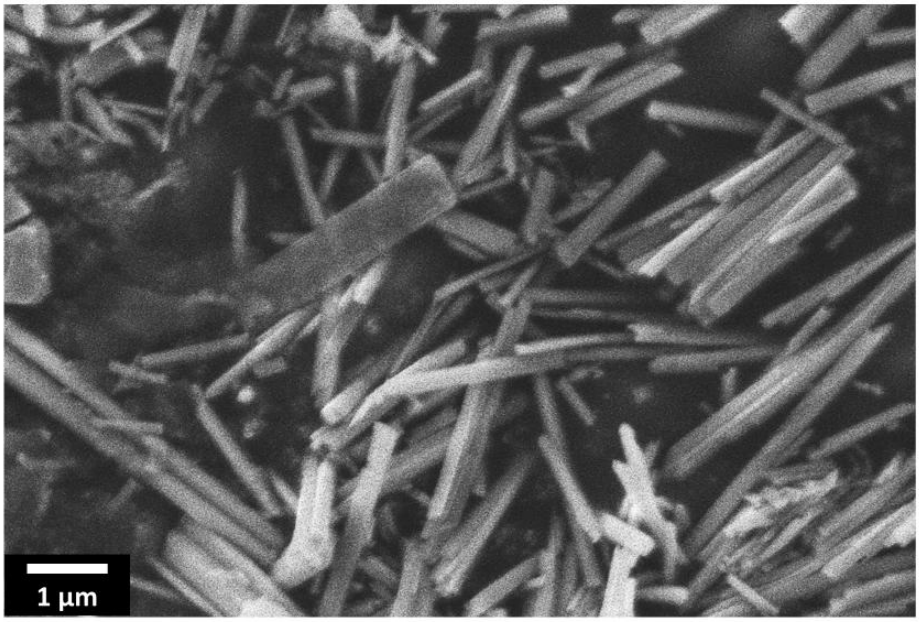

Figure S1.2: SEM image of as-synthesized $K_2Ti_4O_9$, showing rod-like morphology.

Table S1.1: ICP analysis of elements present in as-synthesized HTO, showing trace amounts of K, indicating successful proton exchange.

Sample	Element	Mass (%)
HTO	**K**	**0.22**
	Ti	**52.1**

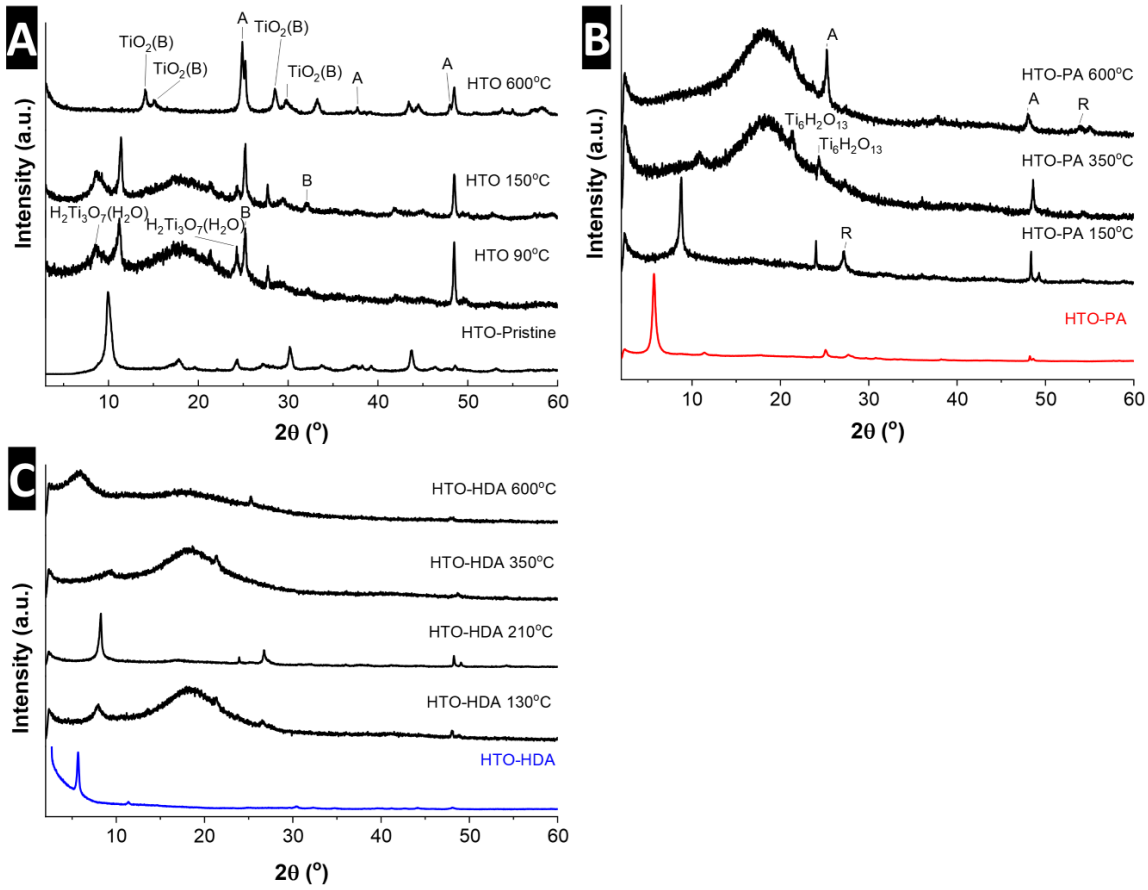

Figure S1.3: Powder XRD patterns obtained for the as-synthesized powder samples before heating (bottom diffractograms), and after holding at different temperatures corresponding to mass loss stages in A) HTO, B) HTO-PA, and C) HTO-HDA. Different phases appear at various stages of heating. A: anatase, B: brookite, R: rutile. The peaks are indexed according to PDF 00-021-1272 (anatase), PDF 00-015-0875 (brookite), PDF 00-021-1276 (rutile), PDF 01-080-9016 ($H_2Ti_3O_7 \cdot H_2O$), and simulated XRD patterns from The Materials Project[85] for TiO_2(B) and $Ti_6H_2O_{13}$.

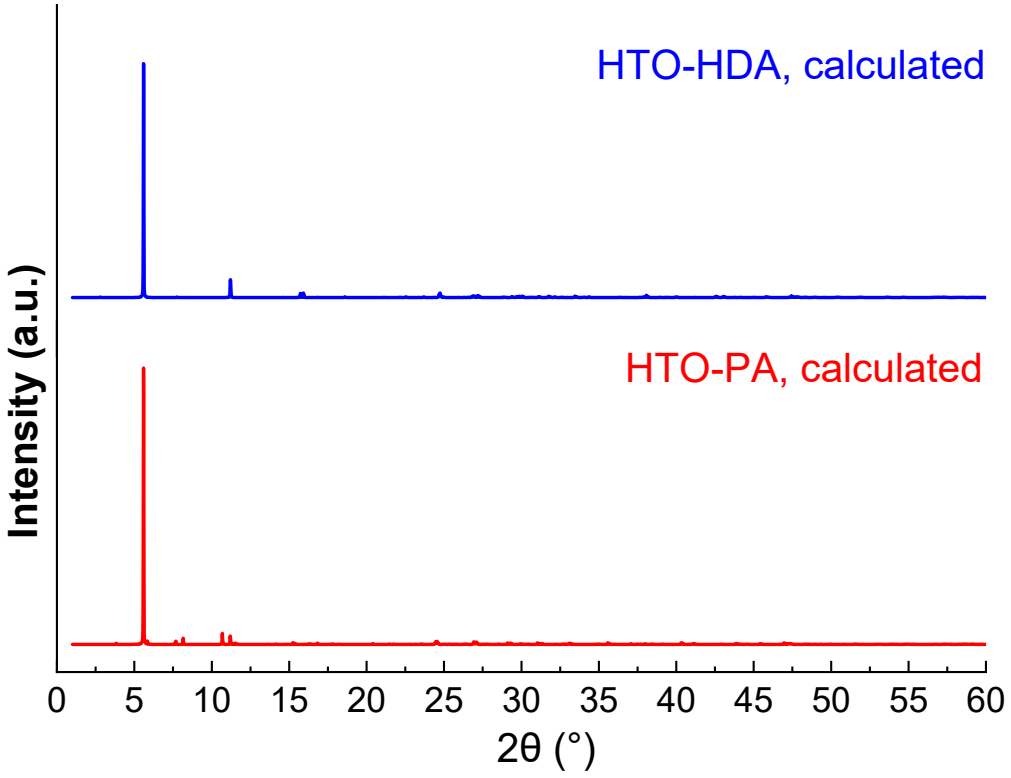

Figure S1.4: Calculated powder XRD patterns of HTO-PA and HTO-HDA, using the CIF data obtained from DFT calculations.

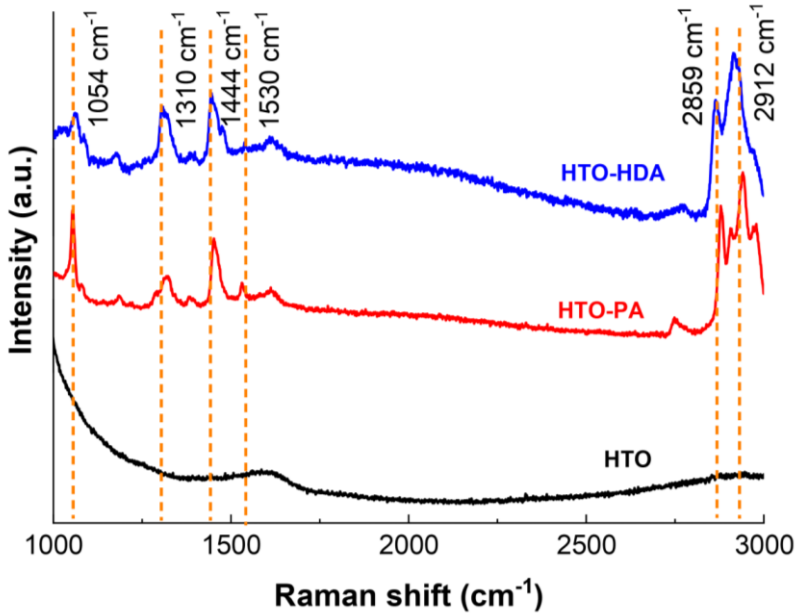

Figure S1.5: Raman spectra in the range 1000 to 3000 cm^{-1}, showing the peaks characteristic of the organic pillar amine molecules.

In pillared HTO-PA and HTO-HDA, spectral features relating to the organic components are detected, which are absent in pristine HTO. Particularly, the peaks at 1054, 1310, 1444, cm^{-1} is characteristic of C-N stretching, C–C–H, and CH_2 vibrations, respectively. Low intensity peaks at 1530 cm^{-1} are assigned to ammonium bending mode, which is consistent with previous reports stating that *n*-alkylamines are present in the interlayer of titanate compounds in their cationic forms. The high wavenumber bands at 2859 and 2912 cm^{-1} can be assigned to CH_2 symmetric and CH_2 asymmetric stretching modes, respectively.[259-260]

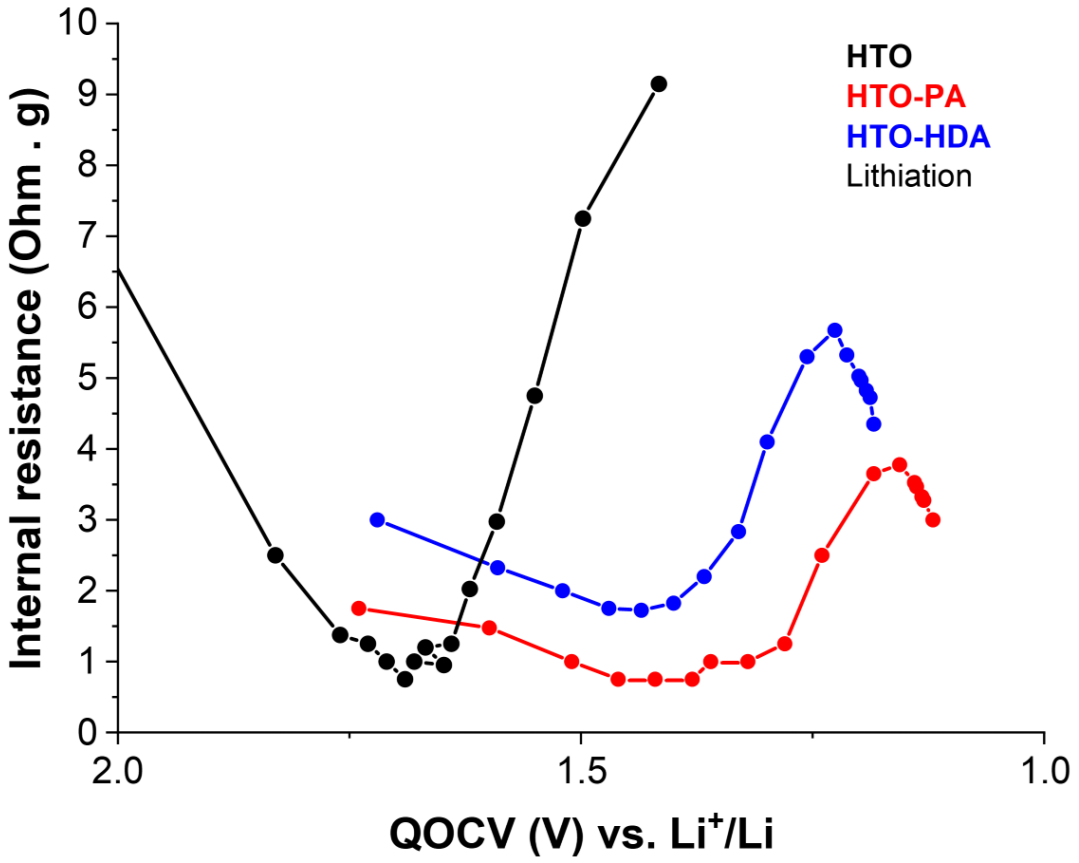

Figure S1.6: Internal resistance values for the three electrodes during the first lithiation cycle, obtained from GITT measurement.

The internal resistance is calculated by dividing the overpotential (η) by the current. The overpotential η is defined by the difference between quasi-open circuit voltage (QOCV, potential after 2h of rest) and the measured potential after the current pulse (closed circuit voltage, CCV).[261]

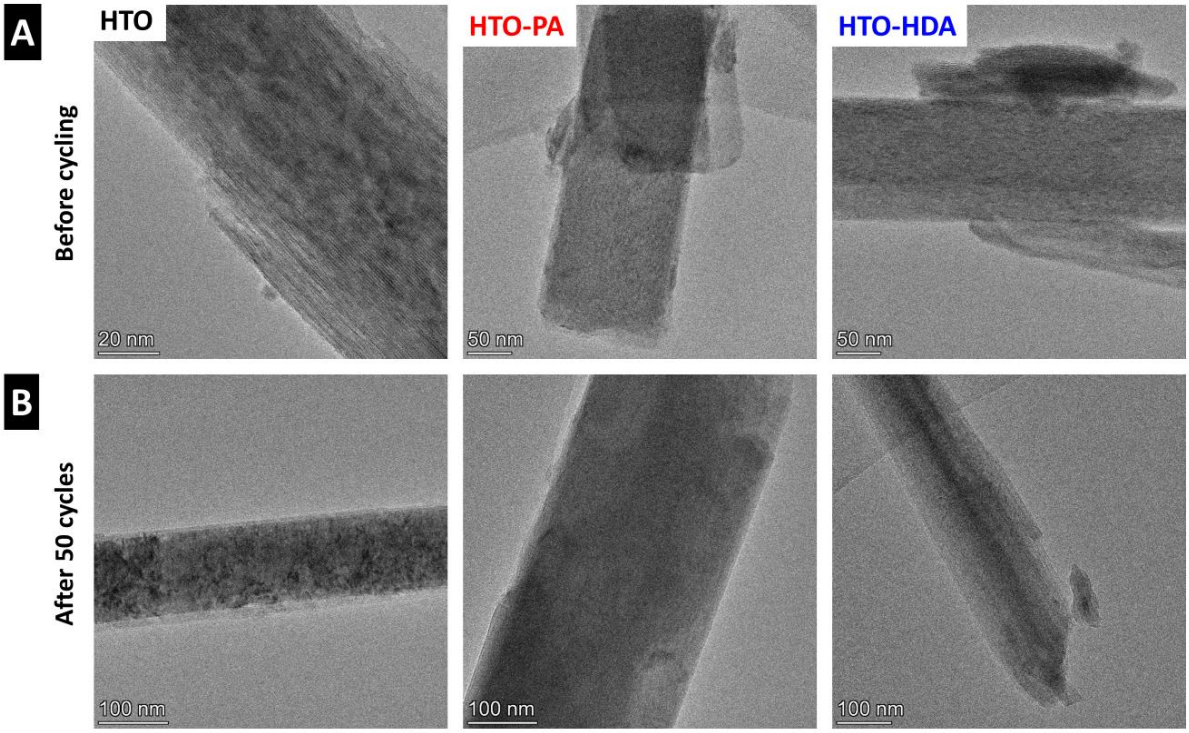

Figure S1.7: Post-mortem TEM images of HTO, HTO-PA, and HTO-HDA electrodes A) before cycling, and B) after 50 cycles. The rod-like morphology is maintained after cycling and no signs of exfoliation or structural degradation are visible.

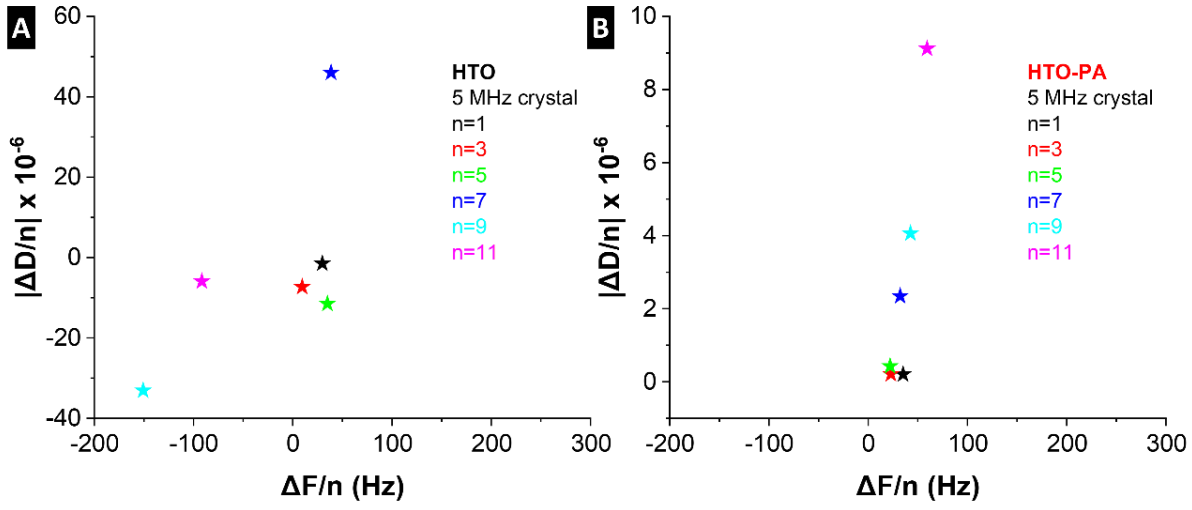

Figure S1.8: Dissipation vs. frequency plots verifying the stiffness of A) HTO and B) HTO-PA coatings on the quartz crystal.

For a stiff coating where the Sauerbrey equation can be applied, the frequency shift of the electrode, in air, should be independent of n, and the dissipation factor changes D/n should

be relatively small across all overtones. The overtone number, n, refers to the multiple of the fundamental frequency the crystal is vibrating at. For example, in this work, the fundamental frequency ($n = 1$) of the crystal is 5 MHz, hence the 3rd overtone ($n = 3$) would be 15 MHz, and so on. [252]

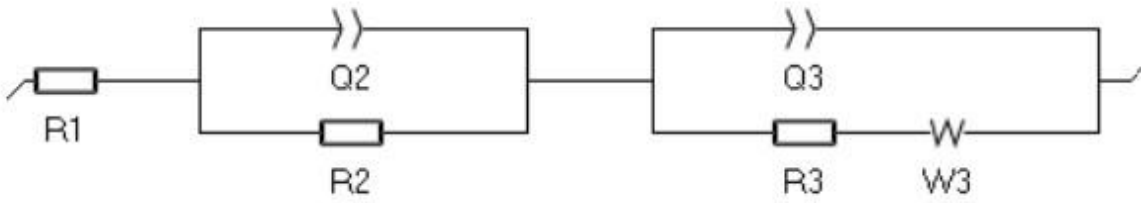

Figure S1.9: Equivalent circuit used in the fitting of impedance spectroscopy data shown in this work. R1: bulk resistance of the cell, compromising electrolyte, separator, and electrodes. R2, Q2: resistance and capacitance of the interfacial layer, respectively. R3: charge transfer resistance, Q3: double-layer capacitance, and W3: Warburg diffusion element.[256] Constant-phase elements (Q) are used instead of capacitors (C) to represent non-ideal double layer behaviour.

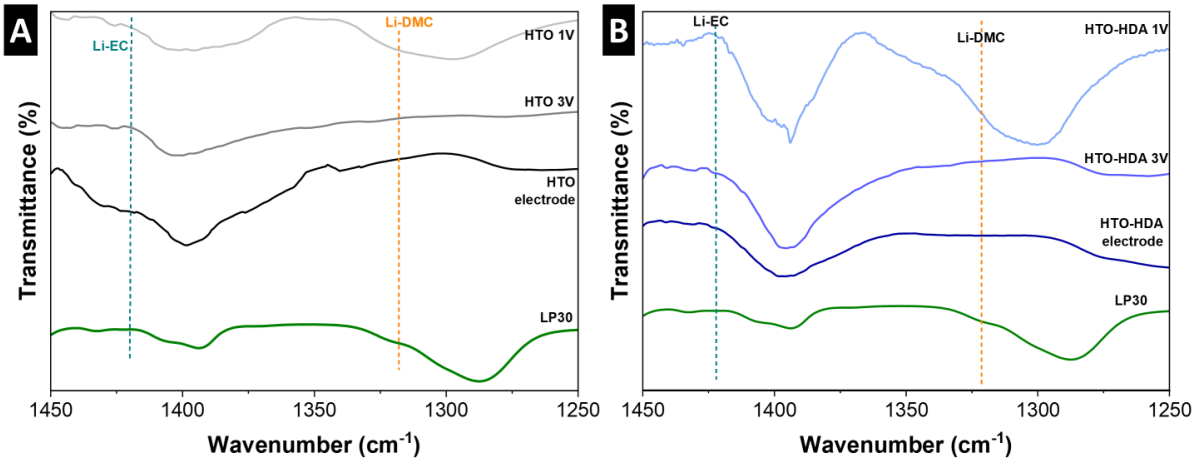

Figure S1.10: FTIR spectra of A) HTO and B) HTO-HDA electrodes after rinsing with DMC and drying in vacuum. The dashed lines indicate wavenumbers for solvated Li: Li^+-DMC at 1321 cm^{-1} and Li^+-EC at 1422 cm^{-1}.

6.2 Pillared layered titanates promote fast Na-ion intercalation

This section is reproduced from the article "Interlayer expansion of hydrogen titanate anodes improves electrochemical Na^+ intercalation kinetics and reversibility", pre-print. DOI: 10.26434/chemrxiv-2024-d9x01

Abstract

Layered titanate materials are a promising class of anodes for sodium-ion intercalation due to their abundance, low cost, and low sodium-ion intercalation potentials. However, their performance is often limited by low sodium ion diffusivity. One effective strategy to overcome these transport limitations is the introduction of molecular pillars, which act as spacers to increase interlayer spacing, enhancing ion diffusivity. Layered hydrogen titanate ($H_2Ti_4O_9 \cdot H_2O$, HTO) was functionalized with a monoamine molecule, propylamine (PA), yielding HTO-PA with expanded interlayer spacing. SEM and AFM analyses show that the morphology and surface topography of the titanate remained unaffected by the functionalization. Thorough electrochemical characterization using cyclic voltammetry, galvanostatic charge-discharge cycling, and GITT, revealed that HTO-PA exhibited improved initial coulombic efficiency, enhanced rate capability, and higher apparent Na-ion diffusion coefficients compared to unmodified HTO. Dilatometric measurements indicate that a larger electrode height change during sodiation of HTO-PA compared to HTO, suggesting the possible intercalation of solvated Na^+ in the expanded titanate structure. These results demonstrate that the modification of titanate structures using molecular pillars is a promising approach for improving ion diffusion kinetics for sodium-ion batteries.

In this work, we explore the functionalization of a layered hydrogen tetratitanate host, $H_2Ti_4O_9 \cdot H_2O$ (HTO), a rod-like phase with a monoclinic crystal structure,[262] by interlayer modulation using *n*-propylamine (PA). PA, a monoamine with a flexible three-carbon chain, attaches to the titanate layers via its amino (NH_2) group, creating a pillared structure (HTO-PA). We investigate how the confinement of organic pillars between the titanate layers impacts the electrochemical performance in a Na-ion system. Additionally, we examine the structural changes that occur in the titanate structure during cycling. Finally, we propose that nanoconfinement, induced by the introduction of organic pillars into a layered structure, can effectively alter the Na-ion storage mechanism in layered titanates, offering a new approach to optimizing their performance.

6.2.1 Physicochemical characterization

Hydrogen tetratitanate (HTO) was synthesized from the precursor potassium tetratitanate ($K_2Ti_4O_9$, KTO) by proton exchange, and subsequently subjected to organic functionalization with PA, resulting in interlayer expansion as illustrated in (**Fig. 6.9A**). Powder XRD diffractograms (**Fig. 6.9B**) show diffraction patterns of the as-synthesized KTO, HTO and HTO-PA. The expansion of the (200) plane interlayer distance from 0.88 nm in HTO to 1.58 nm in HTO-PA confirms the successful interlayer functionalization with *n*-propylamine. TGA measurements were conducted from 30 °C to 600 °C in O_2/N_2 atmosphere, and used to estimate the amounts of confined species in the HTO matrix (**Fig. 6.9C**). For pristine HTO, an overall mass loss of 14.2 % is measured, indicating an initial composition with a structural formula $H_2Ti_4O_9 \cdot 1.9H_2O$. While XRD data indicates the successful synthesis of $H_2Ti_4O_9 \cdot H_2O$, we predict that the excess water is a result of adsorbed surface water or insufficient drying. The measured overall mass loss for HTO-PA is 19.7 %, indicating the initial composition $H_2Ti_4O_9 \cdot 1.02PA$.

To examine the effects of the functionalization on particle morphology, scanning electron microscopy (SEM) images were obtained, showing that the rod-like morphology of the titanate sheets was preserved following PA functionalization (**Fig. 6.9D, E**). This is still the same morphology as the KTO rods (**Fig. S2.1**). Atomic force microscopy (AFM) images in tapping mode (**Fig. 6.9F, G**) provide information on surface topography of the HTO and HTO-PA rods. Line profiles, taken along the arrows indicated in the AFM images, exhibit a step-like profile characteristic of layered materials, with an increased average layer thickness in the HTO-PA samples (**Fig. 6.9H, I**). This increased sheet

separation in HTO-PA suggests the formation of a more open microstructure as a result of interlayer functionalization.

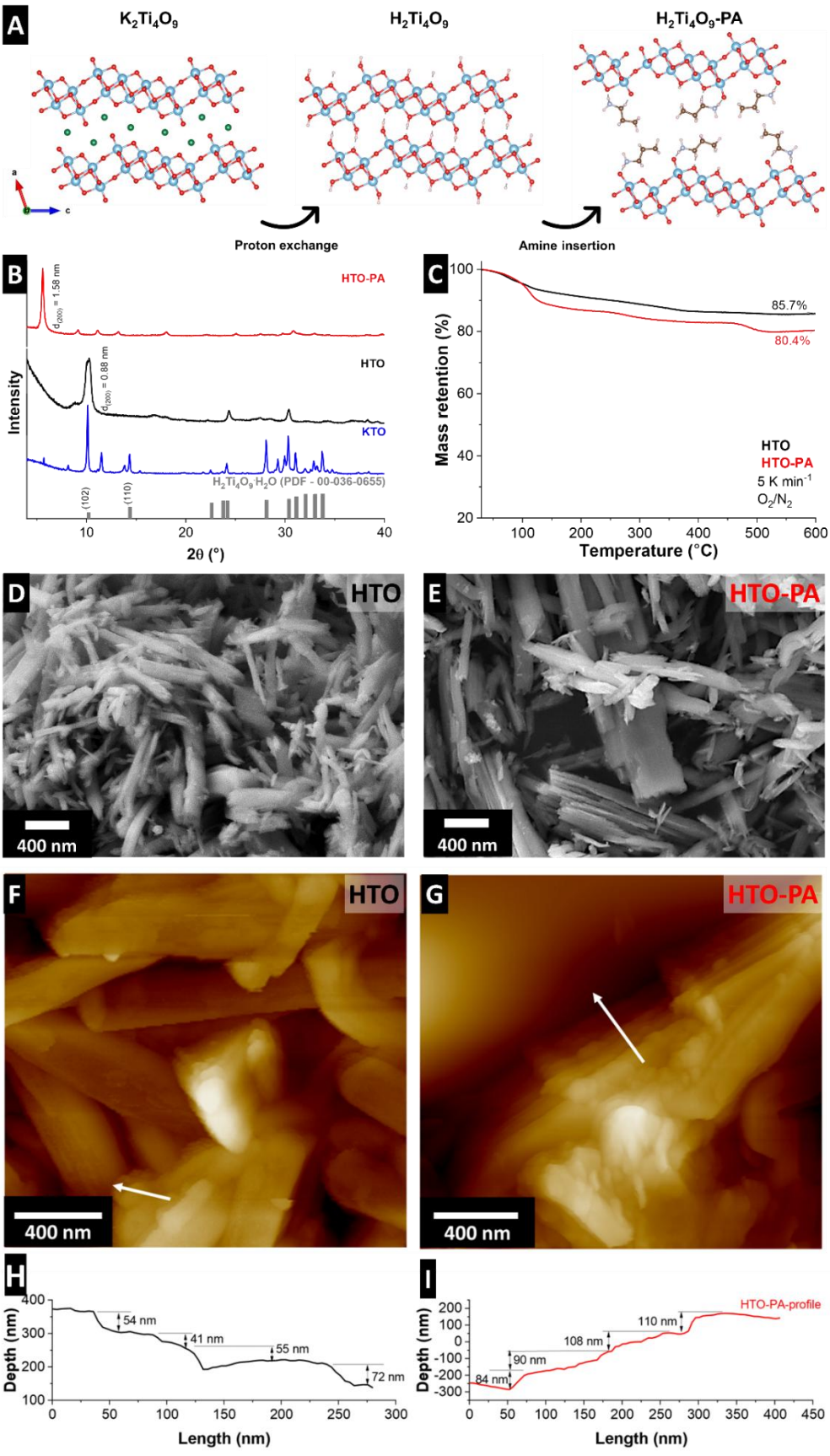

Figure 6.9: Overview of HTO and HTO-PA structural and morphological properties. A) Schematic illustration of proton exchange of KTO, followed by HTO sheets functionalization with PA. B) Powder XRD patterns of the as-synthesized structures and the reported $H_2Ti_4O_9 \cdot H_2O$ PDF. C) TGA measurements of HTO and HTO-PA in O_2/N_2 atmosphere. D), E) SEM micrographs of HTO and HTO-PA. F), G) AFM micrographs of HTO and HTO-PA in tapping mode. H), I) Line profiles of HTO and HTO-PA, taken along the arrows shown in the AFM images.

6.2.2 Electrochemical characterization

The electrochemical Na-ion intercalation behaviour of HTO and HTO-PA was investigated through a series of electrochemical measurements. As indicated by the voltage profile of HTO (**Fig. 6.10A**), the first cycle experiences a large irreversible capacity, likely due to the formation of a solid-electrolyte interface (SEI) or a passivation layer on the titanate electrode surface.[263] In the first sodiation of HTO, a plateau at 1.2 V vs. Na/Na^+ is observed, corresponding to the Ti^{4+}/Ti^{3+} redox pair. Starting from the second cycle, the onsets for the plateaux are lowered, and HTO shows a less pronounced plateau at around 0.8 V during sodiation and 1.1 V during de-sodiation. However, the voltage region below 0.5 V exhibits a sloping profile, suggesting a solid-solution type intercalation mechanism.

In contrast, the voltage profiles for HTO-PA (**Fig. 6.10B**) display a sloping profile throughout the voltage range, with the exception of an irreversible break at *ca*. 0.7 V vs. Na^+/Na, which likely corresponding to Na^+ insertion into carbon.[25] The sloping profiles implies a solid solution mechanism of Na^+ insertion across the whole voltage range, in contrast with many layered titanate electrodes which typically undergo phase transformations due to their wide compositional range.[26,264,265] While in both materials the initial coulombic efficiency (ICE) is rather low, HTO-PA exhibits a higher ICE (50%) compared to HTO (41%). Voltage profiles for HTO and HTO-PA in the potential range 0.3 – 2.5 V vs. Na^+/Na are shown in **Fig. S2.2**.

Cyclic voltammograms (CVs) of HTO and HTO-PA are recorded in sodium-ion cells against Na metal electrodes, at a lower voltage cut-off of 0.2 V vs. Na^+/Na (**Fig. 10C**). CVs recorded at lower voltage cut-off of 0.3 V are indicated in (**Fig. S2.3**). In pristine HTO, the CV at the second cycle displays distinct redox peaks at 0.87 and 1.01 V, which can be attributed to the Ti^{4+}/Ti^{3+} redox couple, analogous to the redox peaks observed in $K_2Ti_4O_9$ at similar potentials.[25] In contrast, the functionalized HTO-PA exhibits no clear redox peaks

at this voltage range. At lower potentials, two additional redox peaks emerge at 0.24 and 0.43 V in the cyclic voltammogram of pristine HTO, indicating Na^+ intercalation. While such low voltages are typically associated with Na^+ intercalation in $Na_2Ti_3O_7$ via a two-phase mechanism,[265] the sloping voltage profiles observed in this range, as discussed previously, suggest a solid-solution Na^+ intercalation process. Conversely, HTO-PA continues to show no clear redox peaks across the examined potential windows. These initial insights from CV and voltage profiles suggest that interlayer pillaring may alter the sodium-ion storage mechanisms in layered titanate anodes, resulting in a CV with no major peaks and voltage profile with no major plateaux, and therefore potentially exhibiting alternative charge storage mechanisms.

A rate capability test was conducted for both HTO and HTO-PA electrodes, with cycling performed down to a low voltage cut-off of 0.2 V (**Fig. 6.10D**). The rate capability plots show that the pillared HTO-PA exhibits enhanced capacity and rate performance at low to medium current densities, achieving an anodic specific capacity of 106.6 mAh g^{-1} at a current rate of 50 mA g^{-1}, compared to 91.5 mAh g^{-1} for HTO. However, at higher current densities of 1 A g^{-1} and above, both electrodes deliver comparable anodic capacities, with 30.6 mAh g^{-1} for HTO, and 28.5 mAh g^{-1} for HTO-PA. A similar trend was found when the same test was performed down to low voltage cut-off of 0.3 V (**Fig. S2.4**). These findings suggest that the sodium intercalation mechanisms differ between the two structures, as evidenced by the variations in their voltage profiles and cyclic voltammograms.

To further investigate the intercalation kinetics in HTO and HTO-PA, galvanostatic intermittent titration technique (GITT) was employed using a 30-minute current pulse of 20 mA g^{-1} and 2-hour rest period (**Fig. 6.10E**). GITT measurements provide insights into the sodiation kinetics through estimations of the ion diffusion coefficient and the internal resistance. The apparent Na^+ diffusion coefficients are shown in **Fig. 6.10D**, where the HTO-PA shows higher D_{Na^+} values across various potentials, indicating a lower Na^+ diffusion barrier and faster ion transport. The internal resistance, calculated by dividing the overpotential by the pulse current, is also shown in **Fig. S2.5**. While the internal resistance for HTO fluctuates across the potential range, reflecting varying diffusion energy barriers during the sodiation process,[266] it remains relatively stable in HTO-PA, consistent with a solid solution insertion mechanism as discussed above. These results suggest that interlayer

pillaring could be a promising approach to developing anodes with rapid Na^+ diffusion kinetics by mitigating the effects of sluggish diffusion.

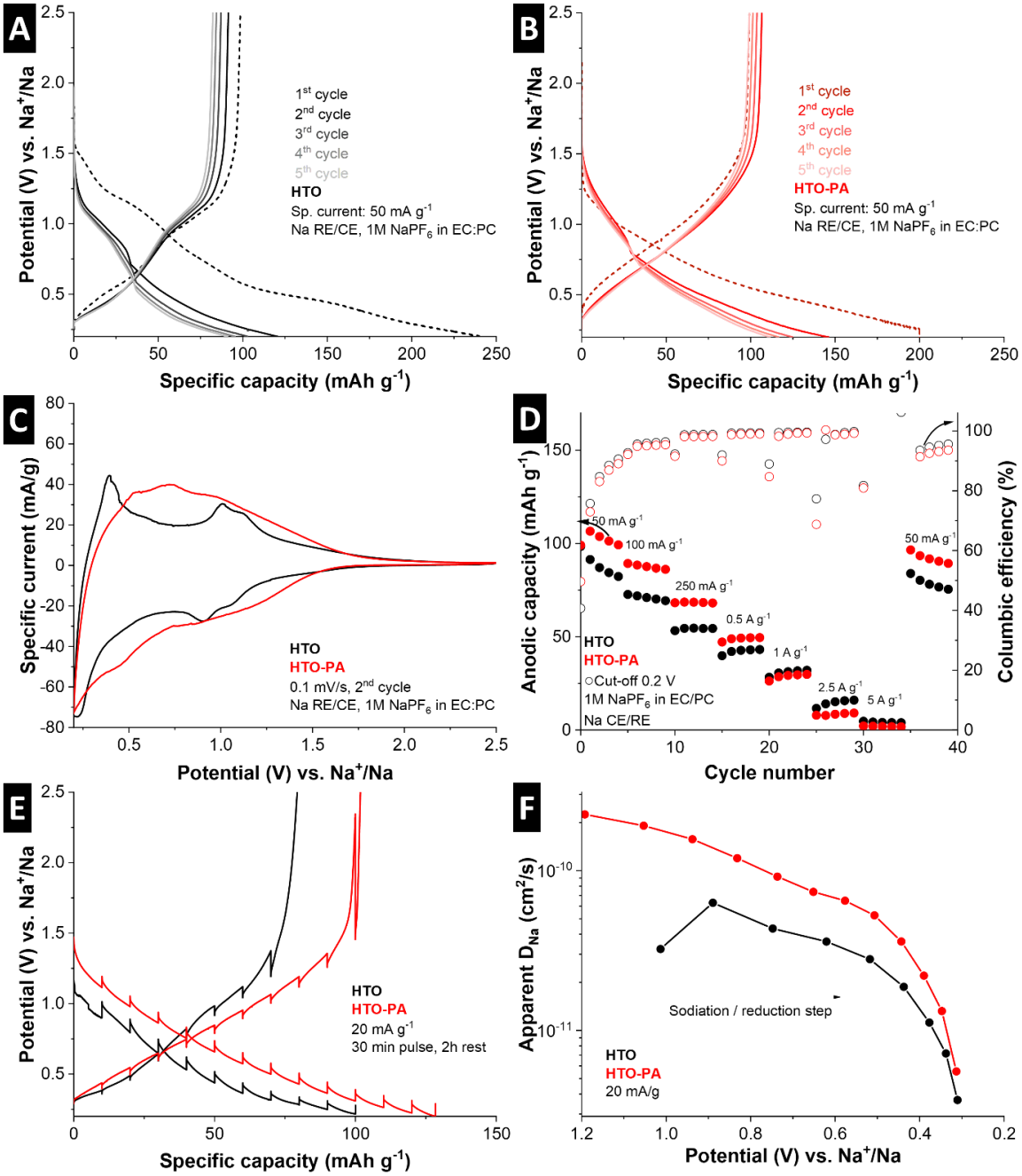

Figure 6.10: Electrochemical assessment of HTO and HTO-PA in a Na-ion cell. A) Voltage profiles of HTO and B) HTO-PA, showing the first 5 cycles at constant current rate of 50 mA g^{-1}. C) CVs of HTO and HTO-PA at scan rate 0.1 mV s^{-1} showing the second cycle at scan rate 0.1 mV s^{-1}. D) Rate handling and coulombic efficiency of HTO and HTO-PA cycled between 2.5 and 0.2 V. E) GITT measurement of HTO and HTO-PA, obtained with 30-min current pulses of 20 mA g^{-1} followed by 2h rest. F) Apparent Na-ion diffusion coefficient in HTO and HTO-PA during sodiation, obtained from GITT measurement.

To establish a relationship between the electrochemical and structural evolution of the two electrodes during cycling, *operando* electrochemical dilatometry was conducted, where the height change was recorded in during 5 sodiation and desodiation cycles (**Fig. 6.11**). In both HTO and HTO-PA, the first cycle shows a large height increase, likely due to the formation of a solid-electrolyte interface layer (SEI). Subsequent cycles, however, show different behaviour of the two electrodes. In HTO, sodiation is accompanied by a relatively smaller height increase (3.7 – 1 %). On the other hand, sodiation in HTO-PA is characterized by a larger height increase (6.1 to 4.1%). The large average increase in height of HTO-PA might indicate the intercalation of a large species, such as solvated Na-ions. On the other hand, the minimal height changes in HTO hint at less minor volumetric changes during cycling, in agreement with the zero-strain characteristic reported in KTO.[25] These insights from ECD results indicate a sodiation mechanism involving minimal volume change in HTO, and one involving large volume changes in HTO-PA.

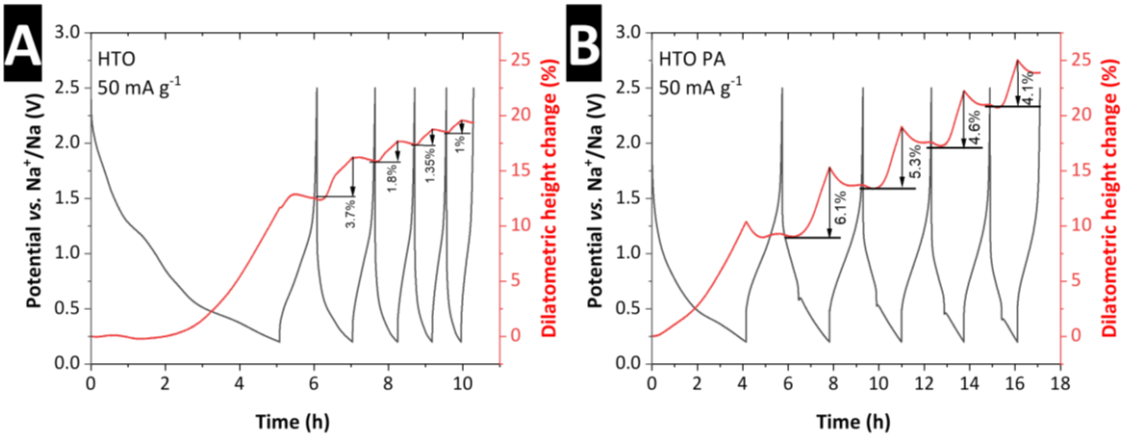

Figure 6.11: *Operando* electrochemical dilatometry measurements of A) HTO and B) HTO-PA, cycled at a specific current of 50 mA g^{-1}.

6.2.3 Conclusion

In conclusion, interlayer pillaring of HTO using a non-cross-linking pillar, PA, creates an expanded structure, where PA molecules act as spacers. The confinement of PA molecules within the interlayer space has implications on the Na intercalation mechanism. Electrochemical measurements indicate different Na-ion storage mechanisms in the two materials: while Na intercalation in HTO is accompanied by distinct peaks on the cyclic voltammogram and plateaux on the voltage profiles, in HTO-PA it is accompanied by relatively a sloping voltage profile and a CV without significant peaks, indicating a

different interaction between the Na ions and the HTO-PA host. Volumetric changes of the structures during cycling were monitored using ECD, where it was found that, while Na intercalation in pristine HTO is accompanied by slight volumetric expansion, it is accompanied by a larger average expansion in HTO-PA. This, combined with the features of the CV and voltage profile, suggests an ion-solvent cointercalation mechanism, where the Na ions are speculated to intercalate with (parts of) its solvation sheath. This work shows the potential of changing the nanoconfinement environment in giving rise to alternative charge storage mechanisms.

6.2.4 Supporting information

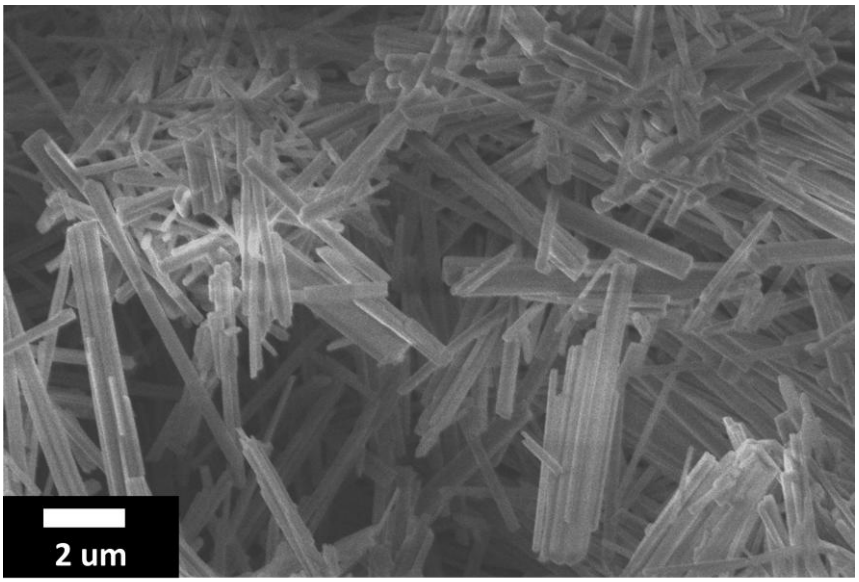

Figure S2.1: SEM image of $K_2Ti_4O_9$ (KTO) rods.

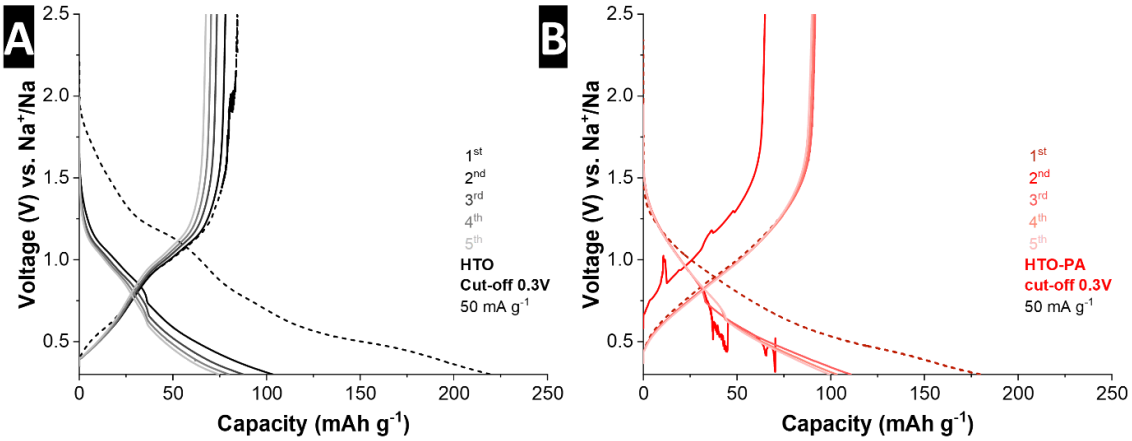

Figure S2.2: Voltage profiles for the first 5 cycles of A) HTO and B) HTO-PA, cycled in the potential range 0.3 – 2.5 V vs. Na^+/Na at current rate 50 mA g^{-1}. The first cycle is shown in dashed lines.

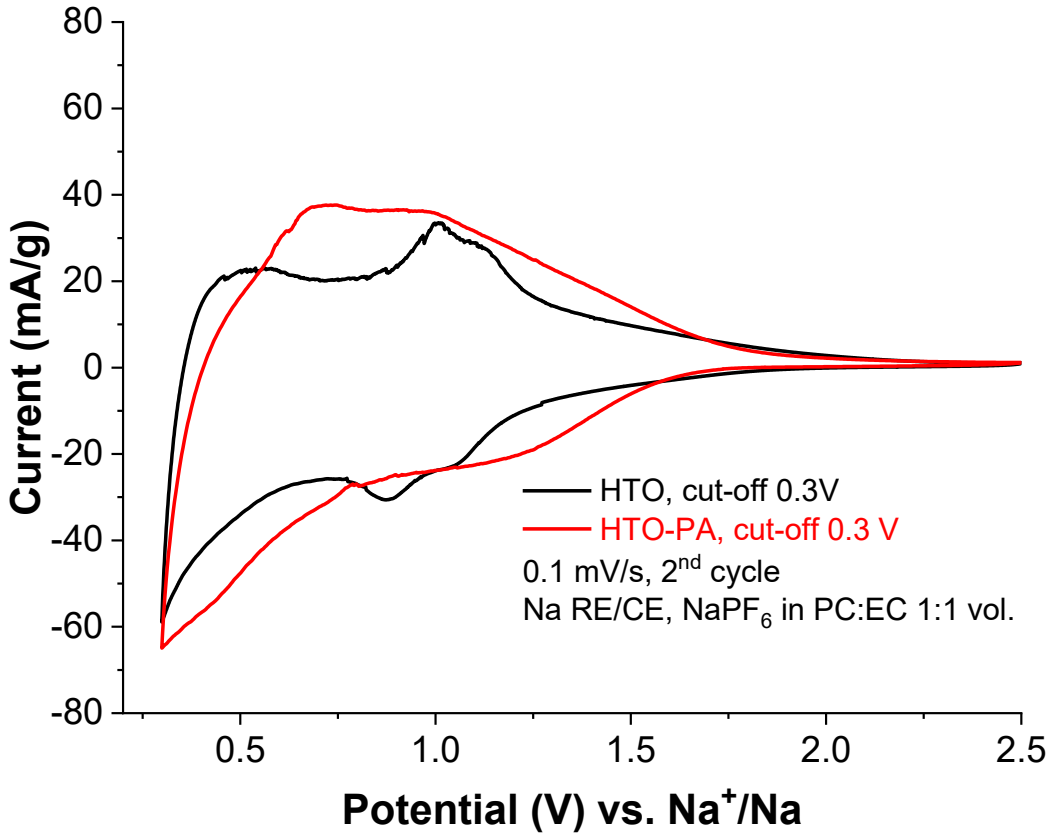

Figure S2.3: CV of HTO and HTO-PA at voltage range 2.5 to 0.3 V vs. Na^+/Na, showing the second cycle at scan rate of 0.1 mV s^{-1}.

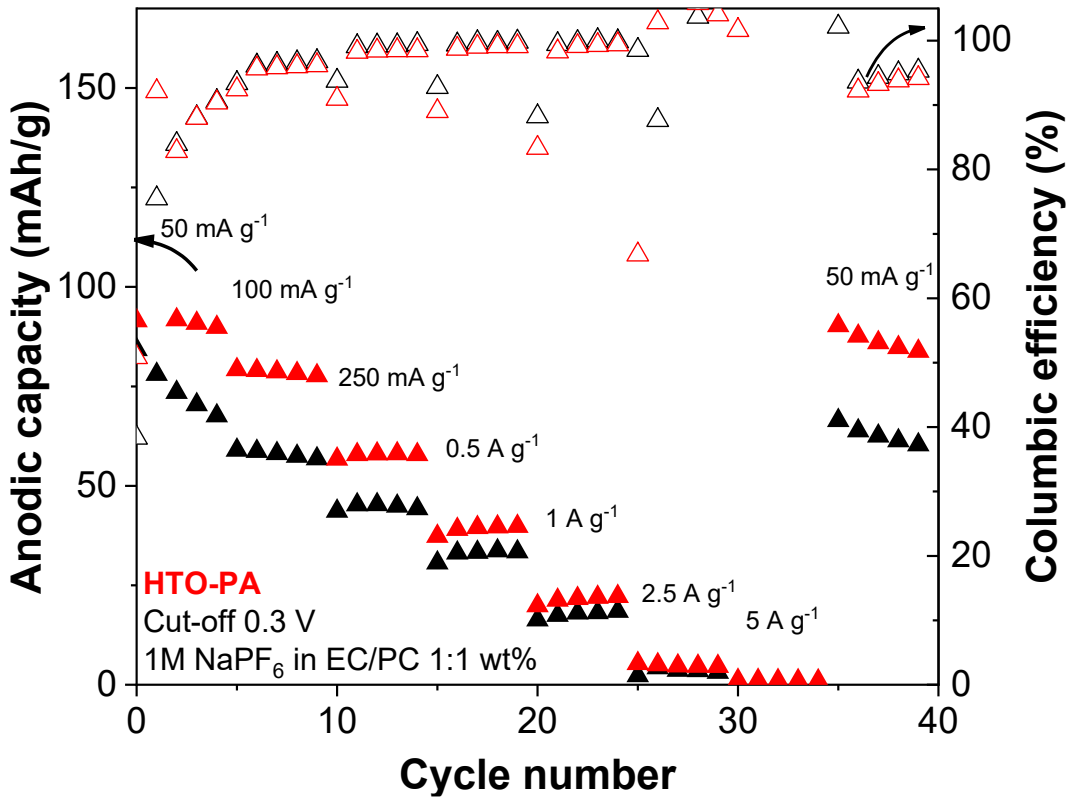

Figure S2.4: Rate handling test of HTO and HTO-PA at lower cut-off of 0.3 V vs. Na^+/Na.

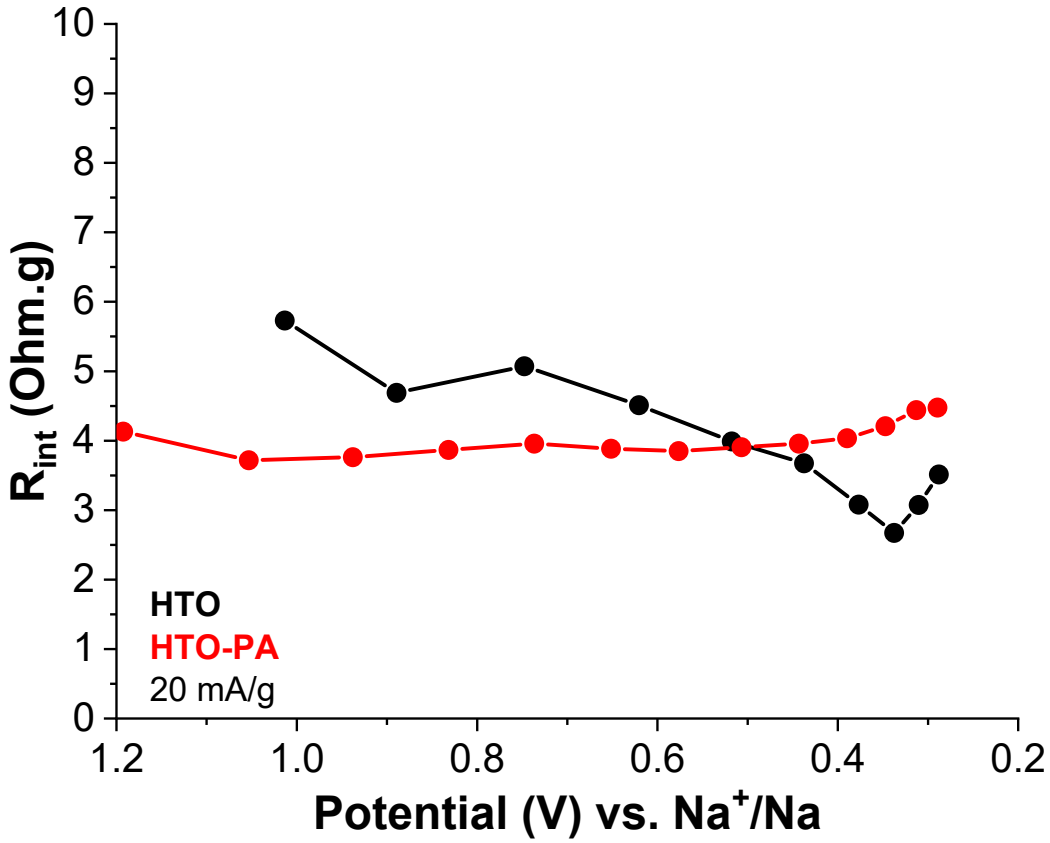

Figure S2.5: Internal resistance (R_{int}) in HTO and HTO-PA obtained from GITT measurement. The values are obtained by dividing the overpotential (difference between quasi-open circuit voltage and the closed-circuit voltage) by the applied current.

6.3 Mechanistic understanding of microstructure formation during synthesis of metal oxide/carbon nanocomposites

*This section is reproduced from the published article "Mechanistic understanding of microstructure formation during synthesis of metal oxide/carbon nanocomposites", **J. Mater. Chem. A**, 2023, 11, 17125-17137, DOI: 10.1039/D3TA01230A*

Abstract

Nanocomposite materials consisting of metal oxide and carbon are of interest as electrode materials for both high rate intercalation-type and high capacity conversion-type charge storage processes. Facile synthesis processes like the pyrolysis of an organic carbon-source can yield a well-dispersed carbon phase within the metal oxide structure. Detailed understanding of the carbon formation process is required to tailor the resulting material microstructure. Herein, both the formation and the final microstructure of a molybdenum oxide/carbon nanocomposite are studied in detail. Octylamine assembled in the interlayer space of layered MoO_3 serves as a carbon source. The structural changes during pyrolysis are characterized using a combination of *in situ* heating X-ray diffraction with simultaneous FTIR- and mass spectroscopy-coupled thermogravimetric analysis experiments. These reveal mobility and partial desorption of octylamine and interlayer water at low temperatures, octylamine decomposition and loss of long-range order at intermediate temperatures, and carbothermic reduction of molybdenum oxide at high temperatures during pyrolysis. The resulting nanocomposite mainly contains nanocrystalline MoO_2 domains surrounded by a well-dispersed carbon phase, as observed with scanning transmission electron microscopy of focus-ion beam prepared cross-sectional lamellae. The electrochemical behaviour is evaluated in organic, lithium-containing electrolyte for both intercalation and conversion-type reactions, showing good intercalation kinetics and a high first cycle efficiency for the conversion-type reaction.

In this study, the microstructural changes during pyrolysis of an octylamine-functionalized molybdenum oxide are systematically analysed. Molybdenum trioxide (α-MoO_3) consists of layers of corner- and edge-sharing distorted MoO_6-octahedra in an orthorhombic crystal structure, where the individual layers are held together by van der Waals forces.[267] MoO_3 is chosen for this study because organic molecules such as alkylamines can assemble in its interlayer space, serving as a confined carbon source.[268] The resulting nanocomposite derived from pyrolysis has relevance for electrochemical applications, because molybdenum oxides can undergo intercalation and conversion reactions with lithium.[269,270] The octylamine (OA) molecule is chosen for its model character, as alkylamines are linear organic molecules which are widely available with variable carbon chain length, allowing to customize the carbon-source molecule.

We employ a combination of *in situ* characterization and X-ray spectroscopy and electron microscopy techniques to analyse the structural and chemical changes of the molybdenum oxide/octylamine material during pyrolysis. We show that carbon formation occurs predominantly within the micron-sized product aggregates and coincides with molybdenum reduction that is accompanied by CO_2 & CO release. Simultaneously, nanosized oxide grains in the range of 5-10 nm are formed within the aggregates that exhibit local variations in oxygen and carbon content. Scanning transmission electron microscopy (STEM) imaging of specimen prepared via focused ion beam (FIB) reveals the microstructure of the materials representative of their bulk volume. The obtained MoO_x-C nanocomposite exhibits improved kinetics for electrochemical intercalation and an enhanced initial Coulombic efficiency for the conversion reaction, depending on the employed potential range, compared to pristine molybdenum oxide samples.

6.3.1 Structural characterization

The synthesis of molybdenum oxide dihydrate ($MoO_3 \cdot 2H_2O$, also referred to as molybdic acid) was performed via the method described by Freedman[229] and the chemical self-assembly reaction of octylamine (OA) in the interlayer of molybdenum oxide was achieved by a wet chemistry synthesis to obtain MoO_x-OA. While in this study, a molar ratio of Mo:OA of 1:1 was chosen, variation of the ratio yields structures with similar crystallography (**Fig. S3.1**). This material was subsequently pyrolyzed at 700 °C for 2 hours under argon flow to form an OA-derived carbonaceous phase. The final product of this

synthesis is a nanocomposite MoO_x-C, as described in the experimental section and shown in the schematic in **Fig. 6.12A**. In the following, we provide mechanistic insight into the synthesis/pyrolysis process and final product structure, pursuant of the overarching goal to understand where a carbonaceous phase forms and how the microstructure evolves in the molybdenum oxide/carbon nanocomposite material. In particular, we aim to answer whether a heterostructured microstructure forms, where in an ideal case, 2D layers of molybdenum oxide and carbon alternate throughout the bulk volume of the structure.

The reaction mechanism of alkylamines with molybdic acids can be likened to that in isostructural tungstic acids, which has been described in literature to occur via a dissolution-reorganization mechanism that leads to a change in the morphology and particle size.[271,272] Scanning electron micrographs of $MoO_3 \cdot 2H_2O$ and MoO_x-OA (**Fig. 6.12B-C**) show an increased particle size after reaction with octylamine. Therefore, we hypothesize that, like in tungstic acids,[271] the alkaline conditions upon octylamine addition lead to an initial dissolution of $MoO_3 \cdot 2H_2O$ and a subsequent reassembly of the structure with octylamine in the interlayer space of MoO_3.

Subsequent pyrolysis of MoO_x-OA to form MoO_x-C leads to a change in particle morphology (**Fig. 6.12D**), most notably, a reduced average particle size from 7.0±2.3 to 1.7 ±0.6 µm (**Fig. S3.2**), indicating significant densification after pyrolysis.

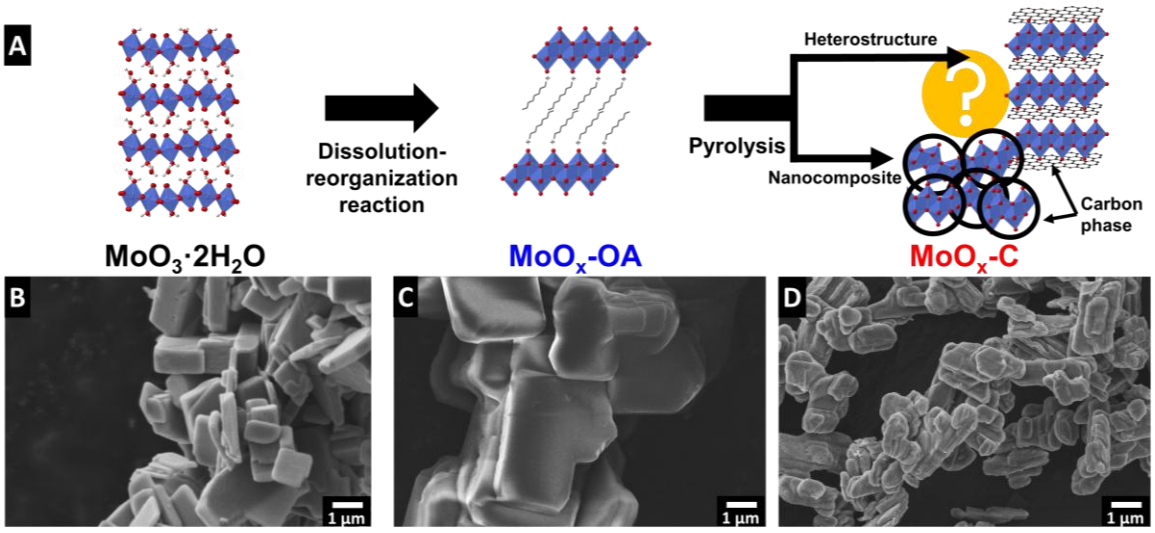

Figure 6.12: (A) Schematic illustration of the synthesis process: Octylamine is assembled in the MoO_3 interlayer space via a dissolution-reorganization reaction; subsequent pyrolysis yields the

carbon-containing nanocomposite. SEM images of (B) molybdenum oxide dihydrate ($MoO_3 \cdot 2H_2O$), (C) MoO_x-OA, and (D) MoO_x-C after pyrolysis in argon at 700 °C.

The Raman spectrum of $MoO_3 \cdot 2H_2O$ (**Fig. 6.13A**) shows the typical Raman signals of α-$MoO_3 \cdot 2H_2O$, where the high intensity peaks at 934 cm^{-1} and 727 cm^{-1} are assigned to the stretching modes of O=Mo and O–Mo_2, respectively.[272] Peaks in lower wavenumber ranges, from 400 to 200 cm^{-1}, are assigned to lattice and deformation modes.[273] After assembly of OA in the interlayer, a sharp peak appears at 896 cm^{-1}, corresponding to Mo-O stretching in $[MoO_4]^{2-}$,[274] suggesting the formation of molybdate as a result of OA functionalization.[276] The other strong peak at 819 cm^{-1} is characteristic of the doubly-coordinated oxygen (O–Mo_2) stretching mode.[276] The Raman peak around 2882 cm^{-1} could be assigned to the asymmetric stretching of the methylene (CH_2) group in octylamine.[277] The Raman spectrum of the pyrolyzed MoO_x-C shows characteristic peaks for MoO_2 according to previous reports (note that a reduced laser power has to be chosen to avoid (re-)oxidation of MoO_2 to MoO_3 during Raman measurement[278]).[279] This suggests that the α-MoO_3 is reduced to MoO_2 during pyrolysis. Successful carbon formation is confirmed by two peaks appearing in MoO_x-C at 1604 and 1357 cm^{-1}, corresponding to bond stretching of pairs of sp^2-carbon (G-mode) and defect-induced breathing modes of sp^2-carbon (D-mode), respectively.[280] In the 2000 to 3000 cm^{-1} range, the absence of the G' band, also called the 2D band, indicates that the formed carbon is highly defective.[281]

Fig. 6.13B shows powder XRD patterns of $MoO_3 \cdot 2H_2O$, MoO_x-OA, and MoO_x-C. Diffraction peaks of the as-synthesized molybdic acid are referenced to $MoO_3 \cdot 2H_2O$ according to PDF 00-016-0497. Upon assembly of OA in the interlayer, a shift of the (020) peak at 12.96° to 3.99° 2θ is observed, corresponding to an expansion of the interlayer, with the d-spacing increasing from the initial 0.68 nm in $MoO_3 \cdot 2H_2O$ to 2.21 nm in MoO_x-OA. Since the octylamine molecule has a chain length of ca. 1.2 nm,[282] the large increase in interlayer spacing in MoO_x-OA suggests a tilted bilayer arrangement of OA molecules between the MoO_x sheets.[268]

After pyrolysis, the XRD pattern of MoO_x-C shows peaks matching with monoclinic MoO_2 reflections according to PDF 00-032-0671, in agreement with Raman measurements. Furthermore, low-intensity signals at ca. 34° 2θ and 39.4° 2θ suggest that traces of Mo_2C and Mo_4O_{11} were also formed, according to PDF 00-011-0680 and PDF 00-005-0337, respectively.

The oxidation states of Mo in the resulting nanocomposite MoO_x-C were investigated by means of XPS. The analysis of Mo 3d is rather complex, and the accurate interpretation is often not well reported. In this case, the Mo 3d (**Fig. 6.13C**) region was analysed following Scanlon *et al*. work, in which the Mo(IV)O_2 consisted of two doublets due to the presence of both screened and unscreened electronic environment of Mo (for more detail see ref. 40).[283] The Mo 3d region indicates the presence of Mo (IV) and Mo (VI) on the MoO_x-C, in agreement with XRD. The formation of the latter species is highly common on Mo(IV) oxides.[284] Nevertheless, the MoOx-C consists mainly of MoO_2 (66 % vs. 33 % of Mo(VI), as also shown in the O 1s spectrum (**Fig. S3.3**). In addition, the C 1s region (**Fig. 6.13D**) displays the presence of Mo_2C and C-C, C-O, and O-C=O species, at 283.6, 285.0, and 286.7 and 288.6 eV in agreement with Raman and XRD.[285,286]

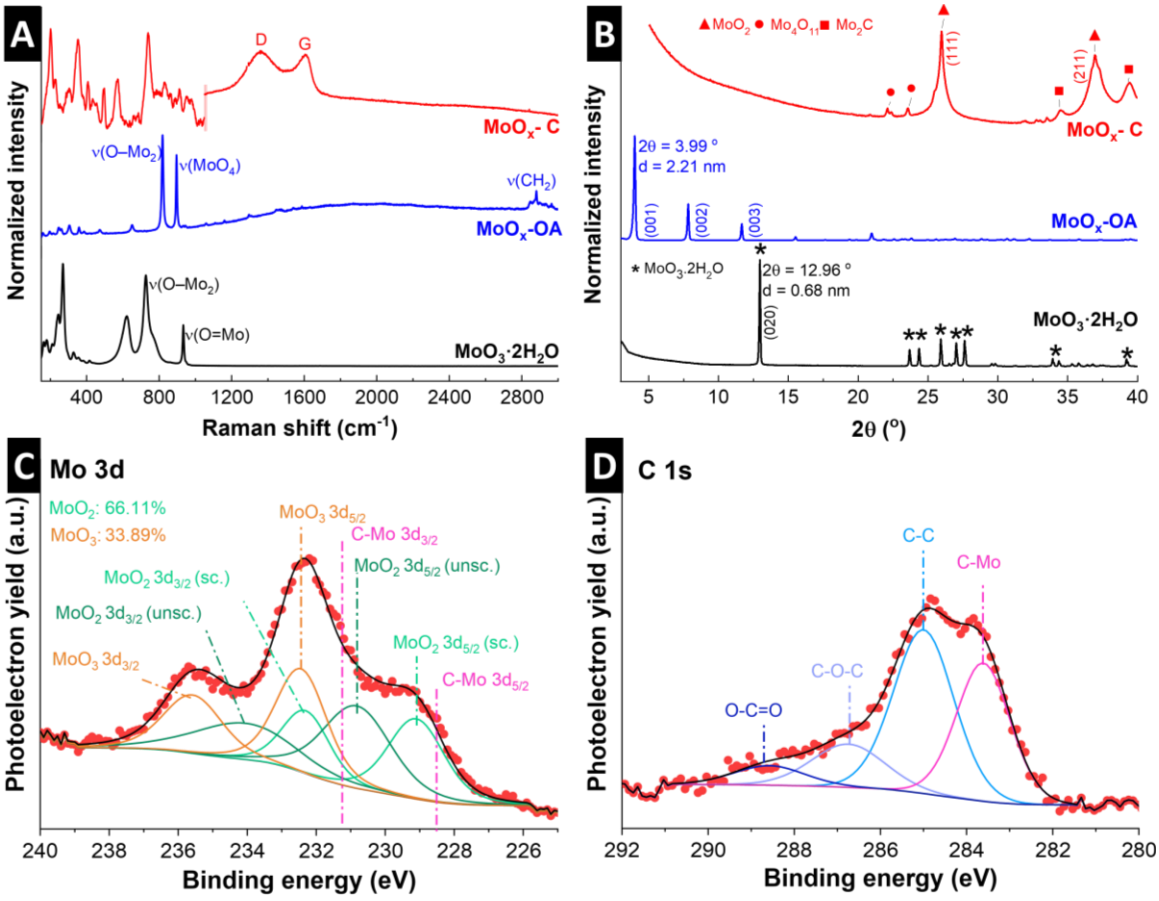

Figure 6.13: Structural characterization of hydrous molybdenum oxide ($MoO_3 \cdot 2H_2O$), molybdenum oxide with octylamines assembled in the interlayer space (MoO_x-OA) and pyrolyzed MoO_x-C: (A) Raman spectra of all samples. Raman spectrum of MoO_x-C consists of two individual

measurements with different laser power: 0.25 mW between 100-1050 cm^{-1} to avoid oxidation of MoO_2 to MoO_3; 5 mW between 1050-3000 cm^{-1} for better resolution of carbon signals (individual full spectra given in **Fig. S3.3**). (B) X-ray diffractograms with referenced peak positions of $MoO_3 \cdot 2H_2O$ (PDF 00-016-0497, asterisk), monoclinic MoO_2 (PDF 00-032-0671, triangle), Mo_2C (PDF 00-011-0680, square), and Mo_4O_{11} (PDF 00-005-0337, circle). (C) Mo 3d, and (D) C 1s X-ray photoelectron spectrum regions of pristine powder MoO_x-C.

To understand the structural evolution of the material during the pyrolysis, we combined *in situ* heating XRD of MoO_x-OA in an inert atmosphere (**Fig. 6.14A, 3B**) with thermogravimetric analysis with simultaneous mass spectroscopy (TGA-MS, **Fig. 6.14C**) and Fourier-transform infrared spectroscopy (TGA-FTIR, **Fig. 6.14D**). The results indicate that MoO_x-OA undergoes three major structural transitions during pyrolysis, which can be conclusively explained in combination with the analysis of the evolving gaseous products via MS and FTIR at different temperatures:

Stage 1: A sudden shift of the diffraction peak at ca. 3.8° 2θ, representative of the interlayer spacing, to a higher diffraction angle (ca. 4.1° 2θ) can be observed at a temperature of ca. 120 °C, indicating an initial shrinking of the interlayer spacing. In the same temperature range (120 – 200 °C), TGA reveals a two-step mass loss of around 24 wt.%, coinciding with the evolution of gaseous species. MS signals in profiles of five mass-to-charge ratio (m/z) signals are detected, namely m/z = 17, 18, 28, 30, and 44. The signals of m/z = 17 (OH^+) and 18 (H_2O^+) suggest the desorption of surface and loosely-bound interlayer water molecules.[287] The m/z = 17 signal can also be assigned to ammonia (NH_3^+), which can result from the decomposition of the OA molecule. The peaks in the profile of m/z = 30 can be assigned to the base peak ion $[CH_2NH_2]^+$, characteristic of β-cleavage of OA molecule.[288,289] Finally, the signal at m/z = 28 can be attributed to hydrocarbons, CO_2, or N_2, and m/z = 44 can be attributed to hydrocarbons (C_3H_8) or CO_2.[287] FTIR results in **Fig. 6.14D** confirm the evolution of mainly molecular OA and water, and small traces of CO_2 and NH_3 as likely OA decomposition product in this temperature range (see the selected FTIR spectra of the pyrolysis gas compared with the typical FTIR spectra of OA, water, NH_3, and CO_2 in **Fig. A3.5A-B**).[290] Hence it can be concluded that loss of loosely bonded OA and water likely by evaporation are the main causes of initial interlayer shrinking, while a first onset of OA decomposition can be detected.

Stage 2: Above 200 °C up to around 350 °C, a continuous shrinking of the interlayer spacing to about 1.7 nm (ca. 5° 2θ) is observed with the intensity strongly reducing before fully disappearing, suggesting complete loss of long-range crystalline order above ca. 350 °C during pyrolysis. The corresponding TGA in this region up to 350 °C detects an accumulated mass loss of ca. 43 wt.% with simultaneous MS signals at m/z = 17,18, and 44. This indicates further release of water and decomposition products of OA (NH_3 and hydrocarbon fragments). From the FTIR spectra of the pyrolysis gas in this temperature range, the evolution of hydrocarbons is evident from the strong absorption between 3000 and 2800 cm^{-1}, but it cannot be assigned univocally to a specific molecule like in the previous temperature range, due to the lack of significant fingerprints in the 1500-650 cm^{-1} region of the interferograms (see the selected FTIR spectra of the pyrolysis gas in **Fig. S3.5C-D**). The detection of a stronger absorption pattern typical of NH_3 in the same temperature range confirms the decomposition of OA, hence the hydrocarbons detected through FTIR could be regarded as decomposition products. Simultaneously, an increase in the CO_2 signal is detected in FTIR above 350 °C (**Fig. S3.5D**), suggesting the onset of (elemental) carbon formation in the material.

Stage 3: Towards the end of the heating step (above 650 °C) and during the two hours holding step at 700 °C in argon (**Fig. 6.14B**), the emergence and intensification of two diffraction peaks at 25.8 and 25.2 °2θ can be detected, indicative of the (111) and (011) signals of monoclinic MoO_2. This can be conclusively linked to the last mass loss step observed above ca. 650 °C (highlighted in purple, accumulated mass loss of 58 wt.%), and an MS signal at m/z = 44, which is attributed to CO_2 and indicative of carbothermic reduction of MoO_3 to MoO_2 with carbon acting as reducing agent.[291] Another strong peak at m/z = 28 can be attributed both to CO_2 and CO, and the FTIR spectra at this temperature confirm the simultaneous presence of these two gases (**Fig. 6.14D** and **Fig. S3.5E**). This is further supported by the detection of MoO_2 after the pyrolysis by Raman results (**Fig. 6.13A**), XRD (**Fig. 6.13B**), and further confirmed by the electrochemical characterization (*vide infra*).

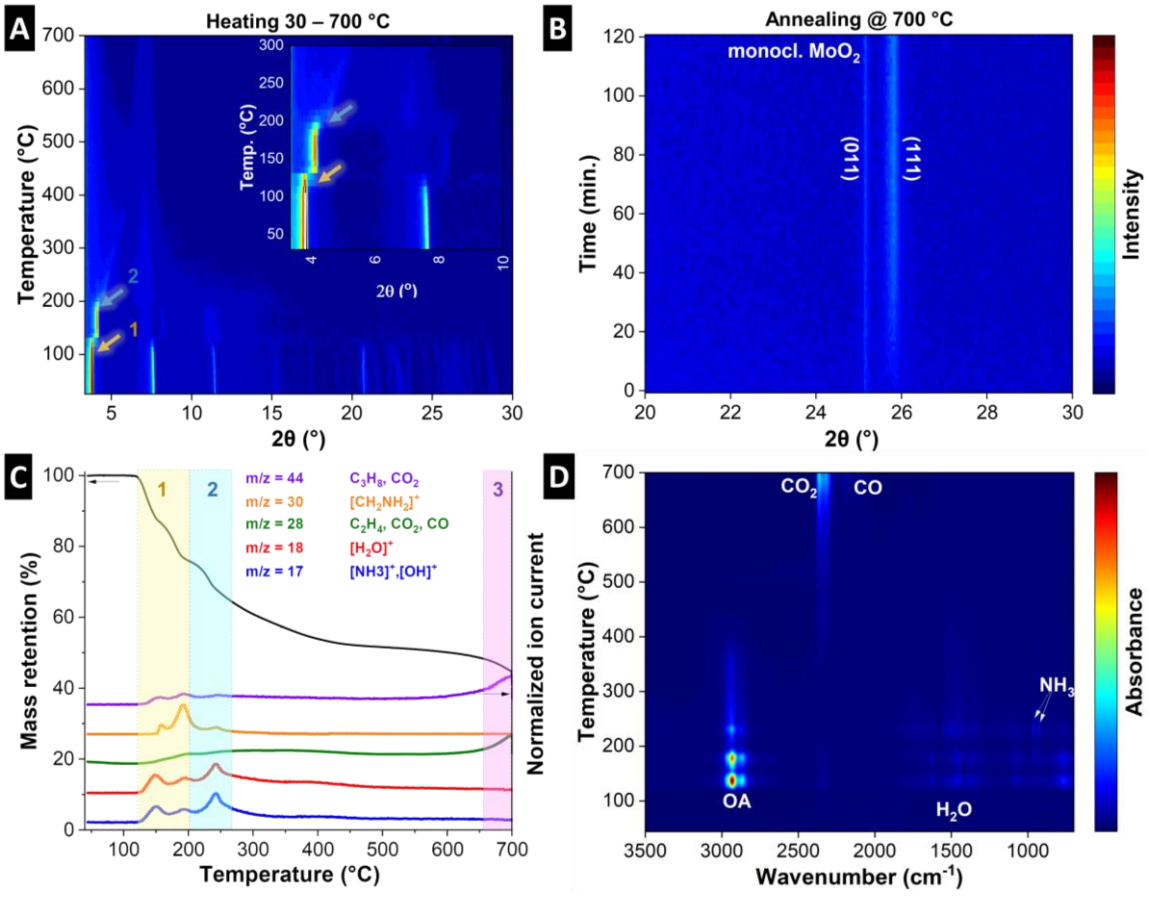

Figure 6.14: (A) *In situ* heating XRD patterns of MoO_x-OA during the heating step of pyrolysis, with inset showing magnified view of the 2θ range 2-10° and temperature range 30-300 °C, (B) *In situ* heating XRD patterns of MoO_x-OA during the two-hour annealing step. (C) Thermogravimetric analysis with mass spectroscopy of MoO_x-OA during the heating step of pyrolysis, detecting gaseous decomposition products with various mass-to-charge ratios (m/z). Three distinct processes occurring during pyrolysis are graphically indicated by colored mass loss regions (yellow, blue, purple), also highlighted by the arrows in the in-situ heating XRD diffractograms. (D) TGA with FTIR analysis of gaseous decomposition products during the heating step of pyrolysis.

The stepwise transformations of MoO_x-OA during pyrolysis, primarily during the heating step with several structural changes and loss of initial long-range order, indicate the formation of an intricate, intraparticle microstructure. Due to the apparent mobility of OA and OA-fragments (i.e., the carbon source) during the heating step, the intraparticle arrangement of the carbon in the nanocomposite product has to be investigated carefully. For this purpose, the microstructural features of MoO_x-C were analysed using scanning transmission electron microscopy (STEM). Electron-transparent lamellae were prepared via focused ion beam (FIB) to observe regions of interest taken from the bulk of MoO_x-C

particles (**Fig. 6.15A**) to reveal a representative intraparticle structure. STEM images show a difference in the Z-contrast for features with a size of 5-10 nm. This indicates the formation of domains or grains in a size range of 5-10 nm with varying elemental composition, as shown in the zoomed-in view in **Fig. 6.15B**. High-resolution STEM micrographs (**Fig. 6.15C, D**) show the presence of nanocrystalline domains homogenously distributed throughout the sample with a size comparable to the sizes of differing Z-contrast. The observation suggests that carbon formation occurred primarily outside the crystalline nanodomains, which contradicts the initially hypothesized formation of a heterostructured, i.e., alternating layer-by-layer arrangement of molybdenum oxide and the carbon phase. Rather, pyrolysis of MoO_x-OA yields a carbon-containing molybdenum oxide nanocomposite. The lattice fringes in **Fig. 6.15C, D** (corresponding HAADF-STEM image in **Fig. S3.6**) show two characteristic distances with slight local variation. The larger one is around 3.5 Å and the smaller around 2.5 Å, in good agreement with the averaged values obtained from XRD for the d-spacings of the (111) plane (3.43 Å) and the (211) plane (2.43 Å) of monoclinic MoO_2. Both of these planes account for the most intense reflections on the XRD diffractogram of MoO_x-C (**Fig. 6.13B**), hence, the nanodomains observed in **Fig. 6.15C, D** can be assigned to monoclinic MoO_2.

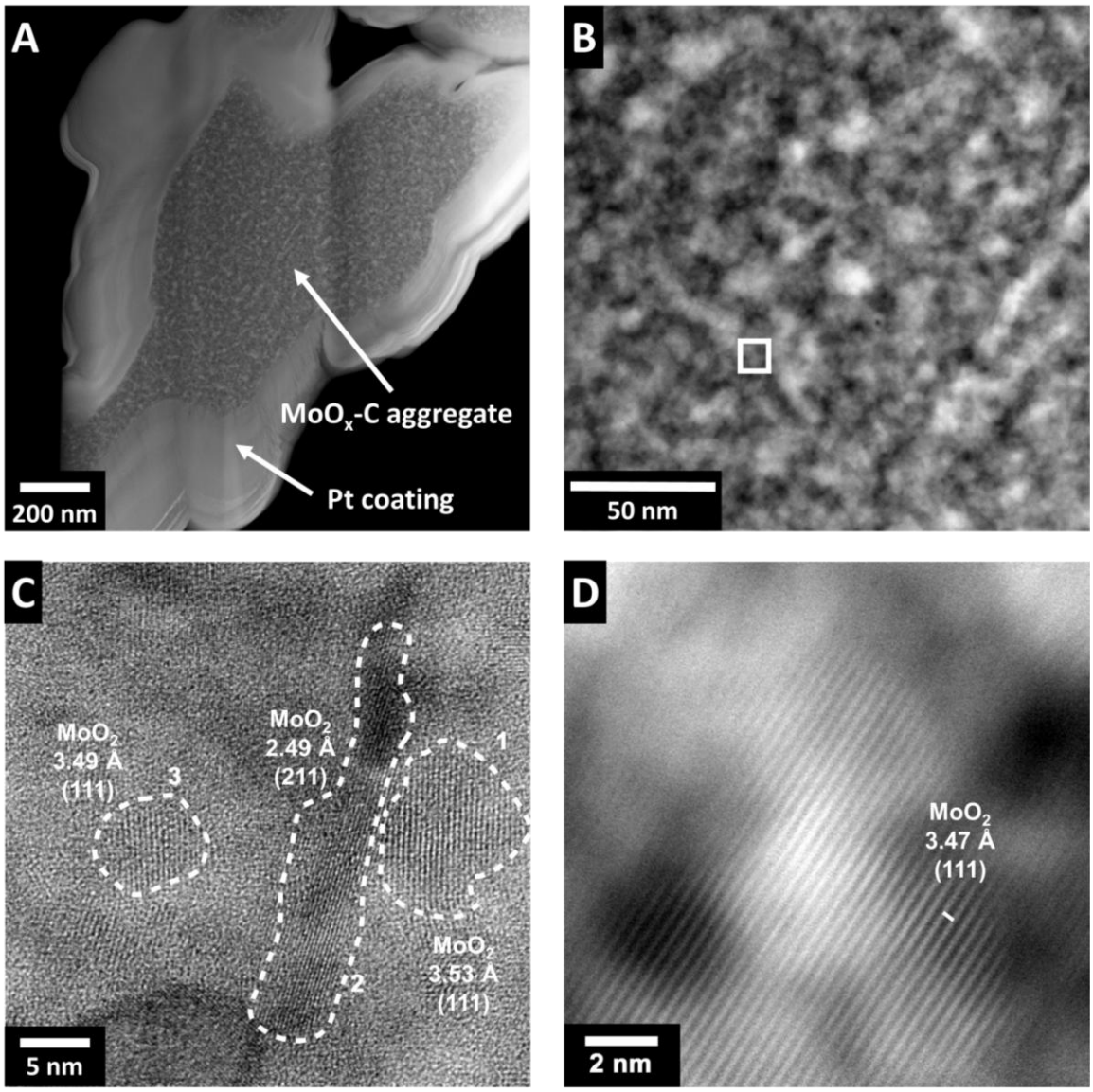

Figure 6.15: Cross-sectional overview of the MoO_x-C hybrid nanostructure. a) HAADF-STEM micrograph of MoO_x-C showing microstructure with non-homogeneous particle composition. b) magnified micrograph of area indicated in b) showing phase Z-contrast variations in MoO_x-C, c) bright field STEM micrograph taken at the area indicated in b). The crystalline domains are highlighted and measurements of planar spacings are indicated on the image. Lattice spacings in regions 1, 2, and 3 are in good agreement with the (111), (211), and (111) planes of MoO_2, respectively. d) high resolution HAADF-STEM image of monoclinic MoO_2 nanodomain.

To investigate the elemental distribution, we performed energy dispersive X-ray spectroscopy (EDS). HAADF -STEM (**Fig. 6.16A**) with EDS elemental mapping of molybdenum, oxygen, and carbon (**Fig. 6.16B-D**) were recorded for FIB-prepared MoO_x-C sample cross-sections. The EDS maps revealed an elemental separation with regions enriched in Mo and C and regions enriched in O. The size of these regions corresponds

well with the domain/grain size identified in HAADF and high-resolution STEM micrographs (**Fig. 6.15**, **Fig. S3.6**). Furthermore, the EDS maps show variations of oxygen- and molybdenum-concentration in the nanosized grains of molybdenum oxide suggesting localized carbothermic reduction of the molybdenum oxide during pyrolysis. EDS spectra indicate that the carbon-concentration is higher in the areas with lower oxygen concentration (**Fig. 6.16E**), suggesting that the carbon formation process and MoO_3 reduction to MoO_2 are correlated. EDS line scan profiles of Mo, O, and C in MoO_x-C are shown in **Fig. S3.7**, where local variations in the concentrations of the three elements are shown. TGA measurements in oxygen reveal that the bulk carbon content of MoO_x-C nanocomposites is ca. 2.7 wt.% (**Fig. S3.8**).

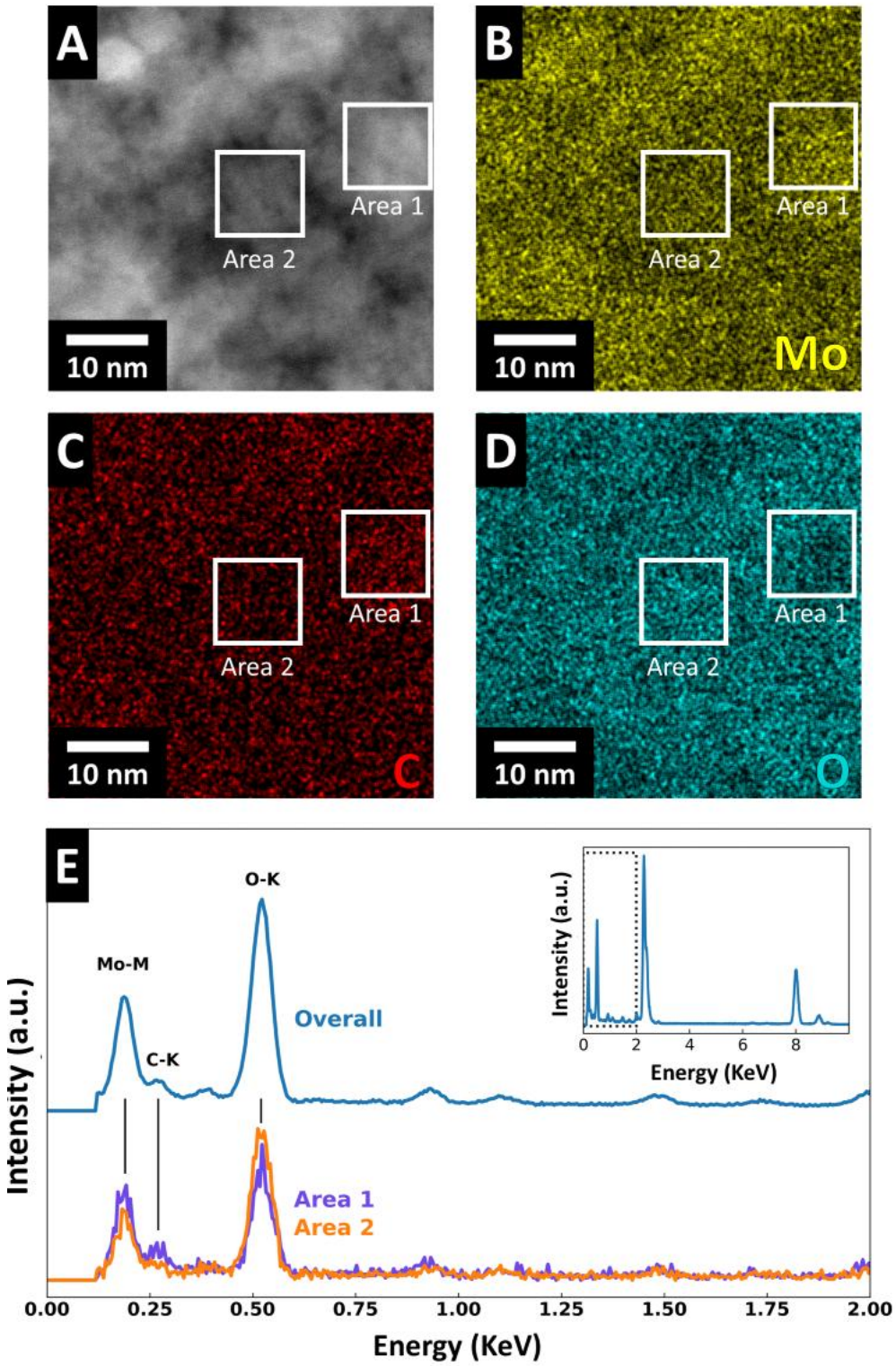

Figure 6.16: (A) HAADF-STEM micrograph showing Z-number contrast and (B-D) EDS mapping with elemental distribution of Mo, C, and O in MoO_x-C. (E) Chemical analysis of the two marked areas by quantitative STEM-EDS spectral imaging analysis.

6.3.2 Electrochemical characterization

To understand the implications of the nanocomposite microstructure in MoO_x-C on electrochemical reactivity, we tested the nanocomposite as an electrode material in standard organic, lithium-containing electrolyte (LP30). Two different potential windows are chosen to establish a complete picture of the electrochemical performance of the electrode material: according to literature, cycling of molybdenum oxides in a potential range of 1 – 3 V vs. Li^+/Li leads to reversible lithium intercalation according to:

$$MoO_3 + xLi^+ + xe^- \rightarrow Li_xMoO_3,\ (x_{max} = \sim 1.5) \qquad (\mathbf{6.1})\ ^{269}$$

and for MoO_2:

$$MoO_2 + xLi^+ + xe^- \rightarrow Li_xMoO_2,\ (x_{max} = \sim 0.98), \qquad (\mathbf{6.2})\ ^{186}$$

resulting in a theoretical capacity for the intercalation reaction of 279 and 209 mAh g^{-1} for MoO_3 and MoO_2, respectively.

After full lithiation, further expansion of the potential range to 0.01 V leads to the conversion-type reaction during the first full reduction according to:

$$MoO_3 + 6\ Li^+ + 6\ e^- \rightarrow Mo + 3Li_2O, \qquad (\mathbf{6.3})$$

and for MoO_2:

$$MoO_2 + 4\ Li^+ + 4\ e^- \rightarrow Mo + 2Li_2O, \qquad (\mathbf{6.4})$$

yielding a theoretical capacity of 1117 and 832 mAh g^{-1} for the conversion reaction during the first full reduction of MoO_3 and MoO_2, respectively.[270] We highlight the corresponding processes known from literature in the cyclic voltammograms obtained in the first charge/discharge cycle for the studied materials (**Fig. S3.8**).

For direct comparison, the electrochemical behaviour of MoO_{3-x}, (i.e., partially reduced molybdenum oxide that underwent the same pyrolysis treatment, but without a carbon source, **Fig. S3.5**) was studied alongside MoO_x-C. This allowed for insights into the influence of the nanocomposite microstructure resulting from the pyrolysis treatment of MoO_x-OA on both, the electrochemical lithium intercalation and conversion reactions.

Electrochemical lithium intercalation

The galvanostatic charge-discharge profiles of MoO_x-C (**Fig. 6.17A**) show Li^+ intercalation with a sloping potential profile below ca. 2 V vs. Li^+/Li, characteristic of solid-solution intercalation without a phase transition in nanosized, monoclinic MoO_2.[183] The specific capacity of 145 mAh g^{-1} indicates the intercalation of 0.69 Li per MoO_2. We hypothesize that the full theoretical capacity of MoO_2 is not reached as a consequence of partial side product formation (Mo_2C, Mo_4O_{11}) formation, as observed by XRD (**Fig. 6.13B**). Hence, future work should focus on eliminating side product formation during pyrolysis to achieve specific capacities closer to the theoretical capacity of MoO_2. For comparison, galvanostatic profiles of MoO_{3-x} (**Fig. 6.17B**) show the characteristic plateau of Li^+ (de-)intercalation into the orthorhombic structure of MoO_3 at 2.67 V (anodic) and ca. 2.15 V (cathodic),[292] with a specific capacity of 240 mAh g^{-1}. Electrodes based on MoO_3 often fail to reach full theoretical capacity due to their limited ionic and electronic conductivities.[293]

Fig. 6.17C shows a comparison of the rate capability of MoO_x-C and MoO_{3-x} at current densities ranging from 50 mA g^{-1} to 3 A g^{-1}. Despite the higher initial capacity of MoO_{3-x}, the cycling stability is poor (decrease from 213 to 173 mAh g^{-1} after 5 cycles at 100 mA g^{-1}). The anodic capacity continues to deteriorate at high currents. Meanwhile, MoO_x-C outperforms MoO_{3-x} at high currents, retaining 41 mAh g^{-1} discharge capacity at 3 A g^{-1}, compared to the negligible 0.6 mAh g^{-1} capacity for MoO_{3-x} at the same specific current.

Fig. 6.17D shows cycling stability for the two materials cycled at a fixed specific current of 1 A g^{-1} for 1,000 cycles. MoO_x-C shows an initial anodic capacity of 110 mAh g^{-1}, which stabilizes to 82 mAh g^{-1} after 1,000 cycles, retaining ca. 75% of the initial capacity. On the other hand, MoO_{3-x} undergoes a rapid capacity decay, with the anodic capacity dropping from 155 to 39 mAh g^{-1} after 1,000 cycles, a loss of more than 74 % of the initial anodic capacity. The averaged Coulombic efficiency of MoO_{3-x}, and MoO_x-C over 1,000 cycles is 99.5 %, and 99.9 %, respectively, demonstrating the absence of significant side reactions specifically in the nanocomposite electrode MoO_x-C.

The improved rate handling behavior, as well as the improved cycling stability and Coulombic efficiency of MoO_x-C, can be attributed to two factors. First, the nanocomposite approach leads to a well-dispersed conductive carbon phase. This improves the electronic conductivity, as demonstrated by a significantly lower impedance as compared to MoO_{3-x} electrodes (**Fig. A3.6**). Second, the carbothermic reduction during the pyrolysis process in

the nanocomposite led to the formation of MoO_2, which was shown to exhibit improved cycling stability compared to MoO_3.[294]

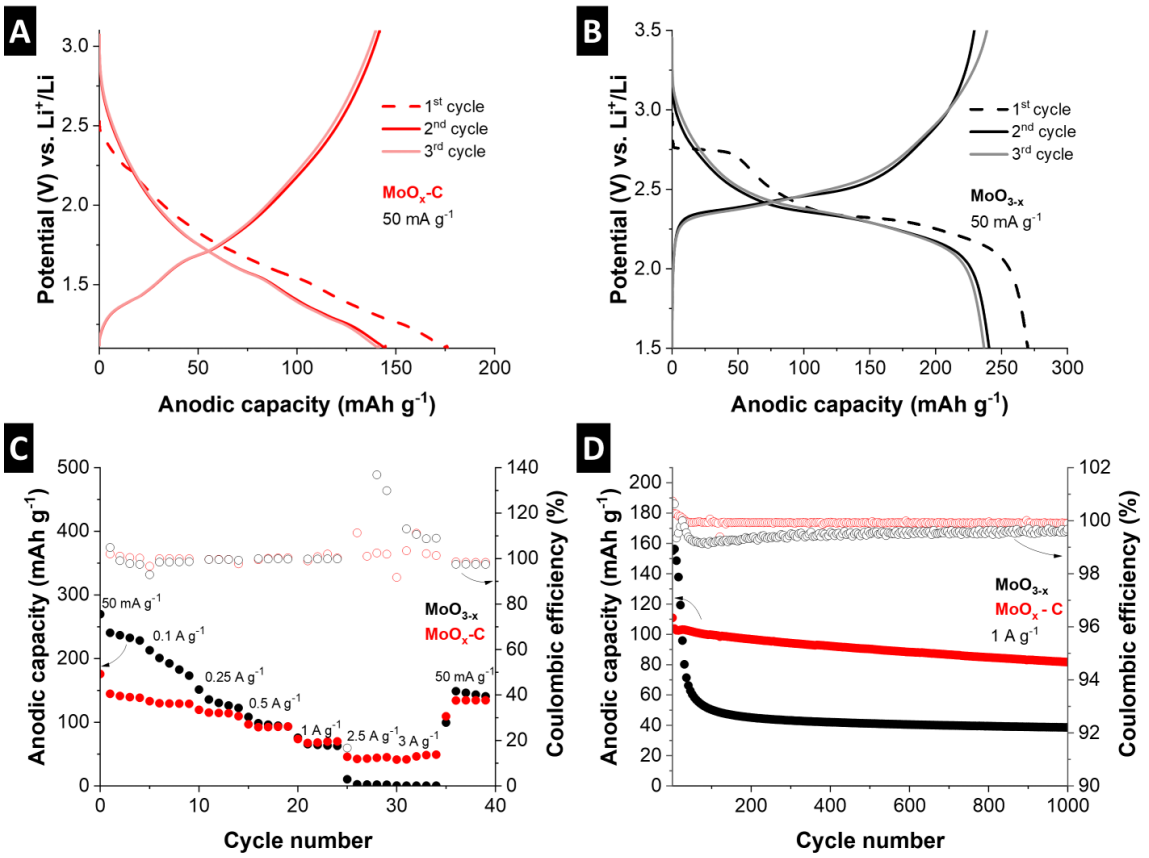

Figure 6.17: First three galvanostatic charge-discharge cycles of (A) MoO_x-C and (B) MoO_{3-x} at 50 mA g^{-1}, (C) rate capability tests at various specific current values from 50 mA g^{-1} to 3 A g^{-1}, then back to 50 mA g^{-1}, in the voltage range 1.5 V to 3.5 V for MoO_{3-x} and 1.1 V to 3.1 V for MoO_x-C , (D) cycling stability test for MoO_{3-x} and MoO_x-C at 1 A g^{-1} for 1,000 cycles.

Electrochemical conversion reaction

Electrochemical cycling of molybdenum oxides to lower cathodic potential limits can lead to an electrochemical conversion reaction, as described in equations **(6.3, 6.4)**, yielding a significant increase in the specific charge storage capacity. To evaluate the conversion reaction behavior, MoO_x-C and MoO_{3-x} were galvanostatically cycled between 0.01 V – 3 V vs. Li^+/Li. The occurrence of a conversion reactions forming Li_2O and metallic Mo during the first electrochemical reduction is indicated by the high capacity in the first cathodic cycle (**Fig. 6.18A**), according to Eq. 3. The nanocomposite MoO_x-C displays a

sloping potential profile below 1 V, whereas the MoO_{3-x} sample exhibits a flat plateau around 0.45 V (**Fig. 6.18B**). The sloping potential profile in MoO_x-C can be explained by the nanoscopic crystalline domain sizes, which can lead to a variation of the thermodynamic redox potential.[295,296] Notably, the initial Coulombic efficiency (ICE) of the nanocomposite MoO_x-C (69 %) is slightly improved compared to MoO_{3-x} (60 %). The anodic capacity in the first three cycles for MoO_x-C drops from 800 to 620 mAh g^{-1}, which indicates ~ 3 electron transfer per MoO_2 and amounts for ca. 75% of the total theoretical conversion capacity of MoO_2. For MoO_{3-x}, the anodic capacity drops from 1200 at the initial cycle to ca. 700 mAh g^{-1} at subsequent cycles, corresponding to the transfer of 3.76 Li and achieving only 63% of the theoretical conversion capacity of MoO_3.

The rate handling performance and cycling stability of the electrochemical conversion reaction in MoO_x-C and MoO_{3-x} were evaluated by galvanostatic charge-discharge at rates ranging from 50 mA g^{-1} to 3 A g^{-1} and at 100 mA g^{-1} for 100 cycles, respectively (**Fig. 6.18C-D)**. While the nanocomposite MoO_x-C outperforms the reference material, the rate handling and cycling stability performance of both materials is limited. For MoO_x-C, significant capacity fading can be observed from 768 mAh g^{-1} to 192 mAh g^{-1} after 25 cycles, where the performance stabilizes. For comparison, the capacity of MoO_{3-x} drops to 165 mAh g^{-1} after about 15 cycles. To explain the improved electrochemical conversion-type charge storage performance of the nanocomposite, the morphology of both electrodes was evaluated via postmortem SEM after 39 cycles (**Fig. S3.7**). The morphological changes of MoO_{3-x} were more severe compared to MoO_x-C.

Future work optimizing MoO_x-C nanocomposite electrodes for conversion-type reactions needs to involve a careful investigation of the electrode microstructure after the initial cathodic cycle, for example via ex situ TEM of a FIB-prepared lamella, to gain further insights on the morphological changes occurring during the electrochemical conversion reaction.

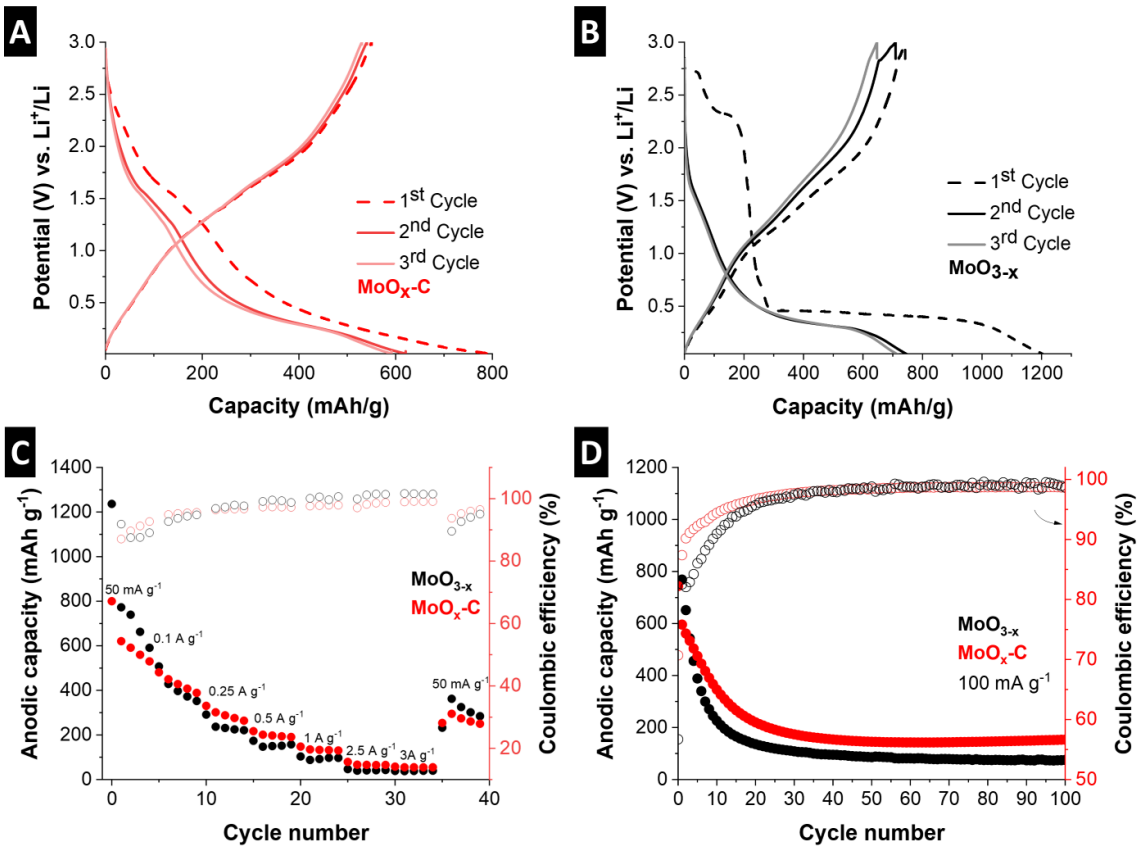

Figure 6.18: (A) Galvanostatic charge-discharge curves of MoO_x-C and (B) MoO_{3-x} at a specific current of 50 mA g^{-1} in the potential range of 0.01 V to 3 V vs. Li^+/Li, (C) rate performance of MoO_{3-x} and MoO_x-C at rates from 50 mA g^{-1} to 3 A g^{-1}, (D) stability test of MoO_{3-x} and MoO_x-C cycled at 100 mA g^{-1}.

6.3.3 Conclusion

In this work, layered molybdenum oxide with octylamine molecules assembled in its interlayer was pyrolyzed to convert the organic molecules to a carbon phase, yielding a nanocomposite MoO_x-C material. The present work set its main focus on analysing the carbon formation and microstructure evolution during pyrolysis and the precise phase distribution in the nanocomposite product.

Processes occurring during pyrolysis were examined with a combination of *in situ* XRD, TGA-MS, and TGA-FTIR experiments. It was found that during the heating step, some loosely bound molecular OA and OA decomposition products escape from the interlayer space before being converted to elemental carbon, and a strong carbothermic reduction of

the oxide takes place above 650 °C. With this knowledge, future directions towards improving the synthesis route can focus the use of more strongly bonded and/or less volatile organic molecules together with faster heating of the material during pyrolysis to obtain more localized carbon formation or a higher carbon content.

Cross-sectional specimens of the resulting MoO_x-C nanocomposite prepared via FIB were analyzed to reveal the intricate intraparticle microstructure. It was found that nanoscopic domains of MoO_2 are surrounded by a carbon phase, and in addition, trace amounts of Mo_2C and Mo_4O_{11} formation could be observed by XRD and XPS. Further tuning the synthesis temperature and time could thus be employed to avoid carbide formation (or to support carbide formation, if desirable).

The electrochemical properties of the resulting MoO_x-C nanocomposite electrode were evaluated in detail for both, intercalation-type and conversion-type charge storage in lithium-containing, organic electrolyte. The electrode significantly outperformed the MoO_{3-x} reference sample in terms of rate handling and stability for lithium intercalation and showed an increase in initial coulombic efficiency for the conversion reaction.

The work can be used as a guideline to obtain transition metal oxide/carbon nanocomposites with desired structural and electrochemical properties. It showcases pitfalls and opportunities arising from the pyrolysis route (organic molecule mobility, carbothermic reduction, carbide formation, etc.) which should be considered in future works.

6.3.4 Supporting information

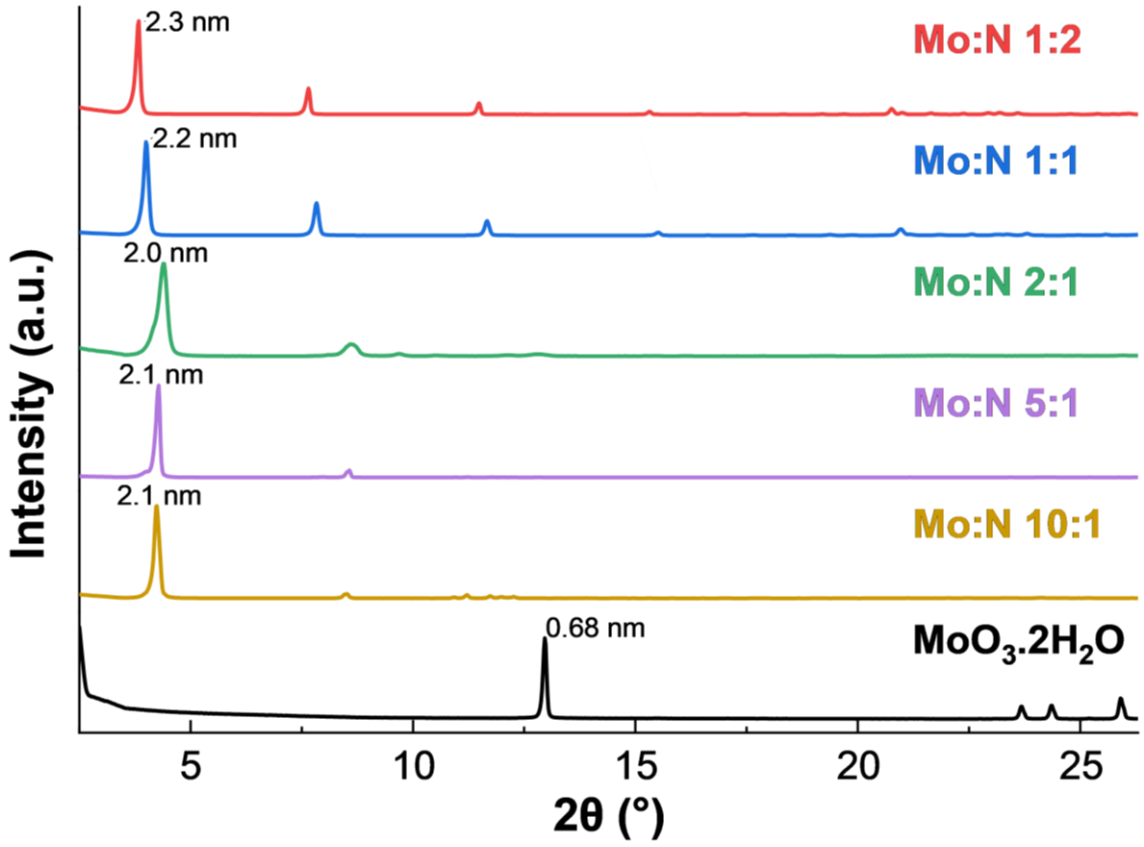

Fig. S3.1: XRD patterns of MoO_x-OA samples that were synthesized using various ratios of molybdenum oxide to octylamine.

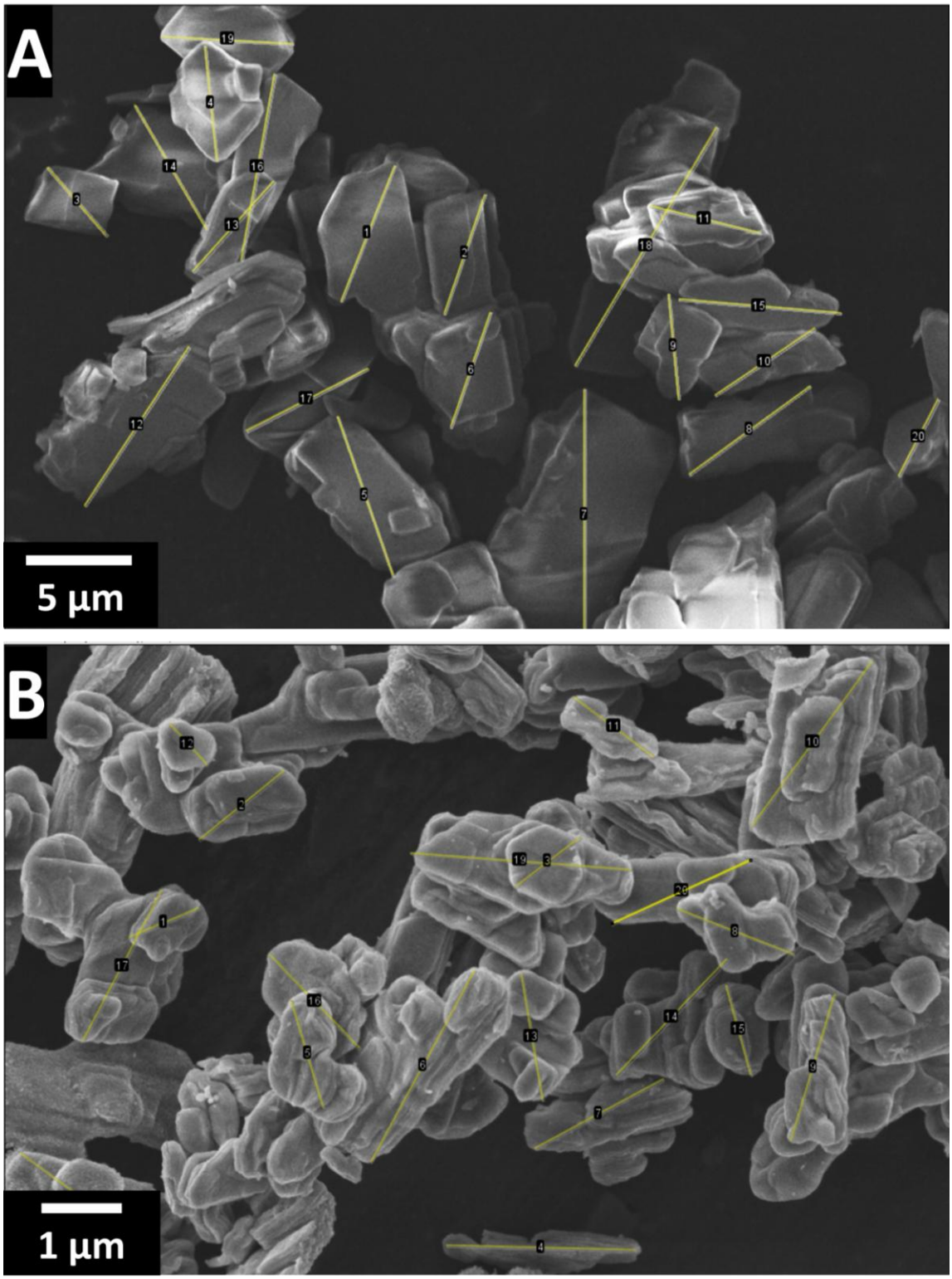

Fig. S3.2: SEM images used for the calculation of the average particle size of (A) MoO_x-OA and (B) MoO_x-C. A total of 20 particles were measured in each case.

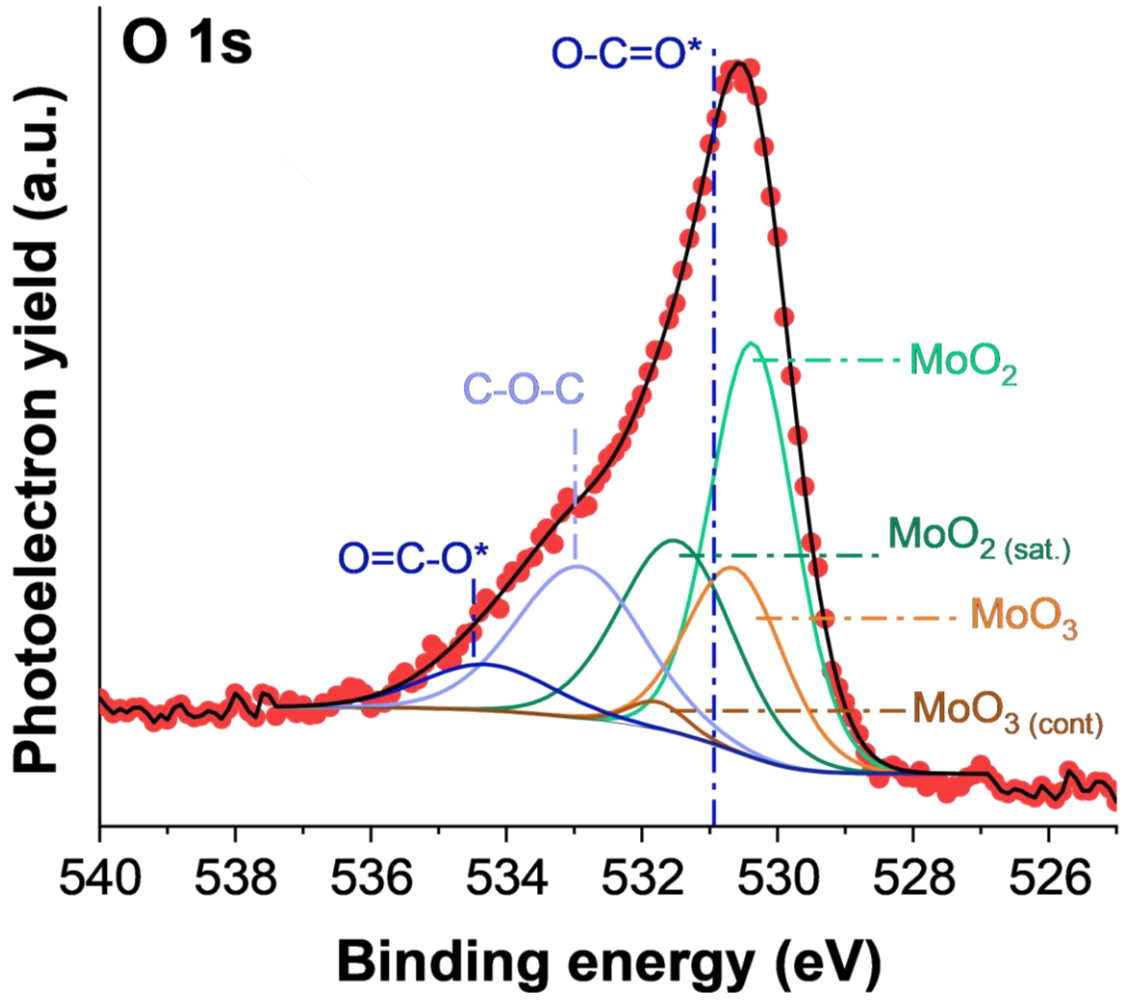

Fig. S3.3: O 1s XPS spectrum of pristine powder MoO_x-C, showing Mo(IV) oxide, Mo(VI) oxide, and carbon/oxygen species.[283,297]

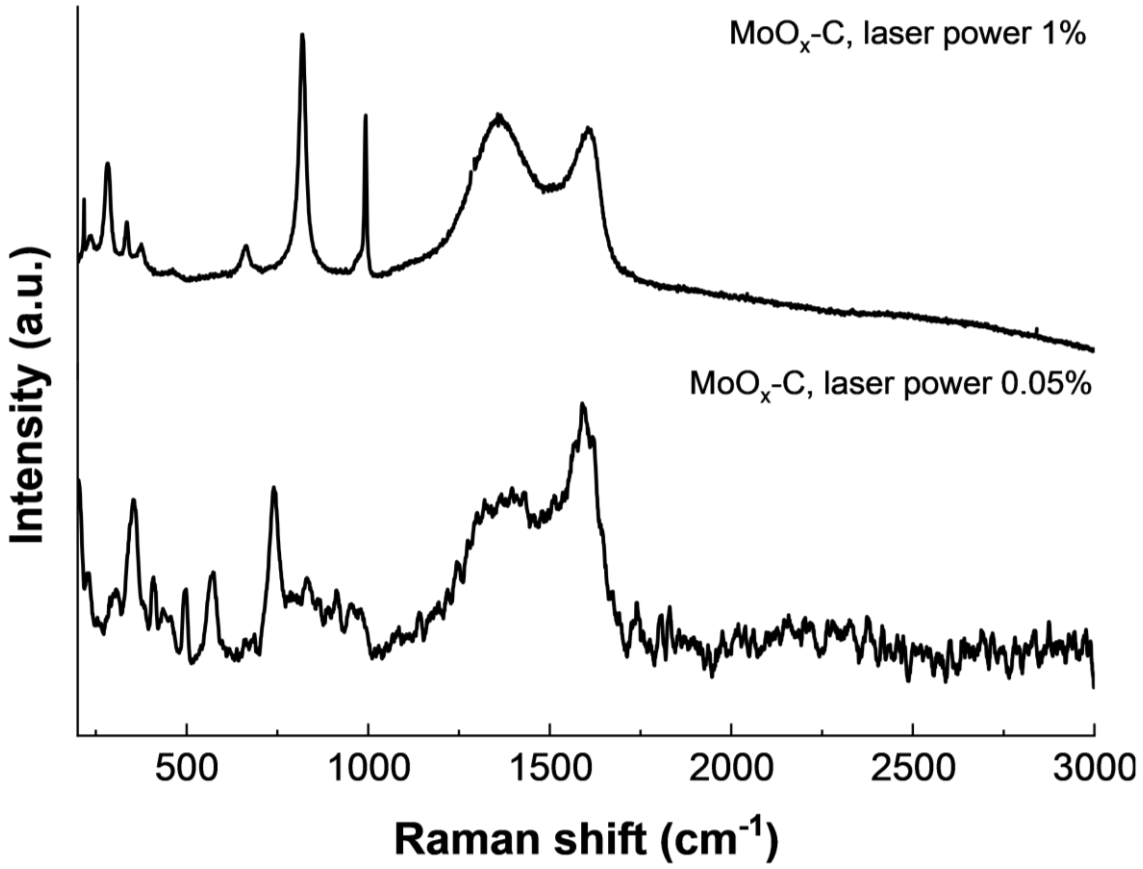

Fig. S3.4: Raman spectra of MoO_x-C acquired at 1 % (5 mW) and 0.05 % (0.25 mW) laser power, demonstrating the transformation from MoO_2 to MoO_3 signals at higher laser power.

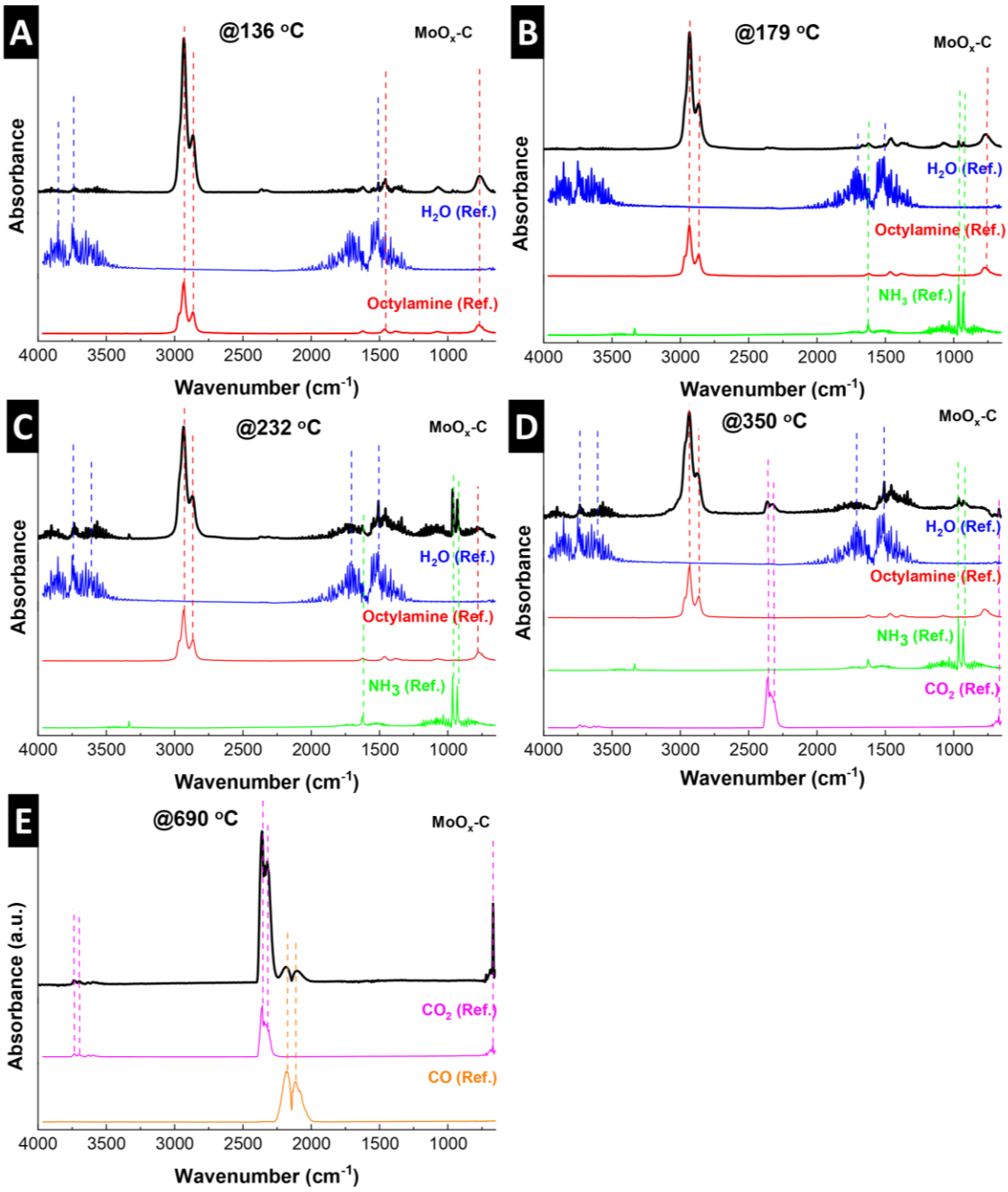

Fig. S3.5: FTIR spectra of the evolving gasses during pyrolysis in the TGA at selected temperatures, compared to typical referenced spectra of assigned molecules according to Ref.[298]

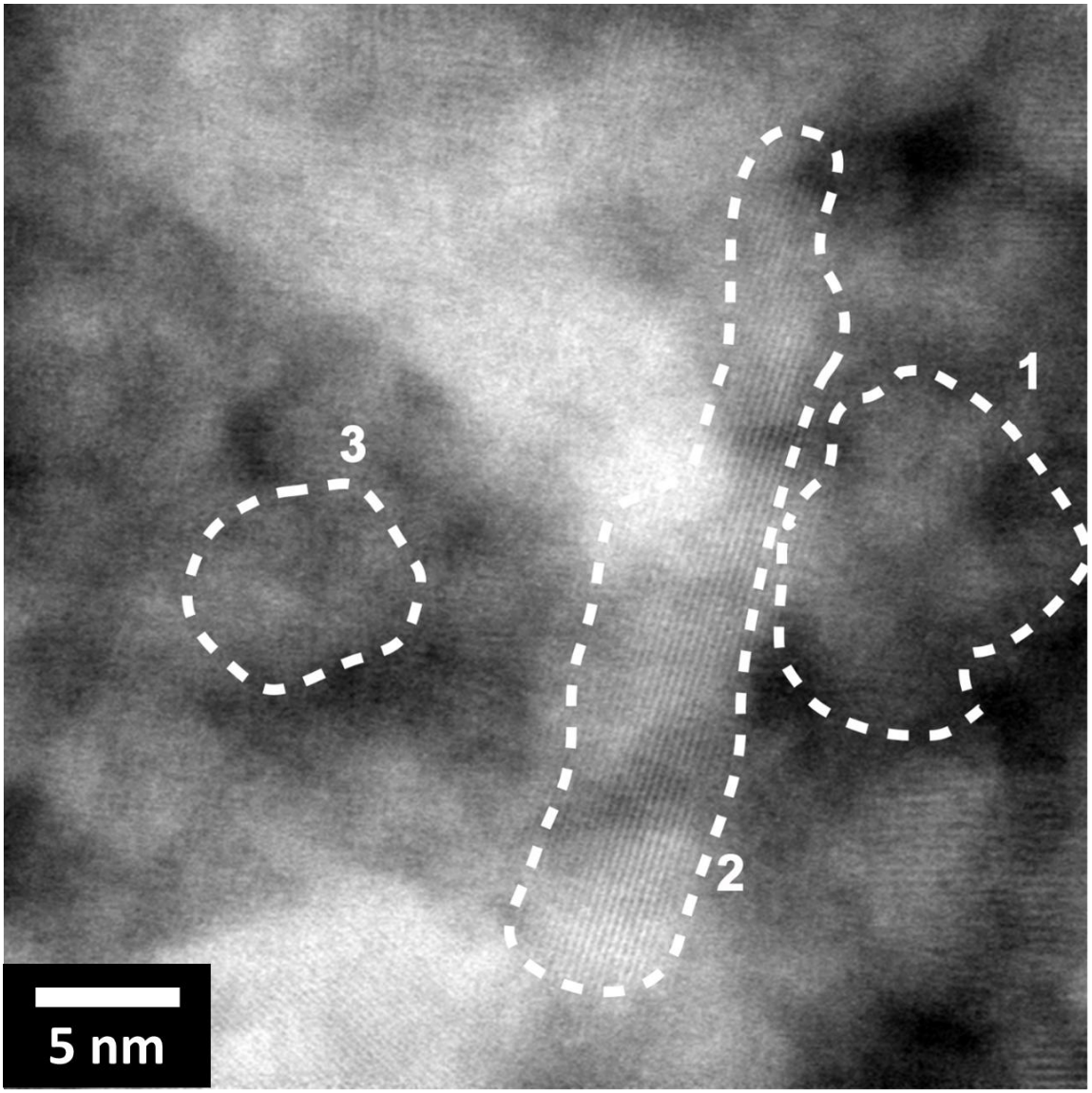

Fig. S3.6: HAADF-STEM of MoO_x-C, corresponding to bright field image shown in Fig. 6.16C. The nanocrystalline domains are highlighted in regions 1, 2, and 3.

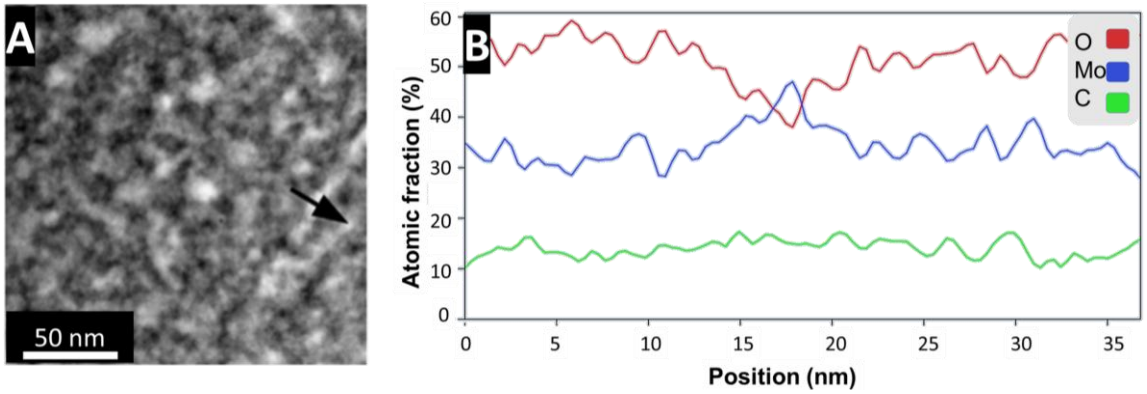

Fig. S3.7: A) STEM-HAADF image of MoO_x-C, B) EDS elemental profiles of O, Mo, and C across the arrow displayed in panel A. Since STEM-EDS is a semi-quantitative method due to peak overlap, chamber contamination, and X-rays emitted from the grid and sample holder, EDS line scanning was chosen instead of showing a discrete EDS spectrum at a specific location.

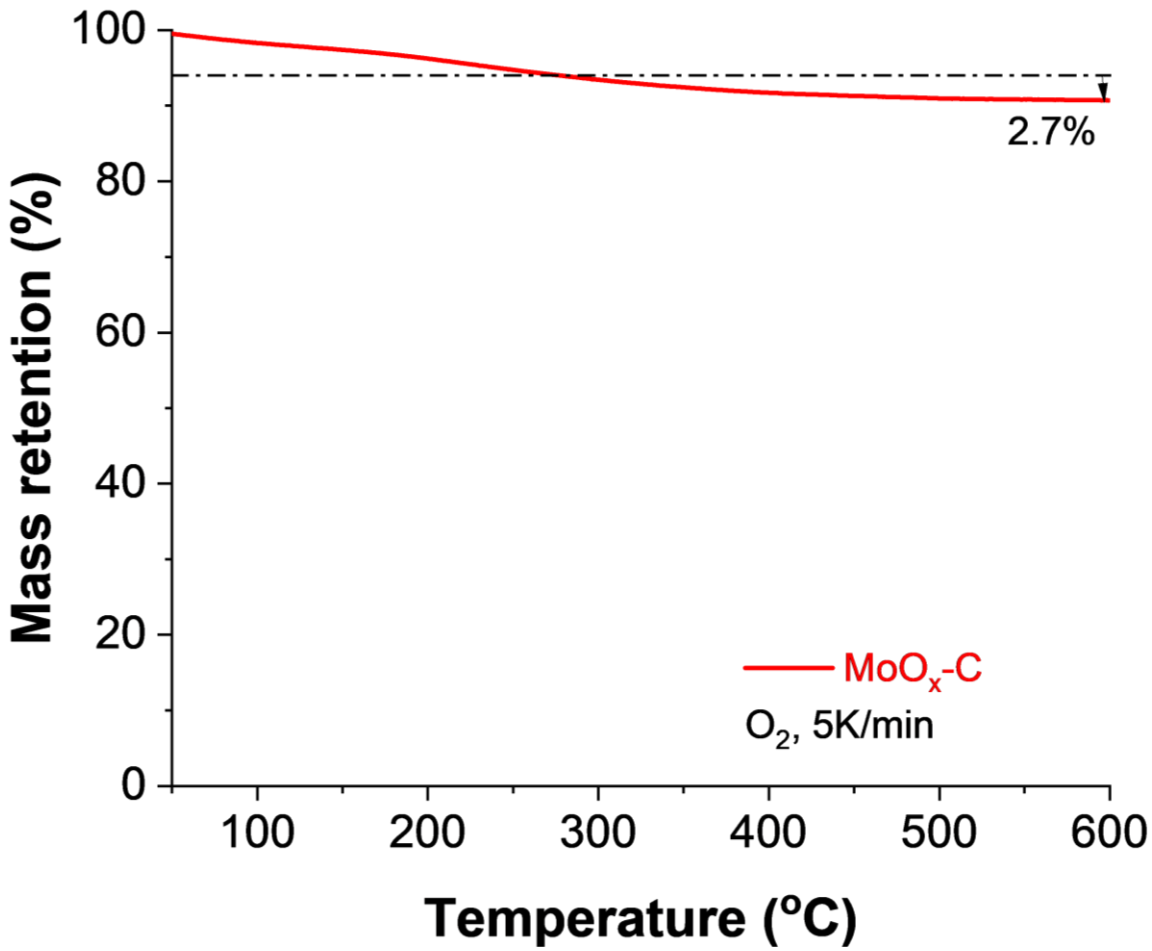

Figure S3.8: TGA of MoO_x-C heating in oxygen atmosphere. Start temperature for mass loss calculation was set to 300°C, since amorphous carbons start to burn off at ca. 320°C.[299]

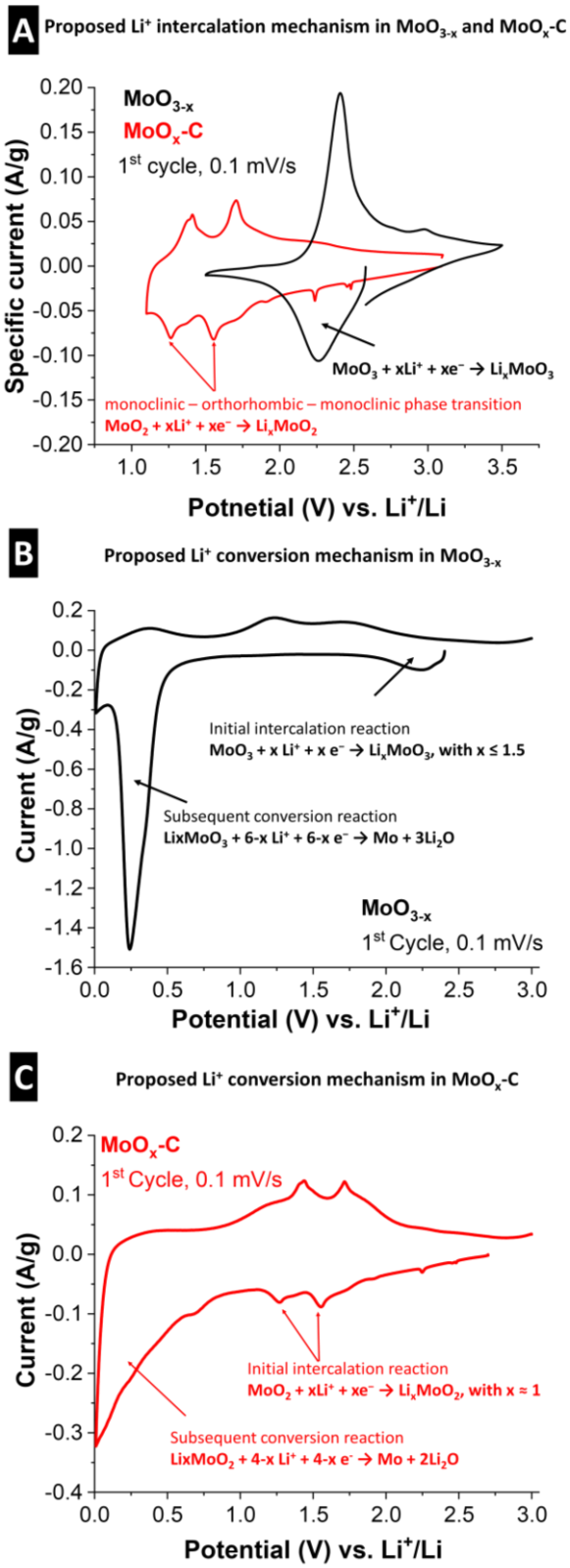

Fig. S3.9: Cyclic voltammograms of MoO_{3-x} and MoO_x-C in the respective first cycle. (A) Within the lithium intercalation potential range and to extended negative potential of 0.01 V vs. Li^+/Li for (B) MoO_{3-x} and (C) MoO_x-C. The charge storage reactions for Li^+ intercalation and conversion reactions are annotated on the graphs.

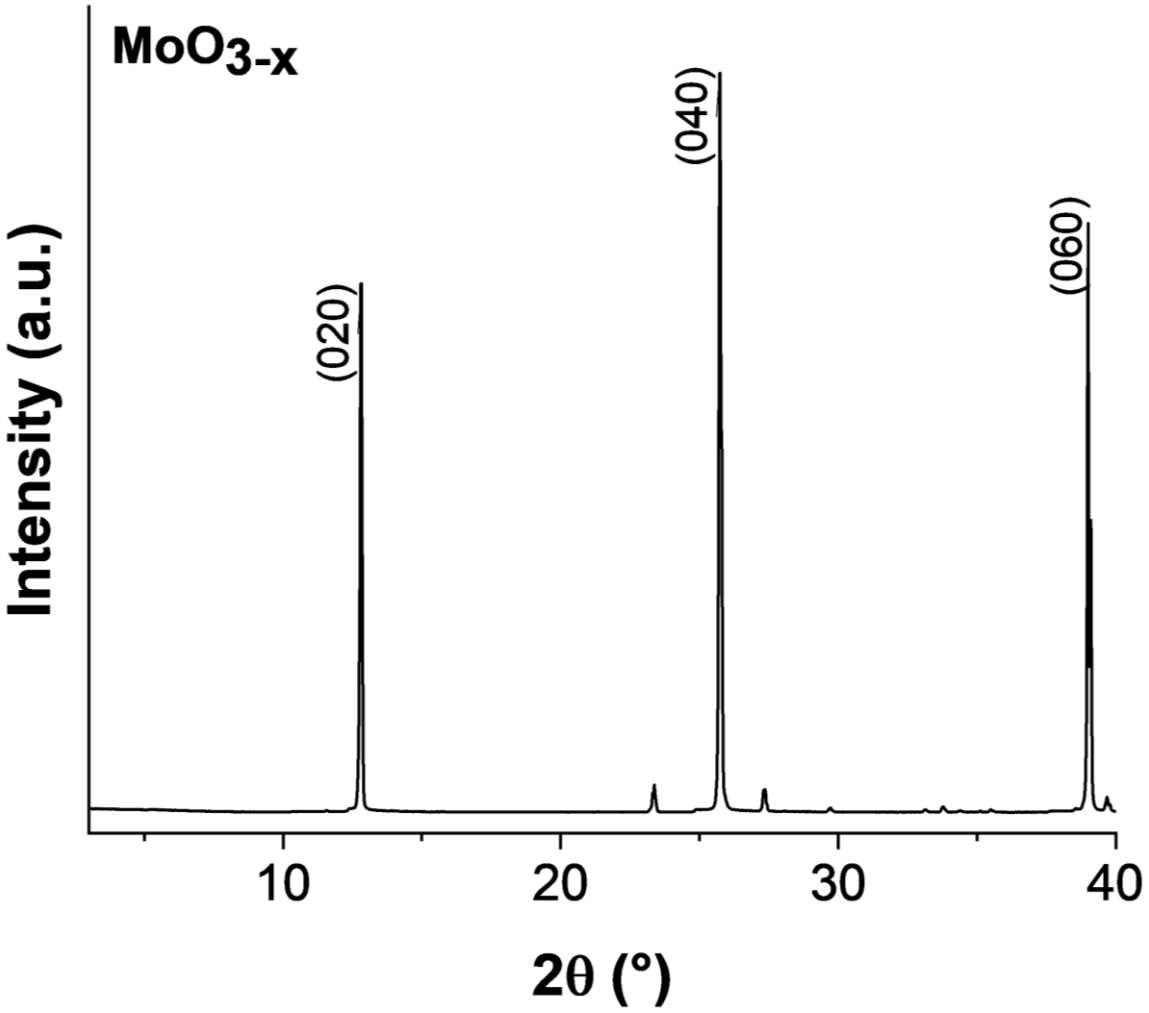

Fig. S3.10: XRD pattern of the as-synthesized reduced MoO_3, labelled in this work as MoO_{3-x}. The sharp (020), (040) and (060) diffraction peaks indicate preferred orientation along [0k0] direction, as described in ref. [300]

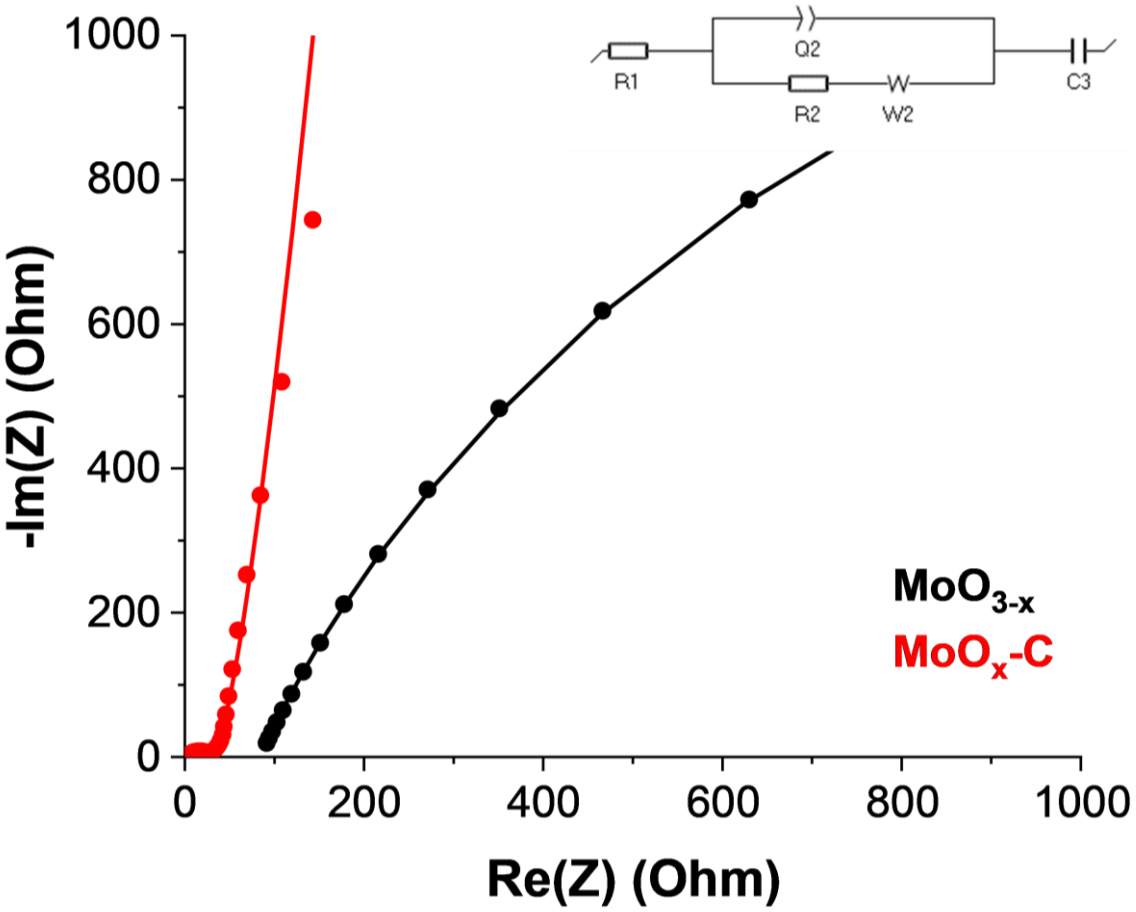

Fig. S3.11: Electrochemical impedance spectra of MoO_{3-x} and MoO_x-C performed at OCV. Solid lines represent the fitted curves obtained by the equivalent circuit in the inset, where R1 is the combined series resistance consisting of the ionic resistance of the electrolyte, the resistance of the active material, and the contact resistance at the electrode/current collector interface,[301] R2 is the charge transfer resistance, Q2 is the constant phase element (used to describe non-ideal capacitive behaviour from double-layer processes), W is the Warburg element (used to describe ion diffusion), and Q3 is the capacitance by faradaic processes, also referred to as limit capacitance.[302]

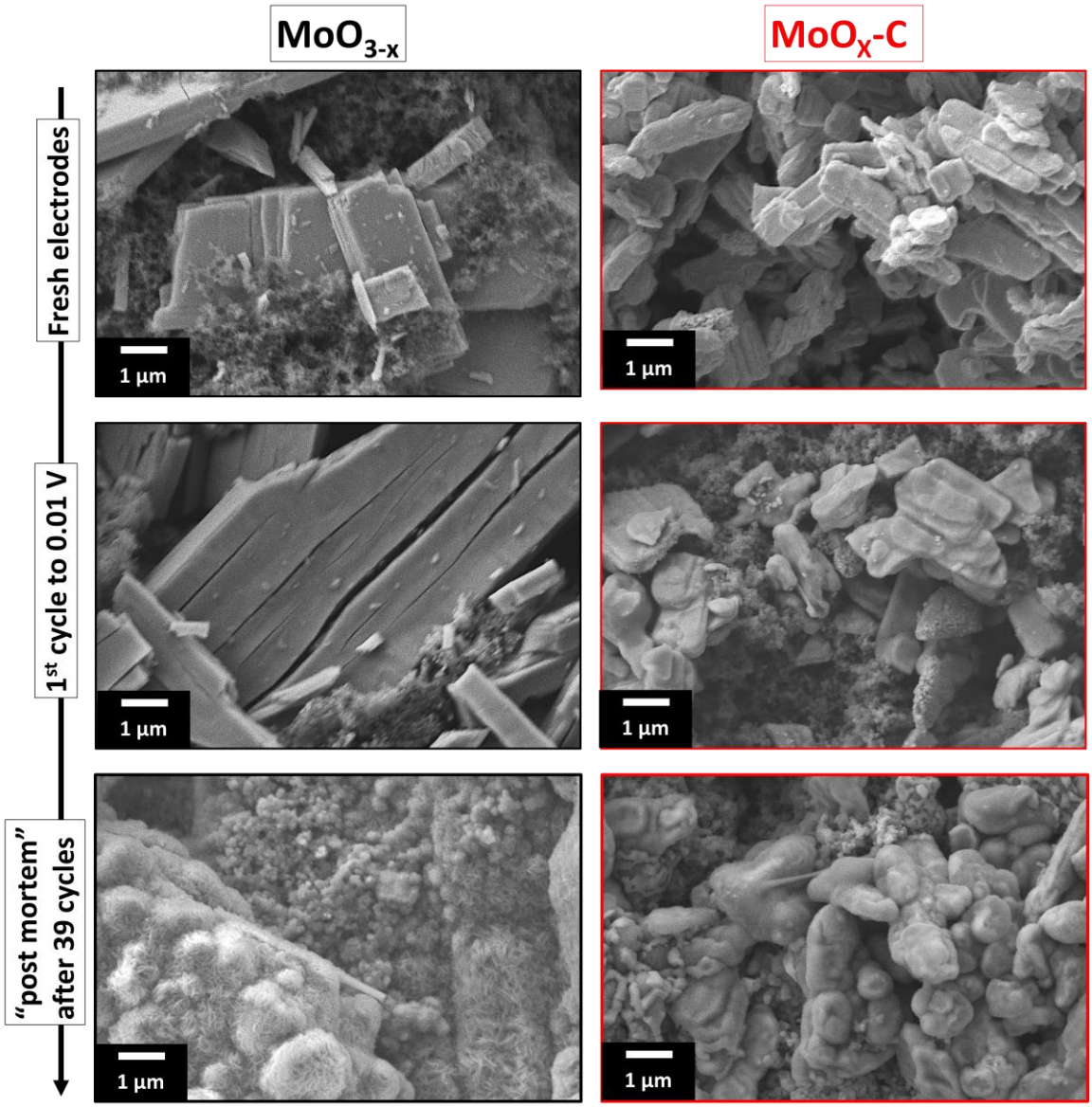

Fig. S3.12: SEM images of the pristine MoO_{3-x} (left column) and MoO_x-C (right column) electrodes (top), and ex situ SEM after the first electrochemical reduction to 0.01 V vs. Li^+/Li (center) and after galvanostatic cycling over 39 cycles (bottom).

7. Summary and Conclusions

In summary, this dissertation focuses on leveraging nanoconfinement modifications in layered electrode materials to address two critical challenges: sluggish ion transport and poor electrical conductivity. Interlayer nanoconfinement environment was modified in layered electrodes by incorporating organic pillar molecules, specifically *n*-alkylamines, via facile synthesis methods, effectively creating interlayer-expanded, pillared structures based on two types of materials: hydrogen titanates ($H_2Ti_4O_9$) and molybdenum oxide (MoO_x).

Firstly, this work addresses ion transport limitations in layered titanates. In our study of layered titanates ($H_2Ti_4O_9$) in Li-ion cells, we demonstrated that interlayer functionalization with a short-chain, non-cross-linking monoamine promotes ion-solvent cointercalation. By expanding the interlayer gap, Li-ions can intercalate along with (portions of) their solvation sheath, resulting in a reduced charge transfer resistance for intercalation. The ion-solvent cointercalation phenomenon enhances high rate capability and enables cycling at low temperatures. To confirm the cointercalation of solvent molecules during lithiation, we employed a comprehensive array of experimental techniques, including *operando* XRD, ECD, EQCM, *ex situ* FTIR, and EIS. These methods collectively validated the ion-solvent cointercalation mechanism in pillared layered titanates.

The effects of nanoconfinement manipulation with organic interlayer pillars are not only observed in Li-ion systems, but also in Na-ion systems, where the development of suitable intercalation anode materials remains a challenge. Examining pillared titanate electrodes in Na-ion cells shows enhanced electrochemical properties. While the unmodified titanate electrode shows distinct peaks on the CV and plateaux on the voltage profiles, the pillared titanate shows a sloping voltage profile, with a higher capacity, an enhanced initial coulombic efficiency, and a higher apparent Na-ion diffusion coefficient. ECD results indicated a greater expansion of the pillared electrode compared to the pristine one during sodiation, suggesting the possible insertion of solvated Na^+ ions, similar to the behaviour observed in Li-ion intercalation in pillared HTO. These finding highlight the potential of interlayer functionalization to improve the intercalation kinetics in Na-ion batteries.

Secondly, the dissertation addresses the challenge of limited electrical conductivity in transition metal oxide electrodes. The incorporation of organic pillar molecules (e.g., octylamine) within layered hosts such as MoO_x provides a pathway to introduce carbon into the microstructure via pyrolysis. The resulting material is a nanocomposite, where a carbon phase is confined among the nanodomains of the oxide phase. This nanocomposite exhibited enhanced electrical conductivity, improved rate capability during intercalation reactions, and higher coulombic efficiency in conversion reactions. A detailed mechanistic study was conducted to understand the formation steps of the metal oxide–carbon nanocomposite. During pyrolysis, loosely attached organic pillar molecules are expelled from the structure, and the others are converted to carbon at elevated temperatures. As the temperature increases, carbon may leave the structure as CO or CO_2, simultaneously reducing the oxide matrix. This study elucidates the microstructure evolution during the pyrolysis process in pillared metal oxides, providing a foundation for future research on the intentional design of metal oxide–carbon nanocomposites by targeting specific pyrolysis parameters.

In conclusion, this dissertation lays a foundation for future research on modifying nanoconfinement conditions in layered electrodes, by demonstrating the versatility and effectiveness of interlayer functionalization with organic pillars in optimizing layered electrode materials for energy storage. By showcasing the ability of interlayer functionalization to enhance ion transport, facilitate ion-solvent cointercalation, and improve electrical conductivity through subsequent pyrolysis, this work opens new avenues for exploring electrode nanoconfinement design strategies across a broader range of materials and electrochemical systems. The findings on ion-solvent cointercalation provide a novel perspective on designing electrodes for Li-ion and Na-ion systems, with the potential to expand to other energy storage mechanisms beyond bare ion intercalation. Additionally, the insights gained from the mechanistic study of metal oxide–carbon nanocomposites formation offer a framework for further investigation into the precise control of microstructure during nanocomposite material synthesis. Future research can build on these results by exploring different types of organic pillars, layered host structures, and pyrolysis processes to fine-tune the electrochemical performance of materials, driving advances in high-power, low-temperature, and high-capacity energy storage devices.

List of Abbreviations

2D	two-dimensional
AB	aminobenzene
AC	alternating current
AFM	atomic force microscopy
AQ	aminoquinone
ATR	Attenuated Total Reflection
BA	butylamine
BDA	butane-1,4-diamine
BQ-Al_x	benzoquinone-coordinated Al ions
CAES	compressed air energy storage
CE	counter electrode
CHDA	*1,4*-cyclohexane diamine
CIF	crystallographic information file
Cryo-TEM	cryogenic electron microscopy
CV	cyclic voltammetry
DDA	dodecylamine
DFT	Density function theory
DMC	dimethyl carbonate
DMF	*n,n*-dimethylformamide
DMSO	dimethyl sulfoxide
dTG	derivative thermogravimetry
EA148	ether diamine
EC	ethylene carbonate
ECD	electrochemical dilatometry
EDA	ethylene diamine
EDA-VO	ethylenediamine-functionalized vanadium oxide
EDX	energy dispersive X-ray
EIS	electrochemical impedance spectroscopy
EQCM	electrochemical quartz crystal microbalance
EVs	electric vehicles
FT	fourier transform

GCD	galvanostatic charge and discharge
GITT	galvanostatic intermittent titration technique
GO	graphene oxide
HDA	hexadecylamine
HDA	hexane-1,6-diamine
HM	hydrazine monohydrate
HOPG	highly oriented pyrolytic graphite
HQ	hydroquinone
HRTEM	high resolution transition electron microscopy
HTO	$H_2Ti_4O_9 \cdot H_2O$
HTO-HDA	hexanediamine-pillared $H_2Ti_4O_9$
HTO-PA	propylamine-pillared $H_2Ti_4O_9$
HVO	hydrated vanadium oxide
ICP	inductively coupled plasma
IPA	Isoproplyamine
IR	infrared
KTO	$K_2Ti_4O_9$
LDHs	layered double hydroxides
LIB	lithium-ion battery
LLOs	lithium-rich layered oxides
LP30	1M $LiPF_6$ in 1:1 vol% EC:DMC
MD	molecular dynamics
MS	mass spectrometry
MXLLC	liquid crystal MXene
NB	nitrobenzene
NCO	$Na_{0.71}CoO_2$
NIBs	sodium-ion battery
NMC622	$LiNi_{0.6}Mn_{0.2}Co_{0.2}O_2$
NMP	*n*-methyl-2-pyrrolidone
OA	octylamine
OCP	open circuit potential
OCV	open circuit voltage
OES	optical emission spectrometer

PA	propylamine
PANI	polyaniline
PDF	powder diffraction file
PEDOT	poly(3,4-ethylenedioxythiophene)
PEO	poly (ethylene oxide)
PPY	polypyrrole
PSA	pyridinesulfonic acid
PTFE	polytetrafluoroethylene
PVdF	polyvinyl fluoride
PY	pyrrole
RE	reference electrode
rGO	reduced graphene oxide
SAED	selected area electron diffraction
SAXS	small-angle X-ray scattering
SEI	solid electrolyte interface
SEM	scanning electron microscopy
SMES	superconductive magnetic energy storage
SPE	solid polymer electrolyte
SPEIS	staircase potential electrochemical impedance spectroscopy
TEM	transmission electron microscopy
TGA	thermogravimetric analysis
TMA^+	tetramethyl ammonium
TMD	transition metal dichalcogenides
TMO	transition metal oxide
Tris	tris(2-aminoethyl) amine
WE	working electrode
XPS	X-ray photoelectron spectroscopy
XRD	X-ray diffraction

List of Figures

Figure 1.1: Global surface air temperature anomalies from January 1940 to November 2023, with reference to the 1850-1900 (pre-industrial period). Data from the European Centre for Medium-Range Weather Forecasts (ECMWF), Copernicus Climate Change Service (2023)……...8

Figure 1.2: Ragone plot showing the status of power vs. energy densities of various electrochemical energy storage systems. The arrows depict the trend towards higher specific power for batteries and higher specific energy for electrochemical capacitors. Diagonal lines represent the time constant (operation time). Reproduced from Ref.[4] with permission, copyright © 2020, Springer Nature Limited.....9

Figure 2.1: Schematic illustration of the cell setup of a lithium-ion battery……..13

Figure 2.2: Exemplary energetic profile of a transition state for an intercalant during the charge transfer step, which is reduced for cointercalation. Schematic representation of a multi-step electrochemical (co-) intercalation process. In this process, solvated ions first transport through the liquid electrolyte towards the electrochemical interface, where ions either (partially) retain their solvation sheath (cointercalation) or shed it during the charge transfer step. The ions finally diffuse through the solid-state host to occupy a vacant lattice site. Reproduced with permission from Ref.[14,15] © The Royal Society of Chemistry 2024.15

Figure 2.3: Average voltages and specific capacities of anode materials for NIBs. Reproduced from Ref.[29] with permission from the Royal Society of Chemistry……..….17

Figure 2.4: Nanoconfinement effects in layered titanates……..19

Figure 2.5: Schematic illustration of the main topics discussed in this section, covering pillared layered electrode structures and host-pillar interactions. New properties arising from the functionalization of the layered structures with organic molecules are highlighted, and characterization methods specific to them are discussed…….....21

Figure 2.6: A) Structures of common layered TMD electrode materials. Illustrated using VESTA software with CIF data from the Materials Project.[85] B) Schematic illustrations of functionalization at the chalcogen vacancies and amide functionalization, reproduced from

Ref.[79,86] with permission from Springer Nature Limited and Creative Commons public use license. C) Functionalization by a pre-lithiation step, adapted from Ref.[87] with permission from Wiley-VCH Verlag GmbH & Co. KGaA, Weinheim. D) *in situ* pillaring of TiS_2 by electrolyte additive, adapted with permission from Ref.[78] E) TMD functionalization with a dual functionality thiol, reproduced with permission from Ref.[82] Copyright © 2015 American Chemical Society. F) Schematic of possible thiol-MoS_2 interactions…….24

Figure 2.7: Covalent pillaring of layered carbon materials. A) Illustrations of carbon materials used in energy storage, drawn using VESTA. GO illustration was reproduced with permission from Ref.[98] Copyright © 2022, American Chemical Society. B) Schematic illustration of graphene functionalization yielding stacked Janus graphene film. Reproduced from Ref.[92] with permission from AAAS. C) XRD patterns of GO-amine compounds and D) *d*-spacing values of amine-GO and amine-rGO pillared compounds (i.e., before and after the reduction of GO). Reproduced from Ref.[93] with permission from Elsevier Ltd…….....26

Figure 2.8: Ionic interactions in pillared TMDs. A) Schematic of electrochemical functionalization of TiS_2 by hexylammonium ions. Reproduced from ref.[99] with permission from Springer Nature Limited. B) Chemical structures of key functional groups in redox-active organic molecules. C) Schematic of ferrocene-functionalized MoS_2 and D) XRD patterns of MoS_2 functionalized with ferrocene (Cp_2Fe), 1,1′-dimethylferrocene ($(MeCp)_2Fe$), and decamethylferrocene ($(Me_5Cp)_2Fe$). The interlayer spacing expands to various extents depending on the identity of the metallocene. Reproduced with permission from Ref.[104] Copyright © 2022, American Chemical Society…….28

Figure 2.9: A) Structures of common layered TMOs, drawn with VESTA© software, CIF data from the Materials Project.[85] B) Structures of several subclasses of amines. C) Powder XRD patterns, and D) SEM images of alkylamine-pillared MoO_3. PA: propylamine, BA: butylamine, OA: octylamine, DDA: dodecylamine, and HDA: hexadecylamine. Reproduced with permission from Ref.[113] Copyright © 2006, American Chemical Society. E) Schematics of alkylammonium ion arrangements in the interlayer of silicates, reproduced with permission from Ref.[114] Copyright © 2006, © 1997 The Chemical Society of Japan. F) Schematic of bottom-up hydrothermal synthesis of BQ-Al_x-pillared MnO_2, reproduced with permission from ref.[116] © 2024 Wiley-VCH GmbH. G) Tetramethyl

ammonium (TMA^+) interlayer functionalization of $KMnO_2$ by protonation and subsequent ion-exchange. Adapted with permission from ref.[119] © 2019 Elsevier B.V…….31

Figure 2.10: A) Structures of some MXenes, drawn with VESTA software, CIF files provided by the Materials Project. Surface terminations not shown. B) Schematic illustration of ion transport in horizontally (left) and vertically (right) aligned $Ti_3C_2T_x$ MXenes. Vertical alignment allows for shorter diffusion paths and therefore fast kinetics. C) Small-angle X-ray scattering (SAXS) measurements of the functionalized (liquid crystal) MXenes (MXLLC) and the hydrogen-bonded pillar molecule $C_{12}E_6$. The scattering vector *q* of the (100) peak is 0.108 Å, from which the *d*-spacing is calculated to be ca. 5.8 nm. Reproduced with permission from Ref.[130] Copyright © 2018, Macmillan Publishers Ltd. D) Schematic of 6 molecules insertion into MXene (IPA: isoproplyamine; HQ: hydroquinone; NMP: N-methyl-2-pyrrolidone; PY: pyrrole; PPY: polypyrrole; and TMA: tetramethylammonium) and E) Dependence of average interlayer distance on the number and type of pillar molecules. Adapted with permission from Ref.[131] Copyright © 2023, American Chemical Society F) Structures of some amides. G) Amide functionalization by hydrogen bond formation in LDH. Reproduced with permission from Ref.[133] © 2017 Elsevier B.V…….34

Figure 2.11: A) Examples of alcohols, B) Illustration of a two-step insertion of alcohols in layered titanoniobates. Reproduced with permission from Ref.[141] Copyright © 2017, American Chemical Society. C) Schematic of covalent and non-covalent functionalization routes of MXenes with aminoquinone (AQ). Adapted with permission from Ref.[143] Copyright © 2020, American Chemical Society. D) Left: Illustration of Li_xMoS_2 functionalized with a crown ether, 15C5. Reproduced with permission from Ref.[145] Copyright © 1996 Sociedade Brasileira de Química. Right: Illustration of azacrown insertion in metal sulfide MS_2. Adapted with permission from ref.[147] Royal Society of Chemistry. E) Modes of non-covalent interactions in pillared layered carbons. Reproduced with permission from Ref.[148] Copyright © 2015 American Chemical Society.....36

Figure 2.12: A) Structures of common polymers used as pillars in layered materials. B) Proposed conformations of PEO in layered hosts, reproduced with permission from Ref.[154,155,172] Copyright © 1991, American Chemical Society, Copyright © 1993 Verlag GmbH & Co. KGaA, Weinheim, Copyright © 1993 Verlag GmbH & Co. KGaA, Weinheim. C) Schematic illustration of *in situ* PANI polymerization in V_2O_5 leading to the

expanded hybrid PVO, reproduced with permission from Ref.[166] Copyright © 2021, American Chemical Society……...41

Figure 2.13: A) DFT modelling of Na^+ intercalation in AB-functionalized graphene at different configurations. The relative energy is indicated with respect to the most stable position. B) Raman shift of G band position during Na^+ intercalation for highly oriented pyrolytic graphite (HOPG), graphene, and AB graphene. The G band shift in AB graphene is indicative of Na^+ intercalation. Reproduced from Ref.[92] with permission from AAAS. C) Galvanostatic cycling of EDA-VO electrode against Zn^{2+}/Zn. Insets: structure of EDA-VO and the corresponding dQ/dV curve. Adapted with permission from Ref.[57] © 2021 Wiley-VCH GmbH. D) Cyclic voltammograms (CVs) of restacked MoS_2 (black) and ferrocene-functionalized MoS_2 (red). Dashed lines represent the Au substrate to account for background current. E) CVs of ferrocene-functionalized MoS_2 in 0.5 M Li_2SO_4 (blue), Na_2SO_4 (purple), and K_2SO_4 (red). F) CVs of ferrocene-intercalated MoS_2 in 0.5 M K_2SO_4 (blue) and in 0.5 M K_2SO_4 with 2 equivalents of 18-crown-6 (red). Reproduced with permission from Ref.[104] Copyright © 2022, American Chemical Society……..43

Figure 2.14: Modifications of ion transport kinetics in layered materials. A) Zn-ion diffusion coefficient in PVO and HVO, B) Nyquist plots of PVO and HVO and 1st and 10th cycles. Reproduced with permission from Ref.[63] © 2020 WILEY-VCH Verlag GmbH & Co. KGaA, Weinheim. C) Calculated binding energy for Zn ion intercalated in V_2O_5 and PANI-V_2O_5 and the corresponding differential charge density illustrations. Yellow and cyan regions represent charge accumulation and depletion. Adapted with permission from Ref.[63] © 2020 WILEY-VCH Verlag GmbH & Co. KGaA, Weinheim. D) Capacitance of chemically reduced GO (CrGO) and thiol-functionalized GO (rGOSH) at different current densities in Zn-ion system. Reproduced with permission from Ref.[174] E) cycling of BQ-Al_x-MnO_2 (pink), compared to Al-MnO_2 (blue) and BQ (green), in Al-ion cell vs. $Zn_{0.5}Al_{0.5}$ anode. Reproduced with permission from Ref.[116] © 2024 Wiley-VCH GmbH. F) CVs of horizontally aligned (6 um and 35 um filtration) $Ti_3C_2T_x$, showing thickness-dependent capacitance, and MXLLC of two different thicknesses showing superior and thickness-independent capacitance. Reproduced with permission from Ref.[130] Copyright © 2018, Macmillan Publishers Ltd. G) Evolution of quasi-equilibrium potential at various states of lithiation in Li_xMoS_2-12C4, as compared to PEO- and Li- MoS_2. Reproduced with permission from Ref.[176] Copyright © 2007 Elsevier Ltd. H) Diffusion coefficient of TiS_2-

diaza-15C5 compared to pristine TiS_2 at different stages of lithiation. Reproduced from Ref.[147] with permission from the Royal Society of Chemistry……....46

Figure 2.15: A) Structural evolution during cycling of PANI-V_2O_5: Interlayer distance *d* estimated from the (001) diffraction peak (blue) and an additional peak (001)* appearing at lower voltages (red). Reproduced with permission from Ref.[63] © 2020 WILEY-VCH Verlag GmbH & Co. KGaA, Weinheim. B) Pillaring prevents restacking of graphene layers. C) I-V curves of functionalized and pristine V_2O_5 showing higher electronic conductivity due to enhanced mixed valence in Pyridene-V_2O_5. Adapted with permission from Ref.[179] © 2019 WILEY-VCH Verlag GmbH & Co. KGaA, Weinheim. D) Carbon-to-oxygen ratio and resistivity vales for (left to right): ethylenediamine, 2,6-diaminoanthraquinone, and 1,4-phenylenediamine- functionalized GO. Adapted with permission from Ref.[94] © 2022 Elsevier Inc. E) Structures of expanded vanadium oxide (EVO) and PEDOT-functionalized vanadium oxide (VOP) and the corresponding calculated density of state. Adapted with permission from Ref.[170] © 2021 Wiley-VCH GmbH. F) Contact angle measurements for AB, NB- functionalized, and pristine graphene. Reproduced from Ref.[92] with permission from AAAS……....49

Figure 2.16: A) Capacity retention of PANI and MoS_2-PANI. Reproduced with permission from Ref. [164] Copyright © 2014 Elsevier B.V. B) Electrical conductivity of PANI and PANI-based composite electrodes. Reproduced with permission from ref.[149] Copyright © 1993 Verlag GmbH & Co. KGaA, Weinheim…….51

Figure 2.17: Opportunities and challenges of interlayer functionalization of layered materials…….52

Figure 2.18: Schematic of nanocomposite formation from the pyrolysis of as pillared TMO precursor…….54

Figure 3.1: Overview of the objectives of this dissertation, aimed at addressing challenges related to layered electrode materials……..56

Figure 4.1: Schematic representation of Bragg diffraction……...…….57

Figure 4.2: Components of a coin cell designed for *in situ* XRD experiments.....58

Figure 4.3: Schematic showing the basic principle of ATR-FTIR……..59

Figure 4.4: Types of interactions of incident light with sample. Adapted from Ref.[204].....61

Figure 4.5: A) Schematic showing the main parts of a TGA instrument and B) an illustration of the resulting mass loss *vs*. temperature plot……...61

Figure 4.6: Schematic of electron beam interaction with a sample in electron microscopy.....63

Figure 4.7: Schematic of AFM working principle……...…….. 65

Figure 4.8: Schematic of EQCM crystal response when measuring a rigid and a non-rigid film…….68

Figure 4.9: Illustration of 2- and 3-electrode configurations of lithium-ion battery cells. Reproduced with permission from Ref.[218] © 2019 Elsevier Ltd.....70

Figure 4.10: Schematic of cyclic voltammograms of capacitive, pseudocapacitive, and batter-like behaviour, inspired by Ref.[219] with permission from the American Chemical Society, Copyright © 2018..... 71

Figure 4.11: Schematic of GCD profiles of capacitive, pseudocapacitive, and battery-like electrodes showing linear and non-linear evolution of potential with time…….....72

Figure 4.12: Illustration of a Nyquist plot and the corresponding equivalent circuit representation……74

Figure 6.1: Structure and composition of HTOs: Scanning electron microscopy images of (A) $H_2Ti_4O_9{\cdot}H_2O$ (HTO), (B) HTO-HDA and (C) HTO-PA. (D) Powder XRD patterns of HTO, HTO-PA, HTO-HDA, and the PDF of $H_2Ti_4O_9{\cdot}H_2O$ as reported in the literature. (E) TGA and dTG (derivative thermogravimetry) plots for HTO, HTO-PA and HTO-HDA, showing mass loss steps and quantities. Optimized crystal structures of (F) HTO-PA and (G) HTO-HDA, obtained from DFT calculations and considering structural formulae derived from TGA……..90

Figure 6.2: Transmission electron microscopy images and selected area electron diffraction pattern (area indicated by red circle) of (A-C) HTO, (D-F) HTO-PA, and (G-I) HTO-HDA.....92

Figure 6.3: (A) Raman spectra, and XPS of (B) Ti 2p and (c) N 1s regions of HTO, HTO-PA, and HTO-HDA samples……...94

Figure 6.4: Electrochemical performance of HTO and pillared HTO in the Li-ion system. A-C) Galvanostatic charge and discharge plots of HTO, HTO-PA, and HTO-HDA showing the first 5 cycles at specific current rate 50 mA g^{-1} and the number of Li ions per Ti. D) CVs of HTO, HTO-PA, and HTO-HDA showing the 2nd cycle, cycled at scan rate 0.1 mV s^{-1} E) Rate handling of HTO, HTO-PA, and HTO-HDA, showing anodic capacity at various values of specific current and the corresponding coulombic efficiency of each cycle. F) Cycling performance of HTO, HTO-PA, and HTO-HDA at specific current rate 0.5 A g^{-1} and the corresponding coulombic efficiency……...96

Figure 6.5: *Operando* X-ray diffraction for A) HTO, B) HTO-PA, and C) HTO-HDA, highlighting changes to the (200) plane peak during 2 cycles of galvanostatic charge and discharge at a current rate of 50 mA g^{-1}……...98

Figure 6.6: Electrochemical dilatometry measurement of A) HTO, B) HTO-PA. EQCM measurements of C) HTO, and B) HTO-PA, showing mass change with cycling. Data is displayed for the third cycle. Mass change vs. charge of E) HTO and F) HTO-PA. Molar mass of the intercalating species is indicated by the slope.....100

Figure 6.7: A) Electrochemical impedance spectroscopy (EIS) Nyquist plots for HTO and HTO-PA at OCV, fitted using the equivalent circuit shown in the inset. B) R_{ct} values at different stages of lithiation and delithiation for HTO and HTO-PA. Error bars are based on multiple measurements. C) FTIR spectra for LP30 and HTO-PA electrodes at various states of charge. Peak positions for the vibration of EC- and DMC-solvated Li are highlighted by dashed lines.....101

Figure 6.8: A) Voltage profiles for HTO, HTO-PA, and HTO-HDA cycled at -20 °C at current rate 50 mA g^{-1}, showing the second cycles. Overpotential is calculated by the difference in voltage at the midpoint of capacity. B) Rate handling of the three materials at different current rates, C) Full cell voltage profiles for HTO against NMC (dashed lines) and HTO-PA against NMC (solid lines) at N/P ratio of 1.4. Dashed lines refer to HTO-based cells, solid lines refer to HTO-PA-based cells.....102

Figure S1.1: powder XRD pattern of as-synthesized $K_2Ti_4O_9$ and the corresponding PDF data……... 104

Figure S1.2: SEM image of as-synthesized $K_2Ti_4O_9$, showing rod-like morphology…...104

Figure S1.3: Powder XRD patterns obtained for the as-synthesized powder samples before heating (bottom diffractograms), and after holding at different temperatures corresponding to mass loss stages in A) HTO, B) HTO-PA, and C) HTO-HDA. Different phases appear at various stages of heating. A: anatase, B: brookite, R: rutile. The peaks are indexed according to PDF 00-021-1272 (anatase), PDF 00-015-0875 (brookite), PDF 00-021-1276 (rutile), PDF 01-080-9016 ($H_2Ti_3O_7 \cdot H_2O$), and simulated XRD patterns from The Materials Project[85] for TiO_2(B) and $Ti_6H_2O_{13}$.....105

Figure S1.4: Calculated powder XRD patterns of HTO-PA and HTO-HDA, using the CIF data obtained from DFT calculations……...…….106

Figure S1.5: Raman spectra in the range 1000 to 3000 cm^{-1}, showing the peaks characteristic of the organic pillar amine molecules…….106

Figure S1.6: Internal resistance values for the three electrodes during the first lithiation cycle, obtained from GITT measurement..... 107

Figure S1.7: Post-mortem TEM images of HTO, HTO-PA, and HTO-HDA electrodes A) before cycling, and B) after 50 cycles. The rod-like morphology is maintained after cycling and no signs of exfoliation or structural degradation are visible…….108

Figure S1.8: Dissipation vs. frequency plots verifying the stiffness of A) HTO and B) HTO-PA coatings on the quartz crystal…….108

Figure S1.9: Equivalent circuit used in the fitting of impedance spectroscopy data shown in this work. R1: bulk resistance of the cell, compromising electrolyte, separator, and electrodes. R2, Q2: resistance and capacitance of the interfacial layer, respectively. R3: charge transfer resistance, Q3: double-layer capacitance, and W3: Warburg diffusion element.[258] Constant-phase elements (Q) are used instead of capacitors (C) to represent non-ideal double layer behaviour……..109

Figure S1.10: FTIR spectra of A) HTO and B) HTO-HDA electrodes after rinsing with DMC and drying in vacuum. The dashed lines indicate wavenumbers for solvated Li: Li^+-DMC at 1321 cm^{-1} and Li^+-EC at 1422 cm^{-1}……..109

Figure 6.9: Overview of HTO and HTO-PA structural and morphological properties. A) Schematic illustration of proton exchange of KTO, followed by HTO sheets functionalization with PA. B) Powder XRD patterns of the as-synthesized structures and the reported $H_2Ti_4O_9{\cdot}H_2O$ PDF. C) TGA measurements of HTO and HTO-PA in O_2/N_2 atmosphere. D), E) SEM micrographs of HTO and HTO-PA. F), G) AFM micrographs of HTO and HTO-PA in tapping mode. H), I) Line profiles of HTO and HTO-PA, taken along the arrows shown in the AFM images……...113

Figure 6.10: Electrochemical assessment of HTO and HTO-PA in a Na-ion cell. A) Voltage profiles of HTO and B) HTO-PA, showing the first 5 cycles at constant current rate of 50 mA g^{-1}. C) CVs of HTO and HTO-PA at scan rate 0.1 mV s^{-1} showing the second cycle at scan rate 0.1 mV s^{-1}. D) Rate handling and coulombic efficiency of HTO and HTO-PA cycled between 2.5 and 0.2 V. E) GITT measurement of HTO and HTO-PA, obtained with 30-min current pulses of 20 mA g^{-1} followed by 2h rest. F) Apparent Na-ion diffusion coefficient in HTO and HTO-PA during sodiation, obtained from GITT measurement...115

Figure 6.11: *Operando* electrochemical dilatometry measurements of A) HTO and B) HTO-PA, cycled at a specific current of 50 mA g^{-1}……...116

Figure S2.1: SEM image of $K_2Ti_4O_9$ (KTO) rods.....118

Figure S2.2: Voltage profiles for the first 5 cycles of A) HTO and B) HTO-PA, cycled in the potential range 0.3 – 2.5 V vs. Na^+/Na at current rate 50 mA g^{-1}. The first cycle is shown in dashed lines…….118

Figure S2.3: CV of HTO and HTO-PA at voltage range 2.5 to 0.3 V vs. Na^+/Na, showing the second cycle at scan rate of 0.1 mV s^{-1}…….119

Figure S2.4: Rate handling test of HTO and HTO-PA at lower cut-off of 0.3 V vs. Na^+/Na……..120

Figure S2.5: Internal resistance (R_{int}) in HTO and HTO-PA obtained from GITT measurement. The values are obtained by dividing the overpotential (difference between quasi-open circuit voltage and the closed-circuit voltage) by the applied current…….121

Figure 6.12: (A) Schematic illustration of the synthesis process: Octylamine is assembled in the MoO_3 interlayer space via a dissolution-reorganization reaction; subsequent pyrolysis yields the carbon-containing nanocomposite. SEM images of (B) molybdenum oxide dihydrate ($MoO_3 \cdot 2H_2O$), (C) MoO_x-OA, and (D) MoO_x-C after pyrolysis in argon at 700 °C.....124

Figure 6.13: Structural characterization of hydrous molybdenum oxide ($MoO_3 \cdot 2H_2O$), molybdenum oxide with octylamines assembled in the interlayer space (MoO_x-OA) and pyrolyzed MoO_x-C: (A) Raman spectra of all samples. Raman spectrum of MoO_x-C consists of two individual measurements with different laser power: 0.25 mW between 100-1050 cm^{-1} to avoid oxidation of MoO_2 to MoO_3; 5 mW between 1050-3000 cm^{-1} for better resolution of carbon signals (individual full spectra given in Fig. S3.3). (B) X-ray diffractograms with referenced peak positions of $MoO_3 \cdot 2H_2O$ (PDF 00-016-0497, asterisk), monoclinic MoO_2 (PDF 00-032-0671, triangle), Mo_2C (PDF 00-011-0680, square), and Mo_4O_{11} (PDF 00-005-0337, circle). (C) Mo 3d, and (D) C 1s X-ray photoelectron spectrum regions of pristine powder MoO_x-C……....126

Figure 6.14: (A) *In situ* heating XRD patterns of MoO_x-OA during the heating step of pyrolysis, with inset showing magnified view of the 2θ range 2-10° and temperature range 30-300 °C, (B) *In situ* heating XRD patterns of MoO_x-OA during the two-hour annealing step. (C) Thermogravimetric analysis with mass spectroscopy of MoO_x-OA during the heating step of pyrolysis, detecting gaseous decomposition products with various mass-to-charge ratios (m/z). Three distinct processes occurring during pyrolysis are graphically indicated by colored mass loss regions (yellow, blue, purple), also highlighted by the arrows in the in-situ heating XRD diffractograms. (D) TGA with FTIR analysis of gaseous decomposition products during the heating step of pyrolysis.....129

Figure 6.15: Cross-sectional overview of the MoO_x-C hybrid nanostructure. a) HAADF-STEM micrograph of MoO_x-C showing microstructure with non-homogeneous particle composition. b) magnified micrograph of area indicated in b) showing phase Z-contrast variations in MoO_x-C, c) bright field STEM micrograph taken at the area indicated in b).

The crystalline domains are highlighted and measurements of planar spacings are indicated on the image. Lattice spacings in regions 1, 2, and 3 are in good agreement with the (111), (211), and (111) planes of MoO_2, respectively. d) high resolution HAADF-STEM image of monoclinic MoO_2 nanodomain……131

Figure 6.16: (A) HAADF-STEM micrograph showing Z-number contrast and (B-D) EDS mapping with elemental distribution of Mo, C, and O in MoO_x-C. (E) Chemical analysis of the two marked areas by quantitative STEM-EDS spectral imaging analysis……...133

Figure 6.17: First three galvanostatic charge-discharge cycles of (A) MoO_x-C and (B) MoO_{3-x} at 50 mA g^{-1}, (C) rate capability tests at various specific current values from 50 mA g^{-1} to 3 A g^{-1}, then back to 50 mA g^{-1}, in the voltage range 1.5 V to 3.5 V for MoO_{3-x} and 1.1 V to 3.1 V for MoO_x-C , (D) cycling stability test for MoO_{3-x} and MoO_x-C at 1 A g^{-1} for 1,000 cycles……136

Figure 6.18: (A) Galvanostatic charge-discharge curves of MoO_x-C and (B) MoO_{3-x} at a specific current of 50 mA g^{-1} in the potential range of 0.01 V to 3 V vs. Li^+/Li, (C) rate performance of MoO_{3-x} and MoO_x-C at rates from 50 mA g^{-1} to 3 A g^{-1}, (D) stability test of MoO_{3-x} and MoO_x-C cycled at 100 mA g^{-1}.....138

Fig. S3.1: XRD patterns of MoO_x-OA samples that were synthesized using various ratios of molybdenum oxide to octylamine……140

Fig. S3.2: SEM images used for the calculation of the average particle size of (A) MoO_x-OA and (B) MoO_x-C. A total of 20 particles were measured in each case……141

Fig. S3.3: O 1s XPS spectrum of pristine powder MoO_x-C, showing Mo(IV) oxide, Mo(VI) oxide, and carbon/oxygen species.[284,297]……...142

Fig. S3.4: Raman spectra of MoO_x-C acquired at 1 % (5 mW) and 0.05 % (0.25 mW) laser power, demonstrating the transformation from MoO_2 to MoO_3 signals at higher laser power……....143

Fig. S3.5: FTIR spectra of the evolving gasses during pyrolysis in the TGA at selected temperatures, compared to typical referenced spectra of assigned molecules according to Ref.[299]……...144

Fig. S3.6: HAADF-STEM of MoO_x-C, corresponding to bright field image shown in Fig. 6.16C. The nanocrystalline domains are highlighted in regions 1, 2, and 3……...145

Fig. S3.7: A) STEM-HAADF image of MoO_x-C, B) EDS elemental profiles of O, Mo, and C across the arrow displayed in panel A. Since STEM-EDS is a semi-quantitative method due to peak overlap, chamber contamination, and X-rays emitted from the grid and sample holder, EDS line scanning was chosen instead of showing a discrete EDS spectrum at a specific location……....146

Figure S3.8: TGA of MoO_x-C heating in oxygen atmosphere. Start temperature for mass loss calculation was set to 300°C, since amorphous carbons start to burn off at ca. 320°C.[300]……...……146

Fig. S3.9: Cyclic voltammograms of MoO_{3-x} and MoO_x-C in the respective first cycle. (A) Within the lithium intercalation potential range and to extended negative potential of 0.01 V vs. Li^+/Li for (B) MoO_{3-x} and (C) MoO_x-C. The charge storage reactions for Li^+ intercalation and conversion reactions are annotated on the graphs.....147

Fig. S3.10: XRD pattern of the as-synthesized reduced MoO_3, labelled in this work as MoO_{3-x}. The sharp (020), (040) and (060) diffraction peaks indicate preferred orientation along [0k0] direction, as described in ref. [301]…….148

Fig. S3.11: Electrochemical impedance spectra of MoO_{3-x} and MoO_x-C performed at OCV. Solid lines represent the fitted curves obtained by the equivalent circuit in the inset, where R1 is the combined series resistance consisting of the ionic resistance of the electrolyte, the resistance of the active material, and the contact resistance at the electrode/current collector interface,[302] R2 is the charge transfer resistance, Q2 is the constant phase element (used to describe non-ideal capacitive behaviour from double-layer processes), W is the Warburg element (used to describe ion diffusion), and Q3 is the capacitance by faradaic processes, also referred to as limit capacitance.[302]…….149

Fig. S3.12: SEM images of the pristine MoO_{3-x} (left column) and MoO_x-C (right column) electrodes (top), and ex situ SEM after the first electrochemical reduction to 0.01 V vs. Li^+/Li (center) and after galvanostatic cycling over 39 cycles (bottom)……....150

References

(1.) Trends and Projections in Europe 2023 — *European Environment Agency*; 2023.

(2.) Paris Agreement. *International Legal Materials* 2016, 55.

(3.) International Energy Agency, I. *The Power of Transformation - Wind, Sun and the Economics of Flexible Power Systems 2024*.

(4.) Simon, P.; Gogotsi, Y. Perspectives for Electrochemical Capacitors and Related Devices. *Nature Materials* 2020, 19, 1151–1163.

(5.) Passerini, S., Barelli, L., Baumann, M., Peters, J., Weil, M. Emerging Battery Technologies to Boost the Clean Energy Transition, *The Materials Research Society Series* 2024.

(6.) Nitta, N.; Wu, F.; Lee, J. T.; Yushin, G. Li-Ion Battery Materials: Present and Future. *Materials Today* 2015, 18, 252–264.

(7.) Fleischmann, S.; Spencer, M. A.; Augustyn, V. Electrochemical Reactivity under Confinement Enabled by Molecularly Pillared 2D and Layered Materials. *Chemistry of Materials* 2020, 32, 3325–3334.

(8.) Goodenough, J. B.; Park, K. S. The Li-Ion Rechargeable Battery: A Perspective. *Journal of the American Chemical Society* 2013, 135, 1167–1176.

(9.) Whittingham, M. S. Intercalation Chemistry and Energy Storage. *Journal of Solid State Chemistry* 1979, 29, 303–310.

(10.) Yoffe, A. D. Physical Properties of Intercalated Solids. *Solid State Ionics* 1983, 9–10, 59–69.

(11.) Whittingham, M. S.; Jacobson, J. A. *Intercalation Chemistry* 1982.

(12.) Julien, C.; Nazri, G. A. Intercalation Compounds for Advanced Lithium Batteries. *Handbook of Advanced Electronic and Photonic Materials and Devices* 2001, 99–184.

(13.) Müller-Warmuth, W.; Schöllhorn, R.; Physics and Chemistry of Materials with Low-Dimensional Structures. *Progress in Intercalation Research* 1994.

(14.) Guo, H.; Elmanzalawy, M.; Sivakumar, P.; Fleischmann, S. Unifying Electrolyte Formulation and Electrode Nanoconfinement Design to Enable New Ion–Solvent Cointercalation Chemistries. *Energy & Environmental Science* 2024, 17, 2100–2116.

(15.) Xu, K.; Von Wald Cresce, A. Li+-Solvation/Desolvation Dictates Interphasial Processes on Graphitic Anode in Li Ion Cells. *Journal of Materials Research* 2012, 27, 2327–2341.

(16.) Yoshino, A.; Sanechika, K.; Nakajima, T. Secondary Battery 1986.

(17.) Delmas, C. Sodium and Sodium-Ion Batteries: 50 Years of Research. *Advanced Energy Materials* 2018, 8, 1703137.

(18.) Titirici, M.-M.; Johansson, P.; Ribadeneyra, M. C.; Au, H.; Innocenti, A.; Passerini, S.; Petavratzi, E.; Lusty, P.; Tidblad, A. A.; Naylor, A. J.; Younesi, R.; Chart, Y. A.; Aspinall, J.; Pasta, M.; Orive, J.; Babual, L. M.; Reynaud, M.; Latham, K. G.; Hosaka, T.; Komaba, S.; Bitenc, J.; Ponrouch, A.; Zhang, H.; Armand, M.; Kerr, R.; Howlett, P. C.; Forsyth, M.; Brown, J.; Grimaud, A.; Vilkman, M.; Dermenci, K. B.; Mousavihashemi, S.; Berecibar, M.; Marshall, J. E.; McElroy, C. R.; Kendrick, E.; Safdar, T.; Huang, C.; Zanotto, F. M.; Troncoso, J. F.; Dominguez, D. Z.; Alabdali, M.; Vijay, U.; Franco, A. A.; Pazhaniswamy, S.; Grant, P. S.; Guzman, S. L.; Fehse, M.; Mestres, M. G.; Antuñano, N. 2024 Roadmap for Sustainable Batteries. *Journal of Physical Letters: Energy* 2024, 6, 041502.

(19.) Usiskin, R.; Lu, Y.; Popovic, J.; Law, M.; Balaya, P.; Hu, Y. S.; Maier, J. Fundamentals, Status and Promise of Sodium-Based Batteries. *Nature Reviews Materials* 2021, 6, 1020–1035.

(20.) Keller, M.; Buchholz, D.; Passerini, S.; Keller, M.; Buchholz, D.; Passerini, S. Layered Na-Ion Cathodes with Outstanding Performance Resulting from the Synergetic Effect of Mixed P- and O-Type Phases. *Advanced Energy Materials* 2016, 6, 1501555.

(21.) Singh, B.; Wang, Z.; Park, S.; Gautam, G. S.; Chotard, J. N.; Croguennec, L.; Carlier, D.; Cheetham, A. K.; Masquelier, C.; Canepa, P. A Chemical Map of NaSICON Electrode Materials for Sodium-Ion Batteries. *Journal of Materials Chemistry A* 2021, 9, 281–292.

(22.) Zhang, W.; Zhang, F.; Ming, F.; Alshareef, H. N. Sodium-Ion Battery Anodes: Status and Future Trends. *EnergyChem* 2019, 1, 100012.

(23.) Xia, X.; Obrovac, M. N.; Dahn, J. R. Comparison of the Reactivity of NaxC6 and Li XC6 with Non-Aqueous Solvents and Electrolytes. *Electrochemical and Solid-State Letters* 2011, 14, A130.

(24.) Doeff, M. M.; Cabana, J.; Shirpour, M. Titanate Anodes for Sodium Ion Batteries. *Journal of Inorganic and Organometallic Polymers and Materials* 2014, 24, 5–14.

(25.) Zheng, X.; Li, P.; Zhu, H.; Zhao, G.; Rui, K.; Shu, J.; Xu, X.; Wang, X.; Sun, W.; Dou, S. X. Understanding the Structural and Chemical Evolution of Layered Potassium Titanates for Sodium Ion Batteries. *Energy Storage Materials* 2020, 25, 502–509.

(26.) Senguttuvan, P.; Rousse, G.; Seznec, V.; Tarascon, J. M.; Palacín, M. R. Na2Ti3O7: Lowest Voltage Ever Reported Oxide Insertion Electrode for Sodium Ion Batteries. *Chemistry of Materials* 2011, 23, 4109–4111.

(27.) Shirpour, M.; Cabana, J.; Doeff, M. Lepidocrocite-Type Layered Titanate Structures: New Lithium and Sodium Ion Intercalation Anode Materials. *Chemistry of Materials* 2014, 26, 2502–2512.

(28.) Shirpour, M.; Cabana, J.; Doeff, M. New Materials Based on a Layered Sodium Titanate for Dual Electrochemical Na and Li Intercalation Systems. *Energy & Environmental Science* 2013, 6, 2538–2547.

(29.) Kang, H.; Liu, Y.; Cao, K.; Zhao, Y.; Jiao, L.; Wang, Y.; Yuan, H. Update on Anode Materials for Na-Ion Batteries. *Journal of Materials Chemistry A* 2015, 3, 17899–17913.

(30.) Senguttuvan, P.; Rousse, G.; Seznec, V.; Tarascon, J.; Palacin, M. R. Na2Ti3O7: Lowest Voltage Ever Reported Oxide Insertion Electrode for Sodium Ion Batteries. *Chemistry of Materials* 2011, 42, 4109–4111.

(31.) Shirpour, M.; Cabana, J.; Doeff, M. Lepidocrocite-Type Layered Titanate Structures: New Lithium and Sodium Ion Intercalation Anode Materials. *Chemistry of Materials* 2014, 26, 2502–2512.

(32.) Yin, W.; Ahn, J.; Barim, G.; Alvarado, J.; Doeff, M. M. Tailoring Stepped Layered Titanates for Sodium-Ion Battery Applications. *Accounts of Materials Research* 2024, 5, 8, 933–943.

(33.) Saothayanun, T. K.; Sirinakorn, T. T.; Ogawa, M. Ion Exchange of Layered Alkali Titanates (Na2Ti3O7, K2Ti4O9, and Cs2Ti5O11) with Alkali Halides by the Solid-State Reactions at Room Temperature. *Inorganic Chemistry* 2020, 59, 4024–4029.

(34.) Liu, T.; Miao, L.; Yao, F.; Zhang, W.; Zhao, W.; Yang, D.; Feng, Q.; Hu, D. Structure, Properties, Preparation, and Application of Layered Titanates. *Inorganic Chemistry* 2024, 63, 1–26.

(35.) Izawa, H.; Kikkawa, S.; Koizumi, M. Ion Exchange and Dehydration of Layered Titanates, Na2Ti3O7 and K2Ti4O9. *Journal of Physical Chemistry* 1982, 86, 5023–5026.

(36.) Sasaki, T.; Watanabe, M.; Michiue, Y.; Komatsu, Y.; Izumi, F.; Takenouchi, S. Preparation and Acid-Base Properties of a Protonated Titanate with the Lepidocrocite-like Layer Structure. *Chemistry of Materials* 1995, 7, 1001–1007.

(37.) Anasori, B.; Lukatskaya, M. R.; Gogotsi, Y. 2D Metal Carbides and Nitrides (MXenes) for Energy Storage. *Nature Reviews Materials* 2017, 2, 16098.

(38.) Li, Y.; Shao, H.; Lin, Z.; Lu, J.; Liu, L.; Duployer, B.; Persson, P. O. Å.; Eklund, P.; Hultman, L.; Li, M.; Chen, K.; Zha, X. H.; Du, S.; Rozier, P.; Chai, Z.; Raymundo-Piñero, E.; Taberna, P. L.; Simon, P.; Huang, Q. A General Lewis Acidic Etching Route for Preparing MXenes with Enhanced Electrochemical Performance in Non-Aqueous Electrolyte. *Nature Materials* 2020, 19, 894–899.

(39.) Chen, T.; Xue, L.; Shi, Z.; Qiu, C.; Sun, M.; Zhao, Y.; Liu, J.; Ni, M.; Li, H.; Xu, J.; Xia, H. Interlayer Modulation of Layered Transition Metal Compounds for Energy Storage. *ACS Applied Materials and Interfaces* 2022, 14, 54369–54388.

(40.) Zhang, Y.; Ang, E. H.; Yang, Y.; Ye, M.; Du, W.; Li, C. C. Interlayer Chemistry of Layered Electrode Materials in Energy Storage Devices. *Advanced Functional Materials* 2021, 31, 2007358.

(41.) Mukherjee, S.; Quilty, C. D.; Yao, S.; Stackhouse, C.; Wang, L.; Takeuchi, K. J.; Takeuchi, E. S.; Wang, F.; Marschilok, A. C.; Pomerantseva, E. The Effect of Chemically Preintercalated Alkali Ion on Structure of Layered Titanates and Their Electrochemistry in Aqueous Energy Storage Systems. *Journal of Materials Chemistry A* 2020, 8, 18220-18231.

(42.) Fleischmann, S.; Sun, Y.; Osti, N. C.; Wang, R.; Mamontov, E.; Jiang, D. E.; Augustyn, V. Interlayer Separation in Hydrogen Titanates Enables Electrochemical Proton Intercalation. *Journal of Materials Chemistry A* 2020, 8, 412–421.

(43.) Chen, C.; Li, N. W.; Zhang, X. Y.; Zhang, C. H.; Qiu, J.; Yu, L. Interlayer-Expanded Titanate Hierarchical Hollow Spheres Embedded in Carbon Nanofibers for Enhanced Na Storage. *Small* 2022, 18, 2107890.

(44.) Ali, S.; Zhang, Y.; Yang, H.; Xu, T.; Wang, Y.; Cui, J.; ten Elshof, J. E.; Shan, C.; Xu, H.; Yuan, H. Altering the Alkaline Metal Ions in Lepidocrocite-Type Layered

Titanate for Sodium-Ion Batteries. *ACS Applied Materials and Interfaces* 2023, 15, 5028–5037.

(45.) Que, L.; Wu, J.; Lan, Z.; Xie, Y.; Yu, F.; Wang, Z.; Meng, J.; Zhang, X. Potassium-based Dual-ion Batteries Operating at -60 °C Enabled By Co-Intercalation Anode. *Advanced Materials* 2023, 35, 2307592.

(46.) Izawa, H.; Kikkawa, S.; Koizumi, M. Formation and Properties of N-Alkylammonium Complexes with Layered Tri- and Tetra-Titanates. *Polyhedron* 1983, 2, 741–744.

(47.) Ogawa, M.; Takizawa, Y. Intercalation of Alkylammonium Cations into a Layered Titanate in the Presence of Macrocyclic Compounds. *Chemistry of Materials* 1999, 11, 30–32.

(48.) Airoldi, C.; Nunes, L. M.; De Farias, R. F. The Intercalation of N-Alkyldiamines into Crystalline Layered Titanate. *Materials Research Bulletin* 2000, 35, 2081–2090.

(49.) Jeffery, A. A.; Pradeep, A.; Rajamathi, M. Preparation of Titanate Nanosheets and Nanoribbons by Exfoliation of Amine Intercalated Titanates. *Physical Chemistry Chemical Physics* 2016, 18, 12604–12609.

(50.) Piao, M.; Oh, S. M.; Lim, J.; Kim, S. H.; Kim, S. C.; Jo, Y. K.; Han, O. H.; Hwang, S. J. Critical Role of the Chemical Environment of Interlayer Na Sites: An Effective Way to Improve the Na Ion Electrode Activity of Layered Titanate. *ACS Applied Materials and Interfaces* 2018, 10, 33112–33123.

(51.) Guo, H.; Elmanzalawy, M.; Sivakumar, P.; Fleischmann, S. Unifying Electrolyte Formulation and Electrode Nanoconfinement Design to Enable New Ion – Solvent Cointercalation Chemistries. *Energy & Environmental Science* 2024, 17, 2100–2116.

(52.) Chen, T.; Xue, L.; Shi, Z.; Qiu, C.; Sun, M.; Zhao, Y.; Liu, J.; Ni, M.; Li, H.; Xu, J.; Xia, H. Interlayer Modulation of Layered Transition Metal Compounds for Energy Storage. *ACS Applied Materials and Interfaces* 2022, 14, 54369–54388.

(53.) Peng, L.; Zhu, Y.; Peng, X.; Fang, Z.; Chu, W.; Wang, Y.; Xie, Y.; Li, Y.; Cha, J. J.; Yu, G. Effective Interlayer Engineering of Two-Dimensional VOPO4 Nanosheets via Controlled Organic Intercalation for Improving Alkali Ion Storage. *Nano Letters* 2017, 17, 6273–6279.

(54.) Hu, X.; Wang, D.-P.; Xia, X.-H.; Chen, Y.-X.; Liu, H.-B.; Gu, Z.-Q. Pillared Graphene Sheets with High-Rate Performance as Anode Material for Lithium-Ion Batteries. *Journal for Nanoscience and Nanotechnology* 2019, 19, 7269–7277.

(55.) Tian, W.; VahidMohammadi, A.; Wang, Z.; Ouyang, L.; Beidaghi, M.; Hamedi, M. M. Layer-by-Layer Self-Assembly of Pillared Two-Dimensional Multilayers. *Nature Communications* 2019, 10, 1–10.

(56.) Liu, Z.; Sun, H.; Qin, L.; Cao, X.; Zhou, J.; Pan, A.; Fang, G.; Liang, S. Interlayer Doping in Layered Vanadium Oxides for Low-Cost Energy Storage: Sodium-Ion Batteries and Aqueous Zinc-Ion Batteries. *ChemNanoMat* 2020, 6, 1553–1566.

(57.) Ma, X.; Cao, X.; Yao, M.; Shan, L.; Shi, X.; Fang, G.; Pan, A.; Lu, B.; Zhou, J.; Liang, S. Organic–Inorganic Hybrid Cathode with Dual Energy-Storage Mechanism for Ultrahigh-Rate and Ultralong-Life Aqueous Zinc-Ion Batteries. *Advanced Materials* 2022, 34, 2105452.

(58.) Huang, Y.; Liang, J.; Wang, C.; Yin, S.; Fu, W.; Zhu, H.; Wan, C. Hybrid Superlattices of Two-Dimensional Materials and Organics. *Chemical Society Reviews* 2020, 49, 6866–6883.

(59.) Rasamani, K. D.; Alimohammadi, F.; Sun, Y. Interlayer-Expanded MoS2. *Materials Today* 2017, 20, 83–91.

(60.) Xue, X.; Chen, R.; Yan, C.; Zhao, P.; Hu, Y.; Kong, W.; Lin, H.; Wang, L.; Jin, Z.; Xue, X. L.; Chen, R. P.; Yan, C. Z.; Zhao, P. Y.; Hu, Y.; Kong, W. H.; Lin, H. N.; Wang, L.; Jin, Z. One-Step Synthesis of 2-Ethylhexylamine Pillared Vanadium Disulfide Nanoflowers with Ultralarge Interlayer Spacing for High-Performance Magnesium Storage. *Advanced Energy Materials* 2019, 9, 1900145.

(61.) Goloveshkin, A. S.; Bushmarinov, I. S.; Korlyukov, A. A.; Buzin, M. I.; Zaikovskii, V. I.; Lenenko, N. D.; Golub, A. S. Stabilization of 1T-MoS2 Sheets by Imidazolium Molecules in Self-Assembling Hetero-Layered Nanocrystals. *Langmuir* 2015, 31, 8953–8960.

(62.) Huang, J.; Wang, Z.; Hou, M.; Dong, X.; Liu, Y.; Wang, Y.; Xia, Y. Polyaniline-Intercalated Manganese Dioxide Nanolayers as a High-Performance Cathode Material for an Aqueous Zinc-Ion Battery. *Nature Communications* 2018, 9, 1–8.

(63.) Liu, S.; Zhu, H.; Zhang, B.; Li, G.; Zhu, H.; Ren, Y.; Geng, H.; Yang, Y.; Liu, Q.; Chao Li, C.; Liu, S.; Geng, H.; Yang, Y.; Li, C. C.; Zhu, H.; Zhang, B.; Li, G.; Liu, Q.; Ren, Y. Tuning the Kinetics of Zinc-Ion Insertion/Extraction in V2O5 by In Situ

Polyaniline Intercalation Enables Improved Aqueous Zinc-Ion Storage Performance. *Advanced Materials* 2020, 32, 2001113.

(64.) Zhang, Y.; Huixiang Ang, E.; Yang, Y.; Ye, M.; Du, W.; Chao Li, C.; Zhang, Y. F.; Yang, Y.; Ye, M. H.; Du, W. C.; Li, C. C.; Ang, E. H. Interlayer Chemistry of Layered Electrode Materials in Energy Storage Devices. *Advanced Functional Materials* 2021, 31, 2007358.

(65.) Li, M.; Fan, Q.; Gao, L.; Liang, K.; Huang, Q. Chemical Intercalation of Layered Materials: From Structure Tailoring to Applications. *Advanced Materials* 2024, 36, 2312918

(66.) Xue, Y.; Zhang, Q.; Wang, W.; Cao, H.; Yang, Q.; Fu, L. Opening Two-Dimensional Materials for Energy Conversion and Storage: A Concept. *Advanced Energy Materials* 2017, 7, 1602684.

(67.) Zhao, X.; Mao, L.; Cheng, Q.; Liao, F.; Yang, G.; Lu, X.; Chen, L. Interlayer Engineering of Preintercalated Layered Oxides as Cathode for Emerging Multivalent Metal-Ion Batteries: Zinc and Beyond. *Energy Storage Mater* 2021, 38, 397–437.

(68.) Augustyn, V. Tuning the Interlayer of Transition Metal Oxides for Electrochemical Energy Storage. *Journal of Materials Research* 2017, 32, 2–15.

(69.) Chen, X.; Mcdonald, A. R.; Chen, X.; Mcdonald, A. R. Functionalization of Two-Dimensional Transition-Metal Dichalcogenides. *Advanced Materials* 2016, 28, 5738–5746.

(70.) Gamble, F. R.; DiSalvo, F. J.; Klemm, R. A.; Geballe, T. H. Superconductivity in Layered Structure Organometallic Crystals. *Science* 1970, 168, 568–570.

(71.) Whittingham, M. S. The Role of Ternary Phases in Cathode Reactions. *Journal of the Electrochemical Society* 1976, 123, 315–320.

(72.) Li, X.; Shan, J.; Zhang, W.; Su, S.; Yuwen, L.; Wang, L. Recent Advances in Synthesis and Biomedical Applications of Two-Dimensional Transition Metal Dichalcogenide Nanosheets. *Small* 2017, 13, 1602660.

(73.) Chen, X.; Bartlam, C.; Lloret, V.; Moses Badlyan, N.; Wolff, S.; Gillen, R.; Stimpel-Lindner, T.; Maultzsch, J.; Duesberg, G. S.; Knirsch, K. C.; Hirsch, A. Covalent Bisfunctionalization of Two-Dimensional Molybdenum Disulfide. *Angewandte Chemie International Edition* 2021, 60, 13484–13492.

(74.) Jacobson, A. J. Organic and Organometallic Intercalation Compounds of the Transition Metal Dichalcogenides. *Intercalation Chemistry* 1982, 229–265.

(75.) Kumari, S.; Chouhan, A.; Sharma, O. P.; Kuriakose, S.; Tawfik, S. A.; Spencer, M. J. S.; Walia, S.; Sugimura, H.; Khatri, O. P. Structural-Defect-Mediated Grafting of Alkylamine on Few-Layer MoS2and Its Potential for Enhancement of Tribological Properties. *ACS Applied Materials and Interfaces* 2020, 12, 30720–30730.

(76.) Schöllhorn, R.; Weiss, A. Cation Exchange Reactions and Layer Solvate Complexes of Ternary Phases MxMoS2. *Journal of the Less Common Metals* 1974, 36, 229–236.

(77.) Ushakov, I. E.; Goloveshkin, A. S.; Lenenko, N. D.; Ezernitskaya, M. G.; Korlyukov, A. A.; Zaikovskii, V. I.; Golub, A. S. Hydrogen Bond-Driven Self-Assembly between Single-Layer MoS2 and Alkyldiamine Molecules. *Crystal Growth & Design* 2018, 18, 5116–5123.

(78.) Yoo, H. D.; Liang, Y.; Dong, H.; Lin, J.; Wang, H.; Liu, Y.; Ma, L.; Wu, T.; Li, Y.; Ru, Q.; Jing, Y.; An, Q.; Zhou, W.; Guo, J.; Lu, J.; Pantelides, S. T.; Qian, X.; Yao, Y. Fast Kinetics of Magnesium Monochloride Cations in Interlayer-Expanded Titanium Disulfide for Magnesium Rechargeable Batteries. *Nature Communications* 2017, 8, 1–10.

(79.) Voiry, D.; Goswami, A.; Kappera, R.; De, C.; Castro E Silva, C.; Kaplan, D.; Fujita, T.; Chen, M.; Asefa, T.; Chhowalla, M. Covalent Functionalization of Monolayered Transition Metal Dichalcogenides by Phase Engineering. *Nature Chemistry* 2015, 7, 45–49.

(80.) Mei, L.; Cao, Z.; Ying, T.; Yang, R.; Peng, H.; Wang, G.; Zheng, L.; Chen, Y.; Tang, C. Y.; Voiry, D.; Wang, H.; Farimani, A. B.; Zeng, Z. Simultaneous Electrochemical Exfoliation and Covalent Functionalization of MoS2 Membrane for Ion Sieving. *Advanced Materials* 2022, 34, 2201416.

(81.) Schwarz, A.; Alon-Yehezkel, H.; Levi, A.; Yadav, R. K.; Majhi, K.; Tzuriel, Y.; Hoang, L.; Bailey, C. S.; Brumme, T.; Mannix, A. J.; Cohen, H.; Yalon, E.; Heine, T.; Pop, E.; Cheshnovsky, O.; Naveh, D. Thiol-Based Defect Healing of WSe2 and WS2. *npj 2D Materials and Applications* 2023, 7, 1–9.

(82.) Sim, D. M.; Kim, M.; Yim, S.; Choi, M. J.; Choi, J.; Yoo, S.; Jung, Y. S. Controlled Doping of Vacancy-Containing Few-Layer MoS2 via Highly Stable Thiol-Based Molecular Chemisorption. *ACS Nano* 2015, 9, 12115–12123.

(83.) Syari'Ati, A.; Kumar, S.; Zahid, A.; Ali El Yumin, A.; Ye, J.; Rudolf, P. Photoemission Spectroscopy Study of Structural Defects in Molybdenum Disulfide (MoS2) Grown by Chemical Vapor Deposition (CVD). *Chemical Communications* 2019, 55, 10384–10387.

(84.) Chen, X.; Berner, N. C.; Backes, C.; Duesberg, G. S.; McDonald, A. R. Functionalization of Two-Dimensional MoS2: On the Reaction Between MoS2 and Organic Thiols. *Angewandte Chemie International Edition* 2016, 55, 5803–5808.

(85.) Jain, A.; Ong, S. P.; Hautier, G.; Chen, W.; Richards, W. D.; Dacek, S.; Cholia, S.; Gunter, D.; Skinner, D.; Ceder, G.; Persson, K. A. Commentary: The Materials Project: A Materials Genome Approach to Accelerating Materials Innovation. *APL Materials* 2013, 1, 11002.

(86.) Chou, S. S.; De, M.; Kim, J.; Byun, S.; Dykstra, C.; Yu, J.; Huang, J.; Dravid, V. P. Ligand Conjugation of Chemically Exfoliated MoS2. *Journal of the American Chemical Society* 2013, 135, 4584–4587.

(87.) Vishnoi, P.; Sampath, A.; Waghmare, U. V.; Rao, C. N. R. Covalent Functionalization of Nanosheets of MoS2 and MoSe2 by Substituted Benzenes and Other Organic Molecules. *Chemistry – A European Journal* 2017, 23, 886–895.

(88.) Georgakilas, V.; Otyepka, M.; Bourlinos, A. B.; Chandra, V.; Kim, N.; Kemp, K. C.; Hobza, P.; Zboril, R.; Kim, K. S. Functionalization of Graphene: Covalent and Non-Covalent Approaches, Derivatives and Applications. *Chemical Reviews* 2012, 112, 6156–6214.

(89.) Dai, L. Functionalization of Graphene for Efficient Energy Conversion and Storage. *Accounts of Chemical Research* 2013, 46, 31–42.

(90.) Liao, L.; Peng, H.; Liu, Z. Chemistry Makes Graphene beyond Graphene. *Journal of the American Chemical Society* 2014, 136, 12194–12200.

(91.) Georgakilas, V.; Otyepka, M.; Bourlinos, A. B.; Chandra, V.; Kim, N.; Kemp, K. C.; Hobza, P.; Zboril, R.; Kim, K. S. Functionalization of Graphene: Covalent and Non-Covalent Approaches, Derivatives and Applications. *Chemical Reviews* 2012, 112, 6156–6214.

(92.) Sun, J.; Sadd, M.; Edenborg, P.; Grönbeck, H.; Thiesen, P. H.; Xia, Z.; Quintano, V.; Qiu, R.; Matic, A.; Palermo, V. Real-Time Imaging of Na+ Reversible Intercalation in "Janus" Graphene Stacks for Battery Applications. *Sci Advances* 2021, 7, 812–840.

(93.) Song, B.; Zhao, J.; Wang, M.; Mullavey, J.; Zhu, Y.; Geng, Z.; Chen, D.; Ding, Y.; Moon, K. sik; Liu, M.; Wong, C. P. Systematic Study on Structural and Electronic Properties of Diamine/Triamine Functionalized Graphene Networks for Supercapacitor Application. *Nano Energy* 2017, 31, 183–193.

(94.) Lee, J.; Kim, C.; Cheong, J. Y.; Kim, I. D. An Angstrom-Level d-Spacing Control of Graphite Oxide Using Organofillers for High-Rate Lithium Storage. *Chem* 2022, 8, 2393–2409.

(95.) Chen, W.; Wu, K.; Liu, Q.; Lu, M. Functionalization of Graphite via Diels-Alder Reaction to Fabricate Poly (Vinyl Alcohol) Composite with Enhanced Thermal Conductivity. *Polymer* 2020, 186, 122075.

(96.) Hossain, M. Z.; Shimizu, N. In Situ Functionalization of Graphene with Reactive End Group through Amine Diazotization. *Journal of Physical Chemistry C* 2017, 121, 25223–25228.

(97.) Zhao, G.; Jiang, L.; He, Y.; Li, J.; Dong, H.; Wang, X.; Hu, W. Sulfonated Graphene for Persistent Aromatic Pollutant Management. *Advanced Materials* 2011, 23, 3959–3963.

(98.) Meshhal, M.; Kühn, O. Diffusion of Water Confined between Graphene Oxide Layers: Implications for Membrane Filtration. *ACS Applied Nano Materials* 2022, 5, 11119–11128.

(99.) Wan, C.; Gu, X.; Dang, F.; Itoh, T.; Wang, Y.; Sasaki, H.; Kondo, M.; Koga, K.; Yabuki, K.; Snyder, G. J.; Yang, R.; Koumoto, K. Flexible N-Type Thermoelectric Materials by Organic Intercalation of Layered Transition Metal Dichalcogenide TiS2. *Nature Materials* 2015, 14, 622–627.

(100.) Cameron, J. M.; Holc, C.; Kibler, A. J.; Peake, C. L.; Walsh, D. A.; Newton, G. N.; Johnson, L. R. Molecular Redox Species for Next-Generation Batteries. *Chemical Society Reviews* 2021, 50, 5863–5883.

(101.) Song, Z.; Zhan, H.; Zhou, Y. Anthraquinone Based Polymer as High Performance Cathode Material for Rechargeable Lithium Batteries. *Chemical Communications* 2009, 4, 448–450.

(102.) Song, Z.; Zhan, H.; Zhou, Y. Polyimides: Promising Energy-Storage Materials. *Angewandte Chemie International Edition* 2010, 49, 8444–8448.

(103.) Karon, K.; Lapkowski, M. Carbazole Electrochemistry: A Short Review. *Journal of Solid State Electrochemistry* 2015, 19, 2601–2610.

(104.) Kuo, D. Y.; Rice, P. S.; Raugei, S.; Cossairt, B. M. Charge Transfer in Metallocene Intercalated Transition Metal Dichalcogenides. *Journal of Physical Chemistry C* 2022, 126, 13994–14002.

(105.) Feng, J. K.; Cao, Y. L.; Ai, X. P.; Yang, H. X. Polytriphenylamine: A High Power and High Capacity Cathode Material for Rechargeable Lithium Batteries. *Journal of Power Sources* 2008, 177, 199–204.

(106.) Nanda, J.; Augustyn, V. *Transition Metal Oxides for Electrochemical Energy Storage*, 2022.

(107.) Dong, Y.; Li, J. Oxide Cathodes: Functions, Instabilities, Self Healing, and Degradation Mitigations. *Chemical Reviews* 2023, 123, 2, 811–833.

(108.) Yang, L.; Heinlein, J.; Hua, C.; Gao, R.; Hu, S.; Pfefferle, L.; He, Y. Emerging Dual-Functional 2D Transition Metal Oxides for Carbon Capture and Utilization: A Review. *Fuel* 2022, 324, 124706.

(109.) Lagaly, G. Interaction of Alkylamines with Different Types of Layered Compounds. *Solid State Ionics* 1986, 22, 43–51.

(110.) Alberti, G.; Costantino, U. Intercalation Chemistry of Acid Salts of Tetravalent Metals with Layered Structure and Related Materials. In *Intercalation Chemistry* 1982, 147–180.

(111.) Wang, R.; Lu, X.; Hao, L.; Jiao, W.; Liu, W.; Zhang, J.; Yuan, F.; Yang, F. Enhanced and Tunable Photochromism of MoO3–Butylamine Organic–Inorganic Hybrid Composites. *Journal of Material Chemistry C* 2017, 5, 427–433.

(112.) Chen, D.; Liu, M.; Yin, L.; Li, T.; Yang, Z.; Li, X.; Fan, B.; Wang, H.; Zhang, R.; Li, Z.; Xu, H.; Lu, H.; Yang, D.; Sun, J.; Gao, L. Single-Crystalline MoO 3 Nanoplates: Topochemical Synthesis and Enhanced Ethanol -Sensing Performance. *Journal of Material Chemistry* 2011, 21, 9332–9342.

(113.) Shukoor, M. I.; Therese, H. A.; Gorgishvili, L.; Glasser, G.; Kolb, U.; Tremel, W. From Layered Molybdic Acid to Lower-Dimensional Nanostructures by Intercalation of Amines under Ambient Conditions. *Chemistry of Materials* 2006, 18, 2144–2151.

(114.) Ogawa, M.; Kuroda, K. Preparation of Inorganic–Organic Nanocomposites through Intercalation of Organoammonium Ions into Layered Silicates. *Bulletin of the Chemical Society of Japan* 1997, 70, 2593–2618.

(115.) Airoldi, C.; Nunes, L. M.; De Farias, R. F. The Intercalation of N-Alkyldiamines into Crystalline Layered Titanate. *Materials Research Bulletin* 2000, 35, 2081–2090.

(116.) Meng, H.; Ran, Q.; Zhu, M. H.; Zhao, Q. Z.; Han, G. F.; Wang, T. H.; Wen, Z.; Lang, X. Y.; Jiang, Q. Benzoquinone-Lubricated Intercalation in Manganese Oxide for High-Capacity and High-Rate Aqueous Aluminum-Ion Battery. *Small* 2024, 2310722.

(117.) Dong, S.; Lv, N.; Wu, Y.; Zhang, Y.; Zhu, G.; Dong, X. Titanates for Sodium-Ion Storage. *Nano Today* 2022, 42, 101349.

(118.) Izawa, H.; Kikkawa, S.; Koizumi, M. Formation and Properties of N-Alkylammonium Complexes with Layered Tri- and Tetra-Titanates. *Polyhedron* 1983, 2, 741–744.

(119.) Wang, M.; Yagi, S. Layered Birnessite MnO2 with Enlarged Interlayer Spacing for Fast Mg-Ion Storage. *Journal of Alloys and Compounds* 2020, 820, 153135.

(120.) Liu, Y.; Pan, Z.; Tian, D.; Hu, T.; Jiang, H.; Yang, J.; Sun, J.; Zheng, J.; Meng, C.; Zhang, Y. Employing “One for Two” Strategy to Design Polyaniline-Intercalated Hydrated Vanadium Oxide with Expanded Interlayer Spacing for High-Performance Aqueous Zinc-Ion Batteries. *Chemical Engineering Journal* 2020, 399, 125842.

(121.) Hu, S.; Pillai, A. S.; Liang, G.; Pang, W. K.; Wang, H.; Li, Q.; Guo, Z. Li-Rich Layered Oxides and Their Practical Challenges: Recent Progress and Perspectives. *Electrochemical Energy Reviews* 2019, 2, 277–311.

(122.) Liu, W.; Oh, P.; Liu, X.; Myeong, S.; Cho, W.; Cho, J.; Liu, W.; Oh, P.; Liu, X.; Myoeng, S.; Cho, W.; Cho, J. Countering Voltage Decay and Capacity Fading of Lithium-Rich Cathode Material at 60 °C by Hybrid Surface Protection Layers. *Advanced Energy Materials* 2015, 5, 1500274.

(123.) Zhou, R.; Wang, M.; Wei, W.; Li, J.; Tong, Y.; Liang, B.; Chen, F.; Liu, G.; Luo, M. Enhanced Desalination Capacity and Stability of Alkylamine-Modified Na0.71CoO2for Capacitive Deionization. *ACS Sustainable Chemistry & Engineering* 2021, 9, 1949–1957.

(124.) Khandelwal, M.; Hur, S. H.; Chung, J. S. Tailoring the Structural Properties of Simultaneously Reduced and Functionalized Graphene Oxide via Alkanolamine(s)/Alkyl Alkanolamine for Energy Storage Applications. *Chemical Engineering Journal* 2019, 363, 120–132.

(125.) Gogotsi, Y.; Anasori, B. The Rise of MXenes. *ACS Nano* 2019, 13, 8491–8494.

(126.) Bao, Z.; Lu, C.; Cao, X.; Zhang, P.; Yang, L.; Zhang, H.; Sha, D.; He, W.; Zhang, W.; Pan, L.; Sun, Z. Role of MXene Surface Terminations in Electrochemical Energy Storage: A Review. *Chinese Chemical Letters* 2021, 32, 2648–2658.

(127.) Arole, K.; Blivin, J. W.; Saha, S.; Holta, D. E.; Zhao, X.; Sarmah, A.; Cao, H.; Radovic, M.; Lutkenhaus, J. L.; Green, M. J. Water-Dispersible Ti3C2Tz MXene Nanosheets by Molten Salt Etching. *iScience* 2021, 24, 103403.

(128.) Ghidiu, M.; Naguib, M.; Barsoum, M. W. Chemical and Electrochemical Intercalation of Ions and Molecules into MXenes. *2D Metal Carbides and Nitrides (MXenes): Structure, Properties and Applications* 2019, 161–175.

(129.) Mozafari, M.; Soroush, M. Surface Functionalization of MXenes. *Materials Advances* 2021, 2, 7277–7307.

(130.) Xia, Y.; Mathis, T. S.; Zhao, M. Q.; Anasori, B.; Dang, A.; Zhou, Z.; Cho, H.; Gogotsi, Y.; Yang, S. Thickness-Independent Capacitance of Vertically Aligned Liquid-Crystalline MXenes. *Nature* 2018, 557, 409–412.

(131.) Qiu, X.; Dai, L.; Li, H.; Qu, K.; Li, R. Pillaring Behavior of Organic Molecules on MXene: Insights from Molecular Dynamics Simulations. *Langmuir* 2023, 27, 57.

(132.) Karmakar, A.; Pombeiro, A. J. L. Recent Advances in Amide Functionalized Metal Organic Frameworks for Heterogeneous Catalytic Applications. *Coordination Chemistry Reviews* 2019, 395, 86–129.

(133.) Li, X.; Hao, X.; Wang, Z.; Abudula, A.; Guan, G. In-Situ Intercalation of NiFe LDH Materials: An Efficient Approach to Improve Electrocatalytic Activity and Stability for Water Splitting. *Journal of Power Sources* 2017, 347, 193–200.

(134.) Mashtalir, O.; Naguib, M.; Mochalin, V. N.; Dall'Agnese, Y.; Heon, M.; Barsoum, M. W.; Gogotsi, Y. Intercalation and Delamination of Layered Carbides and Carbonitrides. *Nature Communications* 2013, 4, 1–7.

(135.) Ledoux, R. L.; White, J. L. Infrared Studies of Hydrogen Bonding Interaction between Kaolinite Surfaces and Intercalated Potassium Acetate, Hydrazine, Formamide, and Urea. *Journal of Colloid and Interface Science* 1966, 21, 127–152.

(136.) Cao, W. T.; Chen, F. F.; Zhu, Y. J.; Zhang, Y. G.; Jiang, Y. Y.; Ma, M. G.; Chen, F. Binary Strengthening and Toughening of MXene/Cellulose Nanofiber Composite Paper with Nacre-Inspired Structure and Superior Electromagnetic Interference Shielding Properties. *ACS Nano* 2018, 12, 4583–4593.

(137.) An, H.; Habib, T.; Shah, S.; Gao, H.; Patel, A.; Echols, I.; Zhao, X.; Radovic, M.; Green, M. J.; Lutkenhaus, J. L. Water Sorption in MXene/Polyelectrolyte Multilayers for Ultrafast Humidity Sensing. *ACS Applied Nano Materials* 2019, 2, 948–955.

(138.) He, L.; Wang, J.; Wang, B.; Wang, X.; Zhou, X.; Cai, W.; Mu, X.; Hou, Y.; Hu, Y.; Song, L. Large-Scale Production of Simultaneously Exfoliated and Functionalized Mxenes as Promising Flame Retardant for Polyurethane. *Composites Part B: Engineering* 2019, 179, 107486.

(139.) Ghidiu, M.; Lukatskaya, M. R.; Zhao, M. Q.; Gogotsi, Y.; Barsoum, M. W. Conductive Two-Dimensional Titanium Carbide 'Clay' with High Volumetric Capacitance. *Nature* 2014, 516, 78–81.

(140.) Kittaka, S.; Yamamoto, H.; Higuma, S.; Sasaki, T. Intercalation of N-Alcohols in Vanadium Pentaoxide Hydrate from the Vapour Phase. *Journal of the Chemical Society, Faraday Transactions* 1992, 88, 715–718.

(141.) Thomas, C. I.; Karppinen, M. Intercalation of Primary Alcohols into Layered Titanoniobates. *Inorganic Chemistry* 2017, 56, 9132–9138.

(142.) Boykin, J. R.; Smith, L. J. Rapid Microwave-Assisted Grafting of Layered Perovskites with n-Alcohols. *Inorganic Chemistry* 2015, 54, 4177–4179.

(143.) Boota, M.; Urbankowski, P.; Porzio, W.; Barba, L.; Osti, N. C.; Bleuel, M.; Keum, J. K.; Mamontov, E. Understanding Functionalization of Titanium Carbide (MXene) with Quinones and Their Pseudocapacitance. *ACS Applied Energy Materials* 2020, 3, 4127–4133.

(144.) Ruiz-Hitzky, E.; Aranda, P.; Casal, B. New Polyoxyethylene Intercalation Materials in Vanadium Oxide Xerogel. *Journal of Materials Chemistry* 1992, 2, 581–582.

(145.) Nelson Lara; Eduardo Ruiz-Hitzky. Intercalation of Oxyethylene Compounds (Crown-Ethers and PEO) into Molybdenum Disulfide. *Journal of the Brazilian Chemical Society* 1996, 7, 193–197.

(146.) Zhan, J.; Lei, Z.; Zhang, Y. Non-Covalent Interactions of Graphene Surface: Mechanisms and Applications. *Chem* 2022, 8, 947–979.

(147.) Villanueva, A.; Ruiz-Hitzky, E. Intercalation Materials from Azamacrocycles and Layered Sulfides: Electrical and Electrochemical Behaviour. *Journal of Materials Chemistry* 2004, 14, 824–829.

(148.) Chen, X.; Chen, B. Macroscopic and Spectroscopic Investigations of the Adsorption of Nitroaromatic Compounds on Graphene Oxide, Reduced Graphene Oxide, and Graphene Nanosheets. *Environmental Science & Technology* 2015, 49, 6181–6189.

(149.) Ruiz-Hitzky, E. Conducting Polymers Intercalated in Layered Solids. *Advanced Materials* 1993, 5, 334–340.

(150.) He, S.; Sun, X.; Zhang, H.; Yuan, C.; Wei, Y.; Li, J. Preparation Strategies and Applications of MXene-Polymer Composites: A Review. *Macromolecular Rapid Communications* 2021, 42, 2100324.

(151.) Pan, X. ren; Wang, M.; Qi, X. dong; Zhang, N.; Huang, T.; Yang, J. hui; Wang, Y. Fabrication of Sandwich-Structured PPy/MoS2/PPy Nanosheets for Polymer Composites with High Dielectric Constant, Low Loss and High Breakdown Strength. *Composites Part A: Applied Science and Manufacturing* 2020, 137, 106032.

(152.) Liang, Y.; Yoo, H. D.; Li, Y.; Shuai, J.; Calderon, H. A.; Robles Hernandez, F. C.; Grabow, L. C.; Yao, Y. Interlayer-Expanded Molybdenum Disulfide Nanocomposites for Electrochemical Magnesium Storage. *Nano Letters* 2015, 15, 2194–2202.

(153.) Li, Y.; Liang, Y.; Robles Hernandez, F. C.; Deog Yoo, H.; An, Q.; Yao, Y. Enhancing Sodium-Ion Battery Performance with Interlayer-Expanded MoS2–PEO Nanocomposites. *Nano Energy* 2015, 15, 453–461.

(154.) Liu, Y. J.; Kanatzidis, M. G.; DeGroot, D. C.; Schindler, J. L.; Kannewurf, C. R. Intercalation of Poly(Ethylene Oxide) in V2O5Xerogel. *Chemistry of Materials* 1991, 3, 992–994.

(155.) Ruiz-Hitzky, E.; Jimenez, R.; Casal, B.; Manriquez, V.; Ana, A. S.; Gonzalez, G. PEO Intercalation in Layered Chalcogenides. *Advanced Materials* 1993, 5, 738–741.

(156.) Ruiz-Hitzky, E.; Aranda, P.; Casal, B. New Polyoxyethylene Intercalation Materials in Vanadium Oxide Xerogel. *Journal of Materials Chemistry* 1992, 2, 581–582.

(157.) Zhang, X.; Zeng, X.; Yang, M.; Qi, Y. Investigation of a Branchlike MoO3/Polypyrrole Hybrid with Enhanced Electrochemical Performance Used as an Electrode in Supercapacitors. *ACS Applied Materials and Interfaces* 2014, 6, 1125–1130.

(158.) Xie, A.; Tao, F.; Chen, P.; -, al; Cao, Y.; Qi, Y.; Meng, X.; Liu, J.; An, J.; Ma, Y.; De, S.; Dey, A.; De, S. K. Characterization and Electrical Properties of Vanadyl

Phosphate–Polypyrrole Nanocomposites. *Journal of Physics D: Applied Physics* 2006, 39, 500.

(159.) Wang, L.; Schindler, J.; Thomas, J.A.; Kannewurf, C. R.; Kanatzidis, M. G. Entrapment of Polypyrrole Chains between MoS2 Layers via an in Situ Oxidative Polymerization Encapsulation Reaction. *Chemistry of Materials* 1995, 7, 55.

(160.) Tian, Y.; Song, X.; Liu, J.; Zhao, L.; Zhang, P.; Gao, L.; Tian, Y.; Song, X. F.; Liu, J.; Zhao, L.; Zhang, P.; Gao, L. Generation of Monolayer MoS2 with 1T Phase by Spatial-Confinement-Induced Ultrathin PPy Anchoring for High-Performance Supercapacitor. *Advanced Materials Interfaces* 2019, 6, 1900162.

(161.) Feng, Z.; Sun, J.; Liu, Y.; Jiang, H.; Cui, M.; Hu, T.; Meng, C.; Zhang, Y. Engineering Interlayer Space of Vanadium Oxide by Pyridinesulfonic Acid-Assisted Intercalation of Polypyrrole Enables Enhanced Aqueous Zinc-Ion Storage. *ACS Applied Materials and Interfaces* 2021, 13, 61154–61165.

(162.) Huang, W.S.; Humphrey, B. D.; Macdiarmid, A. G. Polyaniline, a Novel Conducting Polymer Morphology and Chemistry of Its Oxidation and Reduction in Aqueous Electrolytes. *Journal of the Chemical Society, Faraday Transactions 1: Physical Chemistry in Condensed Phases* 1986, 82, 2385–2400.

(163.) Yu, H.; Long, Y.; Chen, D.; Dong, X.; Ye, X.; Zhang, Y.; Li, F.; Xu, Y.; Tao, Y.; Yang, Q. H. Proton Is Essential or Not: A Fresh Look on Pseudocapacitive Energy Storage of PANI Composites. *Small* 2024, 20, 2303832.

(164.) Wang, J.; Wu, Z.; Hu, K.; Chen, X.; Yin, H. High Conductivity Graphene-like MoS2/Polyaniline Nanocomposites and Its Application in Supercapacitor. *Journal of Alloys and Compounds* 2015, 619, 38–43.

(165.) Kumar, N. A.; Choi, H. J.; Shin, Y. R.; Chang, D. W.; Dai, L.; Baek, J. B. Polyaniline-Grafted Reduced Graphene Oxide for Efficient Electrochemical Supercapacitors. *ACS Nano* 2012, 6, 1715–1723.

(166.) Yin, C.; Pan, C.; Liao, X.; Pan, Y.; Yuan, L. Regulating the Interlayer Spacing of Vanadium Oxide by in Situ Polyaniline Intercalation Enables an Improved Aqueous Zinc-Ion Storage Performance. *ACS Applied Materials and Interfaces* 2021, 13, 39347–39354.

(167.) Li, R.; Xing, F.; Li, T.; Zhang, H.; Yan, J.; Zheng, Q.; Li, X. Intercalated Polyaniline in V2O5 as a Unique Vanadium Oxide Bronze Cathode for Highly Stable Aqueous Zinc Ion Battery. *Energy Storage Materials* 2021, 38, 590–598.

(168.) Murugan, A. V.; Quintin, M.; Delville, M. H.; Campet, G.; Gopinath, C. S.; Vijayamohanan, K. Exfoliation-Induced Nanoribbon Formation of Poly(3,4-Ethylene Dioxythiophene) PEDOT between MoS2 Layers as Cathode Material for Lithium Batteries. *Journal of Power Sources* 2006, 156, 615–619.

(169.) Xu, L.; Zhang, Y.; Feng, L.; Li, X.; An, Q. A Facile Preparation Method for MoS2 Nanosheets and Their Well-Controllable Interfacial Assembly with PEDOT: PSS for Effective Electrochemical Hydrogen Evolution Reactions. *Journal of Materials Science* 2021, 56, 7008–7021.

(170.) Yao, Z.; Yu, Y.; Wu, Q.; Cui, M.; Zhou, X.; Liu, J.; Li, C.; Yao, Z. G.; Yu, Y. F.; Wu, Q. P.; Cui, M. N.; Zhou, X. J.; Liu, J. J.; Li, C. L. Maximizing Magnesiation Capacity of Nanowire Cluster Oxides by Conductive Macromolecule Pillaring and Multication Intercalation. *Small* 2021, 17, 2102168.

(171.) Namsheer, K.; Rout, C. S. Conducting Polymers: A Comprehensive Review on Recent Advances in Synthesis, Properties and Applications. *RSC Advances* 2021, 11, 5659–5697.

(172.) Ruiz-Hitzky, E. Conducting Polymers Intercalated in Layered Solids. *Advanced Materials* 1993, 5, 334–340.

(173.) Van Der Ven, A.; Bhattacharya, J.; Belak, A. A. Understanding Li Diffusion in Li-Intercalation Compounds. *Accounts of Chemical Research* 2013, 46, 1216–1225.

(174.) Valentini, C.; Montes-García, V.; Ciesielski, A.; Samorì, P. Boosting Zinc Hybrid Supercapacitor Performance via Thiol Functionalization of Graphene-Based Cathodes. *Advanced Science* 2024, 11, 2309041.

(175.) Kepp, K. P. A Quantitative Scale of Oxophilicity and Thiophilicity. *Inorganic Chemistry* 2016, 55, 9461–9470.

(176.) Santa Ana, M. A.; Mirabal, N.; Benavente, E.; Gómez-Romero, P.; González, G. Electrochemical Behavior of Lithium Intercalated in a Molybdenum Disulfide-Crown Ether Nanocomposite. *Electrochimica Acta* 2007, 53, 1432–1438.

(177.) Zhou, Y. N.; Ma, J.; Hu, E.; Yu, X.; Gu, L.; Nam, K. W.; Chen, L.; Wang, Z.; Yang, X. Q. Tuning Charge–Discharge Induced Unit Cell Breathing in Layer-Structured Cathode Materials for Lithium-Ion Batteries. *Nature Communications 2014*, 5, 1–8.

(178.) Li, J.; Östling, M. Prevention of Graphene Restacking for Performance Boost of Supercapacitors—A Review. *Crystals* 2013, 3, 163–190.

(179.) Dong, J.; Jiang, Y.; Wei, Q.; Tan, S.; Xu, Y.; Zhang, G.; Liao, X.; Yang, W.; Li, Q.; An, Q.; Mai, L.; Dong, J.; Jiang, Y. L.; Wei, Q. L.; Tan, S. S.; Xu, Y. N.; Zhang, G. B.; Liao, X. B.; Yang, W.; Li, Q. D.; An, Q. Y.; Mai, L. Q. Strongly Coupled Pyridine-V2O5·nH2O Nanowires with Intercalation Pseudocapacitance and Stabilized Layer for High Energy Sodium Ion Capacitors. *Small* 2019, 15, 1900379.

(180.) Xiao, B. Intercalated Water in Aqueous Batteries. *Carbon Energy* 2020, 2, 251–264.

(181.) Wang, J.; Jiang, D.; Zhang, M.; Sun, Y.; Jiang, M.; Du, Y.; Liu, J. Ice Crystal-Assisted Intercalation of PANI within Ti3C2Tx MXene Thin Films for Flexible Supercapacitor Electrodes with Simultaneously High Mechanical Strength and Rate Performance. *Journal of Materials Chemistry A* 2023, 11, 1419–1429.

(182.) Sun, Q.; Cheng, H.; Nie, W.; Lu, X.; Zhao, H. A Comprehensive Understanding of Interlayer Engineering in Layered Manganese and Vanadium Cathodes for Aqueous Zn-Ion Batteries. *Chemistry – An Asian Journal* 2022, 17, e202200067

(183.) Kim, H.-S.; Cook, J. B.; Tolbert, S. H.; Dunn, B. The Development of Pseudocapacitive Properties in Nanosized-MoO2. *Journal of the Electrochemical Society* 2015, 162, A5083–A5090.

(184.) Tang, W.; Peng, C. X.; Nai, C. T.; Su, J.; Liu, Y. P.; Reddy, M. V. V.; Lin, M.; Loh, K. P. Ultrahigh Capacity Due to Multi-Electron Conversion Reaction in Reduced Graphene Oxide-Wrapped MoO2 Porous Nanobelts. *Small* 2015, 11, 2446–2453.

(185.) He, C.; Wu, S.; Zhao, N.; Shi, C.; Liu, E.; Li, J. Carbon-Encapsulated Fe3O4 Nanoparticles as a High-Rate Lithium Ion Battery Anode Material. *ACS Nano* 2013, 7, 4459–4469.

(186.) Yao, Y.; Chen, Z.; Yu, R.; Chen, Q.; Zhu, J.; Hong, X.; Zhou, L.; Wu, J.; Mai, L. Confining Ultrafine MoO2 in a Carbon Matrix Enables Hybrid Li Ion and Li Metal Storage. *ACS Applied Materials and Interfaces* 2020, 12, 40648–40654.

(187.) Dubal, D. P.; Ayyad, O.; Ruiz, V.; Gómez-Romero, P. Hybrid Energy Storage: The Merging of Battery and Supercapacitor Chemistries. *Chemical Society Reviews* 2015, 44, 1777–1790.

(188.) Fleischmann, S.; Tolosa, A.; Presser, V. Design of Carbon/Metal Oxide Hybrids for Electrochemical Energy Storage. *Chemistry – A European Journal* 2018, 24, 12143–12153.

(189.) Lou, X. W.; Deng, D.; Lee, J. Y.; Archer, L. A. Preparation of SnO2/Carbon Composite Hollow Spheres and Their Lithium Storage Properties. *Chemistry of Materials* 2008, 20, 6562–6566.

(190.) Clites, M.; Andris, R.; Cullen, D. A.; More, K. L.; Pomerantseva, E. Improving Electronic Conductivity of Layered Oxides through the Formation of Two-Dimensional Heterointerface for Intercalation Batteries. *ACS Applied Energy Materials* 2020, 3, 3835–3844.

(191.) Norouzi, N.; Omo-Lamai, D.; Alimohammadi, F.; Averianov, T.; Kuang, J.; Yan, S.; Wang, L.; Stavitski, E.; Leshchev, D.; Takeuchi, K. J.; Takeuchi, E. S.; Marschilok, A. C.; Bock, D. C.; Pomerantseva, E. The Dopamine Assisted Synthesis of MoO3/Carbon Electrodes With Enhanced Capacitance in Aqueous Electrolyte. *Frontiers in Chemistry* 2022, 10, 873462.

(192.) Norouzi, N.; Averianov, T.; Kuang, J.; Bock, D. C.; Yan, S.; Wang, L.; Takeuchi, K. J.; Takeuchi, E. S.; Marschilok, A. C.; Pomerantseva, E. Hierarchically Structured MoO2/Dopamine-Derived Carbon Spheres as Intercalation Electrodes for Lithium-Ion Batteries. *Materials Today Chemistry* 2022, 24, 100783.

(193.) Andris, R.; Averianov, T.; Pomerantseva, E. Phase Transformation and Electrochemical Charge Storage Properties of Vanadium Oxide/Carbon Composite Electrodes Synthesized via Integration with Dopamine. *Journal of the American Ceramic Society* 2023, 106, 120–132.

(194.) Barim, G.; Dhall, R.; Arca, E.; Kuykendall, T. R.; Yin, W.; Takeuchi, K. J.; Takeuchi, E. S.; Marschilok, A. C.; Doeff, M. M. Heterostructured Lepidocrocite Titanate-Carbon Nanosheets for Electrochemical Applications. *ACS Appl. Nano Materials* 2022, 5, 678–690.

(195.) Zhao, C.; Wang, X.; Kong, J.; Ang, J. M.; Lee, P. S.; Liu, Z.; Lu, X. Self-Assembly-Induced Alternately Stacked Single-Layer MoS2 and N-Doped Graphene: A Novel van Der Waals Heterostructure for Lithium-Ion Batteries. *ACS Applied Materials and Interfaces* 2016, 8, 2372–2379.

(196.) Pomerantseva, E.; Gogotsi, Y. Two-Dimensional Heterostructures for Energy Storage. *Nature Energy* 2017, 2, 17089.

(197.) Khan, A.; Azadmanjiri, J.; Wu, B.; Liping, L.; Sofer, Z.; Min, J. Atomically Thin Nanosheets Confined in 2D Heterostructures: Metal-Ion Batteries Prospective. *Advanced Energy Materials* 2021, 11, 2100451.

(198.) Bragg, W. H.; Bragg Apr, W. L.; H Bragg, B. W.; Professor of Physics, C. The Reflection of X-Rays by Crystals. *Proceedings of the Royal Society of London. Series A, Containing Papers of a Mathematical and Physical Character* 1913, 88, 428–438.

(199.) Appendix E: Fourier Transform Infrared Spectroscopy. *Surface Design: Applications in Bioscience and Nanotechnology* 2009, 476–478.

(200.) Weiling, M.; Pfeiffer, F.; Baghernejad, M.; Weiling, M.; Pfeiffer, F.; Baghernejad, M. Vibrational Spectroscopy Insight into the Electrode|electrolyte Interface/Interphase in Lithium Batteries. *Advanced Energy Materials* 2022, 12, 2202504.

(201.) Flores, E.; Novák, P.; Berg, E. J. In Situ and Operando Raman Spectroscopy of Layered Transition Metal Oxides for Li-Ion Battery Cathodes. *Frontiers Energy Research* 2018, 6, 384736.

(202.) Haro-Poniatowski, E.; Julien, C.; Pecquenard, B.; Livage, J.; Camacho-López, M. A. Laser-Induced Structural Transformations in MoO3 Investigated by Raman Spectroscopy 1998.

(203.) Knirsch, K. C.; Berner, N. C.; Nerl, H. C.; Cucinotta, C. S.; Gholamvand, Z.; McEvoy, N.; Wang, Z.; Abramovic, I.; Vecera, P.; Halik, M.; Sanvito, S.; Duesberg, G. S.; Nicolosi, V.; Hauke, F.; Hirsch, A.; Coleman, J. N.; Backes, C. Basal-Plane Functionalization of Chemically Exfoliated Molybdenum Disulfide by Diazonium Salts. *ACS Nano* 2015, 9, 6018–6030.

(204.) Mosca, S.; Conti, C.; Stone, N.; Matousek, P. Spatially Offset Raman Spectroscopy. *Nature Reviews Methods Primers* 2021, 1, 1–16.

(205.) Saadatkhah, N.; Carillo Garcia, A.; Ackermann, S.; Leclerc, P.; Latifi, M.; Samih, S.; Patience, G. S.; Chaouki, J. Experimental Methods in Chemical Engineering: Thermogravimetric Analysis—TGA. *Canadian Journal of Chemical Engineering* 2020, 98, 34–43.

(206.) Elmanzalawy, M.; Innocenti, A.; Zarrabeitia, M.; Peter, N. J.; Passerini, S.; Augustyn, V.; Fleischmann, S. Mechanistic Understanding of Microstructure Formation during Synthesis of Metal Oxide/Carbon Nanocomposites. *Journal of Materials Chemistry A* 2023, 11, 17125–17137.

(207.) Zhou, W.; Apkarian, R.; Wang, Z. L.; Joy, D. Fundamentals of Scanning Electron Microscopy (SEM). *Scanning Microscopy for Nanotechnology: Techniques and Applications* 2006, 1–40.

(208.) Appendix G: Scanning Electron Microscopy. *Surface Design: Applications in Bioscience and Nanotechnology* 2009, 483–484.

(209.) Appendix B: Atomic Force Microscopy. *Surface Design: Applications in Bioscience and Nanotechnology* 2009, 467–470.

(210.) Tsai, W. Y.; Wang, R.; Boyd, S.; Augustyn, V.; Balke, N. Probing Local Electrochemistry via Mechanical Cyclic Voltammetry Curves. *Nano Energy* 2021, 81, 105592.

(211.) Luo, C.; Wang, C.; Wu, X.; Zhang, J.; Chu, J. In Situ Transmission Electron Microscopy Characterization and Manipulation of Two-Dimensional Layered Materials beyond Graphene. *Small* 2017, 13, 1604259.

(212.) Shin, Y.; Stepien, D.; Hepp, M.; Butz, B.; Bresser, D.; Fleischmann, S. Cryogenic Electron Microscopy Workflows for the Characterization of Electrochemical Interfaces and Interphases in Batteries. *Journal of Power Sources* 2023, 556, 232515.

(213.) Sauerbrey, G. Verwendung von Schwingquarzen Zur Wägung Dünner Schichten Und Zur Mikrowägung. *Zeitschrift für Physik* 1959, 155, 206–222.

(214.) Dargel, V.; Shpigel, N.; Sigalov, S.; Nayak, P.; Levi, M. D.; Daikhin, L.; Aurbach, D. In Situ Real-Time Gravimetric and Viscoelastic Probing of Surface Films Formation on Lithium Batteries Electrodes. *Nature Communications 2017*, 8, 1–8.

(215.) Levi, M. D.; Daikhin, L.; Aurbach, D.; Presser, V. Quartz Crystal Microbalance with Dissipation Monitoring (EQCM-D) for in-Situ Studies of Electrodes for Supercapacitors and Batteries: A Mini-Review. *Electrochemistry Communications* 2016, 67, 16–21.

(216.) Heubner, C.; Maletti, S.; Lohrberg, O.; Lein, T.; Liebmann, T.; Nickol, A.; Schneider, M.; Michaelis, A. Electrochemical Characterization of Battery Materials in 2-Electrode Half-Cell Configuration: A Balancing Act Between Simplicity and Pitfalls. *Batteries & Supercaps* 2021, 4, 1310–1322.

(217.) Chen, Z.; Zhang, L.; Wu, X.; Song, K.; Ren, B.; Li, T.; Zhang, S. Effect of N/P Ratios on the Performance of LiNi0.8Co0.15Al0.05O2||SiOx/Graphite Lithium-Ion Batteries. *Journal of Power Sources* 2019, 439, 227056.

(218.) Nölle, R.; Beltrop, K.; Holtstiege, F.; Kasnatscheew, J.; Placke, T.; Winter, M. A Reality Check and Tutorial on Electrochemical Characterization of Battery Cell Materials: How to Choose the Appropriate Cell Setup. *Materials Today* 2020, 32, 131–146.

(219.) Gogotsi, Y.; Penner, R. M. Energy Storage in Nanomaterials - Capacitive, Pseudocapacitive, or Battery-Like? *ACS Nano* 2018, 12, 2081–2083.

(220.) Middlemiss, L. A.; Rennie, A. J. R.; Sayers, R.; West, A. R. Characterisation of Batteries by Electrochemical Impedance Spectroscopy. *Energy Reports* 2020, 6, 232–241.

(221.) Lazanas, A. C.; Prodromidis, M. I. Electrochemical Impedance Spectroscopy─A Tutorial. *ACS Measurement Science Au* 2023, 3, 162–193.

(222.) Meddings, N.; Heinrich, M.; Overney, F.; Lee, J. S.; Ruiz, V.; Napolitano, E.; Seitz, S.; Hinds, G.; Raccichini, R.; Gaberšček, M.; Park, J. Application of Electrochemical Impedance Spectroscopy to Commercial Li-Ion Cells: A Review. *Journal of Power Sources* 2020, 480, 228742.

(223.) Kresse, G.; Furthmüller, J. Efficiency of Ab-Initio Total Energy Calculations for Metals and Semiconductors Using a Plane-Wave Basis Set. *Computational Materials Science* 1996, 6, 15–50.

(224.) Kresse, G.; Furthmüller, J. Efficient Iterative Schemes for Ab Initio Total-Energy Calculations Using a Plane-Wave Basis Set. *Physical Review B* 1996, 54, 11169.

(225.) Perdew, J. P.; Burke, K.; Ernzerhof, M. Generalized Gradient Approximation Made Simple. *Physical Review Letters* 1996, 77, 3865.

(226.) Blöchl, P. E. Projector Augmented-Wave Method. *Physical Review B* 1994, 50, 17953.

(227.) Monkhorst, H. J.; Pack, J. D. Special Points for Brillouin-Zone Integrations. *Physical Review B* 1976, 13, 5188.

(228.) Grimme, S.; Antony, J.; Ehrlich, S.; Krieg, H. A Consistent and Accurate Ab Initio Parametrization of Density Functional Dispersion Correction (DFT-D) for the 94 Elements H-Pu. *Journal of Chemical Physics* 2010, 132, 154104.

(229.) Freedman, M. L. Precipitation of Molybdenum (VI) in Strongly Acid Solutions. *Journal of Chemical & Engineering Data* 1963, 8, 113–116.

(230.) Walton, J.; Wincott, P.; Fairley, N.; Carrick, A. *Peak Fitting with CasaXPS: A Casa Pocket Book* 2010.

(231.) Weingarth, D.; Zeiger, M.; Jäckel, N.; Aslan, M.; Feng, G.; Presser, V. Graphitization as a Universal Tool to Tailor the Potential-Dependent Capacitance of Carbon Supercapacitors. *Advanced Energy Materials* 2014, 4, 1400316.

(232.) Hu, D.; Miao, L.; Zhang, Z.; Li, L.; Wang, Y.; Cheng, H.; Sewvandi, G. A.; Feng, Q.; Fan, M.; Zhao, L. One-Dimensional Piezoelectric BaTiO3 Polycrystal of Topochemical Mesocrystal Conversion from Layered H2Ti4O9·H2O Single Crystal. *Crystal Growth & Design* 2018, 18, 7264–7274.

(233.) Gao, T.; Fjellvåg, H.; Norby, P. Crystal Structures of Titanate Nanotubes: A Raman Scattering Study. *Inorganic Chemistry* 2009, 48, 1423–1432.

(234.) Fleischmann, S.; Pfeifer, K.; Widmaier, M.; Shim, H.; Budak, Ö.; Presser, V. Understanding Interlayer Deprotonation of Hydrogen Titanium Oxide for High-Power Electrochemical Energy Storage. *ACS Applied Energy Materials* 2019, 2, 3633–3641.

(235.) Fleischmann, S.; Sun, Y.; Osti, N. C.; Wang, R.; Mamontov, E.; Jiang, D. E.; Augustyn, V. Interlayer Separation in Hydrogen Titanates Enables Electrochemical Proton Intercalation. *Journal of Materials Chemistry A* 2020, 8, 412–421.

(236.) Chen, D.; Liu, M.; Yin, L.; Li, T.; Yang, Z.; Li, X.; Fan, B.; Wang, H.; Zhang, R.; Li, Z.; Xu, H.; Lu, H.; Yang, D.; Sun, J.; Gao, L. Single-Crystalline MoO3 Nanoplates: Topochemical Synthesis and Enhanced Ethanol-Sensing Performance. *Journal of Materials Chemistry* 2011, 21, 9332–9342.

(237.) Zhou, C.; Wang, D.; Lagunas, F.; Atterberry, B.; Lei, M.; Hu, H.; Zhou, Z.; Filatov, A. S.; Jiang, D.; Rossini, A. J.; Klie, R. F.; Talapin, D. V. Hybrid Organic–Inorganic Two-Dimensional Metal Carbide MXenes with Amido- and Imido-Terminated Surfaces. *Nature Chemistry* 2023, 15, 1722–1729.

(238.) Karol, J.; Ogolla, C. O.; Dillenz, M.; Sotoudeh, M.; Vollmer, E.; Zarrabeitia, M.; Groß, A.; Butz, B.; Fleischmann, S. Nanoconfinement Geometry of Pillared V2O5 Determines Electrochemical Ion Intercalation Mechanism and Diffusion Pathway. *ChemRxiv* 2024

(239.) Amorim da Costa, A. M.; Marques, M. P. M.; Batista de Carvalho, L. A. E. The Carbon□hydrogen Stretching Region of the Raman Spectra of 1,6-Hexanediamine: N-Deuteration, Ionisation and Temperature Effects. *Vibrational Spectroscopy* 2002, 29, 61–67.

(240.) Tao, G.; Fjellvåg, H.; Norby, P. Raman Scattering Properties of a Protonic Titanate HxTi 2-x/4□x/4O4·H2O (□, Vacancy; x = 0.7) with Lepidocrocite-Type Layered Structure. *Journal of Physical Chemistry B* 2008, 112, 9400–9405.

(241.) Byeon, S. H.; Lee, S. O.; Kim, H. Structure and Raman Spectra of Layered Titanium Oxides. *Journal of Solid State Chemistry* 1997, 130, 110–116.

(242.) Qian, L.; Du, Z. L.; Yang, S. Y.; Jin, Z. S. Raman Study of Titania Nanotube by Soft Chemical Process. *Journal of Molecular Structure* 2005, 749, 103–107.

(243.) Hu, D.; Miao, L.; Zhang, Z.; Li, L.; Wang, Y.; Cheng, H.; Sewvandi, G. A.; Feng, Q.; Fan, M.; Zhao, L. One-Dimensional Piezoelectric BaTiO3 Polycrystal of Topochemical Mesocrystal Conversion from Layered H2Ti4O9·H2O Single Crystal. *Crystal Growth & Design* 2018, 18, 7264–7274.

(244.) Jiang, F.; Zheng, Z.; Xu, Z.; Zheng, S. Preparation and Characterization of SiO2-Pillared H2Ti4O9 and Its Photocatalytic Activity for Methylene Blue Degradation. *Journal of Hazardous Materials* 2009, 164, 1250–1256.

(245.) Je, A.; Nethravathi, C.; Rajamathi, M. Nitrogen-Doped Alkylamine-Intercalated Layered Titanates for Photocatalytic Dye Degradation. *ACS Omega* 2019, 4, 1, 1575–1580.

(246.) Hua, Y.; Subramaniam, V. P.; Gong, D.; Tang, Y.; Highfield, J.; Pehkonen, S. O.; Pichat, P.; Schreyer, M. K.; Chen, Z. Nitrogen-Sensitized Dual Phase Titanate / Titania for Visible-Light Driven Phenol Degradation. *Journal of Solid State Chemistry* 2012, 196, 518–527.

(247.) Wang, J.; Polleux, J.; Lim, J.; Dunn, B. Pseudocapacitive Contributions to Electrochemical Energy Storage in TiO 2 (Anatase) Nanoparticles. *Journal of Physical Chemistry C* 2007, 111, 14925–14931.

(248.) Saeed, S.; Fleischmann, S.; Kobayashi, T.; Jusys, Z.; Mamontov, E.; Osti, N. C.; Holzapfel, N. P.; Song, H.; Wang, T.; Dai, S.; Jiang, D.; Augustyn, V. Oxide Acidity Modulates Structural Transformations in Hydrogen Titanates during Electrochemical Li-Ion Insertion. *Journal of the American Chemical Soc*iety 2024, 146, 42, 28795–28808

(249.) Escher, I.; Hahn, M.; Ferrero, G. A.; Adelhelm, P. A Practical Guide for Using Electrochemical Dilatometry as Operando Tool in Battery and Supercapacitor Research. *Energy Technology* 2022, 10, 2101120.

(250.) Goktas, M.; Bolli, C.; Berg, E. J.; Novák, P.; Pollok, K.; Langenhorst, F.; Roeder, M. v.; Lenchuk, O.; Mollenhauer, D.; Adelhelm, P. Graphite as Cointercalation Electrode for Sodium-Ion Batteries: Electrode Dynamics and the Missing Solid Electrolyte Interphase (SEI). *Advanced Energy Materials* 2018, 8, 1702724.

(251.) Escher, I.; Kravets, Y.; Ferrero, G. A.; Goktas, M.; Adelhelm, P. Strategies for Alleviating Electrode Expansion of Graphite Electrodes in Sodium-Ion Batteries Followed by In Situ Electrochemical Dilatometry. *Energy Technology* 2021, 9, 2000880.

(252.) Shpigel, N.; Levi, M. D.; Aurbach, D. EQCM-D Technique for Complex Mechanical Characterization of Energy Storage Electrodes: Background and Practical Guide. *Energy Storage Materials* 2019, 21, 399–413.

(253.) Miranda, J.; Franklin, G.; Mathis, T. S.; Taberna, P. L.; Simon, P. Unraveling the Two-Phase Lithiation Process in TiS2 by Using the Combination of Operando EQCM and Electrochemical Dilatometry Techniques. *Energy Storage Materials* 2024, 65, 103105.

(254.) Nikitina, V. A.; Vassiliev, S. Y.; Stevenson, K. J. Metal-Ion Coupled Electron Transfer Kinetics in Intercalation-Based Transition Metal Oxides. *Advanced Energy Materials* 2020, 10, 1903933.

(255.) Nikitina, V. A. Charge Transfer Processes in the Course of Metal-Ion Electrochemical Intercalation. *Curr Opin Electrochem* 2020, 19, 71–77.

(256.) Xu, K.; Cresce, A. Von; Lee, U. Differentiating Contributions to "Ion Transfer" Barrier from Interphasial Resistance and Li+ Desolvation at Electrolyte/Graphite Interface. *Langmuir* 2010, 26, 11538–11543.

(257.) Choi, W.; Shin, H. C.; Kim, J. M.; Choi, J. Y.; Yoon, W. S. Modeling and Applications of Electrochemical Impedance Spectroscopy (EIS) for Lithium-Ion Batteries. *Journal of Electrochemical Science and Technology* 2020, 11, 1–13.

(258.) Rodionov, I. A.; Maksimova, E. A.; Pozhidaev, A. Y.; Kurnosenko, S. A.; Silyukov, O. I.; Zvereva, I. A. Layered Titanate H2Nd2Ti3O10 Intercalated With N-Butylamine: A New Highly Efficient Hybrid Photocatalyst for Hydrogen Production From Aqueous Solutions of Alcohols. *Frontiers in Chemistry* 2019, 7, 504080.

(259.) Kurnosenko, S. A.; Voytovich, V. V.; Silyukov, O. I.; Minich, I. A.; Malygina, E. N.; Zvereva, I. A. Inorganic-Organic Derivatives of Layered Perovskite-like Titanates HLnTiO4 (Ln = La, Nd) with n-Amines and n-Alcohols: Synthesis,

Thermal, Vacuum and Hydrolytic Stability. *Ceramics International* 2022, 48, 7240–7252.

(260.) Tahara, S.; Ichikawa, T.; Kajiwara, G.; Sugahara, Y. Reactivity of the Ruddlesden-Popper Phase H2la 2Ti3O10 with Organic Compounds: Intercalation and Grafting Reactions. *Chemistry of Materials* 2007, 19, 2352–2358.

(261.) Kim, J.; Park, S.; Hwang, S.; Yoon, W. S. Principles and Applications of Galvanostatic Intermittent Titration Technique for Lithium-Ion Batteries. *Journal of Electrochemical Science and Technology* 2022, 13, 19–31.

(262.) Izawa, H.; Kikkawa, S.; Kolzuml, M. Ion Exchange and Dehydration of Layered Titanates, Na2Ti3O7 and K2Ti4O9. *Journal of Physical Chemistry* 1982, 86, 5023–5026.

(263.) Cao, M.; Shi, Z.; Chen, W.; Li, X.; Ma, Y.; Zhang, C. K2Ti4O9 Nanoribbon Arrays Functionalized with Graphene Quantum Dots for Superior Pseudocapacitive Sodium Storage. *ChemElectroChem* 2021, 8, 3410–3415.

(264.) Trinh, N. D.; Crosnier, O.; Schougaard, S. B.; Brousse, T. Synthesis, Characterization and Electrochemical Studies of Active Materials for Sodium Ion Batteries. *ECS Transactions* 2011, 35, 91–98.

(265.) Rudola, A.; Sharma, N.; Balaya, P. Introducing a 0.2 V Sodium-Ion Battery Anode: The Na2Ti3O7 to Na3 − XTi3O7 Pathway. *Electrochemistry Communications* 2015, 61, 10–13.

(266.) Song, J.; Xiao, D.; Jia, H.; Zhu, G.; Engelhard, M.; Xiao, B.; Feng, S.; Li, D.; Reed, D.; Sprenkle, V. L.; Lin, Y.; Li, X. A Comparative Study of Pomegranate Sb@C Yolk–Shell Microspheres as Li and Na-Ion Battery Anodes. *Nanoscale* 2018, 11, 348–355.

(267.) Yebka, B.; Julien, C.; Nazri, G. A. Electrochemical Behavior of Hydrated Molybdenum Oxides in Rechargeable Lithium Batteries. *Ionics* 1999, 5, 236–243.

(268.) Chen, D.; Liu, M.; Yin, L.; Li, T.; Yang, Z.; Li, X.; Fan, B.; Wang, H.; Zhang, R.; Li, Z.; Xu, H.; Lu, H.; Yang, D.; Sun, J.; Gao, L. Single-Crystalline MoO3 Nanoplates: Topochemical Synthesis and Enhanced Ethanol-Sensing Performance. *Journal of Materials Chemistry* 2011, 21, 9332–9342.

(269.) Yu, A.; Kumagai, N.; Liu, Z.; Lee, J. Y. Preparation of Sodium Molybdenum Oxides by a Solution Technique and Their Electrochemical Performance in Lithium Intercalation. *Solid State Ionics* 1998, 106, 11–18.

(270.) Jung, Y. S.; Lee, S.; Ahn, D.; Dillon, A. C.; Lee, S. H. Electrochemical Reactivity of Ball-Milled MoO3-y as Anode Materials for Lithium-Ion Batteries. *Journal of Power Sources* 2009, 188, 286–291.

(271.) Chen, D.; Li, T.; Yin, L.; Hou, X.; Yu, X.; Zhang, Y.; Fan, B.; Wang, H.; Li, X.; Zhang, R.; Hou, T.; Lu, H.; Xu, H.; Sun, J.; Gao, L. A Comparative Study on Reactions of N-Alkylamines with Tungstic Acids with Various W-O Octahedral Layers: Novel Evidence for the "Dissolution- Reorganization" Mechanism. *Materials Chemistry and Physics* 2011, 125, 838–845.

(272.) Spencer, M. A.; Fortunato, J.; Augustyn, V. Electrochemical Proton Insertion Modulates the Hydrogen Evolution Reaction on Tungsten Oxides. *Journal of Chemical Physics* 2022, 156, 064704.

(273.) Seguin, L.; Figlarz, M.; Cavagnat, R.; Lassègues, J.-C. Infrared and Raman Spectra of MoO3 Molybdenum Trioxides and MoO3·xH2O Molybdenum Trioxide Hydrates. *Spectrochimica Acta Part A* 1995, 51, 1323–1344.

(274.) Jiang, J.; May, I.; Sarsfield, M. J.; Ogden, M.; Fox, D. O.; Jones, C. J.; Mayhew, P. A Spectroscopic Study of the Dissolution of Cesium Phosphomolybdate and Zirconium Molybdate by Ammonium Carbamate. *Journal of Solution Chemistry* 2005, 34, 443–468.

(275.) Frost, R. L.; Bouzaid, J.; Butler, I. S. Raman Spectroscopic Study of the Molybdate Mineral Szenicsite and Comparison with Other Paragenetically Related Molybdate Minerals. *Spectroscopy Letters* 2007, 40, 603–614.

(276.) Lu, X.; Wang, R.; Yang, F.; Jiao, W.; Liu, W.; Hao, L.; He, X. Preparation of MoO3 QDs through Combining Intercalation and Thermal Exfoliation. *Journal of Materials Chemistry C* 2016, 4, 6720–6726.

(277.) Amorim, A. M.; Geraldes, C. F. G. C.; Teixeira, J. J. C. A Raman Spectroscopic Study of Molecular Interaction in Long-Chain Primary Amines Systems. *Journal of Raman Spectroscopy* 1982, 13, 56–62.

(278.) Camacho-López, M. A.; Escobar-Alarcón, L.; Picquart, M.; Arroyo, R.; Córdoba, G.; Haro-Poniatowski, E. Micro-Raman Study of the m-MoO2 to a-MoO3 Transformation Induced by Cw-Laser Irradiation. *Optical Materials* 2011, 33, 480–484.

(279.) Spevack, P. A.; McIntyre, N. S. Thermal Reduction of MoO3. *Journal of Physical Chemistry* 1992, 96, 9029–9035.

(280.) Ferrari, A. C.; Robertson, J. Interpretation of Raman Spectra of Disordered and Amorphous Carbon. *Physical Review B* 2000, 61, 14095–14107.

(281.) Kaniyoor, A.; Ramaprabhu, S. A Raman Spectroscopic Investigation of Graphite Oxide Derived Graphene. *AIP Advances* 2012, 2, 032183.

(282.) Wang, Z.; Wen, X.-D.; Hoffmann, R.; Son, J. S.; Li, R.; Fang, C.-C.; Smilgies, D.-M.; Hyeon, T. Reconstructing a Solid-Solid Phase Transformation Pathway in CdSe Nanosheets with Associated Soft Ligands. *Proceedings of the National Academy of Sciences* 2010, 107, 17119–17124.

(283.) Scanlon, D. O.; Watson, G. W.; Payne, D. J.; Atkinson, G. R.; Egdell, R. G.; Law, D. S. L. Theoretical and Experimental Study of the Electronic Structures of MoO 3 and MoO2. *Journal of Physical Chemistry C* 2010, 114, 4636–4645.

(284.) Baltrusaitis, J.; Mendoza-Sanchez, B.; Fernandez, V.; Veenstra, R.; Dukstiene, N.; Roberts, A.; Fairley, N. Generalized Molybdenum Oxide Surface Chemical State XPS Determination via Informed Amorphous Sample Model. *Applied Surface Science* 2015, 326, 151–161.

(285.) Wang, D.; Wang, J.; Luo, X.; Wu, Z.; Ye, L. In Situ Preparation of Mo2C Nanoparticles Embedded in Ketjenblack Carbon as Highly Efficient Electrocatalysts for Hydrogen Evolution. *ACS Sustainable Chemistry & Engineering* 2018, 6, 983–990.

(286.) Biesinger, M. C. Accessing the Robustness of Adventitious Carbon for Charge Referencing (Correction) Purposes in XPS Analysis: Insights from a Multi-User Facility Data Review. *Applied Surface Science* 2022, 597, 153681.

(287.) McLafferty, F. W.; Turecek, F. *Interpretation of Mass Spectra*, 1993.

(288.) Bowen, R. D.; Maccoll, A. Low Energy, Low Temperature Mass Spectra. *Organic Mass Spectrometry* 1983, 18, 576–581.

(289.) Chen, B.; Liu, J.; Chen, H.; Chen, W.; Lin, C. Comparison of the Characteristic Mass Fragmentations of Phenethylamines and Tryptamines by Electron Ionization Gas Chromatography Mass Spectrometry, Electrospray and Matrix-Assisted Laser Desorption Ionization Mass Spectrometry. *Applied Science* 2018, 8, 1022.

(290.) Wallace, W. E. Mass Spectra. *NIST Chemistry WebBook* 2018, 69, 20899.

(291.) Trif, L.; Franguelli, F. P.; Lendvay, G.; Majzik, E.; Béres, K.; Bereczki, L.; Szilágyi, I. M.; Pawar, R. P.; Kótai, L. Thermal Analysis of Solvatomorphic Decakis

(Dimethylammonium) Dihydrogendodecatungstate Hydrates. *Journal of Thermal Analysis and Calorimetry* 2021, 144, 81–90.

(292.) Swiatowska-Mrowiecka, J.; de Diesbach, S.; Maurice, V.; Zanna, S.; Klein, L.; Briand, E.; Vickridge, I.; Marcus, P. Li-Ion Intercalation in Thermal Oxide Thin Films of MoO3 as Studied by XPS, RBS, and NRA. *Journal of Phyical Chemistry C* 2008, 112, 11050–11058.

(293.) Tao, T.; Glushenkov, A. M.; Zhang, C.; Zhang, H.; Zhou, D.; Guo, Z.; Liu, H. K.; Chen, Q.; Hu, H.; Chen, Y. MoO3 Nanoparticles Dispersed Uniformly in Carbon Matrix: A High Capacity Composite Anode for Li-Ion Batteries. *Journal of Materials Chemistry* 2011, 21, 9350–9355.

(294.) Fleischmann, S.; Zeiger, M.; Quade, A.; Kruth, A.; Presser, V. Atomic Layer-Deposited Molybdenum Oxide/Carbon Nanotube Hybrid Electrodes: The Influence of Crystal Structure on Lithium-Ion Capacitor Performance. *ACS Applied Materials & Interfaces* 2018, 10, 18675–18684.

(295.) Okubo, M.; Hosono, E.; Kim, J.; Enomoto, M.; Kojima, N.; Kudo, T.; Zhou, H.; Honma, I. Nanosize Effect on High-Rate Li-Ion Intercalation in LiCoO2 Electrode. *Journal of the American Chemical Society* 2007, 129, 7444–7452.

(296.) Fleischmann, S.; Kamboj, I.; Augustyn, V. Nanostructured Transition Metal Oxides for Electrochemical Energy Storage. In *Transition Metal Oxides for Electrochemical Energy Storage*; 2022; 183–212.

(297.) Wagner, C. D.; Riggs, W. M.; Davis, L. E.; Moulder, J. F.; Muilenberg, G. E. *Handbook of X-Ray Photoelectron Spectroscopy* 1979.

(298.) William E. Wallace. Infrared Spectra in *NIST Chemistry WebBook, NIST Standard Reference Database Number 69*.

(299.) Kim, K. S.; Imris, M.; Shahverdi, A.; Alinejad, Y.; Soucy, G. Single-Walled Carbon Nanotubes Prepared by Large-Scale Induction Thermal Plasma Process: Synthesis, Characterization, and Purification. *Journal of Physical Chemistry C* 2009, 113, 4340–4348.

(300.) Kim, H. S.; Cook, J. B.; Lin, H.; Ko, J. S.; Tolbert, S. H.; Ozolins, V.; Dunn, B. Oxygen Vacancies Enhance Pseudocapacitive Charge Storage Properties of MoO3−x. *Nature Materials* 2016, 16, 454–460.

(301.) Gamby, J.; Taberna, P. L.; Simon, P.; Fauvarque, J. F.; Chesneau, M. Studies and Characterisations of Various Activated Carbons Used for Carbon/Carbon Supercapacitors. *Journal of Power Sources* 2001, 101, 109–116.

(302.) Kumar, S.; Rehman, M. A.; Lee, S.; Kim, M.; Hong, H.; Park, J. Y.; Seo, Y. Supercapacitors Based on Ti3C2Tx MXene Extracted from Supernatant and Current Collectors Passivated by CVD-Graphene. *Scientific Reports* 2021, 11, 1–9.

List of Publications

- **Elmanzalawy, M.**, Song, H., Tobis, M., Leiter, R., Choi, J., Moon, H., Tsai, W-Y., Jiang, D., and Fleischmann, S. (2025), Nanoconfinement-Induced Electrochemical Ion-Solvent Cointercalation in Pillared Titanate Host Materials. *Angewandte Chemie International Edition*, 64, e202423593. https://doi.org/10.1002/anie.202423593

- **Elmanzalawy**, M., Tobis, M., Tsai, W-Y., and Fleischmann, S. (2024), Interlayer expansion of hydrogen titanate anodes improves electrochemical Na^+ intercalation kinetics and reversibility, pre-print. DOI: 10.26434/chemrxiv-2024-d9x01

- Tobis, M., **Elmanzalawy, M.**, Choi, J., Frąckowiak, E., & Fleischmann, S. (2024). Controlling Structure and Morphology of MoS2 via Sulfur Precursor for Optimized Pseudocapacitive Lithium Intercalation Hosts. *Batteries & Supercaps*, e202400277. https://doi.org/10.1002/BATT.202400277

- Guo, H., **Elmanzalawy, M.**, Sivakumar, P., & Fleischmann, S. (2024). Unifying electrolyte formulation and electrode nanoconfinement design to enable new ion–solvent cointercalation chemistries. *Energy & Environmental Science*, *17*(6), 2100–2116. https://doi.org/10.1039/D3EE04350A

- **Elmanzalawy, M.**, Innocenti, A., Zarrabeitia, M., Peter, N. J., Passerini, S., Augustyn, V., & Fleischmann, S. (2023). Mechanistic understanding of microstructure formation during synthesis of metal oxide/carbon nanocomposites. *Journal of Materials Chemistry A*, *11*(32), 17125–17137. https://doi.org/10.1039/D3TA01230A

- Abdelkader, M., **Elmanzalawy, M.**, & Pauliukaite, R. (2022). 3-D Electrodes for Electrochemical Sensors: Review in Different Approaches. *IEEE Sensors Journal*, *22*(24), 23620–23632. https://doi.org/10.1109/JSEN.2022.3220815

- **Elmanzalawy, M.**, Sanchez-Ahijón, E., Kisacik, O., Carretero-González, J., & Castillo-Martínez, E. (2022). High Conductivity in a Fluorine-Free K-Ion Polymer Electrolyte. *ACS Applied Energy Materials*, *5* (7), 9009–9019. https://doi.org/10.1021/acsaem.2c01485

In preparation:

- **Elmanzalawy, M**., Fleischmann, S. "Organic interlayer functionalization of layered materials", in preparation.

Conferences and Symposia Contributions

- **M. Elmanzalawy**, M. Tobis, S. Fleischmann. Nanoconfinement-induced solvent co-intercalation in layered titanates enables fast lithiation kinetics. (Poster) at the GDCh Electrochemistry 2024 Conference, **2024**, Braunschweig, Germany.

- **M. Elmanzalawy**, S. Fleischmann. Solvent co-intercalation induced by nanoconfinement chemistry in layered titanates enables fast lithiation kinetics. (Poster) at the Lorentz Center Workshop on electrochemical energy storage in 2D and layered materials, **2023**, Leiden, the Netherlands. **Awarded best poster**.

- **M. Elmanzalawy**, S. Fleischmann. Improved electrochemical Li intercalation kinetics by tuning the interlayer environment of layered hydrogen titanates. (Poster) at the 74th Annual Meeting of the International Society of Electrochemistry, **2023**, Lyon, France.

- A. Ares Dorado, **M. Elmanzalawy**, J. Carretero-González, E. Castillo-Martinez. Electrolitos sólidos basados en óxido de polietileno libre de flúor para baterías de ion potasio. (Poster) at XLIII Reunión del Grupo Especializado de Electroquímica de la RSEQ, **2023**, Ciudad Real, Spain.

- **M. Elmanzalawy**, S. Fleischmann. Optimizing interlayer chemistry of layered titanates for improved Li+ intercalation kinetics. (Talk) at the 12th HIU Biennial Meeting, **2023**, Ulm, Germany.

- **M. Elmanzalawy**, S. Fleischmann. Optimizing interlayer chemistry of layered titanates for improved lithium intercalation kinetics and efficiency. (Talk) at the 2nd German-French Workshop on High Power Devices, **2023**, Nantes, France.

- **M. Elmanzalawy**, S. Fleischmann. n-alkylamine Functionalization of Hydrogen Tetratitanate. (Talk) at the 2nd EMG meeting, Leibniz Institute for New Materials (INM), **2023**, Saarbrucken, Germany.

- **M. Elmanzalawy**, Y. Shin, N. J. Peter, S. Fleischmann. Mechanistic understanding of 2D metal oxide – carbon heterostructure formation using pyrolysis. (Poster) at the International Battery Association Hybrid Conference, **2022**, Bled, Slovenia.

Acknowledgements

First and foremost, I would like to thank my supervisor, Dr. Simon Fleischmann, who gave me great guidance and support during this PhD, and even before that in Toulouse. His insight and constructive input have been invaluable, and allowed me to grow as a scientist. My sincere appreciation goes to Dr. Wan-Yu Tsai, for her support and mentorship during my time in Lille, both on the scientific and personal level. Financial support towards my stay in Lille through the KHYS Research Travel Grant is gratefully acknowledged.

My sincere appreciation goes to co-authors from HIU and beyond, who made this work possible. To all the friends I made at HIU, I appreciate you so much for your kindness. This has been an amazing 3-year journey, and I will remember it with fondness. I would like to thank the technical staff of HIU for efforts to make our labs safe and functional. I appreciated lovely conversations with Achim, whose positivity always brightened my day.

While the choice to uproot my life and pursue a PhD in Germany was, to say the least, scary, I could not have made it without the wonderful people I have met along the way. Thank you, Buraq, and I wish I had met you sooner. Your combined strength and softness inspire me so much. Thank you, Gaurav, and I wish you lived closer. Thank you Yuyoung and Anthony, for having been a major source of support (and laughter, and delicious food) during challenging times. Thank you, Milene, for being my wiser and cooler friend. Thank you, Nadine, for being the best neighbour I could ask for. Thank you, Nada and Timo, for our fun times together, and for your support in tough times. To the friends I made in Lille: Louis, Houssine, Milan, Paul, and Nano, thank you all for making me feel so welcome and I hope our paths cross again.

Thank you, Nesma, for being my rock for 11 years, for sticking through the good, the bad, and the ugly, and above all for believing in me. Words cannot describe how grateful I am to have you in my life. Thank you, Mirna, and Aya for being amazing friends. For you I would cross the Suez desert at 37°C weather.

Finally, this work is dedicated to my family. My parents, Adel and Entessar, and my brother, Mohamed, for their constant and unconditional support. I miss you very much every day. If I have achieved anything meaningful in life, it is because of you.